Preparation and characterization of protein templated metal nano-formulations and their wound healing applications

Thesis submitted in the fulfillment of the requirement of the degree of

Doctor of Philosophy

Submitted by

Deepinder Sharda

(Reg. No. 901909028)

Under the Supervision of

Dr. Diptiman Choudhury

(Associate Professor)

Department of Chemistry & Biochemistry

Co-leader of Cancer Detection and Treatment

Center of Excellence in Emerging Materials

Department of Chemistry and Biochemistry

Thapar Institute of Engineering and Technology

Patiala-147004, Punjab, India

December - 2024

Certificate

This is to certify that thesis entitled **"Preparation and characterization of protein templated metal nano-formulations and their wound healing applications"** being submitted by Deepinder Sharda **in the fulfilment of the requirement for the award of the Degree of Philosophy**, Department of Chemistry and Biochemistry, Thapar Institute of Engineering and Technology, Patiala, is an authentic record of candidate's own work carried out by him from December 2019 to September 2024 in this institute under our supervision and guidance. The matter embodied in this thesis has not been submitted in part or full to any other university or institute for the award of any degree in India or Abroad.

(Supervisor)

Dr. Diptiman Choudhury

Associate Professor

Department of Chemistry & Biochemistry

Co-leader of Cancer Detection and Treatment

Centre of Excellence in Emerging Materials

(TIET-VT, CEEMS)

TIET, Patiala - 147004

(Head)

Dr. Manmohan Chhibber

Professor & Head

Department of Chemistry & Biochemistry

TIET, Patiala - 147004

Candidate's Declaration

I, hereby declare that the work presented in the thesis entitled "**Preparation and characterization of protein templated metal nano-formulations and their wound healing applications**" in partial **fulfilment of the requirement for the award of the Degree of Philosophy**, Department of Chemistry and Biochemistry, Thapar Institute of Engineering and Technology, Patiala, is an authentic record of my own work carried out under the supervision of Dr. Diptiman Choudhury (Associate Professor, Department of Chemistry and Biochemistry, TIET, Patiala, India). The matter embodied in this thesis has not been submitted in part or full to any other university or institute for the award of any degree in India or Abroad.

Deepinder Sharda

Deepinder Sharda

Acknowledgements

I wholeheartedly thank my mighty God for giving me the vision, power, spirit and endurance to complete the interesting research.

Completion of this doctoral dissertation was possible with the support of people. I would like to express my sincere gratitude to all of them.

First and foremost, I would like to express my sincere gratitude to my esteemed research supervisor, **Dr. Diptiman Choudhury** for introducing me to this exciting field of science. His valuable guidance, continuous support, motivation, patience, scholarly insights, and consistent encouragement have been instrumental throughout my Ph.D. work. I have learned extensively from him, including how to view established questions from new perspectives and how to approach problems with systematic thinking. Despite his busy schedules, he have always been available to clarify my doubts, for which I am deeply appreciative. It has been a tremendous privilege to undertake my doctoral program under his guidance and to benefit from his research expertise. His mentorship has provided me with a comprehensive and enriching experience. His persistent courage and confidence will continue to inspire me, and I look forward to further engaging with his innovative ideas.

I extend my heartfelt gratitude to **Dr. Manmohan Chhibber, Professor and Head, DCBC, TIET, Patiala**. I am sincerely thankful to my doctoral committee members, **Dr. Manmohan Chhibber (Professor and Head, Department of Chemistry and Biochemistry), Dr. Vijay Luxami (Professor, Department of Chemistry and Biochemistry)** and **Dr. Siddharth Sharma (Professor, Department of Biotechnology)** for their valuable feedback during half yearly progress reports and dedication to ensuring the highest quality of research.

I am also very thankful to **Dr. Padmakumar Nair, Director, TIET and Dr. N. Tejo Prakash, Dean of Research and Development Cell (DoRDC)** for providing an excellent research environment and top-notch facilities for execution of my project work. Also, I would like to acknowledge the laboratories like **SAI Labs**, **TIET, Patiala**, **TIET-SEM Lab**, **Centre of Excellence in Emerging Materials (CEEMS)**, **TIET-VT and Sprint Testing Solutions, Mumbai** from where I received significant assistance with characterization.

I wish to extend my sincerest thanks to Dr. Amanpreet Kaur, to have been granted with the wonderful opportunity to collaborate with her, allowing me to broaden my horizons. My research progress would not have been as seamless without the financial backing provided by Indian Council of Medical Research (project no. 17X(3)/Adhoc/3/2022-ITR).

I extend my special thanks to **Komal Attri** for her compassionate support and constant motivation in every aspect. I am grateful to my seniors and fellow lab mates **Dr. Pawandeep Kaur, Dr. Vanshita Goel, Poulomi Chandra, Parmandeep Kaur, Sunidhi Sharma, Sanchi Sharma and Sukhmanpreet Kaur** for their generous sharing of knowledge, insights and companionship during this academic journey. The cooperative atmosphere within the academic community has deeply enhanced my experience and expanded my outlook.

I am profoundly grateful to my friends **Anjali Sharma, Disha Jindal, Isha Tanwar** for their unwavering emotional support and their presence in every possible way. Their encouragement, empathy, and companionship have provided a steady source of strength throughout my journey.

I am deeply indebted to **my family**, my father, **Mr. Bhupinder Kumar Sharda**, my mother, **Mrs. Rita Sharma**, my grandfather, **Mr. Ram Sarup Sharda**, my grandmother, **Mrs. Devki Devi** and my brother, **Mr. Dinkar Sharda** for their resolute support, encouragement and patience throughout my Ph.D. journey. They always stood by my side, whether facing challenges or celebrating triumphs. Their beliefs in my abilities fuels my confidence and determination to pursue my dreams.

Throughout this journey, I have encountered both challenges and rewards. I feel incredibly lucky to have received support and encouragement from many exceptional individuals. Thank you all for contributing significantly to my academic and personal development. Thank you for your everlasting love and support.

“DEVOTED TO
MY BELOVED
FAMILY”

Abbreviations

Å	Angstrom
AgNPs	Silver nanoparticles
Akt	Protein kinase B
ATCC	American Type Culture Collection
bFGF	Basal fibroblast Growth Factor
BSA	Bovine Serum Albumin
cm	Centimeter
CO_2	Carbon dioxide
˚C	Degree Celsius
CD	Circular Dichroism
CI	Combination Index
$CoCl_2.\ 6H_2O$	Cobalt chloride hexahydrate
$CuSO_4$	Copper sulfate
dl	Decilitre
DLS	Dynamic Light Scattering
DMEM	Dulbecco's Modified Eagle Medium
DMSO	Dimethyl sulphoxide
ECNP	Empty chitosan nanoparticles
EDAX	Electron dispersive X-ray spectroscopy
ERK	Extracellular signal regulated kinase
eNOS	Endothelial nitric oxide synthase
FOXO	Fork head box protein
FTIR	Fourier transform infrared
gm	Gram
GH	Growth hormone
ΔG	Gibbs free energy
h/hr	Hour
HCl	Hydrochloric acid
HEKa	Human Epidermal Keratinocytes (adult)
HIF	Hypoxia inducible factor
HR-TEM	High Resolution-Transmission Electron Microscopy
ΔH	Change in entropy
JAK	Janus kinase

JNK	Jun N-terminal kinase
ICNP	Insulin loaded chitosan nanoparticles
ICoNPs	Insulin Cobalt nanoparticles
ICuQCs	Insulin copper quantum clusters
ICu-AgNSCs	Insulin copper-silver nanosubclusters
IFN	Interferon-alpha
IGF	Insulin-like growth factor
IGF-1R	Insulin-like growth factor 1 receptor
IHC	Immuno-histochemical
IL	Interleukin
IR	Insulin receptor
IL-IR	Interleukin insulin receptor
INiQCs	Insulin nickel quantum clusters
KBr	Potassium bromide
$KMnO_4$	Potassium permanganate
K_d	Dissociation constant
Kg	Kilogram
M1	Pro-inflammatory macrophages
M2	Anti-inflammatory macrophages
MAPK	Mitogen-activated protein kinase
MEK	MAPK ERK kinase
mg	Milligram
MIB	Metal ion binding
min	Minutes
mm	Millimetre
MMP	Matrix metalloproteinase
mTOR	Mechanistic target of rapamycin
MTT	3-(4, 5-dimethylthiazol-2-yl)-2, 5-diphenyltetrazolium bromide
mV	Millivolt
µl	Microliter

µM	Micro molar
NADH	Nicotinamide adenine dinucleotide
NADP	Nicotinamide adenine dinucleotide phosphate
NaOH	Sodium hydroxide
NFkβ	Nuclear factor kappa beta
$NiSO_4$	Nickel sulphate
NK	Natural killer
nm	Nanometre
NO	Nitric oxide
NOX	NADP oxidase
Nrf-2	Nuclear factor erythroid 2-related factor 2
OD	Optical density
PBS	Phosphate buffered saline
PDB	Protein data bank
PEG	Polyethylene glycol
PFK-1	6-phosphofructo-1- kinase
pH	Potential of hydrogen
PI	Propidium iodide
PI3K	Phosphoinositide-3-kinase
PKC	Protein kinase C
QCs	Quantum clusters
QDs	Quantum dots
QY	Quantum Yield
%	Percentage
ROS	Reactive oxygen species
s	Seconds
SAED	Selected area electron diffraction
SD	Standard deviation
SERS	Surface Enhanced Raman Scattering
SPR	Surface plasmon resonance
STAT	Signal transducer and activator of transcription
STEM	Scanning Transmission Electron Microscope
STZ	Streptozotocin
TGF	Transforming growth factor
TEM	Transmission electron microscope

TLR	Toll like receptor
TNF	Tumor necrosis factor
TPP	Tripolyphosphate
UV	Ultra violet
VEGF	Vascular endothelial growth factor
WHO	World Health Organisation

Table of Contents

Contents	**Page no.**
Abstract	1
Chapter 1. Introduction and Literature Review	3
1.1. Introduction	4
1.2. Structural details of major proteins and growth factors and their potential role in skin wound healing	6
1.2.1. Insulin	6
1.2.2. Silk Fibroin	8
1.2.3. Keratin	9
1.2.4. Collagen	10
1.2.5. Heparin	10
1.2.6. Fibroblast Growth Factor	11
1.2.7. Vascular Endothelial Growth Factor	12
1.2.8. Epidermal Growth Factor	12
1.2.9. Platelet-Derived Growth Factor	12
1.3. Synthesis of protein-based nano-formulations	12
1.3.1. Emulsification Technique	13
1.3.2. Complex Coacervation	13
1.3.3. Desolvation	13
1.3.4. Electrospray Technique	14
1.3.5. Other Techniques	14
1.4. Kinetic and thermodynamic study of protein-based nano-formulations	15
1.5. Protein-based nano-formulations in normal and diabetic wound healing	17
1.5.1. Insulin-based formulations	17
1.5.2. Silk fibroin-based formulations	18
1.5.3. Keratin-based formulations	19
1.5.4. Collagen-based formulation	19
1.5.5. Heparin-based formulations	19
1.6. Growth factors and growth regulators in wound healing	26
1.7. Conclusion and Future Directions	28
Chapter 2. Insulin-cobalt core-shell nanoparticles for receptor-targeted bioimaging and diabetic wound healing	
Abstract	30
2.1. Introduction	31
2.2. Materials and Methods	33
2.2.1. Chemicals and Cell line	33
2.2.2. Synthesis of insulin-protected cobalt nanoparticles	33
2.2.3. Study of particle size, morphology, and elemental analysis	33
2.2.4. *in silico* studies	33
2.2.5. Study of cobalt -insulin interaction using spectroscopy	34
2.2.6. Drug loading and release kinetics	34
2.2.7. Study of absorption and fluorescence spectroscopic study	35
2.2.8. Stoichiometry ratio of Co^{2+} ions: insulin protein	35
2.2.9. *in vitro* studies	35
2.2.9.1. Cell viability	35

2.2.9.2. Internalization study of nanoparticles into cells	36
2.2.9.3. Fluorescence Bioimaging	36
2.2.9.4. Effect of ICoNPs on recovery of the normal and diabetic wound, *in vitro*¸ using phase contrast imaging	36
2.2.10. Determination of combination index (CI) for cobalt-insulin	36
2.2.11. Statistical analysis	37
2.3. Results and Discussions	37
2.3.1. Structure, Composition, and stoichiometry of metal insulin nanoparticles	37
2.3.2. *in silico* studies to monitor the interactions between insulin and cobalt ions using Metal-ion Binding Residue templates	38
2.3.3. FTIR, Raman Spectra, and CD spectroscopy for the interactions between protein and metal ions after the formation of nanoparticles	38
2.3.4. Drug loading and release kinetic studies	41
2.3.5. Spectroscopic changes after synthesis of core-shell nanoparticles using absorbance and fluorescence spectra	42
2.3.6. *in vitro* cell studies	43
2.3.6.1. HEKa cell viability assay	43
2.3.6.2. STEM analysis for cellular internalization of ICoNPs	44
2.3.6.3. Fluorescence microscope bioimaging	44
2.3.6.4. HEKa cell migration assay in diabetic and normal wound conditions	45
2.3.7. Combination index of cobalt and insulin	47
2.4. Conclusion	48
Chapter 3. Protection of lead-induced cytotoxicity using paramagnetic Nickel-Insulin paramagnetic quantum clusters	
Abstract	50
3.1. Introduction	51
3.2. Materials and Methods	52
3.2.1. Materials	52
3.2.2. Preparation of Insulin Quantum clusters with Nickel metal salt	52
3.2.3. Spectroscopic characterization of INiQCs	52
3.2.3.1. UV-Visible spectroscopy	52
3.2.3.2. Fluorescence spectroscopy	52
3.2.4. FTIR analysis	53
3.2.5. Morphological and Elemental analysis using DLS and HRTEM	53
3.2.6. Stoichiometry ratio of Ni^{2+} ions: insulin protein	53
3.2.7. *in silico* studies	54
3.2.8. Cytotoxicity testing	54
3.2.9. Fluorescence Bioimaging	55
3.2.10. Effect of INiQCs on recovery of wound in presence of toxic element Pb^{2+} using phase contrast and fluorescence imaging	55
3.3. Results and Discussions	55
3.3.1. Absorbance spectra	55
3.3.2. Fluorescence spectra	55
3.3.3. Structure, Composition and stoichiometry of metal insulin clusters	55
3.3.4. Metal-ion Binding Residue templates	55
3.3.5. Quantum yield determination	56
3.3.6. FTIR Spectra	57

3.3.7. Heavy metal (Pb^{2+}) detection by luminescence quenching	59
3.3.8. HEK 293 cell viability and migration assay	60
3.3.9. Fluorescence microscope bioimaging	62
3.4. Conclusion	63
Chapter 4: Insulin-Infused Bimetallic Nano-subclusters as Multifunctional agents for ROS Scavenging, Antibacterial Resilience, and Accelerated *in vitro* cell migration	
Abstract	65
4.1. Introduction	66
4.2. Materials and Methods	67
4.2.1. Chemicals and cell line	67
4.2.2. Synthesis of bimetallic nano subclusters	68
4.2.3. Study of interactions using spectroscopic techniques	68
4.2.4. Study of particle size, morphology, and elemental analysis	68
4.2.5. Drug loading and release kinetics	68
4.2.6. *in vitro studies*	69
4.2.6.1. Cell viability	69
4.2.6.2. Effect of ICu-AgNSCs on the cell migration, *in vitro* using phase contrast imaging	69
4.2.6.3. Antioxidant activity against H_2O_2-induced cytotoxicity	69
4.2.6.4. Detection of ROS measurement using DCFDA	70
4.2.7. Antibacterial activity of synthesized ICu-AgNSCs	70
4.2.8. Determination of combination index (CI) for $AgNO_3$ and ICuQCs	70
4.2.9. Statistical analysis	71
4.3. Results and Discussions	71
4.3.1. Spectroscopic analysis	71
4.3.1.1. Spectroscopic changes using absorbance spectra after synthesis of ICu-AgNSCs	71
4.3.1.2. FTIR and Raman Spectra for monitoring the interactions between protein and metal ions after the formation of nano subclusters	71
4.3.2. Structure, Composition, and stoichiometry of metal insulin nano subclusters	74
4.3.3. Drug loading and release kinetic studies	76
4.3.6. *in-vitro* studies	76
4.3.4.1. Heka Cell viability assay	76
4.3.4.2. HEKa cell migration assay in diabetic and normal conditions	78
4.3.4.3. Antioxidant activity against H_2O_2 induced cytotoxicity	80
4.3.4.4. Intracellular ROS measurement	81
4.3.5. Antibacterial effect on Gram-positive and Gram-negative strains	82
4.3.6. Combination index of silver nanoparticles and insulin copper quantum clusters	82
4.4 Conclusion	83
Chapter 5: Chitosan-insulin nano-formulations as critical modulators of inflammatory cytokines and Nrf-2 pathway to accelerate burn wound healing	
Abstract	85
5.1. Introduction	86
5.2. Materials and Methods	88

5.2.1. Materials	88
5.2.2. Synthesis of ECNP and ICNP nanoparticles	88
5.2.3. Particle size and morphological analysis	88
5.2.4. FTIR analysis	88
5.2.5. Protein loading and release kinetics	89
5.2.6. Cell viability studies	89
5.2.7. *in vitro* wound healing assay	89
5.2.8. Determination of combination index (CI) for chitosan-insulin	89
5.2.9. *in vivo* studies	90
5.2.9.1. Experimental animal accusation and maintenance	90
5.2.9.2. Third-degree Burn wound induction in mice	90
5.2.9.3. Treatment and measurement of burn wound healing	90
5.2.9.4. Wound tissue collection and histological staining	90
5.2.9.5. Masson's trichrome staining for collagen	91
5.2.9.6. Collection of plasma and analysis of cytokine	91
5.2.9.7. Immunohistochemical staining of burn wound skin tissues	91
5.2.10. Statistical analysis	92
5.3. Results and Discussions	92
5.3.1. Structure and Morphological Studies	92
5.3.2. FTIR Spectra showed conformational changes at the protein level due to chitosan-insulin interactions	94
5.3.3. Protein loading and release kinetics studies	95
5.3.4. Cell viability studies	96
5.3.5. *in vitro* HEKa cell migration studies	97
5.3.6. Combination index of chitosan and insulin	101
5.3.7. Chitosan insulin nano-formulation accelerates burn wound healing through collagen deposition and tissue remodeling	102
5.3.8. Chitosan insulin nano-formulation regulates pro and anti-inflammatory cytokines	104
5.3.9. Chitosan insulin nano-formulation regulates Nrf-2 expression	105
5.4. Conclusion	107
Chapter 6: Conclusion and Future Perspectives	109
6.1. Conclusion	109
6.2. Future Perspectives of Protein-based metallic nanoformulations in wound healing	110
References	112
List of Publications	139

Abstract

The skin is the largest human body organ that, by acting as a barrier, assists in preventing the entry of harmful microbes into the body. It can self-heal to a certain extent, which is impaired in case of extensive damage caused by chemical or physical shock. Wound healing activates multiple physiological and simultaneous phases, such as hemostasis, inflammation, proliferation, and remodeling. Different approaches have been used to treat chronic wounds, ranging from multiple dressings, stem cell-based therapies, and the use of growth factors. But still, certain limitations prevent their effective utilization, including delayed healing due to moisture, such as in alginate-based materials, delay due to poor aeration in hydrocolloidal dressings, poor mechanical strength in hydrogels, expensive production in therapies involving stem cells and growth factors and poor cost-effectiveness. Wound treatment gain enormous interest of investigators, but there is a lack of efficient therapeutic intervention. The cost of healing ranges between $28.1 billion and $96.8 billion for acute and chronic wounds, and the maximum amount is used for surgical wounds, followed by diabetic ulcers. The alarming rise in chronic wounds, the increasing old-age population, and the hiking number of surgeries are some factors driving the growth of the wound care market. The number of patients affected by chronic wounds is approximately 5.7 million people in the United States alone, and an estimated cost of USD 25 billion is spent per year.

Nanotechnology played a vital role in equipping us with promising approach for achieving target specific and efficient delivery through innovating protein-functionalized nanoparticles using growth factors, anti-diabetic wound healing agents (insulin), and extracellular proteins (keratin, heparin, and silk fibroin) as they are critical in enhancing cell proliferation, migration, ECM production, angiogenesis, and inflammation regulation. This led to the emergence of, protein-functionalized nanoparticles as a potential agents for accelerating healing in patients with delayed or impaired healing. Although insulin has huge potential as an anti-diabetic agent, but its role has rarely been explored in the field of wound-healing.

This work aims to develop optimized protein-based nanoformulations for wound healing purposes as they can have sustained drug release, reduced administration frequency, an adequate concentration of medicine for an extended period, higher potency in wound recovery compared to the free proteins, high protein stability, easy transport through the body and less denaturation under environmental conditions, all work together to form advanced formulations critical for wound healing. Further, the high surface area to volume ratio, water solubility, stability, biocompatibility, target specificity, and biodegradability have given an upper hand to using nanoformulations over traditional therapeutics. Thus, I have synthesized protein-templated metal nanoformulations for their potential role as wound-healing agents under normal and diabetic conditions.

The thesis entitled **"Preparation and characterization of protein templated metal nano-formulations and their wound healing applications"** represents the findings of the study, and it is organized into five chapters:

Chapter 1: Introduction and Literature Review

Chapter 2: Insulin-cobalt core-shell nanoparticles for receptor-targeted bioimaging and diabetic wound healing

Chapter 3: Protection of lead-induced cytotoxicity using paramagnetic Nickel-Insulin Quantum Clusters

Chapter 4: Insulin-Infused Bimetallic Nano-subclusters as Multifunctional Agents for ROS Scavenging, Antibacterial Resilience, and Accelerated *in vitro* cell migration

Chapter 5: Chitosan-insulin nano-formulations as critical modulators of inflammatory cytokines and Nrf-2 pathway to accelerate burn wound healing

Chapter 1: Protein-modified nanomaterials: emerging trends in skin wound healing

Abstract

Prolonged inflammation can impede wound healing, regulated by several proteins and cytokines, including IL-4, IL-10, IL-13, and TGF-β. Researchers have investigated the concentration-dependent effects of these molecules at the target site to develop them as wound-healing agents by regulating signaling strength. Nanotechnology has provided a promising approach to achieve tissue-targeted delivery and increased effective concentration by developing protein-functionalized nanoparticles with growth factors (EGF, IGF, FGF, PDGF, TGF-β, TNF-α, and VEGF), anti-diabetic wound healing agents (insulin), and extracellular proteins (keratin, heparin, and silk fibroin). These molecules are critical in promoting cell proliferation, migration, ECM production, angiogenesis, and inflammation regulation. Therefore, protein-functionalized nanoparticles have emerged as a potential strategy for improving wound healing in delayed or impaired healing cases. This review summarizes the preparation and applications of these nanoparticles for normal or diabetic wound healing and highlights their potential to enhance wound healing **(Figure. 1**).

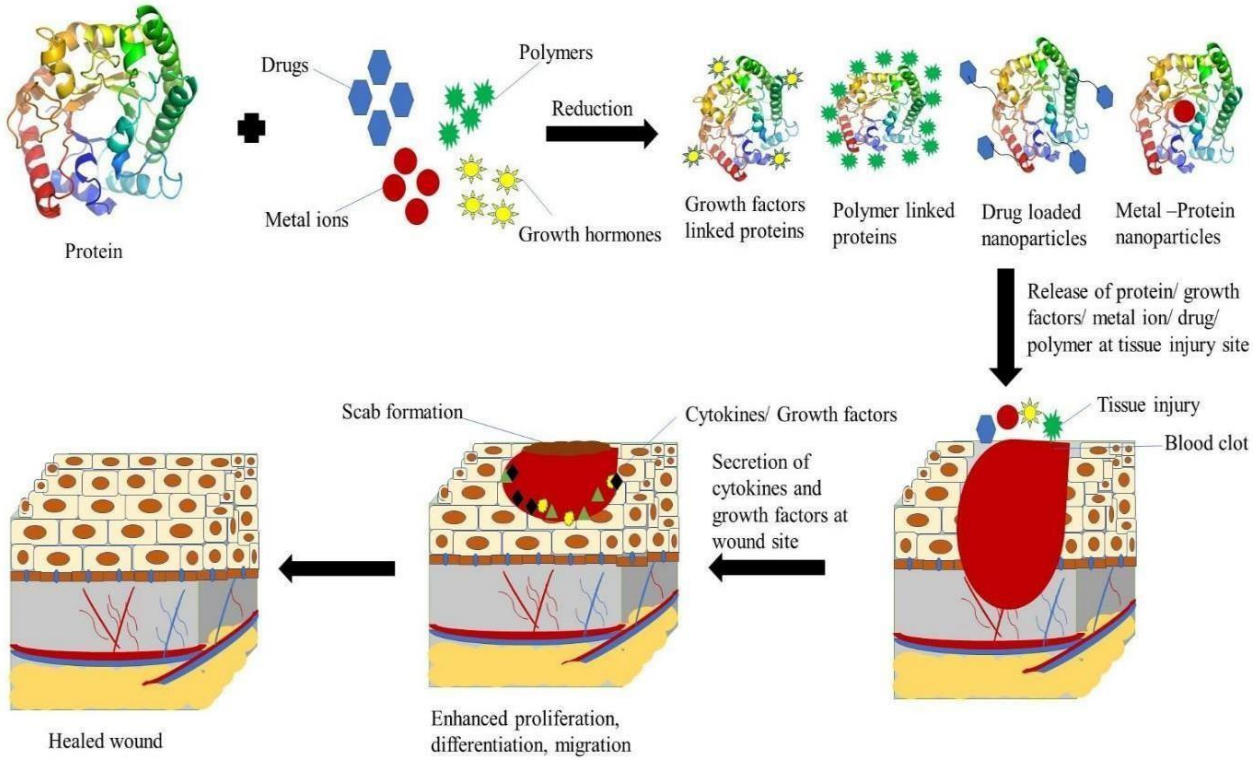

Figure. 1. *Schematic representation of the development and application of protein-linked nano-formulations for wound healing. Proteins in combination with different metal ions, polymers, drugs, and growth hormones, followed by their reduction to form protein-linked nanoformulations were assessed for their wound-healing activity. The release of these formulations at the wound site promotes the secretion of cytokines and hormones essential for enhancing cell proliferation, differentiation, and remodeling to accelerate tissue healing.*

1.1 Introduction

Nanomaterials have high drug-loading efficacy, which can be attributed to a higher ratio of surface area-to-volume. They respond quickly to any minute alteration in the surrounding environment, like a magnetic field, pH, and temperature [1]. The bio-nano materials like peptides, biomolecules, enzymes, and protein functionalized formulations have various biological applications ranging from bioimaging [2], catalysis [3], fluorescent bio labeling [4],[5] hyperthermia [6],[7] tissue engineering [8], gene and drug delivery [9],[10] and so on. Moreover, protein-functionalized and stabilized nanomaterials exhibit numerous features such as sensing, biocompatibility, plasmon-enhanced catalysis, targeted nanocarriers, and drug delivery [11],[12]. The constituting units of the proteins behave not only as reducing and chelating agents that help in developing nanoclusters but also allow crystalline [13],[14] and amorphous [15] growth of the nanostructures of different sizes and shapes [16]. The target-specific binding ability of proteins enhances their action efficiency and helps to cure the wound [15],[17]. However, the poor permeability through membranes, short half-life, and high enzymatic degradation risk pose severe issues in targeting specific delivery of potent therapeutic proteins and thus require slight modifications for efficient delivery [18],[19]. Protein functionalized nano-formulations, such as protein-capped metal nanoparticles, protein-encapsulated nanostructures, and protein nanocarriers, including hydrogels, scaffolds, liposomes, nanotubes, nano gels, nanoparticles, polymeric particles and poly(ester amide) PEA (synthesized using amino acids, diacids, and diols) were developed to effectively transport the protein/drug at the effected site [20],[21].

The largest human body organ, the skin, prevent microbial entry into body by acting as a barrier. The skin consists mainly of epidermal, dermal, and hypodermal layers, which contain certain hormonal glands, hair, and nerve endings that make the skin a complex organ. It can self-heal to a certain extent, which is impaired in case of extensive injury caused by chemical or physical shock, making recovery challenging [22]. Wound healing is a cumbersome procedure which activates a series of physiological and simultaneous phases such as hemostasis, inflammation, proliferation, and remodeling [23],[24], which significantly affect the effective wound or infected area treatment. The classical process of healing begins with the hemostasis, which includes clot formation due to the activation of platelets that release the chemokines and growth factors (including fibroblasts and keratinocytes) at the wound site and act as critical parameters of hemostasis and coagulation. They further assist in preventing the entry of bacteria at the affected site and regulate antimicrobial peptide production by expressing distinct toll-like receptors (TLR) [25],[26]. After this inflammatory phase begins, which is quite complex due to the extrinsic and intrinsic factors and the excessive and limited, both inflammation conditions delay the wound healing and promote injury. It acts as the primary defense system against pathogenic invasion. It is started in response to signals induced by injury, the release of damage-associated molecular patterns, and pathogen-associated molecular patterns by necrotic cells and damaged tissue and bacterial components, respectively. Proinflammatory cytokines promote vasodilation, and these proinflammatory signals and activated signaling pathways stimulate the secretion of cytokines by neutrophils. Neutrophils, by phagocytosis, remove the necrotic tissue and pathogens and cause the secretion of antimicrobial peptides, proteolytic enzymes, and eicosanoids [27],[28]. Following this, the proliferative phase begins, in which there is the accumulation of cells and connective tissues along with the activation of numerous factors, including fibroblasts, keratinocytes, macrophages, angiogenesis factors, and endothelial cells across the wound site. Keratinocytes are responsible for regenerating the epidermis by differentiation and basement membrane reformation. Fibroblasts play a role in developing the matrix consisting of granulation tissue, which comprises fibronectin, proteoglycans, and immature collagen, which collectively work as a scaffold essential for cell adhesion and migration across the injury [29],[30]. During angiogenesis, the generation of new blood vessels occurs to fulfill the demand for highly proliferative regenerative tissue, and macrophages assist in guiding vessel tips together and eradicating the superfluous vessels by phagocytosis for making new vasculature critical

for transportation across the site [31],[32]. In the last phase of remodeling, the extracellular matrix is resynthesized to maintain the balance between the death of old cells and the formation of new cells. Fibroblasts are the primary cells crucial for remodeling by replacing the fibrin clot with fibronectin, proteoglycan, and collagen fibril synthesis. Collagen III is finally replaced with collagen I, which enhances the tensile strength of wound scar and helps wound closure at a faster pace [33],[34],[35]. In the initial healing stages, cytokine release and leukocyte activation by macrophages occur and exhibit a proinflammatory environment [36]. The potent release of anti-inflammatory cytokines, insulin-like growth factor (IGF), and proteins like insulin are crucial for aiding in efficient wound healing, which is initiated by inducing angiogenesis and reepithelialization [37]. The proteins (insulin, collagen, keratin, gelatin), growth factors such as insulin-like growth factors (IGF), epidermal growth factors (EFG), fibroblast growth factors (FGF), platelet-derived growth factor (PDGF), transforming growth factor-beta 1 (TGF-β1), tumor necrosis factor-alpha (TNF-α), and vascular endothelial growth factor (VEGF), etc. help in decreasing the proliferation of cells, inflammatory response and tissue remodeling [38],[39]. The growth factors act as the endothelial signaling factors, which assist in regulating the cellular processes during wound healing. Numerous researchers have explored the critical role they play in modulating the recovery effects in normal and diabetic conditions. The treatment of wounds at a faster pace is highly dependent upon cytokine transitioning from pro-inflammatory to anti-inflammatory ones [40]. In chronic wounds, a halt in the conversion of cytokines from one form to another causes a prolonged proinflammatory phase, which eventually results in delayed wound healing [41].

Depending upon these protein and growth factor features and their role in normal and diabetic wound healing, there is a vast importunity to design reliable and cost-effective wound dressings, and protein-functionalized nanoformulations are the ones that have high wound healing potency, target specificity, and easy to synthesize using green methods. The significance of this field is very diverse as the treatment of chronic wounds is becoming difficult day by day due to the development of antibiotic resistance against the available medications, degradation of formulations under unfavorable conditions, uncontrolled drug release, and less target specificity and efficiency. The cost of healing ranges fall between $28.1 billion and $96.8 billion for acute and chronic wounds, and the maximum amount is used for surgical wounds, and diabetic ulcers [42]. The enhanced ubiquity of chronic wounds, the increasing aging population, and the increasing number of surgeries are some factors driving the need for improvement in the wound care market. The number of patients affected by chronic wounds is nearly 5.7 million in the United States alone, and an evaluated expanse of USD 25 billion is spent per year [43]. Recent advancements in bionanomaterials have led researchers towards developing optimized protein-based nanoformulations for wound healing purposes as they showed sustained drug release, reduced administration frequency, an adequate concentration of medicine for an extended period, higher efficacy in injury recovery in comparison to free proteins, high protein stability, easy transport through the body and less denaturation under environmental conditions, all work together to form advanced formulations critical for wound healing. The high surface area to volume ratio, water solubility, stability, biocompatibility, target specificity, and biodegradability have given an upper hand to the use of nanoformulations over traditional therapeutics. All these factors have significantly contributed to gaining the enormous interest of researchers in this desirable field for developing and exploring better futuristic approaches in synthesizing protein-functionalized materials [44]. **Figure. 2** Shows various proteins and growth factors primarily used in wound healing, along with the significant nano-formulations being developed using them.

This review article focuses on protein-functionalized nanomaterials for wound healing applications. The key terms covered in this article include protein-functionalized nanoparticles, bio-nano materials, drug delivery, tissue engineering, gene delivery, cytokines, growth factors, inflammation, macrophages, angiogenesis, and skin regeneration. Other terms discussed include bioimaging, catalysis, fluorescent bio-labeling, hyperthermia, plasmon-enhanced catalysis, and targeted nanocarriers. The article highlights the advantages of protein-functionalized nanomaterials over

only protein, including their high drug-loading efficacy, quick response to environmental changes, and target-specific binding ability. This review demonstrates the enormous possibilities of developing green and biocompatible protein nanoformulations with high efficacy and specificity for wound healing applications.

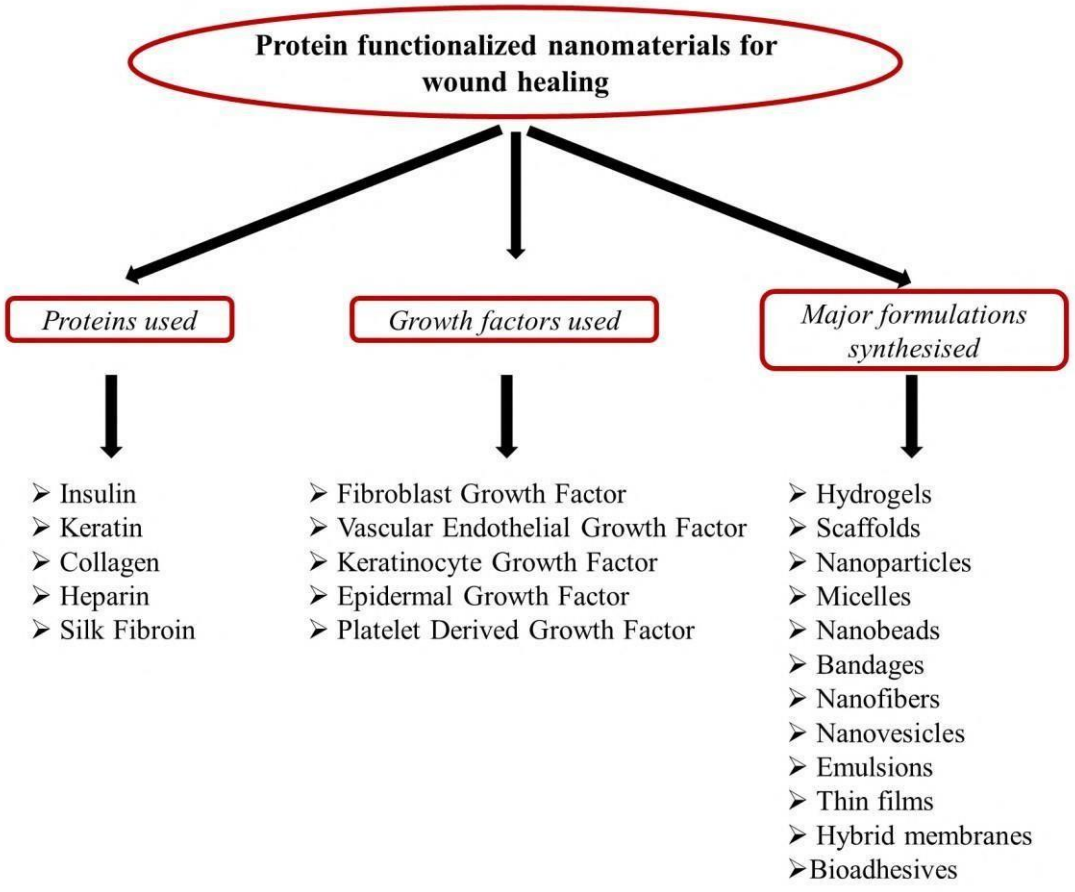

Figure. 2. *Overview of different proteins and growth factors widely used for making various nano-formulations for wound healing and skin regeneration activity.*

1.2 Structural details of major proteins and growth factors and their potential role in skin wound healing

Several proteins are involved in wound healing, including anti-diabetic proteins such as insulin or extracellular matrix proteins such as heparin, keratin, silk fibroin, and collagen. I will discuss them briefly in the coming sections.

1.2.1 Insulin – It is derived from its inactive form, proinsulin, in which the N-terminal of chain A is connected with the C-terminal of chain B through a C-peptide, which is removed during the maturation. Insulin is a peptide hormone composed of two chains of polypeptides, A and B, which are composed of 51 amino acids, of which 17 are proteinogenic amino acids. The two chains are interconnected via three disulfide bridges, and its folding occurs with three alpha-helices (two in chain A and 1 in chain B) and a small β-sheet segment. The existence of both the zinc ions and phenolic ligands helps in the dimerization of insulin and further promotes the formation of hexamers **(Figure. 3A).** The molecular weight of insulin is around 5 kDa. Depending upon its structure and low molecular weight, it is widely employed for synthesizing biocompatible, non-toxic nanoformulations that can be easily inserted into the body or topically applied over the wound, hence promoting wound healing by following critical mechanisms. It is responsible for stimulating the uptake of glucose by cells and thus regulates blood glucose levels. It also plays essential roles

in cellular differentiation, lipid and protein biosynthesis, growth factor activity, and wound healing. It also acts as a growth factor and increases the migration ability of cells, thereby aiding in wound healing [45],[46]. On the cell surface, receptor tyrosine kinase transmembrane signaling proteins are present and are associated with insulin receptors. The tissue recovery begins after activation of Akt and Erk signaling pathways. [47],[48]. Insulin induces the synthesis of proteins by the PI3K and Akt pathway, which helps form 4EBPI and Ribosomal protein S6 essential for cell survival. Insulin is known to showcase anti-inflammatory potential by modulating distinct pathways like Akt and PI3K after binding with IGF receptors. These pathways further enhance cellular growth and angiogenesis by activating STAT-3 [39]. In addition, insulin is responsible for inactivating the TNFα-mediated inflammatory pathway, that further inactivates the proinflammatory cytokines [39]. Insulin enhances the proliferation, migration, and secretion of different cells, including keratinocytes, fibroblasts, and endothelial cells [49]. Hence, it is used in integration with other wound dressings due to its low cost compared with different growth regulators [46]. Insulin signaling in wound healing plays a critical part in cell proliferation, migration, along with the development of new blood vessels, making it an essential peptide hormone for wound healing, as shown in **Figure. 4**.

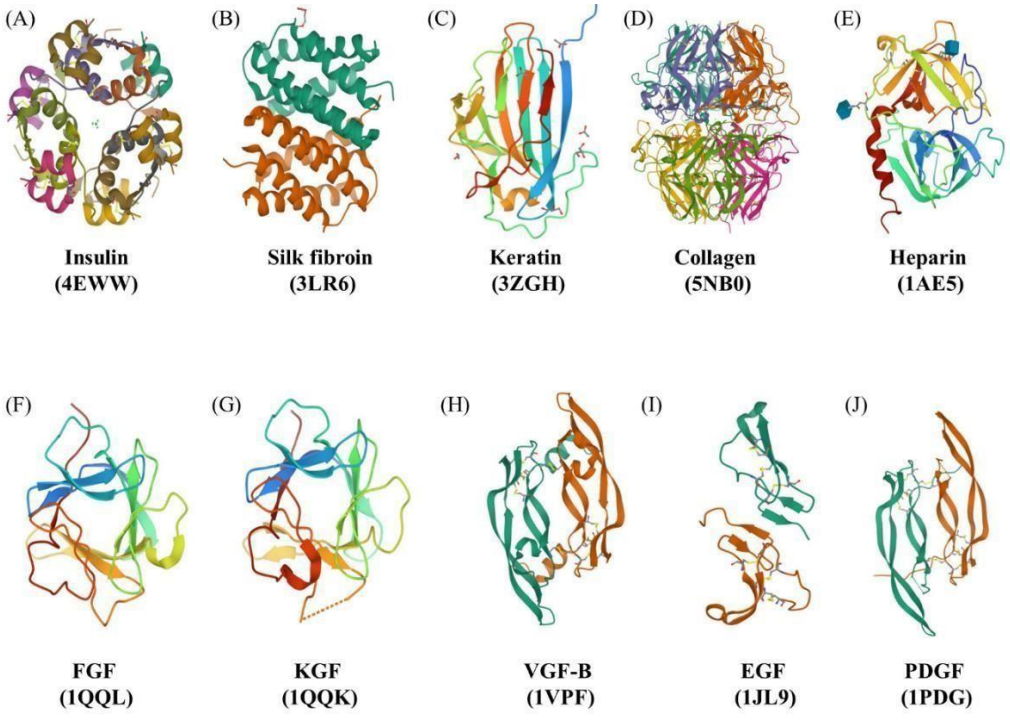

Figure. 3. *The crystal structures of different proteins and growth factors along with their PDB IDs a) Insulin, b) Silk fibroin, c) Keratin, d) Collagen, and e) Heparin f) Fibroblast Growth Factor (FGF), g) Keratinocyte Growth Factor (KGF), h) Vascular Growth Factor (VGF-B) i) Epidermal Growth Factor (EGF) and j) Platelets Derived Growth Factor (PDGF).*

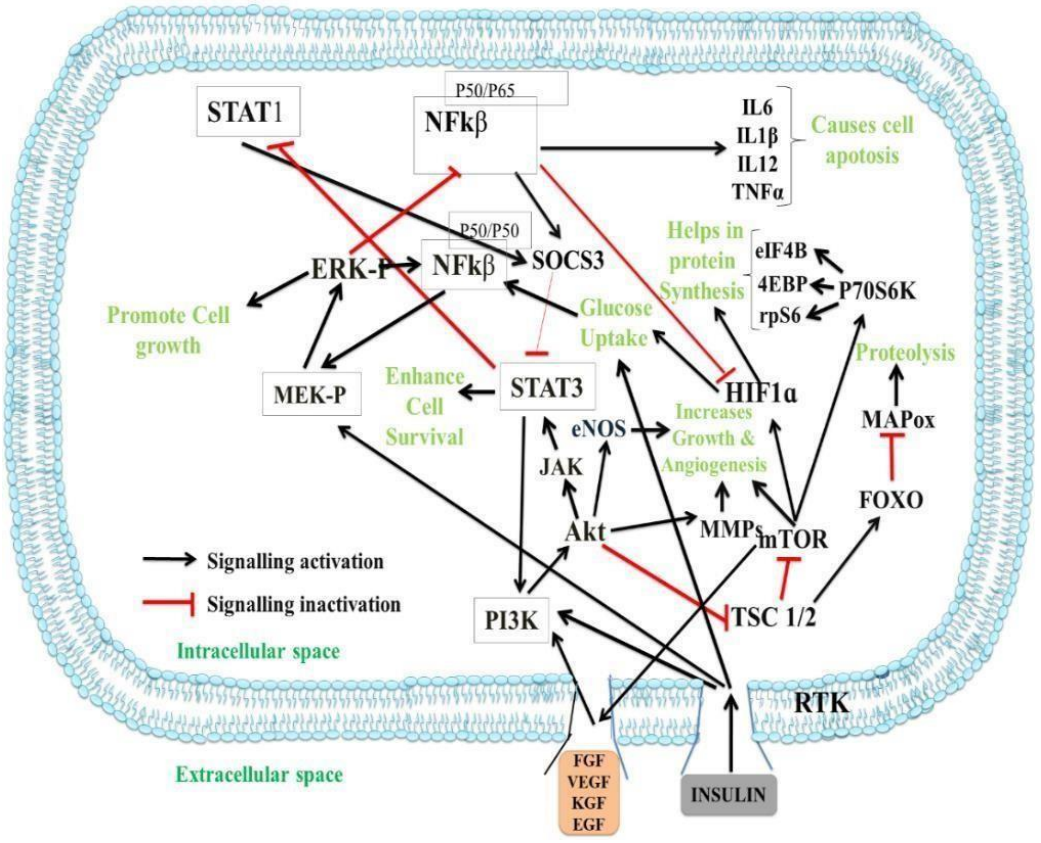

Figure. 4. *The signaling pathway followed by insulin and other growth factors for wound recovery. The generation of IFN-γ and TNF-α activated the STAT-1, IRF-3, and NF-kβ, which are responsible for the secretion of IL-10, IL-12, and other interleukins for the transition of proinflammatory cytokines to anti-inflammatory ones and promotes healing.*

1.2.2 Silk fibroin – It is derived from Bombyx mori, and is an organic fibrous protein that acts as an crucial biomaterial for tissue healing and regeneration [50]. Also, it is the major formational of silk and consists of a polypeptide chain having 200-350 kDa molecular weight. The repetitive units of heavy (hydrophobic) and light (hydrophilic) chains with terminal N and C constitute the primary silk fibroin structure, and the disulfide bonds connect the two chains. Glycoprotein P25 provides integrity to the above chains. The molar ratio is found to be 6:6:1 of the heavy chain, light chain, and P25 (**Figure. 3B**). The amino acids present in the hydrophobic chain include 45.9% glycine (Gly), 30.3% alanine (Ala), 12.1% serine (Ser), 5.3% tyrosine (Tyr), and 1.8% valine (Val). In comparison, the hydrophilic chain consists of 14% alanine (Ala), 10% serine (Ser), 9% glycine (Gly), and acetylated N-terminal Ser residues [51]. The structure of silk fibroin is such that it acts as a tissue scaffold or mesh for the attachment of growing cells and promotes functional tissue regeneration, which is crucial for healing. Further, the β-sheet pattern is high in silk fibroin, which promotes cell attachment and growth in mesenchymal stem cells. It enhances growth, differentiation, and adherence of various cells, including keratinocytes, endothelial cells, epithelial cells, fibroblasts, and osteoblasts, promoting wound healing [52],[53]. In addition to its biomaterial role, silk fibroin regulates different signaling pathways crucial for wound healing. The NF-κB pathway is activated by silk fibroin, causing the upregulation of genes responsible for cell proliferation, migration, and angiogenesis. Silk fibroin also activates ERK1/2 and Akt signaling pathways, ultimately causing increased cell proliferation, migration, and synthesis of extracellular matrix [54]. Due to its biocompatibility, non-toxicity, non-carcinogenicity, and less immunogenicity, silk fibroin is extensively studied in various biomedical and biological areas, and its ability to regulate different signaling pathways and support various cell functions make it a

promising biomaterial for wound healing applications [34],[55]. **(Figure. 5)**.

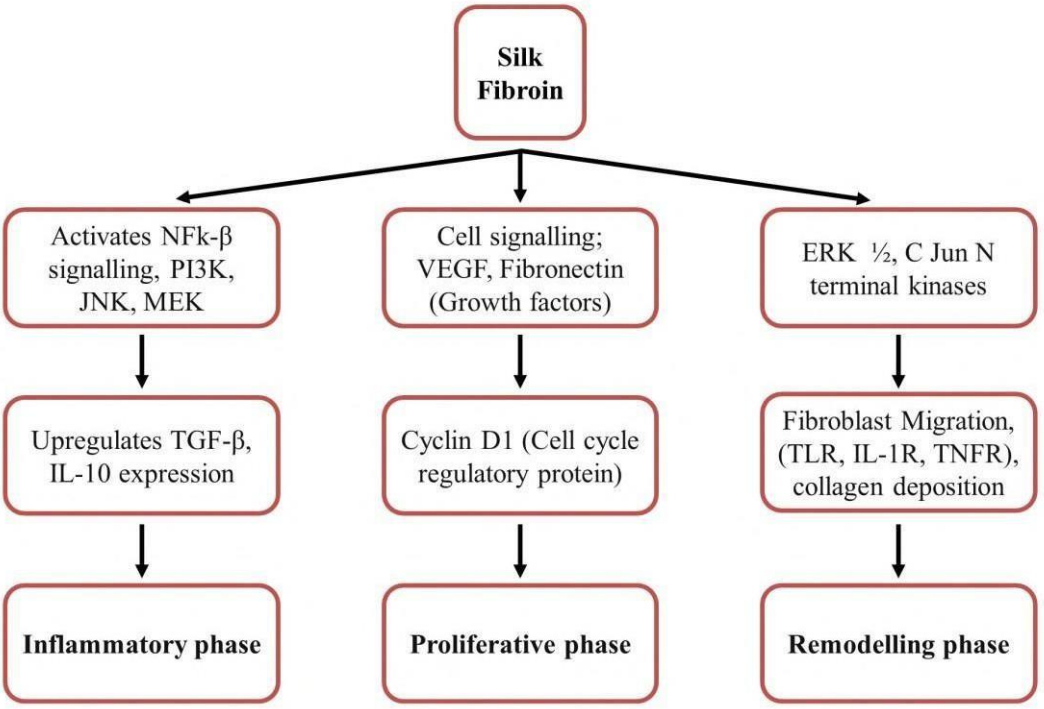

Figure. 5. *The illustration of potential role and signaling pathway followed by silk fibroin in wound healing activity by modulating the inflammatory, proliferative, and remodeling phase of healing.*

1.2.3 Keratin – Keratin is a natural fibrous protein found in both humans and animals [56]. It is a scleroprotein made up of different amino acid residues but mainly rich in cysteine and intra and intermolecular hydrogen, disulfide, and ionic bonds, along with hydrophobic interactions connecting these amino acids. Generally, it is found in two forms: alpha keratins, which involve the arrangement of polypeptide chains in the form of alpha helices, and filaments having a diameter of 7-10 nm, whereas the beta keratins comprise beta sheets, which are of 3-4 nm diameter **(Figure. 3C)**. The alpha form is dominant in hairs, nails, horns, wool, and stratum corneum, whereas the beta form is common in feathers, reptilian claws, and scales [57]. Based on the structure, keratin is used for making scaffolds as it contains both alpha and beta forms, which help in cell adhesion to the scaffold and enhance their proliferation and differentiation. Further, if motifs, which are responsible for cell binding, are present, they promote the ability to promote cellular attachment. In various forms, such as hydrogels, scaffolds, and films, it has been widely used for bone regeneration, nerve regeneration, cell culture, and wound healing [58]. Keratin supports wound healing by accelerating hemostasis, promoting cell growth, and upregulating the expression of proteins relevant to wound healing. Additionally, it enhances plasma coagulation and lateral growth of fibrils [59],[60]. Previous studies have shown that keratin can arrest hemorrhage in bleeding animals, increase fibroblast proliferation and attachment, and upregulate the expression of keratinocytes involved in migration and collagen deposition [61],[62]. The mechanism underlying keratin-mediated wound healing is complex. TNFα activates the NFκβ/C/EBPβ, and IL-1 activates the C/EBPβ, which in turn activates the K6 keratin. IFN γ upregulates STAT1, activating the k6 and k17 keratins. Similarly, the k16 and k6 get activated by EGF/ TGF α. All three keratins, K6, K16, and K17, activate the keratinocytes and promote E-cadherin secretion or phosphorylation of EGFR, ERK1/2, and K6, which increases epidermal differentiation and ultimately enable wound healing [63],[64]
1.2.4 as shown in **Figure. 6**.

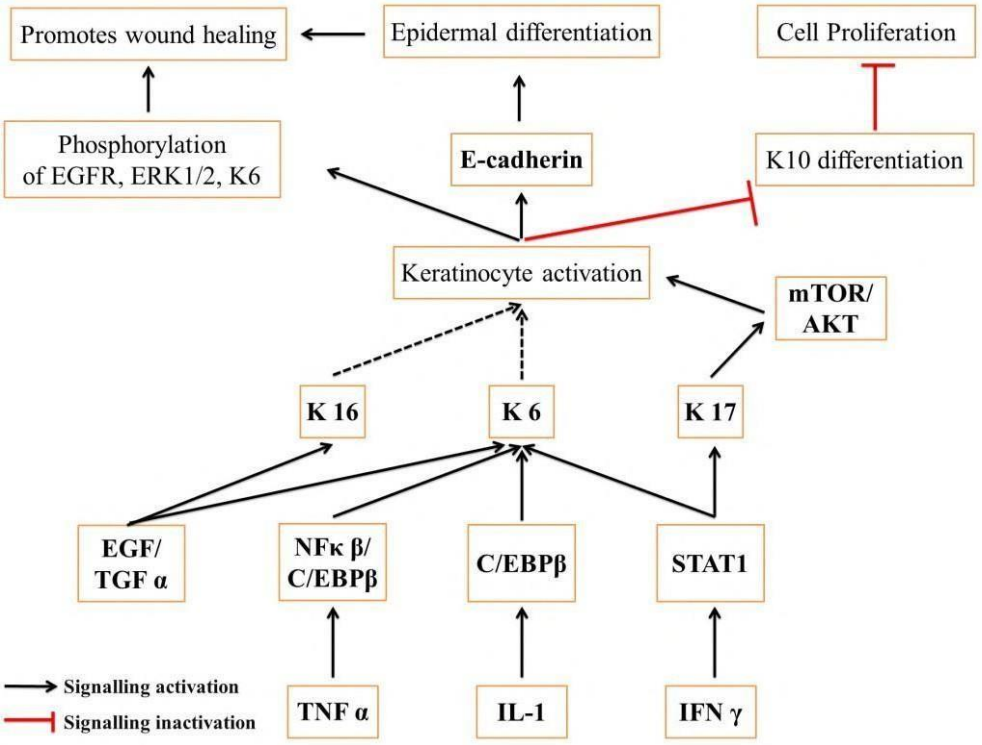

Figure. 6. *The demonstration of signaling pathway followed by the keratin protein in wound healing. The three significant keratins, K6, K16, and K17, get secreted in response to injury and activate the keratinocytes, further promoting epidermal regeneration and wound healing.*

1.2.5 Collagen – Collagen is a fiber-based protein which provides structural support to the extracellular matrix and is essential for tissue repair and regeneration. Skin mainly consists of collagen I. Collagen fiber has a spiral structure, and each fiber is up to 3 μm in diameter. Each fiber further consists of bundles of small fibrils, and the diameter of each fibril is 10-300 nm in diameter and several micrometers long. Fibrills are made up of triple-stranded collagen molecules. Based on this triple helix structure, the strands are interwoven together, which allows the robust structure to maintain itself in tissues for years due to its stereo-dynamic stability, as given in **(Figure. 3D)** [65]. Due to its fiber-like nature, it is widely employed for making scaffolds that have the potency of enhanced cellular attachment and thus promote wound healing activity by providing space for cell growth and differentiation. Collagen-based products are gaining interest for their wound-healing abilities because of their potential to promote healing by enhancing cell proliferation, angiogenesis, and collagen deposition [66],[67]. Collagen stimulates the expression of growth factors such as TGF-β, activates the MAPK/ERK signaling pathway, and modulates the action of enzymes responsible for wound healing, such as MMPs [68]. Collagen-based biomaterials have enormous potential for wound recovery because of their biocompatibility, biodegradability, and ability to support cell growth and tissue regeneration [69].

1.2.6 Heparin – Heparin is a natural, branched, helical glycosaminoglycan (GAG) with high sulfation and anticoagulant properties. It is basically divided into two main types: unfractionated heparin and low molecular weight heparin. Amongst the naturally occurring GAGs, it is the most sulfated one and composed primarily of tri-sulfated disaccharides of 2-*O*-sulphated α-L-iduronic acid and N-6-*O*-disulphated glucosamine repeating units **(Figure. 3E)**. Heparin molecular weight is 3 to 30 kDa (natural), while that of unfractionated one is 12-16 kDa [70]. It is effective in wound recovery because of its potential to protect growth factors from proteolytic degradation, thus enhancing their bioactivity [71]. It promotes rapid and effective repair of endothelial cells, making

it a useful agent in *in vitro* and *in vivo* wound healing applications [72]. Heparin has been employed in treating burn wounds and diabetic foot ulcers, where it has been shown to decrease wound recovery time and increase capillary circulation. The wound-healing capability of heparin-based formulations is due to their ability to enhance the secretion of various growth factors, like FGF1 and FGF7. FGF1, after binding to its receptor FGF1-R, promotes cell proliferation and angiogenesis, while FGF-7 increases the proliferation of keratinocytes, which is essential for reepithelialization [73]. Heparin also inhibits specific cytokines, including Elastase, Cathepsin G, and IL-8, as well as eosinophil peroxidase, eosinophil cationic protein, and stromal-derived factor-1, which are responsible for the augmentation of inflammation. Overall, heparin-based formulations have shown great potential for wound healing applications because of their ability to promote cell proliferation, angiogenesis, and reepithelialization while inhibiting inflammation, as shown in **Figure. 7**. Using heparin-based formulations in wound healing may cause the development of novel therapies and biomaterials for improving wound healing outcomes [74],[71].

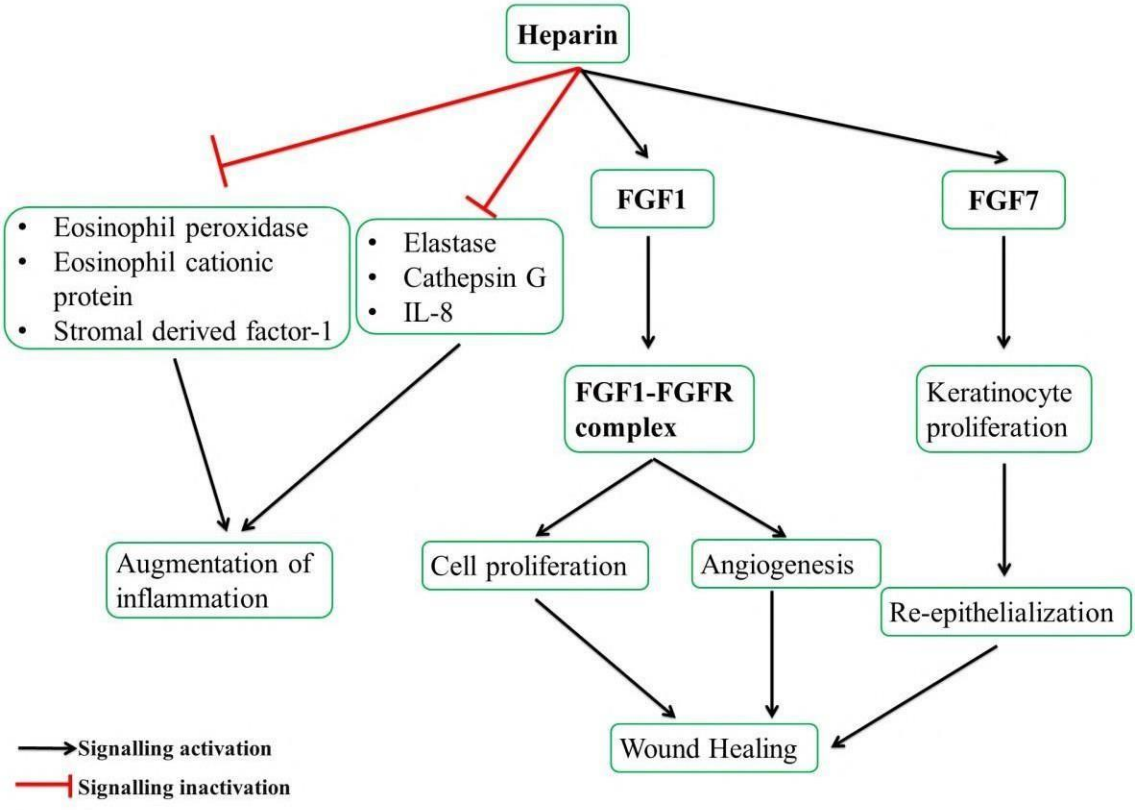

Figure. 7. *The illustration of signaling pathway followed by the heparin protein in wound healing. Heparin promotes the secretion of different fibroblast growth factors causing reepithelialization, migration, and differentiation of growth-promoting cells.*

1.2.7 Fibroblast Growth Factor (FGF) – FGF promote wound healing and includes 22 polypeptides, which are responsible for activating the FGFR1-4 (four receptor-type tyrosine kinases) and promote healing [75]. FGF2 mediates the granulation tissue formation and angiogenesis. FGF2 promotes cell proliferation, differentiation, and migration in various tissues, like skin, bone, cartilage, and muscles [76]. Further, the migration of keratinocytes in wounds, both *in vitro* and on skin samples, is promoted by FGFR-1 and FGFR-2 [77]. FGF7 and FGF10 are responsible for stimulating the endothelial cells and inducing the expression of VEGF, both of which are required for reepithelialization and angiogenesis in its later stages. Further, hair follicles are generated with the help of FGF9, and its overexpression increases hair generation up to three times. Keratinocyte growth factors (KGF) also fall under this category and promote reepithelialization by affecting the morphogenesis, proliferation, and migration of keratinocytes. KGF1 regulates the

inflammatory phase, and its expression is increased by the PDGF and proinflammatory cytokines released from macrophages and leukocytes. KGF2 acts on epithelial cells and is secreted by fibroblasts. It promotes angiogenesis, hair follicle growth, wound closure, scar formation, fibroblast migration, granulation tissue formation, and so on [78],[79] **(Figure. 3F and 3G)**.

1.2.8 Vascular Endothelial Growth Factor (VEGF) – Different cells, including fibroblasts, keratinocytes, platelets, endothelial cells, macrophages, and neurocytes present in the place of injury, express the growth factors of VEGF family. VEGF initiates the scar generation and the early phases of angiogenesis after the tissue injury, and its expression is triggered by the release of hypoxia-inducible factor-1α in response to the blood capillary disruption and hypoxic conditions generated after that at the wound [79]. It also promotes vasculogenesis, reepithelialization, collagen deposition, and enhanced vascular permeability, which allows the inflammatory cells to reach the wounded tissue and initiate proliferation and migration. It also assists in burn wound healing [80]. **(Figure. 3H)**

1.2.9 Epidermal Growth Factor (EGF) – It is a polypeptide chain having 53 amino acid residues and three intramolecular disulfide bonds. The movement and proliferation of fibroblast, endothelial cells, and keratinocytes toward the injury site is initiated by EGF. It also activates the EGF receptor (EGFR), which initiates the signaling pathway involved in promoting cell survival, proliferation, and migration without causing any harm to stem cell pluripotency. EGF is found to enhance the healing rate in diabetic foot ulcers, venous ulcers, and skin grafts by increasing epithelialization [81],[82]. **(Figure. 3I)**

1.2.10 Platelet-Derived Growth Factor (PDGF) – PDGF is secreted as five isoforms by fibroblasts, macrophages, smooth muscle cells, keratinocytes, and endothelial cells. PDGF proteins are present in monomeric forms, and to get themselves biologically active and bind to the PDGF receptors, they form homodimers or heterodimers. The PDGF initiates the differentiation and proliferation of fibroblasts to myofibroblasts. It plays a role in reepithelialization, intraepithelial collagen deposition, inflammatory cell deposition, and stabilization of blood capillaries in granulation tissue. Further, it promotes the secretion of MMPs and thus is critical in the remodeling phase. The PDGF- BB (Becaplermin) is the only recombinant growth factor approved for chronic tissue recovery by the FDA, and it acts as a profibrotic agent [79],[83]. **(Figure. 3J)**

1.3 Synthesis of protein-based nano-formulations

Nanoparticles are promising drug delivery agents for early detection and treatment of different diseases. Different methods have been employed for their synthesis, including colloidal, sonochemical, thermal decomposition, microemulsion, and hydrothermal processes [84],[85]. However, these methods have limitations due to the toxicity of drugs on normal cells and tissues and the difficulty in loading hydrophobic agents [86],[87]. Protein-based nanoformulations are being synthesized to overcome these limitations. Two main synthesis pathways are crosslinking with derivative groups modified on the surface of protein molecules or crosslinking with native proteins' functional groups [88],[89]. Recent techniques involve the electrospray method and desolvation or coacervation process, which provide better control over the size and loading of nucleic acids and therapeutic drugs [90],[91],[92],[93]. UV illumination was used to induce the self-assembly of protein nanoparticles, and solvent extraction or emulsion processes were found to have high encapsulation rates [94]. The heat denaturation process is equipped with targeting moieties but lacks a large particle size. Hence, various synthesis methods with modifications can be employed to efficiently and effectively synthesize protein-functionalized nanoparticles [90]. Here, I am going to discuss some of the most widely employed synthesis methods used for protein-functionalized nanomaterials, as shown in **Figure. 8,** and their advantages and limitations are given in **Table 1** [95]. The synthesis procedure to be followed will be highly dependent on the specific

application and the characteristic features of the resulting nanostructures.

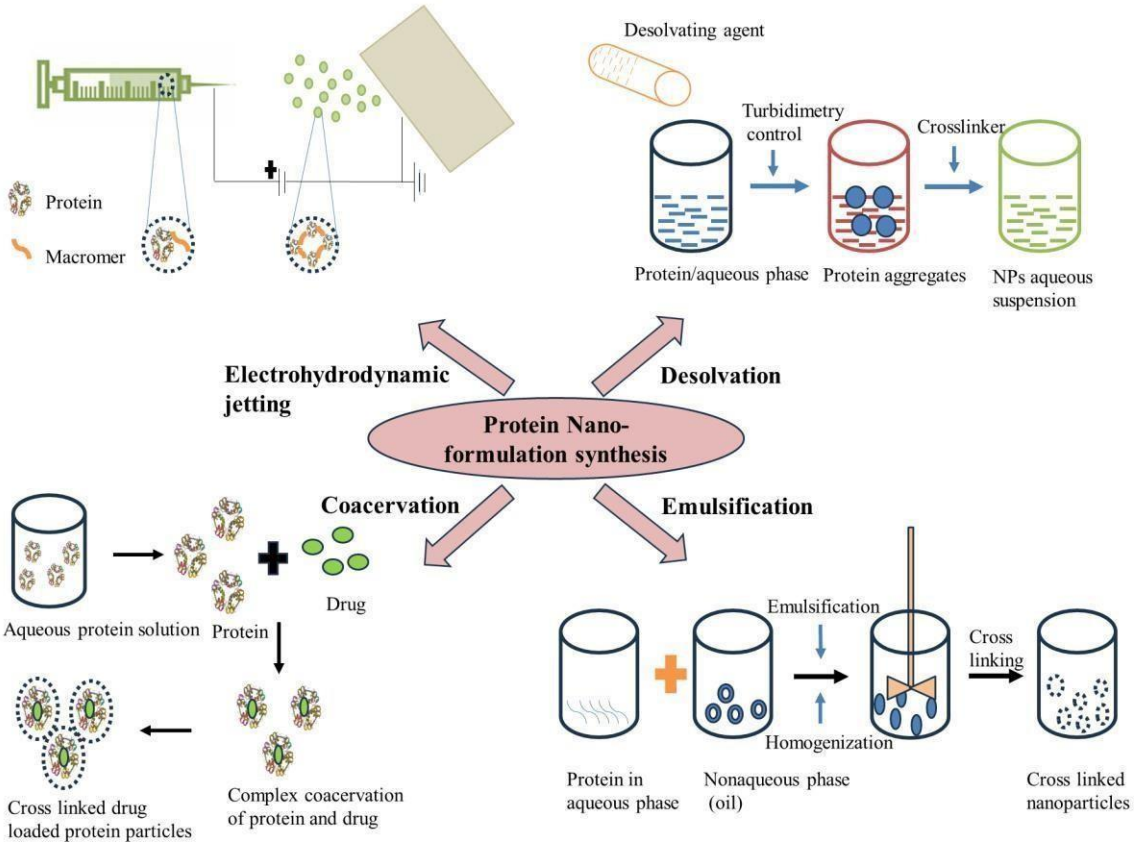

Figure. 8. *The representation of the different techniques being followed for synthesizing the desired protein-functionalized nanoparticles, including emulsification, desolvation, coacervation, and electro-hydrojetting techniques.*

1.3.1 Emulsification technique – In 1972, Scheffel et al. invented the technique for preparing the spheres of albumin protein. This technique involves two distinct phases: the aqueous phase, which is made up of dissolving the protein in distilled water, and the organic phase, in which plant oils are used. The two phases are mixed mechanically by using a homogenizer in a large container until the oil-water or water-oil emulsion is obtained. This emulsion solution is then poured drop by drop into a preheated oil having a temperature of up to 120 ˚C. At this temperature, the water from the emulsion will evaporate, and the irreversible destruction of protein will begin, eventually leading to the synthesis of protein nanoparticles, which will be suspended in an ice bath [96],[97].

1.3.2 Complex coacervation – For the entrapment of DNA, a complex coacervation technique is usually followed. By adjusting the pH, the proteins can be made cationic or anionic due to their amphoteric nature. In this technique, the protein is taken in an aqueous solution, and during its pH adjustment duration, the particles having a positive charge come upward towards the surface. In this solution, a freshly prepared solution of DNA mixed with salt is added. When the DNA and protein interact together, the complex coacervation occurs, followed by the addition of crosslinkers like EDC (1-ethyl-3-(3-dimethyl aminopropyl)carbodiimide) to get the crosslinked protein particles loaded with the DNA. This entrapment of DNA into the protein matrix is completed in the last stage of synthesis. Cationized protein can also be used to make complexes with DNA [98],[99].

1.3.3 Desolvation - Desolvation, also known as the coacervation technique, was developed in 1978 by Martyr and his coworkers. In this technique, protein is taken in an aqueous solution into which a desolvating agent like natural salt or alcohol is added. Adding a desolvation agent starts slow

structural changes in the protein after addition. After a specific time interval, the formation of protein clumps begins, followed by the crosslinking between clumps to yield protein nanoparticles, which are separated from the solution by gradually increasing the turbidity of the solution [100], [101].

1.3.4 Electrospray technique – It is newly developed technique mainly used for elastin and gliadin-based protein nanoparticles. In this technique, a very high voltage is given by using emitter to the protein solution. This emitter is responsible for emitting a liquid jet stream via the nozzle, that is crucial for forming aerosolized-sized liquid droplets. These droplets consist of drugs along with nucleic acid. Through this method, the monodispersity of synthesized nanoparticles is retained [102],[103].

1.3.5 Other techniques - In addition to the methods mentioned earlier, other techniques have been developed to synthesize protein-based nanoformulations. One such technique is the layer-by-layer (LbL) assembly technique that involves the sequential deposition of oppositely charged polyelectrolytes onto a charged surface, such as a protein or a nanoparticle. This method is highly versatile and can be used to create multilayered nanostructures with controlled size and surface charge, allowing for precise control on drug release or therapeutic agents [104],[105]. Another method that has gained attention in recent years is using genetically engineered proteins to synthesize protein-based nanoformulations. By engineering the amino acid sequence of proteins, it is possible to introduce specific functional groups that can be used for crosslinking or chemical modification, giving the ability to adjust size and shape of the resulting nanostructures [106],[107]. Furthermore, there is a rising interest in using biocompatible and biodegradable polymers, like chitosan, alginate, and poly(lactic-co-glycolic acid) (PLGA), for the synthesis of protein-based nanoformulations. These polymers offer several advantages over traditional protein-based formulations, including improved stability, enhanced biocompatibility, and controlled release properties [108],[109],[110].

Table 1: The table provides brief information about the different synthesis techniques being followed, along with some of the significant advantages and disadvantages of each method.

Technique	**Advantage**	**Disadvantage**	**Ref.**
Solvent extraction/ Emulsion process	• The rate of encapsulation is very high • Require basic lab equipment	• Large particle size • Poor drug loading • Uncontrolled drug release	[96],[97]
Complex Coacervation	• Performed under mild conditions • High shell integrity • Excellent drug release efficacy	• Agglomeration chances are high • Easily affected by temperature, pH, ionic strength, composition, and nature of the material.	[98],[99]
Salt precipitation	• A simple and robust technique	• High chances of confirmation and bioactivity loss	[111]
Polyelectrolyte complexation	• Encapsulation efficiency is high	• Affected by pH variations,	[112]

	• Maintains the drug stability	temperature, ionic strength, polyelectrolyte concentration	
Desolvation	• Easy synthesis • Low cost • High yield	• Protein denaturation • Loss of biological activity • Affected by the pH of the protein	[100],[101]
Heat denaturation	• Targeting moieties can be attached • Implemented on a large scale	• Large particle size • Not suggested for heat-sensitive compounds	[113]
UV illumination	• Assist in the self-assembly of proteins	• Chances of agglomeration	[94]
Layer-by-layer assembly	• Multilayered structures Controlled size and surface charge • Monodisperse particles • Unlimited geometry of protein nanoparticles	• Relatively low yield • Computational calculations needed • Affected by protein concentration	[104], [105], [114]
Electrohydrodynamic jetting	• The secondary protein structure retained • Able to trap hydrophobic and hydrophilic drugs • Maintain the narrow dispersity of particles	• Low yield • Affected by the molecular weight of the protein	[102], [103]

1.4 Kinetic and thermodynamic study of protein-based nano-formulations

Thermodynamic and kinetic studies are crucial in thoroughly understanding the interactions between proteins and external agents such as drugs, metal ions, polymers, etc. Thermodynamics critically affects the different parameters, including stability, adsorption, nucleation, and interaction between proteins and the surface of nanoparticles, and helps in the determination of optimal conditions for the development of protein-functionalized nanomaterials having desired characteristic features and applications. The stability of a protein is very crucial for its bioactivity at the targeted site, and with the help of thermodynamics, one can study the structural alterations in proteins, which can be due to various environmental or artificial parameters ultimately causing its misfolding or deactivation and eventually resulting in losing the stability. The surface adsorption of proteins on the molecular surface depends upon certain factors such as size, shape, composition, and the extent of binding interactions both at the surface and within the molecules. The formulations show wide variations in behavior when different proteins are used, which further depends upon the bulk solution constituents, the ratio of sizes between the proteins used, and protein-surface interactions. Additionally, the potential of different proteins to alter their structure after getting

adsorbed greatly affects the kinetics of adsorption. Different adsorption patterns can be obtained based on the internal rates of structural modifications when compared with the protein diffusion, which can also be determined using intermolecular interactions.

Moreover, there is a strong relation between various relaxation times and the kinetics of adsorption, and it depends upon the morphology of particles [115]. A convex isotherm is formed when there is an association between protein and immobilized ligands. In contrast, when a protein molecule is adsorbed on another protein molecule, a sigmoid isotherm is formed, which is concave at low concentrations while convex at higher concentrations. For instance, insulin has concave isotherms at low concentrations [116]. One needs to study different parameters to get information about effect of all these factors. The thermodynamic parameters consist of Gibbs free energy (ΔG), enthalpy (H), and entropy (S), which can be calculated by using the following set of equations for all kinds of protein-based formulations.

$G = - RT \ln K$ ..... (1)

$\ln K = - H/RT + S/T$ .....(2)

$G = H - TS$ .....(3)

Where T is the temperature, and R represents the universal gas constant.

The other factors include K_a (association constant) and Kd (dissociation constant). Different protein-based formulations have different values for these parameters, which are briefly explained using some examples. The adsorption isotherms were plotted to determine the relationship between molecules that get absorbed on the surface and those remaining in the solution to monitor the binding capacity between the insulin protein and different magnetic nanoparticles (MMIP and MNIP). The slope of the adsorption curve increases sharply when a low initial concentration of the sample is used, while at higher concentrations, the slope is almost constant. Additionally, the ΔG values (in kJ/mol) for MMIP and MNIP are -39.2 and -36, the H values (in kJ/mol) are -39.3 and -36, while the ΔS values (in J/mol·K) are -0.26 and -0.27. The negative values of ΔG indicate that insulin adsorption is a spontaneous process.

Conversely, the negative values of ΔH and ΔS indicate that electrostatic forces, hydrogen bonds, and van der Waals forces are involved in insulin adsorption. Similarly, equilibrium results were evaluated using Langmuir and Freundlich isotherms to clarify the binding mechanisms of proteins with external agents. The adsorption kinetic model was used to study the kinetic mechanism of insulin adsorption, and it was observed that adsorption occurs via a pseudo-first-order mechanism during the initial 8 hours due to the presence of empty binding sites and lower concentrations of molecules, while after 8 hours, adsorption occurs via a pseudo-second-order reaction [117]. Similarly, novel nano-insulin formulations were developed using silver nanoparticles. Their ΔG values were found to be -6.72, -6.98, and -7.48 kcal/mol at 27˚C, 32˚C, and 37˚C, respectively, indicating the favorability of the forward reaction with the highest affinity at physiological conditions.

Similarly, the ΔH value is 16.08 kcal/mol, indicating the endothermic nature of the reaction between insulin and AgNPs. Furthermore, it was found that the reaction followed a first-order kinetic model based on the fluorescence quenching of insulin [118]. In the case of regenerated silk fibroin, crystallization is exothermic and is accompanied by entropy reduction when the temperature is kept constant. As the draw ratio increases, thermal stability and crystallinity are observed [119]. For the adsorption of heparin molecules on different molecularly imprinted polymers, the ΔG values were found to be -5.95, -4.70, and -2.73 kJ/mol at 299.15 K, 309.15 K, and 324.15 K, respectively, confirming the feasibility and spontaneity of the adsorption process. Moreover, the values of ΔH are negative, indicating electrostatic interactions between molecules, while the ΔS values are also negative, implying a decrease in entropy due to decreased randomness at the solution-solid binding point [120]. Further, the energy expenditure during the different wound healing phases varies significantly by 50% and 20% in the proliferative and remodeling phases. Also, the thermodynamics greatly influence the inflammatory phase by affecting the key features, including redness, swelling, and heat production during inflammation, of which swelling and redness are influenced by osmotic

pressure and fluid movement. The fluid movement rises by 100 times in order to meet the wound requirements by supplying nutrients and blood to the tissue site. Gibb's free energy plays a vital role in tissue recovery as it affects cell migration, collagen deposition, and angiogenesis. The wounds have a positive ΔG, indicating progress through the phases of wound healing. Chronic wounds have negative ΔG, which suggests that the tissue-recovery procedure is stuck in the inflammatory phase and cannot be proceeded. In this way, kinetic and thermodynamic factors play a crucial role in understanding the stability of nanoparticles and the feasibility of synthesizing protein-based nano-formulations for further applications.

1.5 Protein-based nano-formulations in normal and diabetic wound healing

1.5.1 Insulin-based formulations - Insulin has anti-inflammatory, anti-diabetic, and wound-healing properties by activating the cytokines, thus reducing inflammation. Insulin upregulates the NF-k$\beta^{P50/P50}$ by suppressing the expression of NF-k$\beta^{P50/P65}$ and TNF-α. P65 suppression downregulates IL-12, IL-1β, TNF-α, and IL-6 cytokines at the wound site [121],[122],[123]**.** Inflammatory cytokines inhibition shifts the equilibrium toward anti-inflammatory cytokines expression, like VEGF, IL-4, IL-10, etc., which further induces the proliferation of the cells [124],[125]. Multiple methods have been used to develop insulin-based nanoformulations. In 2017, X. Li and co-workers developed silk fibroin-based microparticles (insulin-SFPs) encapsulating insulin; the particles provide biostability to the insulin and help in its sustained release. The particles showed significant collagen deposition, and vascularisation stimulated the keratinocytes and endothelial cells migration and promoted healing compared to the free insulin [126],[127] **(Figure. 9A)**. In 2018, A. Ehterami et al. followed the ion gelation method for preparing insulin-loaded chitosan particles (insulin-CPs) followed by their coating on poly Ɛ-caprolactone (PCL) (insulin-PCL-CNPs); the particles showed a reduction in inflammatory cytokines infiltration and 96.9 ± 1.11% wound recovery after 14 days [128] **(Figure. 9B)**.

In 2018, DH Abdelkader et al. developed insulin-loaded polyvinyl alcohol borate nanoparticles (insulin-PLGA CNPs), significantly enhancing wound healing. With PLGANP-insulin, 29.15% more wound recovery occurs on the 10th day of the treatment. The insulin embedded in the particles is released by the diffusion method. The difference in wound closure up to 16 days in diabetic rat models treated with control, free insulin, and insulin-loaded PLGA particles showed faster wound healing and increased exudates formation and angiogenesis with insulin PLGA insulin particles [129] **(Figure. 9C)**. In 2019, Kaur P et al. prepared insulin protein-coated silver nanoparticles (insulin-AgNPs) to deliver insulin at the place of injury **(Figure. 9D)**. Along with anti-bacterial effect, AgNPs also have significant role in treating wounds and exhibit anti-inflammatory action. The inflammatory cytokine transition and wound healing properties of AgNPs improved by encapsulating them with insulin. The wound-healing effect of IAgNPs was determined in diabetic and nondiabetic environment. Both free insulin and IAgNPs treatment showed a faster recovery of the wound. 20% and 12%, more rapid wound recovery in diabetic and normoglycemic rats, respectively, on the 5th day of IAgNPs treatment than free insulin 4.67% (diabetic model) and 7.27% (nondiabetic model). After 11 days of IAgNPs treatment, 73.33%, 60.0%, and free insulin, 40% and 33.33%, were observed in diabetic and normoglycemic models, respectively, compared to the respective controls. In addition to the wound contraction assay, the histological expression of the pro- and anti-inflammatory cytokines was also examined. Histological evaluations of rat models exhibited enormous collagen deposition along with reepithelialization. A decrease in the leukocyte infiltration was monitored using IAgNPs and insulin with respect to additional solutions. On the 5th day of treatment, IAgNPs, the proinflammatory cytokines expression level decreases by 50% in both diabetic and nondiabetic groups. On the 11th day, IL-6 and TNF-α decreased by 45% in diabetic and normoglycemic sets. The IL-10 anti-inflammatory cytokines expression level after five days of treatment with IAgNPs increases by 70% and 50% in rat models. On the 11th day, wound healing accelerated by 65% and 50% in nondiabetic and diabetic groups [118]. M.C. Ribeiro et al., used

chitosan to synthesize insulin-loaded nanoparticles (insulin-CNPs) and examined the effect on wound healing. Histological evaluation showed angiogenesis, reduction in inflammatory cells like monocytes, macrophages, neutrophils, keratinocytes, increase in endothelial cell proliferation, collagen deposition, and maturation of wound following treatment compared to free insulin [130] **(Figure. 9E)**. The particles of Poly (lactide-co-glycolide) (insulin-PLGA NPs) loaded with insulin were prepared by Lee J et al. in 2013 by evaporating the solvent using the double emulsion technique. The prepared particles are biodegradable and have viscoelastic properties—the insulin embedded in the particles is released by diffusion. The difference in wound closure in control, free insulin, and insulin-loaded PLGA particles was up to 16 days. With insulin PLGA particles, the healing rate is faster and increases the exudate formation and angiogenesis formation [131].

The nanoclusters (NCs) of insulin with metals have bioimaging properties and wound-healing activity. These NCs comprise several to a hundred metal atoms with an outer layer of protein to protect them from aggregation. Kaur P et al. (2020) prepared insulin copper quantum clusters (Insulin-CuQCs) that exhibited wound healing and bioimaging activity. Similar to Zinc, Copper also promotes cell growth and division. At a 5% concentration of ICuQCs in 24h, there was an almost double increase in HeLa cell growth compared to the control (insulin + Cu salt, insulin, and blank), indicating the ICuQCs' cell growth-promoting effect [14] (**Figure. 9F**). Kaur P et al. (2021) prepared insulin zinc quantum clusters (Insulin-ZnQCs) and tested them for cell migration and bioimaging efficiency using HEKa. The cells incubated with 1.5, 7.5, 30, and 60 µM IZnQCs showed 39.49 ± 1.29%, 42.03 ± 3.04%, 45.25 ± 2.14%, and 52.88 ± 0.83% cell migration, respectively, after 6 hours compared to control. After 12 hours of incubation, cell migration of 27.58 ± 3.72%, 34.08 ± 1.57%, 36.32 ± 1.63%, and 46.86 ± 1.46% occurred with 1.5, 7.5, 30, and 60 µM IZnQCs treatment compared to control. After 24 hours, the % of cell migration was 43.02 ± 1.62%, 46.51 ± 3.38%, 58.60 ± 0.72%, and 67.81 ± 0.83% when compared with control. An increase in migration was observed with an increase in time, and at 24h, maximum wound recovery was observed [15] (**Figure. 9G**). Similarly, insulin-nickel quantum clusters (INiQCs) were prepared by Sharda et al. to test wound healing efficiency in vitro and bioimaging and to detect lead in silico and in vitro. They effectively healed wounds at different concentrations of 1.5, 7.5, 30, and 60 µM after various time intervals of 6, 12, and 24 hours, respectively, and showed bioimaging effects at varying concentrations [16]**.** Also, insulin-cobalt core-shell nanoparticles were synthesized for the treatment of wounds and are found to be very effective against both normal and diabetic wound healing. The effect of particle concentration was studied, and it was found that with increasing concentrations of 1.5, 7.5, 30, and 60 µM, there is accelerated healing rate with time [132]. A hydrogel scaffold was developed using morin incorporated into polysaccharide-protein, which decreased the reepithelialization rate and increased the wound contraction rate by enhancing collagen deposition in diabetic rats [133]. Wan W et al. prepared Gelatine cryogel loaded on the surface of silver nanoparticles (Gelatin-AgNPs-PDGF-BB) at the PDGF-BB bottom layer, which exhibited better wound healing, reepithelialization, angiogenesis, deposition of collagen, and granulation tissue formation in diabetic wounds [134] **(Figure. 9H).**

1.5.2 Silk fibroin-based formulations - Curcumin-loaded silk fibroin conjugated with polycaprolactone or polyvinyl alcohol was used to make a nanofibrous mat for healing diabetic wounds faster in animal models [135]. Maity et al. synthesized antioxidant silk fibroin composite hydrogel to heal diabetic wounds rapidly. They were biocompatible, stimulated fibroblast cell migration, and controlled oxidative stress in vitro [136]. Silk fibroin and silk sericin-based formulations were developed after mixing with aloe vera gel for tissue recovery in diabetic mice, and it was found that the wounds healed within 13 days of applying the formulation, with a wound contraction of 98.33 ± 0.80% [137]. Hydrogel films were created by combining boric acid-impregnated silk fibroin/gelatin and hyaluronic acid, resulting in an improved tissue healing process and increased strength [138]. Silk fibroin interlinked with glycyrrhizic acid and silver hydrogels were also prepared for the effective treatment of wounds with bacterial infection [139].

Additionally, a multitasked aerosolized nanopowder formula made from silk fibroin exhibited antioxidant, anti-bacterial, and enhanced cell proliferation effects, providing a promising approach to wound healing [140]. Wu et al. found that adipose-derived stem cell-seeded silk fibroin-chitosan films improved tissue healing in rat model [141]. Sen et al. synthesized silk fibroin immobilized polyurethane conjugated with epidermal growth factor, which enhanced the rate of burn wound healing of full-thickness burn and reduced proinflammatory cytokines IL-6,8,10 levels in diabetic rats [142]. Silk fibroin-integrated biliverdin-based bioinspired green hydrogel stimulated angiogenesis and wound healing in rat model by exhibiting anti-inflammatory effects [143]. Silk fibroin-hyaluronic acid-based composite scaffolds were developed for monitoring the cellular growth at wound sites and were found to enhance the scarless reconstruction of skin in nude mice with skin tissue defects [144]. Silk fibroin and poly(lactide-co-glycolic acid) nanofiber were loaded with zinc oxide nanoparticles for their successful delivery at the wound site and to promote reepithelialization, collagen deposition, granulation tissue formation, and angiogenesis [145].

1.5.3 Keratin-based formulations -Veerasubramanian et al. developed konjac-glucomannan-keratin hydrogel wound dressings having oat extract, which significantly enhanced the wound treating ability in diabetic conditions by promoting the synthesis and deposition of collagen in the wounded area [146]. In another study, recombinant keratin particles (Keratin-NPs) were prepared by Gao et al. to improve wound healing, vascularisation, epithelization, and collagen deposition [147] **(Figure. 9I)**. Chicken feather proteins were utilized by Kumaran et al. to synthesize keratin hydrogels for treating dermal injuries [148]. Furthermore, keratin hydrogels loaded with ciprofloxacin were developed to promote the healing of full-thickness excision wounds and prevent infection caused by *Pseudomonas aeruginosa* bacteria [149]. Human platelet lysate-loaded keratin hydrogels were also synthesized to exhibit sustained release of pro-regenerative growth factors essential for healing and enhancing cell proliferation without toxicity *in vitro* models [150]. Robert et al. utilized keratin-based wound dressing to treat a patient suffering from recessive dystrophic epidermolysis bullosa in 2012 [151]. Electro-spun fibers, loaded with keratin and hyaluronic acid, were also found to be potent wound dressings because they increase cell viability and proliferation [152]. Keraderm is a matrix dressing obtained from keratin powder by freeze-drying, which is utilized to heal exuding venous ulcers and the complete wound in 30 weeks. Similarly, kerafoam, an absorbent polyurethane foam dressing with keratin film lamination, was developed for highly exuding venous ulcers, which healed completely in 16 weeks. To treat partial-thickness wounds, an absorbable matrix called keramatrix was created, which is found to enhance the epithelialization process of wounds [153].

1.5.4 Collagen-based formulations -Other extracellular proteins, such as amnion and collagen-based composite hydrogels, were developed to treat cutaneous burn wounds by enhancing the reepithelialization abilities [154]. Curcumin-loaded fish scale collagen-hydroxypropyl methyl cellulose nano gel promoted healing with better contractile percentag of the injury and prolonged drug release [155]. Chitosan/collagen scaffolds loaded with Norfloxacin were also developed to enhance skin reconstruction and improve adhesivity and mechanical strength for healing [156]. Sun et al. prepared collagen nanofibres (Coll-NFs) in 2018, which were found to decrease inflammation, promote faster recovery of wounds, and increase angiogenesis [157] **(Figure. 9J).** A matrix of Collagen-laminin having resveratrol loaded with hyaluronic acid-DPPC microparticles was used in treating the injury in diabetic rats, and a controlled drug release was achieved along with its antioxidant activity [158]. Collagen-chitosan scaffolds loaded with pioglitazone were synthesized, which were biocompatible, promoted cell growth, and exhibited enhanced wound contraction in diabetic wounds [159]. In yet another formulation, collagen dressing was loaded with neurotensin, which facilitated the controlled release of drugs in injury area, enhanced reepithelialization, and decreased the secretion of inflammatory cytokines in diabetic foot ulcers [160].

1.5.5 Heparin-based formulations - Heparin micro islands were developed by Pruett et al. in

microporous scaffolds, which promoted diabetic wound healing abilities by epidermal regeneration and re-vascularization [161]. The heparin-poloxamer hydrogel was also developed by Xu et al. using polylysine to heal endometrial injury by controlling KGF release and enhancing adhesiveness [162]. Double emulsion nanoparticles were developed using sulfated alginate and polycaprolactone to improve the delivery of heparin-binding growth factors that promote healing due to connective tissue growth factor secretion [163]. Additionally, pro-angiogenic nanofibrous membranes based on chitosan and heparin were developed using an efficient and new electrospinning method for wound healing applications, which enhanced tissue angiogenesis [164]. Senturk et al. prepared heparin memetic particles (heparin-NFs) in 2016, which were found to enhance reepithelialization, promote a fast transition of proinflammatory to anti-inflammatory cytokines, improve angiogenesis, and lead to high VEGF levels and wound recovery [165] **(Figure. 9K)**. Analyses of reepithelialization, granulation tissue formation, blood vessel density, VEGF, and inflammatory response measurements quantified wound recovery [161]. The synthesis of heparin-based hydrogel incorporating Cu nanozymes was done to inhibit inflammation by decreasing the proinflammatory cytokines and ROS scavenging, which eventually led to wound healing [166]. Lu et al. developed a thermoresponsive hydrogel involving heparin protein with *Lactococcus* incorporated in it, which is helpful in wound healing by promoting angiogenesis, reducing the inflammatory microenvironment across the wound area, and decreasing the risk of systemic toxicities by preventing the entry of bacteria at the infection site [167].

P311 peptide-based micelles were assembled with ROS-responsive polymer for the transformation of an oxidative wound environment to a regenerative environment for tissue recovery by increasing collagen deposition, reepithelialization, cell migration, and granular tissue synthesis [168]. Recently, Ge et al. developed a novel nano armor which assists in the transport of IL-4 by protecting its biological activity and enhancing circulation throughout the blood. The synthesized copolymer consists of two layers: outer polyethylene glycol layer and intermediate rosamirinic acid layer for protecting the innermost IL-4, which is helpful in ROS scavenging, decrease in the secretion of inflammatory cytokines, and M1 to M2 transition crucial for healing [169]. The different nano-formulations obtained by using different proteins, along with their potential outcome, are given in **Table 2.**

Table 2: The table provides information about the different protein functionalized nanomaterials along with the protein used, their key outcomes, and the models on which they were tested to give a detailed knowledge of different formulations

Protein	Formulation	Tested on	Key outcome	Ref.
Insulin	Insulin-encapsulated silk fibroin microparticles	• HaCaT • Sprague Dawley rats	• Sustained release of insulin • Enhanced collagen deposition and vascularization • The accelerated wound closure rate	[127]
	PCL/COLL loaded with insulin chitosan nanoparticles	• L929 • Male Wistar rats	• Enhanced blood compatibility • Protection against bacterial infection • Enhanced cell adhesion, growth, and migration	[127]
	Insulin-loaded Poly(vinyl alcohol)-borate hydrogels	• Male Sprague Dawley rats (diabetic)	• Topical insulin delivery • Granulation tissue formation rate and angiogenesis accelerated • The localized rise in collagen deposition	[131]

	Insulin-loaded chitosan nanoparticles	• Female Wistar rats (diabetic)	• Stimulated vasodilation, proliferation, leukocyte chemotaxis • Accelerated epithelialization and collagen deposition	[128]
	Insulin-loaded core-shell cobalt nanoparticles	• HEKa	• Enhanced cell migration and wound closure rate • Targeted drug delivery • Highly potent for bioimaging	[132]
	Zinc insulin quantum clusters	• HEKa	• Enhanced cell migration and wound closure rate • Targeted drug delivery • Highly potent for bioimaging	[15]
	Insulin-loaded silver nanoparticles	• HEKa • Male Wistar rats	• Regulation of balance between pro and anti-inflammatory cytokines • Enhanced cell migration and wound closure rate • Targeted drug delivery	[14]
	Insulin nickel quantum clusters	• HEK-293	• Enhanced cell migration and wound closure rate • Targeted drug delivery • Highly potent for bioimaging • *in vitro* and in silico lead detection	[16]
Silk Fibroin	Curcumin-loaded polycaprolactone/polyvinyl alcohol-based silk fibroin-based electrospun nanofibrous mat	• Albino female mice	• Antioxidant and anti-inflammatory activity • Restore the skin structure and histology of tissue at a faster pace • Faster wound healing	[135]
	Melanin and berberine amalgamated silk fibroin hydrogel	• NIH3T3 • Wistar rat model (diabetic)	• Enhanced biocompatibility • Prevent oxidative stress • Enhanced migration of fibroblasts, reepithelialization, and wound closure	[136]
	Aloe vera gel-loaded silk fibroin formulations.	• Albino mice (diabetic)	• Enhanced growth of collagen fibers and blood vessels • Much decreased inflammation	[137]
	Silk fibroin/ gelatin/ hyaluronic acid-based films impregnated with boric acid.	• L929	• Increased cell migration activity *in vitro* • Promoted wound healing	[138]
	Silk fibroin crosslinked glycyrrhizic acid and silver hydrogel	• *Staphylococcus aureus* infected	• Enhanced biocompatibility and mechanical properties • Antibacterial and anti-inflammatory effects • Promote tissue regeneration	[139]

		wound in mice • Chorioallantoic membranes		
	Aerosolized nanopowder having neomycin and *Avicenna marina* extract loaded in silk fibroin.	• CRL2522	• Potent increase in cell viability • Enhanced antioxidant activity • Excellent antibacterial activity	[140]
	Adipose-derived stem cell-seeded silk fibroin chitosan film	• Male Sprague Dawley rats (diabetic)	• Accelerated cell growth • Differentiation of adipocyte and osteocyte enhanced • Enhanced granulation tissue formation, capillary formation, reepithelialization	[141]
	Epidermal growth factor conjugated silk fibroin immobilized polyurethane	• NIH3T3 • Rat model (normal and diabetic)	• Enhanced granulation, collagen deposition, reepithelialization • Restoration of proinflammatory cytokines IL-6,8,10 • No sign of infection at the wound site	[142]
	Biliverdin silk fibroin hydrogel	• GL261 • Male BALB/c nude mice	• Enhanced anti-inflammatory effect • Stimulated angiogenesis • Full-thickness wound healing	[143]
	Hyaluronic acid containing silk fibroin scaffold	• HUVEC • Sprague Dawley rats	• Enhanced cell adhesion, proliferation, and differentiation • Regulation of collagen arrangement • Inhibited scar formation	[144]
	Zinc oxide-loaded PLGA/ silk fibroin electrospun membranes	• L929 • Male Sprague Dawley rats	• Enhanced reepithelialization, collagen deposition, granulation tissue formation, and angiogenesis • Antioxidant and antibacterial activity	[145]
Keratin	*Avena sativa* extract loaded konjac glucomannan-keratin hydrogel scaffold	• NIH/3T3 • Male Wistar rats	• Exhibit desirable swelling, biocompatibility, antibacterial, and antioxidant activity. • Enhanced wound contraction and collagen synthesis • Increased epidermis layer and blood vessel synthesis	[146]
	Chlorhexidine loaded poly	• L929	• Reduced inflammation • Enhanced collagen deposition • Antioxidant and antibacterial	[170]

	sulfobetaine/keratin hydrogel.	• Sprague Dawley rats		
	Recombinant keratin nanoparticles	• HaCaT • Male Sprague Dawley rats	• Enhanced cell migration and proliferation • Improved epithelialization, vascularization, remodeling, and collagen deposition • No systemic toxicity *in vivo*	[147]
	Chicken feather keratin hydrogel	• Skin cells	• Enhanced migration of keratinocytes from the boundary to the inner wound site	[148]
	Ciprofloxacin loaded keratin hydrogel.	• Female Yorkshire pigs • *P. aeruginosa*	• Decrease in the amount of *P. aeruginosa* by 99% • Collagen-rich granulation tissue and fibroblasts at the wound site • Enhanced reepithelialization and wound contraction	[149]
	Keratin hydrogel loaded with human platelet lysate	• HDF	• Sustained release of pro-regenerative growth factors • Promoted and supported cell proliferation without causing toxicity for up to three days	[150]
	Keratin-based dressing (keragel T)	• Patient with recessive dystrophic epidermolysis bullosa	• Enhanced keratinocyte proliferation and migration • Accelerated epithelialization, epidermal migration, and keratinocyte activation	[151]
	Nanocomposites based on polycaprolactone/ polyethylene oxide loaded with hyaluronic acid and keratinin	• L929	• Non-toxic nature • Enhanced cell proliferation and viability	[152]
Collagen	Curcumin-loaded fish scale collagen hydroxypropyl methylcellulose nano gel	• Male albino Wistar rats	• High stability, wound contraction ability, and safe for dermatological application	[155]
	Collagen/chitosan-based porous scaffold	• HDF • Male Wistar rats	• Enhanced fibroblast migration and proliferation • Increased collagen deposition and synthesis of Collagen IV • angiogenesis	[171]

	Mupirocin-loaded chitosan microspheres embedded in collagen scaffold	• Unisex Wistar rats	• Collagen deposition • Fibroblast proliferation • No inflammation	[172]
	Norfloxacin-loaded collagen/chitosan scaffold	• Albino rats	• High water uptake and retention ability • Enhanced bioadhesive strength and slow biodegradation • 100% drug release ability • Accelerated tissue regeneration • Intact epidermal and dermal structure	[156]
	Collagen scaffold	• STZ-induced diabetic rat	• Accelerated migration of fibroblasts and keratinocytes • Enhanced angiogenetic activity • Decreased inflammation	[157]
	Collagen-laminin dermal matrix impregnated with resveratrol-loaded hyaluronic acid-DPPC microparticles	• Male Wistar albino rats	• Excellent antioxidant activity eventually promotes wound healing • Enhanced cell proliferation of fibroblasts, keratinocytes, and endothelial cells • Maintain matrix integrity by acting against collagenase	[158]
	Pioglitazone loaded collagen/chitosan scaffold	• 3T3-L1 • Male wistar albino rats	• Optimum porosity, low matrix degradation, sustained drug release • Significant decrease in matrix metalloproteinases-9 • Better growth of fibroblast • Potent anti-inflammatory effect	[159]
	Neurotensin-loaded collagen matrix	• HaCaT • Raw 264.7 • Male C57BL/6 Mice	• Reduced inflammatory cytokine expression • Decreased inflammatory filtrate and metalloproteinases • Increased fibroblast migration • Enhanced deposition of collagen, collagen type III, and alpha 1	[160]
Heparin	Heparin micro islands	• Mice • HDF • HDMVEC	• Epidermal regeneration and revascularization in a diabetic model • Downstream cell migration *in vitro*	[161]
	Heparin/Prussian blue-loaded - nanofibers	• NIH3T3 • C57/BL mice	• Decreases intracellular ROS level • Prevent cells from ROS-mediated apoptosis • Accelerate the inflammatory response and wound healing	[173]

	Heparin-based sericin hydrogel encapsulated fibroblast growth factor	• BALB/c mice • HDF	• Enhanced adhesiveness • Excellent biodegradability • Increased collagen deposition, vascularisation, and reepithelialization	[174]
	Heparin poloxamer	• ECC • Female Sprague Dawley rats	• Enhanced proliferation and angiogenesis of endometrial epithelial cells • Inhibit cellular apoptosis in the endometrium	[162]
	Heparin mimetic alginate sulfate/polycaprolactone nanoparticles	• HaCaT	• Controlled drug delivery • Protection of drug from degradation • Enhanced cellular migration, proliferation, and matrix deposition	[163]
	Heparin-loaded chitosan nanofibers	• chorionic allantoic membrane	• Stimulated angiogenesis	[164]
	Heparin mimetic peptide nanofibers	• Male Sprague Dawley rats (Diabetic)	• Promote angiogenesis, reepithelialization, and inflammatory response • Increased macrophage infiltration and VEGF expression • Induced angiogenesis	[165]
	Cu5.40 loaded heparin hydrogel	• NIH-3T3 • HUVEC • Diabetic mice	• Decreases immune cell influx and inflammatory signals at the wound site by capturing inflammatory chemokines • ROS Scavenging • Promote wound healing	[166]
	Lactococcus-loaded heparin poloxamer hydrogel	• HUVEC • Macrophages • Mice	• Controlled release of bioactive proteins and immune-regulating molecules • Reduces inflammatory microenvironment • Enhanced angiogenesis	[167]
	Heparin-loaded chitosan nanofibers	• chorionic allantoic membrane	• Stimulated angiogenesis	[164]
	Heparin mimetic peptide nanofibers	• Male Sprague Dawley rats (Diabetic)	• Promote angiogenesis, reepithelialization, and inflammatory response • Increased macrophage infiltration and VEGF expression • Induced angiogenesis	[165]

	Cu5.40 loaded heparin hydrogel	• NIH-3T3 • HUVEC • Diabetic mice	• Decreases immune cell influx and inflammatory signals at the wound site by capturing inflammatory chemokines • ROS Scavenging • Promote wound healing	[166]
	Lactococcus-loaded heparin poloxamer hydrogel	• HUVEC • Macrophages • Mice	• Controlled release of bioactive proteins and immune-regulating molecules • Reduces inflammatory microenvironment • Enhanced angiogenesis	[167]

1.6 Growth factors and growth regulators in healing wounds

Growth factors, like proteins, play a crucial role in wound healing. These physiologically active proteins get linked to specific receptors for stimulating molecular mechanisms for various cell functions, supporting cell proliferation, differentiation, migration, metabolism, and wound healing [175]. FGF is known to upregulate the activation of MEK-P, which in turn activates the NF-kβP50/P50 and inhibits NF-kβP50/P65 expression responsible for the activation of proinflammatory cytokines such as IL-1β, IL-6, IL-12, and TNF-α [38],[176]. FGF also upregulates the expression of Akt, which activates eNOS, STAT3, PI3K, and MMP, which are responsible for tissue growth and angiogenesis [177]. Nguyen et al. in 2017 prepared FGF-loaded carboxyl methyl chitosan (CMCS) nanoparticles (FGF-CMCS NPS) using an ionic gelation method for biological applications and FGF-2 remains protected from degradation of trypsin and thus act as an efficient way of FGF2 delivery at wound site for *in vivo* applications [178] **(Figure. 9L).** Butko et al. in 2016 loaded fibroblast growth factor (bFGF) into N-succinyl-chitosan and chitosan/TPP to prepare its nano-formulation with 60% encapsulating efficiency. The bFGF stimulates the transition from inflammation to cell proliferation, remodeling, and wound recovery [179]. Also, Cetin M et al., in 2007, reported bFGF (Basic fibroblast growth factor; belongs to the FGF family), and a pleiotropic growth factor loaded chitosan particles (bFGF-CNPs) with 27.388% encapsulation efficiency and the particles were found to be unaffected in their structure by any changes in release parameters and encapsulation procedure thus maintaining their stability [180] **(Figure. 9M).**

Losi et al. in 2013 prepared bFGF and vascular endothelial growth factor (VEGF) loaded poly lactic-co-glycolic acid (PLGA) nanoparticles (VEGF-PLGA NPs), which had a potential impact on cell division, cell proliferation, collagen deposition, re-epithelization, and helped in wound closure in comparison to controls in addition to angiogenesis [181] **(Figure. 9N)**. VEGF activates PI3K, Akt, and eNOS to support cell growth and angiogenesis [182]. Further, it activates JAK/STAT3, which promotes cell survival and blocks the signaling of pro-inflammatory cytokines STAT1, SOCS, etc. [183]. Chereddy et al., in 2015, treated wounds with VEGF-loaded PLGA nanoparticles, which showed an enhancement in collagen deposition that helps in re-epithelialization, angiogenesis, and complete recovery of the injury in 28 days in comparison to the free GFs [184]. Murphy et al., in 2013, synthesized VEGF-encapsulated PLGA particles (VEGF-PLGA) through leaching and observed 70% recovery within 12 days and was found to enhance the wound healing capacity at a faster pace [185]. Mohandas et al. prepared fibrin nanoparticles for VEGF loading to help improve the angiogenesis, ultimately leading to accelerated healing effect due to blood vessel formation [186] **(Figure. 9O).** An *in vitro* transcription (IVT) method was used to develop VEGF-A mRNA, which is encapsulated for delivery into ionizable lipid-mediated nanoparticles using the microfluidic

method and is found to be very effective in enhancing the proliferation of cells along with efficient delivery of mRNA, is found to be non-toxic in nature and used for diabetic wound healing [187]. A new chitosan-modified hydrogel having silver ions and epidermal growth factor encapsulated in nanoparticles is developed for healing diabetic wounds and exhibited excellent collagen deposition and maturation ability, increased re-epithelialization, and optimized delivery of silver and growth factor at the wound site [188]. A polymeric path containing epidermal growth factor, GelMA hydrogel, and PHBV membranes are developed for treating diabetic wounds. This path not only enhances angiogenesis but also promotes proliferation and differentiation of fibroblasts, endothelial cells, and keratinocytes [189]. In 2018, Pan et al. synthesized Keratinocyte growth factor (KGF) linked gold nanoparticles (KGF-AuNPs), which promote keratinocyte proliferation promotes wound healing through re-epithelisation rather than granulation [190] **(Figure. 9P)**. KGF works similarly to VEGF through the KGF receptor (KGFR) [191]. The similar nanoparticles used for in vivo studies on diabetic rat models by Li et al. showed the binding of KGF with KGF receptors. They enhanced the collagen-I level, TGF-β1, and alpha-smooth actin (α-SMA) that assists in wound healing [192]. Muhamed et al., in 2019, synthesized KGF-loaded nanoparticles (KGF-F NPs) using fibrin which enhanced in vivo migration of cells and wound closure [193],[194] **(Figure. 9Q).** Like other growth factors, EGF also shifts the equilibrium toward the anti-inflammatory cytokines by activating PI3K/Akt, mTOR, MEK-P and STAT 3, etc. [195]. Zhang P et al., in 2020, prepared carboxymethyl chitosan (CC) nanoparticles by hydrophobic conjugation of linoleic acid with the carboxymethyl chitosan and loaded them with recombinant human epidermal growth factor (rh-EGF-CC NPs) [196] **(Figure. 9R).** Controlled release of the loaded unstable growth factor showed the wound healing effect when tested in vitro and in vivo. Even in chronic wounds, CC showed more inflammation recovery and healing efficiency than free rh-EGF. Gainza G et al., in 2014, prepared a similar SLN particle nanocage by emulsification ultrasonication method for loading rh-EGF that showed significant wound healing compared to the free rh-EGF [197]. In chronic wounds, rh-EGF-loaded nanoparticles promote the proliferation of cells, reduce inflammation, and help in re-epithelization and wound healing. Chu et al., in 2010, used identical rh-EGF-loaded SLN particles (rh-EGF-SLNPs) prepared using the double emulsion method [198] **(Figure. 9S).** The growth factor-loaded particles enhance fibroblast proliferation and wound healing in diabetic rat models. Rajam et al., in 2011, prepared EGF and FGF encapsulated inside chitosan tpp nanoparticles having 83% and 84% release capacity, respectively, up to 35 days [199].

Xie et al. used two growth factors, platelet-derived growth factor (PDGF-BB) (**Figure. 3J**) and VEGF; VEGF loaded within the nanofibres and PDGF-BB inside the PLGA nanoparticles [200]. It accelerated wound regeneration, tissue remodeling, and collagen deposition with platelet-derived and VEGF-stimulated angiogenesis. Circolo et al. showed that PDGF decreases the expression of TNF-α and IL-1 inflammatory cytokine [201]. Piran et al. prepared electro-spun embedded chitosan nanoparticles for the controlled release of PDGF-BB (PDGF-BB CNPs) at the site of the wound **(Figure. 9T).** PDGF-BB showed significant changes in the chemotactic behavior of the cells, induced the division of the fibroblasts and neutrophils, caused the migration of the cells at the wound site, and helped in wound closure [202]. On the basis of all the instances mentioned above regarding the utilization of growth factors and growth regulators as potent stimulators of wound healing by regulating cellular proliferation, migration, and differentiation, more research needs to be done to increase their stability, absorption rate, efficacy, target specificity, biocompatibility and growth promoting abilities to yield better outcomes in the near future. The action mechanism of these growth factors is well known to the scientific community, but their application in preclinical and clinical trials is still lacking despite their wonderful features. Moreover, in recent years, the number of patients suffering from intractable wounds, including diabetic ulcers, foot ulcers, etc., is increasing drastically, and to eliminate these ailments, research in the field of understanding the role of growth factors for optimizing the wound surroundings for treatment will be an exciting area of interest.

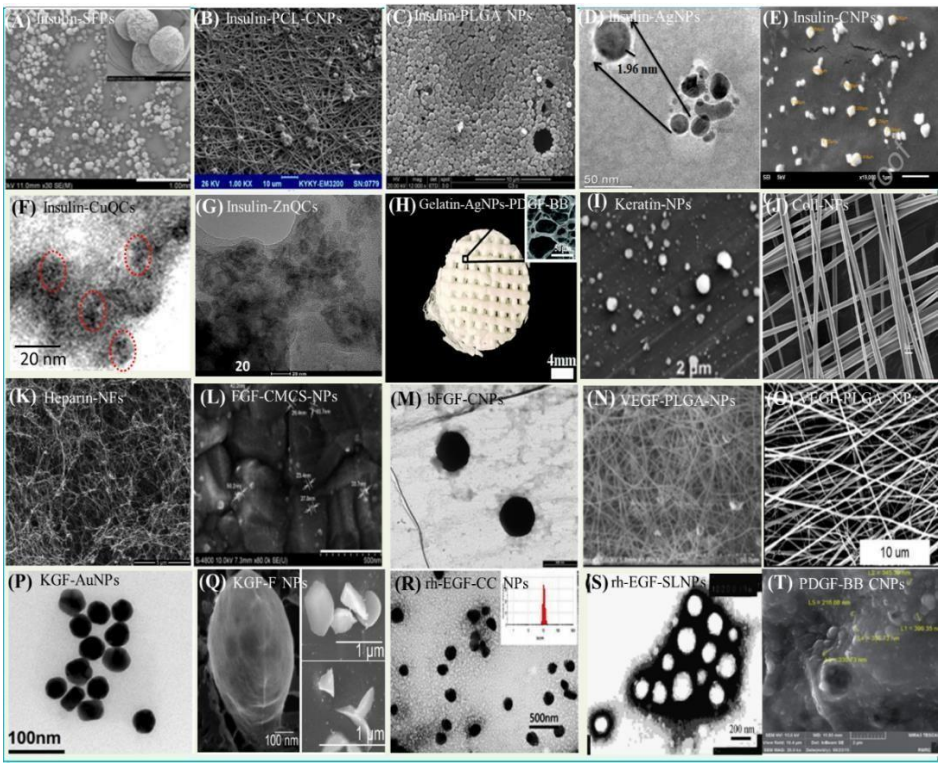

Figure. 9. *SEM/TEM images of the different protein-loaded nano-formulations (A) Insulin-silk fibroin nanoparticles (B) Insulin-PCL-Chitosan nanoparticles (C) Insulin-PLGA nanoparticles (D) Insulin-Ag nanoparticles (E) Insulin-Chitosan nanoparticles (F) Insulin-Cu Quantum clusters (G) Insulin-Zinc quantum clusters (H) Gelatin-AgNPs-PDGF-BB (I) Keratin nanoparticles (J) Collagen nanofibers (K) Heparin nanofibers (L) Fibroblast growth factor-CMCS nanoparticles (M) bFGF loaded chitosan nanoparticles (N) VEGF-PLGA nanoparticles (O) Vascular endothelial growth factor loaded PLGA nanoparticles (P) Keratin Growth factor-Au nanoparticles (Q) KGF loaded fibrin nanoparticles (R) rh-EGF loaded carboxymethyl chitosan nanoparticles (S) rh-EGF loaded solid lipid nanoparticles (T) PDGF-BB nanoparticles [Adapted with permission from ACS, RSC, Elsevier, Taylor and Francis, Springer, Nature].*

1.7 Conclusion and Future Directions

Wound healing involves several phases which occur simultaneously to promote faster recovery and prevent infection. Nano-formulations involving inorganic, organic, or biological precursors have been developed to make the formulations for wound healing biocompatible, cost-effective, and efficient. Protein and growth factors are commonly used due to their unique properties. They control inflammation at the wound site through distinct signaling pathways, leading to fast recovery. Protein-based nano-formulations can be entrapped inside the particle, protein-embedded particles, or loaded on the surface of the particles. Further, the incorporation of proteins into nanoformulations promotes the stability and activity of the proteins by preventing their degradation under unfavorable conditions. These formulations control the release of proteins for a longer time, hence enhancing efficacy and effect at the wound site. They also assist in targeted drug delivery and improve solubility and biocompatibility. The kinetic and thermodynamic behavior of proteins and growth factors based on particles promotes tissue recovery without complications such as infection. An appropriate protein-based healing system in the form of an ointment, dressing, scaffold, hydrogel, film, powder, or electro-spun fibers can be utilized depending on the wound's requirements. Protein-based particles offer many advantages, including biocompatibility, efficiency, size, structure, easy availability, low production cost, and high biological efficiency. They also exhibit bioactivity, biodegradability, non-toxicity, enhanced re-epithelialization, cell growth, wound contraction, better

repair, infection control, and antioxidant abilities.

The demand for protein-functionalized nanomaterials is enormously increasing, and emphasis should be laid on making the synthesis process less cumbersome and more effective. The elaborative discussion of the future perspective of these formulations is very crucial as their development will revolutionize healthcare facilities in wound healing in the near future, and these should be developed by keeping in mind the specific target or the effective area in the body. These formulations have a bright future in therapeutic and theranostics, and they can be used as promising drug carriers, making their delivery targeted and effective. The proteins that can be transformed into scaffolds or fibers have a more comprehensive potency to act as a carrier of different therapeutics, including drugs, dyes, and inorganic and small organic moieties, thus diversifying their potential applications. In the future, these nanoformulations are expected to play a potent role in developing personalized medicine for injury recovery due to the advances in technology, which makes it possible to customize the formulations depending upon the patient's needs and specific features of the wound and ultimately lead to more effective and efficient wound healing by reducing the time and cost of treatment. Furthermore, the commercial potential of protein-based nanoformulations is enormous. With the accelerated occurrence of chronic wounds, the demand for effective and efficient wound healing treatments is rising, and protein-functionalized nanoformulations have the potential to become a widely used treatment option due to their efficacy, safety, and cost-effectiveness. Several companies have already entered the protein-based nanoformulations market. The market is expected to grow rapidly, and the global wound care market is estimated to reach USD 24.8 billion by 2026. Developing new and innovative protein-based nanoformulations could help drive this growth further.

In conclusion, protein-based nanoformulations have shown immense potential in wound healing and have a bright future in both medical and commercial applications. Further research and development in this area will promote the discovery of more effective and efficient wound-healing agents, improving the quality of life across globe.

Chapter 2: Insulin-cobalt core-shell nanoparticles for receptor-targeted bioimaging and diabetic wound healing

Abstract

Diabetic wounds represent a significant issue in medical care and need advanced therapeutic and tissue imaging systems for better management. The utilization of nano-formulations involving proteins like insulin and metal ions plays substantial roles in controlling wound outcomes by decreasing inflammation or reducing microbial load. This work reports the easy one-pot synthesis of extremely stable, biocompatible, and highly fluorescent insulin-cobalt core-shell nanoparticles (ICoNPs) with enhanced quantum yield for their highly specific receptor-targeted bioimaging and normal and diabetic wound healing *in vitro* (HEKa cell line). The particles were characterized using chemical-physical properties, biocompatibility, and wound healing applications. FTIR bands at 670.35 cm^{-1}, 849.79, and 973.73 indicating the Co-O bending, Co-O-OH bond, and Co-OH bending, respectively, confirm the protein-metal interactions, which is further supported by the Raman spectra. *In silico* studies indicate the presence of cobalt binding sites on the insulin chain B at 8 GLY, 9 SER, and 10 HIS positions. The particles exhibit magnificent loading efficiency of 89.48 ± 0.049 % and excellent release properties (86.54 ± 2.15 % within 24 h). Further, based on fluorescent properties, the recovery process can be monitored under an appropriate setup, and the binding of ICoNPs to insulin receptors was confirmed by bioimaging. This work helps synthesize effective therapeutics with numerous wound-healing promoting and monitoring applications (**Figure. 10)**.

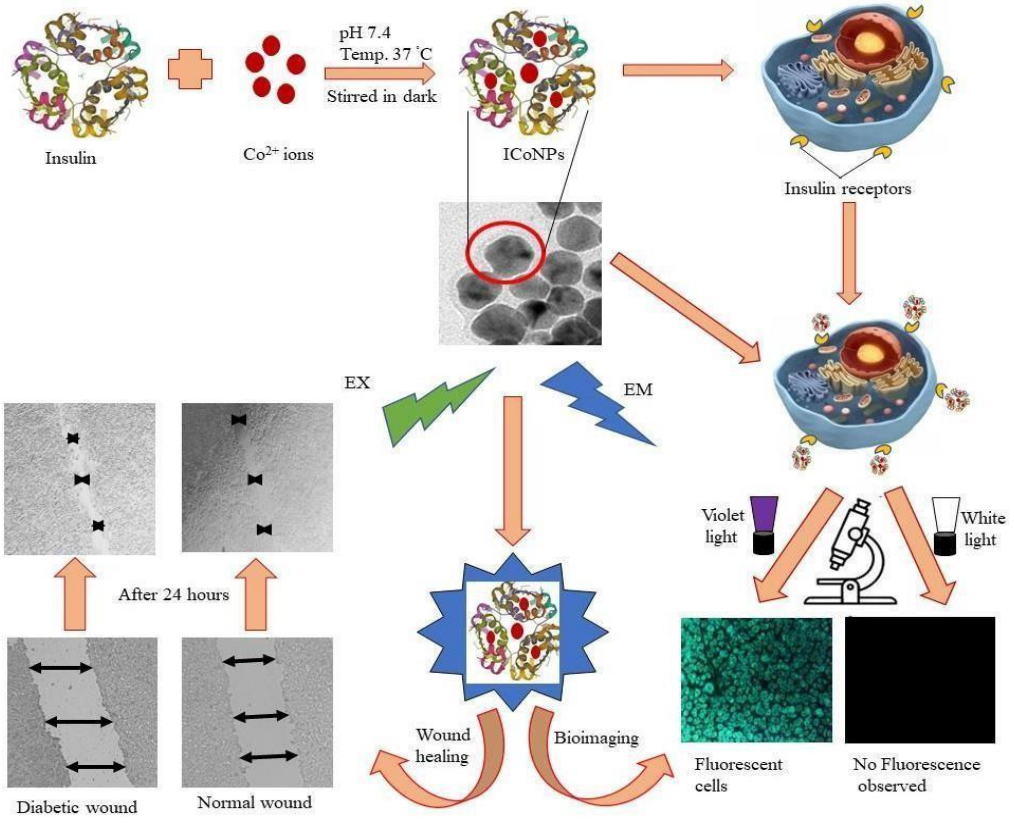

Figure. 10. It depicts the diagramatic presentation for *synthesis of ICoNPs and their potential application as bioimaging agents and wound healing-promoting formulations.*

2.1 Introduction

Wound healing is quite complex process and involves a sequential overlapping cascade of events that comes into action in response to some external chemical or physical stimuli and eventually causes healing by restoring lost tissue [203]. The healing mechanism is categorized into four different phases: hemostasis, inflammation, proliferation, and remodeling [204]. The hemostasis is initiated by clot formation due to platelets' activation, which prevents microbial infestation and promotes matrix organization. In proliferation, the accumulation of cells, connective tissue, growth factors, and angiogenesis factors across the wound occurs. In the remodeling phase there occurs the extracellular matrix resynthesis to maintain the balance between the death of existing cells and the formation of new cells [205],[206]**.** However, the progress monitoring of recovery of wounds always remained a significant challenge before the researchers. In some instances, normal healing gets disrupted and gets arrested in one of the phases due to the loss of balance in the physiological mechanism of healing due to infection, chronic irritation, trauma, the persistence of microbes or other foreign bodies, and ischemia making the wound a chronic one [207],[208],[209] which can be prevented by keeping the wound moist, removing the dead tissues, covering the injury to avoid bacterial infection, and removing the excess tissue fluid [210].

Apart from these issues, the major problem for delayed healing is diabetes mellitus or long-term hyperglycemia, which alters the secretion of cytokines, making wound healing cumbersome [211]. In diabetic conditions, there is the prolonged proinflammatory phase due to the persistent release of proteases, proinflammatory cytokines, and reactive oxygen species and the delayed anti-inflammatory phase because of the low secretion of anti-inflammatory cytokines [212]. Further, the transport of nutrients to the wound site is prevented by atherosclerosis caused by diabetes [213]. It also results in the dysfunction of endothelial cells due to vasodilation induced by pressure [214] and disrupts the processes critical for re-epithelialization, the proliferation of keratinocytes and fibroblasts, synthesis of proteins, and cell migration [215],[216],[217]. Further, it impairs the body's immune response, making the wounds prone to infection and leading to damaged structural components of the extracellular matrix [209]. It also causes free radical damage due to the reduced action potential of certain antioxidant enzymes like glutathione peroxidase and superoxide dismutase [218]. Various advanced bandages have been developed for treating diabetic wounds, overcoming the issues faced in effective healing [219],[42].

Recent advancements in nanotechnology, such as specific physicochemical properties and small size, allow the intracellular delivery of different drugs and biomolecules, protect them from degradation, increase the penetration ability of drugs into the wound, allow the topical application, and enhance the half-life of these agents [220],[221]. It results in a decline in repetitive drug application, thus lowering the cost and making them cost-effective [222],[223]. The metallic nanoparticles possess a high surface-to-volume ratio, higher stability, biocompatibility, safety, and economical rates [223],[224]. Several gold, silver, copper, zinc, and cobalt metallic nanoparticles were prepared to study tissue healing activities in different models [225]. Protein-based nanoparticles are gaining attention due to their high biodegradability, easily metabolizable nature, and the possibility of altering or modifying their surface so that the drugs can attach efficiently. The proteins can be of plant or animal origin, like bovine serum albumin [226], insulin [227], transferrin [228], lactoferrin, and so on, for nano-formulation synthesis [229],[230]. The selection of nanoparticles in treating wounds is based on three parameters: antimicrobial action, role as a delivery agent, and role in the repair process [231].

The use of insulin protein is increasing as the insulin receptors are present on the mammalian cell membranes, and their number differs significantly from just 40 in erythrocytes to 200~300× 10^3 for adipocytes and hepatocytes; however, the number is much more in cancerous cells in comparison with healthy cells [227],[232]. It plays a crucial role as a growth factor that mediates chemotaxis

and pinocytosis, promotes the secretion of cytokines critical for inflammation, and helps in re-epithelialization, essential for wound healing. It works by transitioning cytokines from proinflammatory into anti-inflammatory and promotes the repair and regeneration of wounds [49],[233]. The particles involving insulin exhibit promising applications in bioimaging, normal wound healing, and diabetic wound healing [49],[233],[14],[234]. The metal ions used earlier to form different formulations with insulin include silver, copper, zinc, nickel, etc [232]. Apart from metal-insulin nanoparticles, various other nano-formulations are synthesized using insulin as a healing agent. Chitosan nanoparticles loaded with insulin were synthesized for stimulating inflammatory cell proliferation, angiogenesis, and healing in diabetic rats [130]. Lee et al. reported accelerated diabetic wound repair by promoting epithelialization using core-shell insulin-loaded scaffolds [235]. The synthesis of human keratin-conjugated insulin was reported by Li et al. for their role in full-thickness wound repair in rats by promoting cellular migration [236]. Clinical research was also done to determine the role of insulin further. The insulin injection was used to study the action on systemic glucose levels in blood and healing of diabetic foot ulcers in patients, and found that insulin promotes the formation of vessels and granulation tissue [237]. The impact of topical insulin was studied in 110 patients having diabetes and foot, and it was found that patients treated with insulin gauze dressings had a wound width of 2.46 ± 0.57 cm after two weeks, while patients treated with saline gauze had a diameter of 3.90 ± 0.76 cm indicating the significant effect of insulin [238]. Similarly, a mucoadhesive liposomal gel of insulin was explored on patients having chronic wounds across distinct body parts, demonstrating a more significant impact on test groups than control groups [239].

Cobalt is a micronutrient that regulates various cellular processes. Cobalt mainly functions as a component of hydroxocobalamin, which is crucial for regulating red blood cell production [240]. Cobalamin is the co-factor for two enzymes, methionine synthase, and methyl malonyl-CoA mutase, and the deficiency of methionine synthase is responsible for pernicious anemia [241]. Further, various research works have been done to monitor the effect of cobalt in wound healing as it is found to stabilize HIF-1α and promote VEGF expression by endothelial cells, fibroblasts, bone marrow stromal cells, and mesenchymal cells after incorporation into the silicate-based sol-gel glass, or organic and inorganic hybrid scaffolds [242]. Cobalt ions also help heal wounds and act as an alternative to hypoxia-mimicking agents. It inhibits the activity of PHDs (prolyl 4-hydroxylases), artificially stabilizes the HIF-1α (Hypoxia-inducible factor-1α) under normal conditions, and activates the HIF pathway [243], allowing the formation of the HIF complex, which gets shifted to the nucleus and causes upregulation in the gene expression of multiple genes like VEGF, which are responsible for adaptation to hypoxia [244]. As a result, it promotes angiogenesis during the tissue regeneration process [245]. It was also found that incorporating cobalt ions in titanium-based bone implants enhances their antibacterial activity, indicating the role of cobalt as an antimicrobial agent [246].
Further, the release of cobalt ions from the bioactive glass increases the VEGF protein secretion and osteogenic expression of genes by human bone marrow stromal cells [247], [248]. Moreover, if the cobalt ions are delivered as cobalt chloride, they enhance the secretion of VEGF by endothelial cells [249], fibroblasts [242], and human mesenchymal stem cells [250]. The synthesis of silicate glass fibers for delivering the cobalt ions was done for their chronic wound healing activity by activating the HIF pathway and enhancing the expression of angiogenic genes [251]. Similarly, a bioactive glass was made using the sol-gel method and doped with two different metal ions, including silver and cobalt, for their antibacterial activity in the case of wound healing applications [252]. The various formulations involved the use of carrying concentrations of the cobalt ions. Qingying et al. found the use of Co-Ca/GSA dressing for promoting bacteria-infected wound healing in which varying concentrations of both cobalt and calcium were used, and the concentration up to which cobalt chloride is found to be cytocompatible is 0.25 gm/L [248]. Solanki et al. made a 10 mM stock solution of cobalt chloride, and the concentration of the final solution used for synthesis and further

testing *in vitro* is 300 μM [242]. Chen et al. monitored the action of cobalt chloride on the expression of stem cell markers using stem cells from exfoliated deciduous teeth of a human, which acts as a potential origin for tissue engineering, and treated them with up to 100 μM concentration of cobalt chloride and found out that it is not cytotoxic even after seven days of treatment [253]. Based on all these studies, I have selected the concentrations of cobalt chloride to be incorporated with insulin to administer their effect on wound healing. The maximum concentration used was 60 μM, much less than the concentrations already explored for their wound recovery effect in one form or another. In this study, I am working on the synthesis of novel protein-coated metal core-shell nanoparticles for studying them as normal and diabetic wound healing promoting agents *in vitro* and bioimaging applications. Here, by using one-pot synthesis, I have prepared insulin-cobalt core-shell nanoparticles to check the synergistic effect of insulin and cobalt on treating wounds when applied in the form of particles in the nano range. The effective and efficient healing of wounds is essential for maintaining a person's quality of life. Still, in some instances, the absence of proper internal wound monitoring makes the process even more complex, increasing the cost of treatment and putting risk to a patient's life. To avoid such issues, the developed nanoparticles with the dual ability of healing and bioimaging can be exploited, which paves the way for better wound management.

2.2 Materials and methods

2.2.1 Chemicals and cell line

The metal salt, Cobalt chloride ($CoCl_2$. $6H_2O$), tryptophane, formaldehyde, HCl, and NaOH were of analytical grade and were bought from Sigma Aldrich, India. Recombinant human insulin was purchased from Elli Lilly, India. For cell culture, DMEM cell culture media, Fetal Bovine Serum (FBS), 100X Penicillin-streptomycin, and PBS (pH 7.4) were purchased from HiMedia, India. Human Primary Epithelial Keratinocytes (HEKa cells) ATCC-PCS-200-011 were cultured, maintained, and treated in DMEM containing 5% FBS at 37 $^{\circ}C$ and 5% CO_2.

2.2.2 Synthesis of insulin-protected cobalt nanoparticles

At first, the insulin-protected core-shell cobalt nanoparticles were synthesized by following a previously reported one-pot method in which the pH of the insulin solution, having a final concentration of 1.82 μM, was adjusted to 10.5 using a NaOH solution (0.1N) and kept in the dark. Afterward, a salt solution ($CoCl_2.6H_2O$) of the same molarity was prepared, followed by mixing two solutions in 1:1 by volume, which was further followed by adjustment of the pH of the final solution to 7.4, using HCl (0.1N). The final mixture was placed in the incubator at slow stirring (240 rpm) for 24 h at 37 $^{\circ}C$ [254],[255],[256]. The end product was dialyzed using a 10KDa cut-off dialysis membrane, stored at 4 $^{\circ}C$, and used after that for characterization. Thus, insulin-cobalt nanoparticles were produced and termed ICoNPs.

2.2.3 Study of particle size, morphology, and elemental analysis

The DLS (dynamic light scattering) was done to find out the hydrodynamic size of ICoNPs formed using a Malvern DLS-Zeta size analyzer. After that, to find out the morphology of insulin-linked Cobalt nanoparticles, Scanning Electron Microscopy (SEM JEOL, JSM-6300) and High-Resolution Transmission Electron Microscopy (HRTEM) (Talos F200S G2, Thermo Scientific) were utilized. For this, the samples were kept for centrifugation at 240 rpm for a duration of 15 minutes, then thoroughly washed the pellet to remove any metal salt left unbound or impurities associated with the product. Furthermore, the sample pellet was examined to find out the amount of the elements present by the Energy dispersive X-ray Spectrometer (EDS) (Bruker QUANTAX 200).

2.2.4 *in silico* studies

For determining the potential binding sites for distinct transition metal ions with the desired protein, MIB, a tool for monitoring docking, can be used as a user-friendly and integrated approach for

finding the residues in metal binding sites. Protein chains were taken from the protein data bank (PDB) and were required to operate this online server. The first chain consists of the template protein (T) having length m containing metal-ion, and the second chain consists of query protein (S) having length n. These chains were then aligned in manner to get query protein structure from template protein after alignment. Several different parameters were followed to obtain the desired protein structures. The first and the most crucial parameter is the prediction of binding residues with the twelve transition metal ions, including Ni^{2+}, Cu^{2+}, Mg^{2+}, Ca^{2+}, Hg^{2+}, Cd^{2+}, Co^{2+}, Zn^{2+}, Fe^{2+}, Mn^{2+}, $Cu^{+,}$ and Fe^{3+}. The second factor is that there should be 50 residues in chain length of the polypeptide; otherwise, it will be excluded [257]. The third parameter is the presence of a minimum of two residues for metal ion binding, having the minimum possible distance between the PDB coordinates and the metal center [258]. The fourth crucial parameter is the allotment of a binding score to the residue, which needs to be greater than a particular threshold value assigned and calculated using the root mean square deviation of C-alpha carbons of local structural alignment and BLOSUM62 substitution. If so, only then will there be binding between the residue and the specific metal ion of the transition series. Further, the binding score is represented as Ci and depends upon the target protein's sequence along with the protein's structural conservation[259],[260].

In this manner, the binding site of a particular metal with that of a protein chain can be determined using the MIB tool. The PDB (Protein Data Bank) database was used to extract Human Insulin protein (PDB ID: 4EWW), a polypeptide with two distinct chains denoted as A and B, respectively. In the MIB tool, the Co^{2+} ion was independently docked with human insulin chains A and B, followed by a comparison of the metal ion-binding score with that of the target protein [261].

2.2.5 Study of cobalt -insulin interaction using spectroscopy

To study the metal-protein interactions in the ICoNPs, FTIR was done with Agilent Cary 600 series Spectrophotometer. The potassium bromide (KBr) method was used to prepare the samples, and scanning was done from 400 cm^{-1} to 4000 cm^{-1}.

Furthermore, the same samples were analyzed using Surface Enhanced Raman Scattering (SERS) Spectra to study the structural variation of insulin protein [262]. All the samples were prepared on a silicon wafer ten minutes prior to the experiment. The final product was scanned from 500 cm^{-1} to 1800 cm^{-1}. The LabRam Hr Evolution Horiba instrument, was utilized for recording the Raman spectra of ICoNPs at 785 nm.

In order to monitor any possible modification in the secondary structure of the protein molecule, CD (Circular Dichroism) is the most reliable technique. Further, CD studies were performed to confirm the interaction between insulin and cobalt chloride salt solution (freshly prepared and after one month). I have performed the Circular Dichroism (CD) spectroscopy using the Mos500 CD biologic instrument. The CD studies were conducted at 25 ˚C with 1 ml of sample and scanned in the 200-260 nm wavelength range for pure insulin and insulin cobalt nanoparticles using PBS (pH 7.4) as a solvent.

2.2.6 Drug loading and release kinetics

To monitor the release kinetics, 1 ml of the ICoNPs was undergone centrifugation for 15 min at 10,000 rpm. The Bradford reagent determined Insulin concentrations from the supernatant and the pellet. Further, the insulin release rate was measured at specific time intervals for 40 hours. The absorption values (at 595 nm) were later arranged and plotted to note the proper fashion of drug release using BSA standard curves [263],[264]. In addition, absorbance values were also measured for the same samples at 272nm (excitation of tryptophan) to support the data further.

2.2.7 Study of absorption and fluorescence spectroscopic study

For obtaining the UV- Visible absorbance, the UV-2600 spectrophotometer of Shimadzu was operated between 200-800 nm, and a 4000 µl cuvette of quartz with a path length of 1 cm was used, and the absorbance for insulin, salt solution ($CoCl_2$), and Insulin-linked cobalt core-shell nanoparticles (ICoNPs) were measured.

For measuring the fluorescence data of ICoNPs, Agilent technologies, a Cary Eclipse fluorescence spectrophotometer was used, which helps in determining the fluorescence intensity of protein-linked metal nanoparticles (ICoNPs), insulin, and $CoCl_2$ solution, all having the same concentrations, at 272 nm which is the excitation wavelength, followed by doing an emission scan from 280 nm to 800 nm with excitation and emission slit of 10 mm.

In order to calculate and compare the % enhancement in intrinsic fluorescence intensity of both insulin and ICoNPs, the given equation (a) was used.

$$\% \text{ Change in emission intensity} = \frac{\text{F.I.(ICoNPs)} - \text{F.I.(Insulin)} \times 100\%}{\text{F.I.(Insulin)}} \quad \ldots\ldots(a)$$

The standard tyrosine fluorescence quantum yield was used to calculate the quantum yield of insulin as well as insulin-protected cobalt nanoparticles (ICoNPs), and the given equation (b) was used for further calculations.

$$Q.Y.(S) = \frac{Q.Y.(Tyr) \times I\,(S) \times 1\text{-}10^{-Al}\,(Tyr) \times n^2\,(S)}{I\,(Tyr) \times 1\text{-}10^{-Al}\,(S) \times n^2\,(Tyr)} \quad \ldots\ldots(b)$$

Here, Q.Y.is quantum yield; I is Integrated Emission Intensity; n is the Refractive Index of Solvent; A is the Absorbance at Excitation wavelength; l is the length of absorption cell; Tyr is Tyrosine (reference), and S is Sample.

2.2.8 Stoichiometry ratio of Co^{2+} ions: insulin protein

For evaluating the possible interactions occurring between metal-ligand and complex protein, the stoichiometry of cobalt ions to insulin protein is calculated using the following equation (c)

$$\text{No. of proteins bound to single } Co^{2+} \text{ ion} = \frac{\text{Average no. of bound protein/ml}}{\text{Average no. of } Co^{2+} \text{ ions/ml}} \quad \ldots\ldots.(c)$$

2.2.9 *in vitro studies*

2.2.9.1 Cell viability

To check out the % change in cell growth after treating with samples, the HEKa cell line (Human Epidermal Keratinocytes, adult) was used, and MTT (3-(4,5-dimethylthiazol-2-yl)-2,5-diphenyltetrazolium bromide) assay was performed. In order to perform this assay, HEKa cells were grown in 96 well plates and were kept in the incubator for the cells to grow and become 75-80% confluent with the regular addition of media. Once the plate became confluent, the cells were incubated with ICoNPs, insulin, $CoCl_2$, and a mixture of insulin and $CoCl_2$. To get three concordant readings, four different concentrations of each sample that are 1.5, 7.5, 30, and 60 µM are added to respective wells. After that, the plate was incubated for a time-lapse of 24 h and at 37 ˚C. After 24 h, the media was discarded, and MTT (2mg/ml in 5% ethanol) was added into each well, followed by incubating the plate for 3 h in an incubator. The MTT solution and media were removed from each well after 3 h, followed by adding 200µl dimethyl sulfoxide (DMSO) for dissolving the formazan crystals. The OD was checked at a wavelength of 575 nm. For calculating the % inhibition, the equation used is as follows

$$\% \text{ inhibition} = [1\text{-}(A_t / A_c) \times 100]\ \% \quad \ldots\ldots.(d)$$

Here A_t is the absorbance of the test substance, and A_C is the absorbance of the control solvent for each concentration [265].

2.2.9.2 Internalization study of nanoparticles into cells

STEM analysis was performed to study synthesized nanoparticles' interaction with human cells. The HEKa cells were used to do the internalization studies. The cells were grown in 35 mm plates and left to be confluent till 80-85%. Then, they were treated with ICoNPs and incubated for 24 hours. After 24 hours, the cell trypsinization was done, followed by centrifugation and the pellet fixation using 2.5% glutaraldehyde in 0.03 M phosphate buffer having pH 7.4. Cells were then dehydrated using an ethanol gradient, later coated over 200-mesh uncoated copper grids, and observed under STEM (Carl Zeiss Sigma 500 Microscope).

2.2.9.3 Fluorescence Bioimaging

A Dewinter fluorescence microscope was utilised to get fluorescence imaging. The cells were grown in a 60 mm plate and let be confluent to 75-80%. After that, cells were added on a coverslip, DMEM media was added, and the cells were incubated for 24 h. The samples to be used for bioimaging were kept under UV laminar for 30 minutes. Then, 100µl of the Insulin metal nanoparticles (ICoNPs) were taken from each of the three different concentrations described above for MTT assay and added to the respective coverslip containing HEKa cell line opted for the experiment that is, human epidermal keratinocytes, adults (HEKa). In order to get rid of any impurities, each coverslip was washed with PBS buffer twice, followed by cell fixation by adding 2% of formaldehyde solution. Later on, the images were taken to check the role of insulin-protected cobalt core-shell nanoparticles and the effect of different concentrations of samples on fluorescence intensity.

2.2.9.4 Effect of ICoNPs on recovery of the normal and diabetic wound, *in vitro,* using phase contrast imaging

For monitoring the potential of synthesized nanoparticles on wound healing *in vitro*, the HEKa cells were seeded in 60 mm plates in the presence of glucose (360 mg/dl) for diabetic wounds and in the absence of glucose for normal damages along with DMEM-F12 media. They were kept at 37 $^{\circ}$C and 5% CO_2 level and allowed to grow and be 80-85% confluent, following which the cell scratch method was used to monitor the impact of the treatment on healing. In this, the wound is made by a sharp object, that is, the sterile 200 µl tip, and was incubated with different concentrations of all four samples. Time-lapse imaging was done to find the change in scratch width after 6 h, 12 h, and 24 h at multiple positions for each scratch made in an individual well plate. I took the mean of those independent readings of scratch width for the calculation of the percentage variation in scratch diameter for both the normal and diabetic wounds separately.

2.2.10 Determination of combination index (CI) for cobalt-insulin

The combination index is a quantitative method used to determine the effect of two drugs in combination with one another. The amount of synergism or antagonism is quantified by estimating the drug combination index in investigating synergistic or antagonistic drug combinations. The combination index of CI < 1 indicates that when distinct drugs are administered simultaneously, their combined activity increases, called the synergistic effect. CI = 1 show that one drug does not interfere with the action of the other. Hence, the additive effect and CI >1 indicate the inhibition of drug action by the different drugs, thus called the antagonistic effect. For the calculation of the combination index, the cell viability was determined at different concentrations of cobalt and insulin, and then calculations were done using equation (e).

$$CI = (D)1/(Dx)1 + (D)2/(Dx)2 \quad \ldots\ldots(e)$$

$$\text{Where, } Dx = Dm\,[fa/fu]^{1/m} \quad \ldots\ldots(f)$$

Here, (D)1 and (D)2 denote the concentration of cobalt salt and insulin, respectively. The single drug concentrations giving the same effect (Dx)1 and (Dx)2 are determined using the median effect equation (f). The cell fractions which are affected and unaffected in the median dose are denoted by fa and fu and are equal to $10^{(y\text{-intercept})/m,}$ where m represents the slope median in the median effect plot of log (D) vs. log (fa/fu) [227],[266],[267].

2.2.11 Statistical Analysis

The data here is represented as the mean ± SD of three individual experiments. The one-way ANOVA in MS Excel was used for calculating the corresponding p-value to determine the statistical significance of the data.

2.3 Results and Discussions

2.3.1 Structure, Composition, and stoichiometry of metal insulin nanoparticles

The formation of spherical nanoparticles of ICoNPs having size 13 ± 2 nm was confirmed by scanning electron microscopic images (at a scale of 500 nm) as given in **Figure. 11a** (inset shows the magnified image of core-shell particle which shows the rough surface of nanoparticle due to an outer insulin shell) and transmission electron microscopic images (at a scale of 50 nm) as indicated in **Figure. 11b** and inset of **Figure. 11b** (at a scale of 5 nm to show the lattice fringes and the insulin coating of ~2.5 nm around the cobalt core). The nanoparticles are widely distributed over the protein matrix. Different elements like Co, C, O, N, P, and Si are present in energy-dispersive X-ray spectroscopy. The even distribution and percentage of Co in the particles come out to be 0.18 %, as analyzed by EDS studies as indicated in **Figure. 11c**. The hydrodynamic size of ICoNPs was found to be 35 ± 5 nm, as shown in **Figure. 11d**. After that, the stoichiometric ratio between the insulin protein and Co^{2+} ions was calculated. It was found that ~ 3792 insulin proteins encapsulate one nanoparticle.

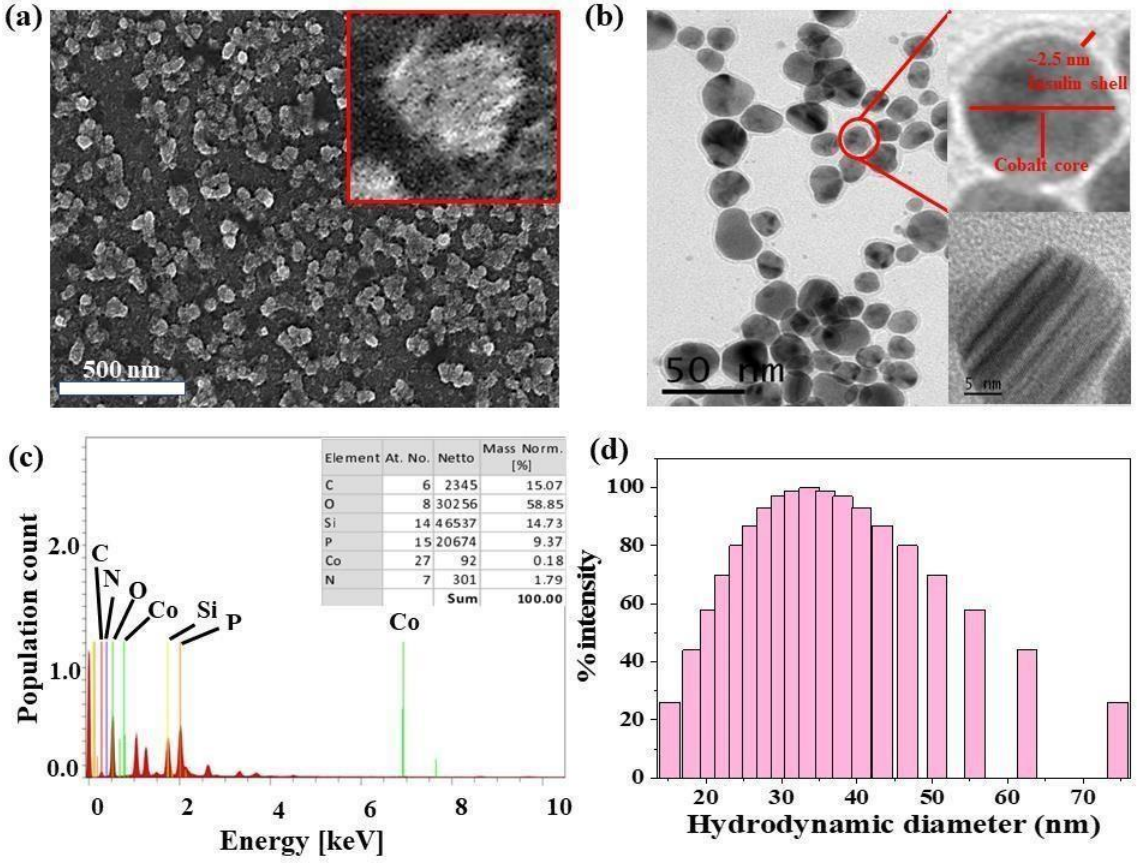

Figure. 11. Morphological Characterization of ICoNPs *(a) SEM micrographs indicating the nanoparticles to be around 10-15 nm at a scale of 100 nm. (b)TEM micrographs of ICoNPs show the nanoparticle size to be ~13 nm at a scale of 50 nm (inset shows particle size at a scale of 5 nm)*

(c) EDS showing the presence of Cobalt ions in the synthesized nanoparticles (inset shows the relative % of each atom present in the sample) (d) DLS spectra showing the hydrodynamic diameter of

ICoNPs versus the % intensity of particles.

2.3.2 *in silico* studies to monitor the interactions between insulin and cobalt ions using Metal-ion Binding Residue templates

With the assistance of the MIB tool, I found the binding sites on Chain B of insulin with which the transition metal Co^{2+} can bind. The metal and proteins interaction is based mainly on the structure and sequence of amino acids in a protein. Firstly, the sequence of insulin was taken from the Protein Data Base (PDB ID: 4EWW) and then inserted in the MIB tool to dock the Co^{2+} ions with both the chains (chain A & B) of insulin. As a result, a binding score was assigned to all residues in the protein. If the binding score exceeds the threshold value, that specific residue is considered the potential site of binding for that specific metal ion. The data indicates that chain A does not show any template indicating the absence of binding sites of Co^{2+} ions with chain A, whereas, in chain B, a binding site was found for Co^{2+} ions. Then, I worked with another software called Maestro. Using this, I have calculated the distance between the metal ions and amino acids, namely 8 GLY, 9 SER, and 10 HIS, present on Chain B of insulin. The distance was found to be 1.69, 3.07, and 3.27, respectively. The binding score was also determined using MIB with different amino acids in chain B of Insulin with Co^{2+} ions, thus finding the best possible sites for attachment. The binding of cobalt ions with various amino acids is determined and visualized through different orientations of the metal-binding amino acids in proteins. The possible binding sites of cobalt ions with other amino acids in insulin are shown in **Figure. 12a** and **Figure. 12b**, the binding score of amino acids with insulin protein is shown in **Figure. 12c**,

2.3.3 FTIR, Raman Spectra, and CD spectroscopy for the interactions between protein and metal ions after the formation of nanoparticles

To figure out the interactions involved in metal-protein binding, FTIR was used for $CoCl_2$, insulin, and ICoNPs. The peaks appeared due to intermolecular interactions of insulin and $CoCl_2$ at different wavenumbers. Firstly, the peak appeared at 506.70 $cm^{-1,}$ which indicates the S-S stretching in insulin and ICoNPs [268]. Then, a peak at 540.25 cm^{-1} in ICoNPs indicates Co-O vibrations [269]. In addition to the second peak, a peak at 670.35 cm^{-1} shows the Co-O bending, confirming the interaction between insulin and $CoCl_2$ [270]. A peak at 784.13 cm^{-1} in $CoCl_2$ shows librational vibrations [271]. Two other peaks at 849.79 and 973.73 indicate the CoO-OH band and Co-OH bending, respectively, in ICoNPs [269],[272]. C-N stretching was observed in insulin and ICoNPs at 1032.13 cm^{-1} [273]. Amide I, Amide II, and Amide III are found at 1631.19 cm^{-1}, 1529.41 cm^{-1}, and 1244.60 $cm^{-1,}$ respectively, in insulin and ICoNPs [273],[268],[274]. C-H bond was obtained in insulin and ICoNPs at 1390.70 cm^{-1} [273]. Deformational scissor water vibrations were observed at 1573.72 cm^{-1} in $CoCl_2$ only [275]. Nitrile stretch was there at 2345.71 cm^{-1} in all three solutions [274]. Intermolecular O-H stretching peaks at 2941.99 cm^{-1} in insulin and ICoNPs, but the peak was observed at 3164.13 cm^{-1} in $CoCl_2$ [273]. A single peak in insulin and nanoparticles indicated amine N-H stretching at 3267.03 $cm^{-1,}$ which was absent in the $CoCl_2$ [276]. For symmetrical and asymmetrical valence vibrations of water, peaks were obtained at 3383.58 cm^{-1} and 3522.29 $cm^{-1,}$ both in $CoCl_2$ but absent in insulin and ICoNPs [275], which is shown in **Figure. 12d**.

Similarly, Raman spectral analysis was used to study the significant conformational changes in insulin after binding with cobalt ions. The S-S stretch and O-C-N bend were observed at 553.29 cm^{-1} and 786.44 $cm^{-1,}$ respectively, in both insulin and ICoNPs [268],[277]. The CoO-OH and Co-OH bond was observed at 895.84 cm^{-1} and 984.75 $cm^{-1,}$ respectively, only in ICoNPs but was absent in insulin [269],[272]. A weak C-N stretching peak was found at 1094.02 cm^{-1} in insulin and 1096.73 cm^{-1} [268]. The C-H bend was seen in insulin at 1343.21 cm^{-1} and in ICoNPs at 1372.70 cm^{-1} [268]. The peak that is responsible for amide-III random coils shifts slightly from 1315.63 cm^{-1} in insulin to 1332.38 cm^{-1} in ICoNPs [278]. However, no such change was observed for amide-III (α – helix), as the peak was found at 1201.87 cm^{-1} in insulin and ICoNPs [279]. A slight shift was observed for

amide-II from 1447.14 cm^{-1} in insulin to 1460.88 cm^{-1} in ICoNPs [280]. The peak for amide-I was observed at 1658.91 cm^{-1} and 1668.54 $cm^{-1,}$ respectively, in insulin and ICoNPs [281]. The peak for the C=O stretch remains unchanged and is found at 1750.73 cm^{-1} in insulin and ICoNPs [268], and this is shown in **Figure. 12e**. The data of FTIR is given in **Table 3** in a comparative manner**,** and Raman spectra are shown in **Table 4**.

Circular Dichroism was performed using insulin protein and ICoNPs (freshly prepared and after one month) to monitor the interactions between protein and salt solution and find the stability of the secondary structure of protein after binding with cobalt chloride. The three significant far UV signals were recorded in both the solutions, including a positive peak at ~ 200 nm and two negative peaks at ~ 208 nm (α-helix) and 218 nm (β sheet), which were indicative of the secondary protein structure. The % variation in the peak at 200 nm is 5.23% and 6.21%, at 208 nm is 3.56 % and 4.24%, and at 218 nm is 4.82% and 5.71% in freshly prepared ICoNPs and ICoNPs after one month respectively and confirmed the protein stability with no significant structural alterations being observed, as shown in **Fig. 13a**.

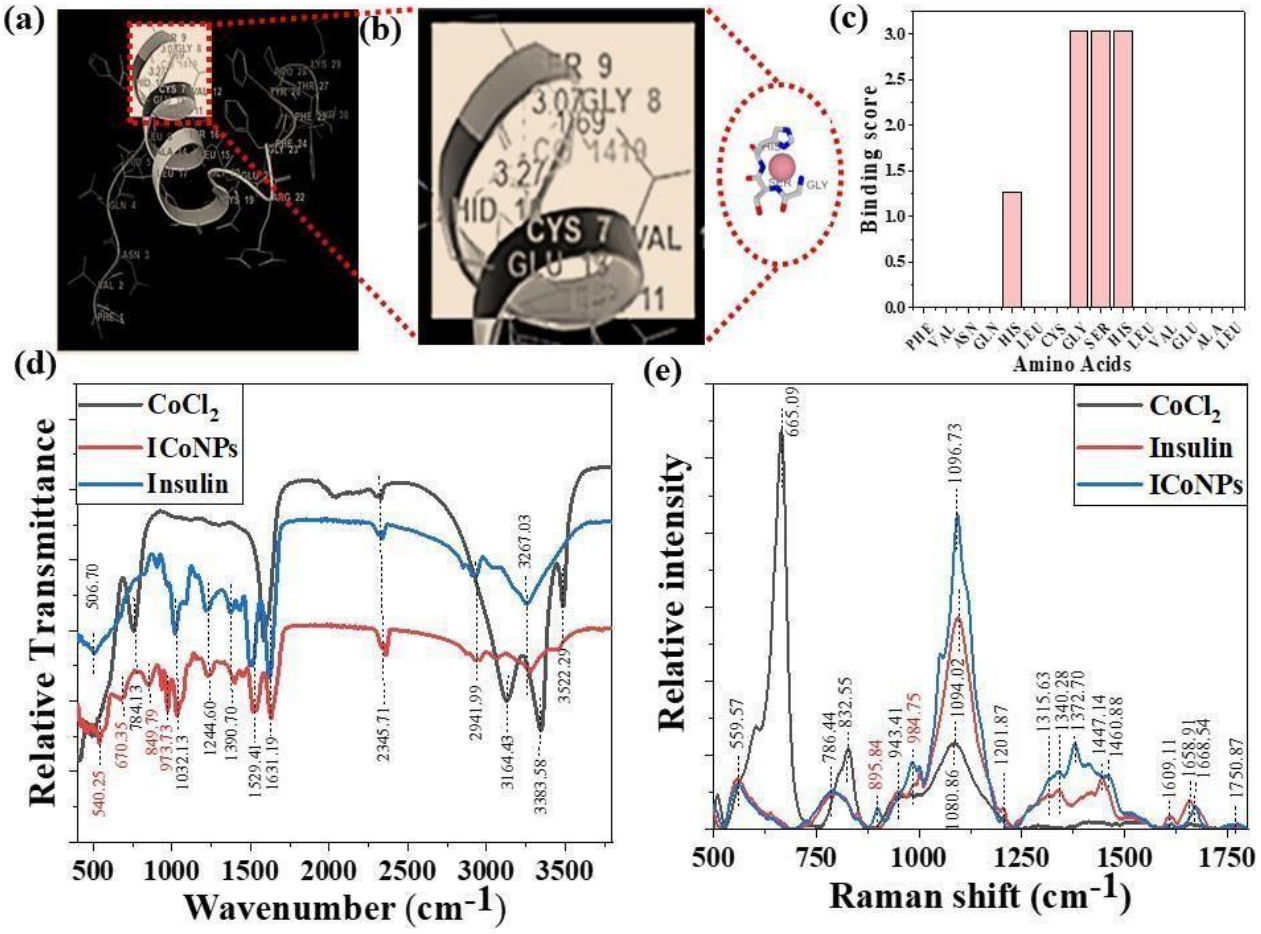

Figure. 12. Study for the structural variations in protein because of insulin-cobalt metal ion interactions to form ICoNPs. *(a) Metal ion binding residues depict the interaction between Chain B of insulin and cobalt ions. (b) the binding sites for cobalt ions at insulin protein with different amino acids within 3.55 A˚ distance along with the distance measured. (c) the binding score of metal ions with other amino acids in the protein chain (d) FTIR spectra of $CoCl_2$, insulin, and ICoNPs in the range 400-4000 cm^{-1} indicate the new bonds between Co-O (vibrations and stretching), CoO-OH bond, and Co-OH bonds which were otherwise not present. (e) Raman spectra of $CoCl_2$, insulin, and ICoNPs indicate the involvement of different functional groups of insulin in synthesizing ICoNPs.*

Table 3: The comparative wavenumber values indicated by FTIR in the range 400-4000 cm^{-1} of $CoCl_2$, insulin, and ICoNPs showing the position of distinct functional groups observed, which coins the interaction amongst $CoCl_2$ and Insulin indicating the formation of ICoNPs.

Functional groups	**$CoCl_2$**	**Insulin**	**ICoNPs**	**Ref.**
S-S stretch	-	506.70	506.70	[268]
Co-O vibrations	-	-	540.25	[269]
Co-O stretching	-	-	670.35	[270]
Librational vibrations	784.13	-	-	[271]
CoO-OH band	-	-	849.79	[269]
Co-OH bending	-	-	973.73	[272]
C-N stretching	-	1032.13	1032.13	[273]
Amide III	-	1244.60	1244.60	[273]
C-H bond	-	1390.70	1390.70	[273]
Amide II C=O stretch	-	1529.41	1529.41	[274]
Deformational scissor vibration of water	1573.72	-	-	[275]
Amide I	-	1631.19	1631.19	[268]
Nitrile stretch	2345.71	2345.71	2345.71	[274]
O-H intermolecular stretching	3164.13	2941.99	2941.99	[273]
Amine N-H stretch	-	3267.03	3267.03	[276]
Symmetrical and asymmetrical valence vibrations of water	3383.58 3522.29	-	-	[275]

Table 4: The comparative wavenumber values indicated by Raman spectra in the range 500-1800 cm^{-1} of $CoCl_2$, insulin, and ICoNPs showing the position of different functional groups present, which coins the interaction amongst $CoCl_2$ and Insulin indicating the formation of ICoNPs.

Functional group	**$CoCl_2$**	**Insulin**	**ICoNPs**	**Ref.**
C=O stretch	-	1750.73	1750.73	[268]
Amide I	-	1658.91	1668.54	[281]
Amide II	-	1447.14	1460.88	[280]
Amide III (α – helix)	-	1201.87	1201.87	[279]
Amide III (random coils)	-	1315.63	1332.38	[278]
C-H bend	-	1343.21	1372.70	[268]
C-N (Weak stretch)	-	1094.02	1096.73	[268]

Co-OH	1080.66	-	984.75	[272]
CoO-OH	832.55	-	895.84	[269]
O-C-N (bend)	-	786.44	786.44	[268]
S-S stretch	665.09	553.29	553.29	[270]

2.3.4 Drug loading and release kinetic studies

The drug loading capacity and release kinetics of ICoNPs were studied, and the encapsulation efficiency of insulin over the cobalt nanoparticles was found to be 89.48 ± 0.049%. The release kinetic studies were performed at physiological conditions with a pH of 7.4 and 37 °C. Burst drug release was observed for the initial 8 h, followed by a sustained drug release afterward. Most of the drug was released by the 40 h. The nanoparticles having a concentration of 3.47 mg/ml were suspended in a dialysis bag, and the absorbance was observed at 595 nm after particular intervals of time. It was found that 92.21 ± 0.03% of the drug was released from ICoNPs by the end of 40 hours, making it an efficient drug delivery system in wound healing applications and is shown in **Figure. 13b** and **Figure. 13c**. For further confirmation of the release kinetics of the particles, OD value was taken at 272 nm (tryptophan absorbance) for all the samples after specific time intervals which shows the gradual increase in OD values with increasing time, indicating the sustained release of insulin from particles and is shown in **Figure. 13d**.

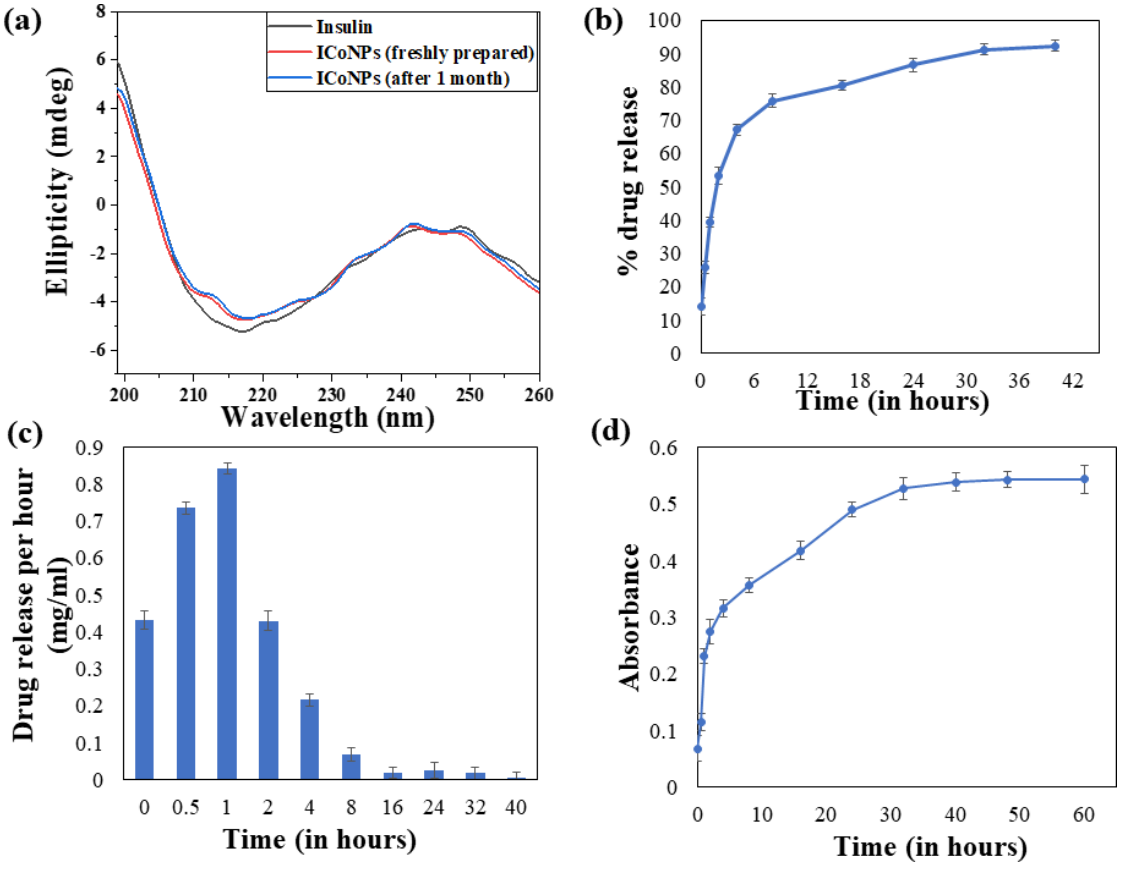

Figure. 13. CD spectroscopy and release kinetics studies of ICoNPs. *(a) Circular dichroism spectroscopy studies showing the stability of insulin protein alone and after interaction with cobalt chloride (ICoNPs) (b) the graph shows the release kinetic studies for determining the % drug being released from the ICoNPs (c) shows the drug release per hour in mg/ml Analysis of the specificity of interaction of insulin and $CoCl_2$ using (d) It shows the release kinetics data when the OD value*

was taken at 272 nm, which is the excitation value of tryptophan. It indicates a sustained drug release pattern, as was confirmed by using the Bradford assay.

2.3.5 Spectroscopic changes after synthesis of core-shell nanoparticles using absorbance and fluorescence spectra

After synthesizing ICoNPs, its spectroscopic characterization was done to observe the absorption and fluorescence intensity of the formed nanoparticles. I have obtained a sharp peak for insulin without any added metal salts at 271.61 with an absorbance value of 0.129, whereas, after the 48 h incubation of insulin with metal salts, an OD value of 0.245 was obtained for particles having a peak at 271.50 nm. This confirms the synthesis of ICoNPs, as shown in **Figure. 14a**. The ICoNPs were then excited at 270 nm to determine the fluorescence intensity. An emission peak ranging from 280-440 nm was obtained with maxima at ~303 nm having an intensity of 304.89 a.u when monitored from 200-800 nm, as shown in **Figure. 14b**. The tyrosine was taken as standard, and the absorption peak after comparison with tyrosine is demonstrated in **Figure. 14c**. The % change in intrinsic fluorescence intensity was found to be 58.88%. Further, to determine the quantum yield of ICoNPs, tyrosine was used as a standard as its quantum yield value is known. The value of quantum yield for insulin comes to be 0.1798, and of ICoNPs turned out to be 0.6825, indicating the fluorescent behavior of formulations synthesized is shown in **Figure. 14d**.

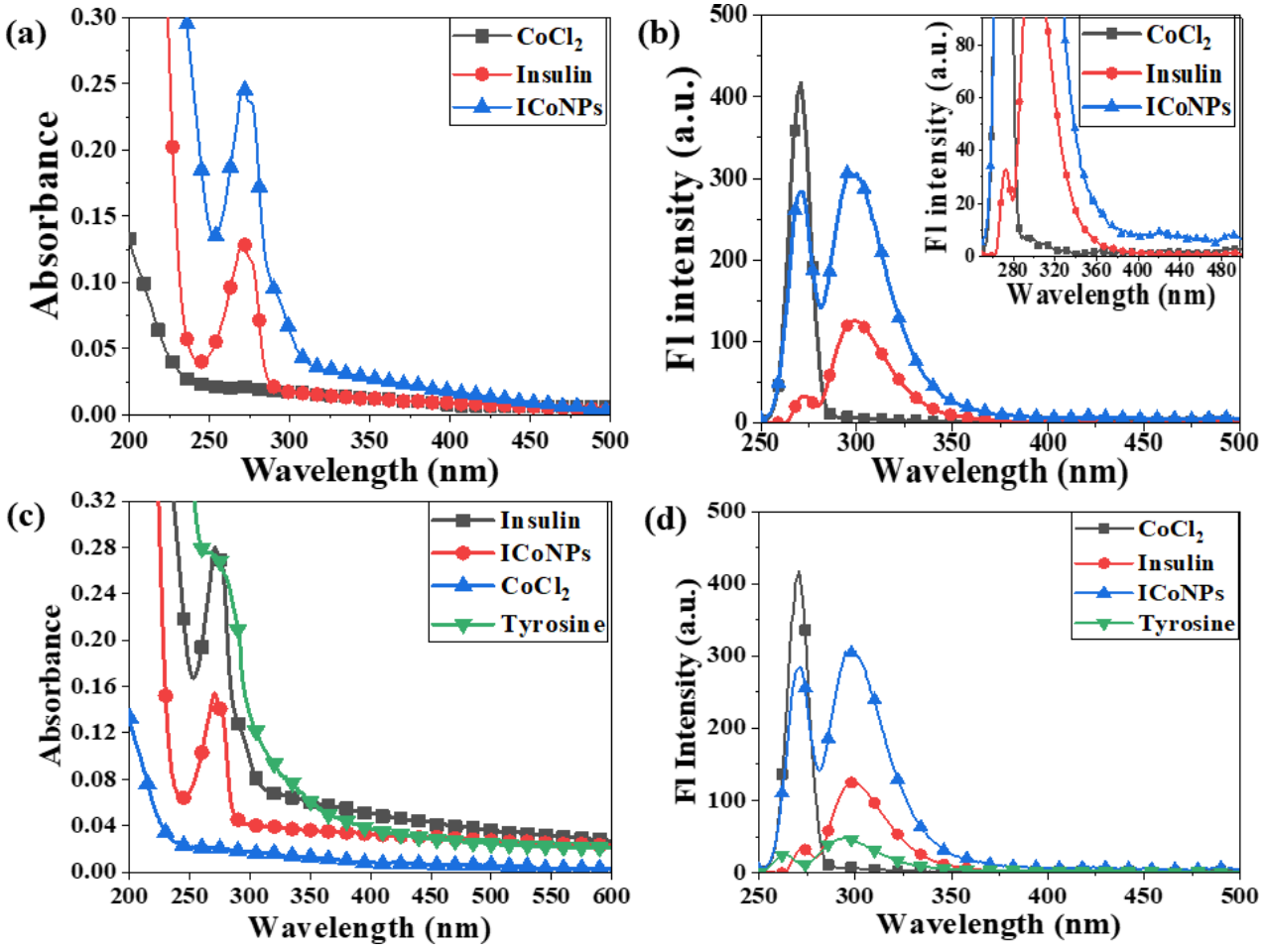

Figure. 14. Physical characterization studies of ICoNPs *(a) UV-Visible absorption spectra of $CoCl_2$, insulin, and ICoNPs showing the peak of insulin alone and after interaction with cobalt (ICoNPs) at ~272 nm (b) emission spectra of ICoNPs after excitation at 272 nm indicates the emission maxima at ~300 nm. Inset shows the trailing of fluorescence from ~ 420 nm onwards (c) It compares absorbance values between Insulin, ICoNPs, $CoCl_2$, and tyrosine (standard) (d) It*

compares the fluorescence intensity value of Insulin, ICoNPs, $CoCl_2$, and tyrosine (standard) to calculate the quantum yield enhancement in insulin and insulin cobalt core-shell nanoparticles.

2.3.6 *in vitro* cell studies

2.3.6.1 HEKa cell viability assay

A cell viability test was done to check whether the samples could be employed for biological purposes, which further depends on the mitochondrial activity of cells. Testing was done for insulin, $CoCl_2$, a mixture of insulin and $CoCl_2$, and ICoNPs using 1.5, 7.5, 30, and 60 µM of concentrations, and the graph was plotted. The cell viability of untreated cells (control) is taken as 100, and the rest of the studies are compared to this. For $CoCl_2$ treated cells, cell viability comes out to be 96.54 ± 6.43 %, 102.12 ± 6.36 %, 106.75 ± 5.58 %, and 110.99 ± 0.77 % for 1.5, 7.5, 30, and 60 µM respectively. Insulin shows 99.65 ± 8.14% for 1.5 µM, 105.02 ± 1.48 % for 7.5 µM, 110.99 ± 2.89 % for 30 µM and 120.26 ± 7.70 % for 60 µM respectively. The cells treated with a combination of insulin and $CoCl_2$ exhibited more cell viability. It is 109.97 ± 2.30 %, 108.32 ± 4.17 %, 122.78 ± 0.28 %, and 127.57 ± 0.56 %, respectively, for 1.5, 7.5, 30, and 60 µM respectively. Cell viability after treatment with core-shell ICoNPs showed much more significant changes, which are 110.44 ± 0.70 % for 1.5 µM, 117.83 ± 8.76 % for 7.5 µM, 134.72 ± 1.76 % for 30 µM and 144.69 ± 0.98 % for 60 µM respectively and comparative data is shown in **Table 5.** The graph demonstrated that none of all four samples is toxic to the cells when used in the above-mentioned concentrations. Moreover, with increasing concentration of samples added, the cell viability enhanced (shown in **Figure. 15**) and was maximum for core-shell ICoNPs formed, indicating that nanoparticles formed are not at all toxic; instead, they help in the cell division and multiplication and thus can be used for wound healing.

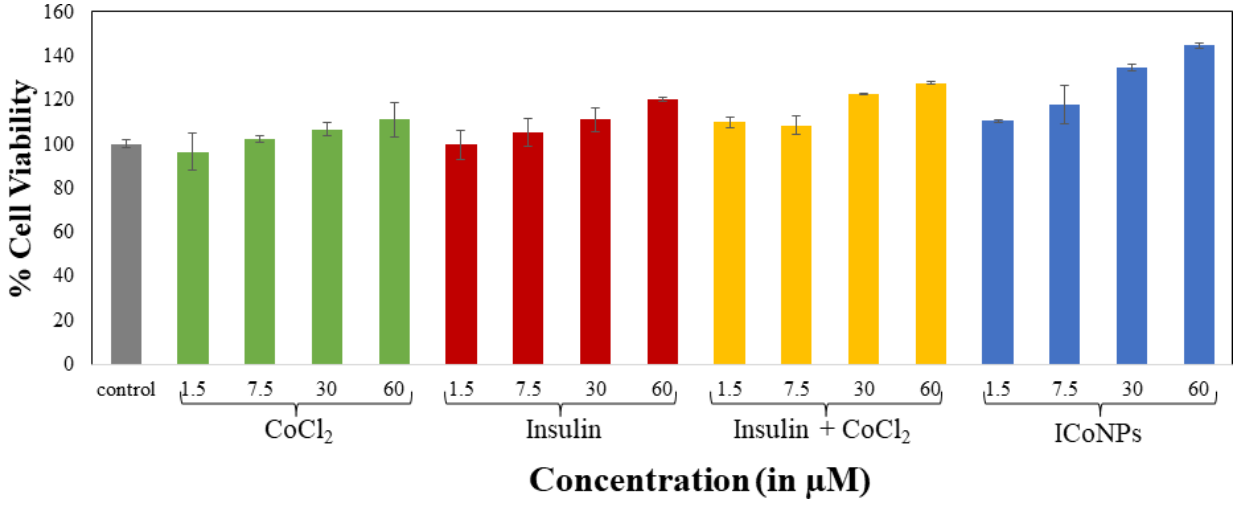

Figure. 15. MTT assay to find viability of HEKa cells. *The data indicates control HEKa cells in comparison to the cells after treatment with varying concentrations of cobalt chloride, insulin, the mixture of insulin and cobalt chloride, and ICoNPs.*

Table 5. The table indicates the % change in mitochondrial reductase activity in the MTT assay for the determination of cellular metabolism rate after treating cells with different concentrations of control ($CoCl_2$, insulin, mixture of $CoCl_2$ and insulin) and ICoNPs, that is, 1.5 µM, 7.5 µM, 30 µM, and 60 µM respectively, for 24 hours.

% Of change in mitochondrial reductase activity				
Dose	**$CoCl_2$**	**Insulin**	**Insulin + $CoCl_2$**	**ICoNPs**
1.5 µM	96.54 ± 6.43	99.65 ± 8.14	109.97 ± 2.30	110.44 ± 0.70
7.5 µM	102.12 ± 6.36	105.02 ± 1.48	108.32 ± 4.17	117.83 ± 8.76
30 µM	106.75 ± 5.58	110.99 ± 2.89	122.78 ± 0.28	134.72 ± 1.76
60 µM	110.99 ± 0.77	120.26 ± 7.70	127.57 ± 0.56	144.69 ± 0.98

2.3.6.2 STEM analysis for cellular internalization of IcoNPs

STEM analysis was performed after incubating the cells with samples to confirm the interaction and internalization of ICoNPs into the skin cells, followed by their fixation and dehydration by ethanol gradient. The cells were observed under the microscope on copper grids. The mechanism behind cellular internalization can be explained as follows. The synthesized nanoparticles comprise the core-shell structure with cobalt as the core covered by an outer insulin shell. This insulin layer is responsible for the interaction of nanoparticles with human cells. The plasma membrane of target cells in the human body has insulin receptors to which insulin binds and exerts the physiological effect. Insulin receptors have two insulin binding sites that exhibit negative co-operativity; that is, insulin binding to one place prevents its binding to the other and keeps them active throughout. Once the particles bind to the receptors, they can enter the cell membrane's lipid bilayer by following energy-independent direct transduction. Moreover, due to the structural similarity between insulin and IGF-I, they also bind to IGF receptors and exhibit anti-inflammatory action. After entering the cell, insulin controls distinct mechanisms, including glucose metabolism, protein biosynthesis, and lipid biosynthesis, and promotes healing. The interaction of ICoNPs with cellular receptors and their internalization into the cell membrane is shown in **Figure. 16 a-d** (at different scales).

2.3.6.3 Fluorescence Microscope Bioimaging

Bioimaging was performed on HEKa cell lines to confirm the broad applications of core-shell insulin-cobalt nanoparticles for cellular imaging. Cells were incubated with particles and showed bright blue fluorescence after binding of ICoNPs to the insulin receptors located on the cell wall of each cell, and the fluorescence was enhanced with a gradual rise in the concentration of ICoNPs. The imaging was performed on both white and violet light. The control cells without treatment with core-shell ICoNPs are shown in **Figure. 16e** in white light and **Figure. 16f** in violet light, indicating no fluorescence in cells. **Figure. 16g, i, and k** show the cells under white light, and **Figure. 16h, j, and l** show the cells in violet light after treatment with varying concentrations of ICoNPs, that is, 7.5 µM, 30 µM, and 60 µM respectively. It suggests the nanoparticles illuminate the cell walls with a bright blue color; therefore, they can be used for bioimaging to monitor the changes inside the cells during the entire healing process.

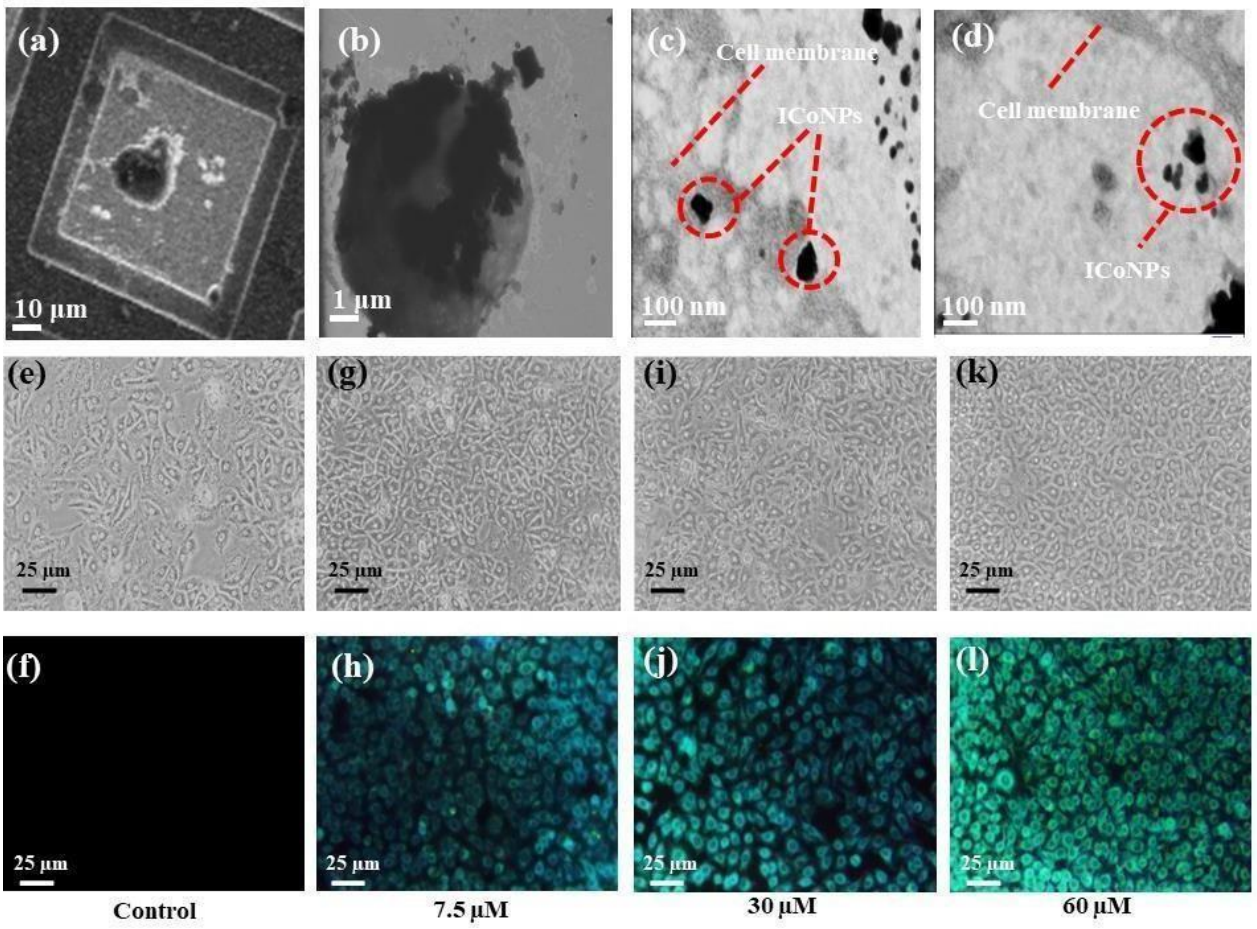

Figure. 16. in vitro studies indicate nanoparticles' internalization into the cells and their role in bioimaging. *(a-b) STEM analysis of cells after incubation with ICoNPs at different scales using a copper grid. (c) The interaction of ICoNPs with the cell membrane receptor leads to its movement inside the lipid bilayer. (d) The presence of ICoNPs inside the cell membrane of HEKa cell when observed under a microscope indicates its internalization. The bioimaging of HEKa cells using varying concentrations of ICoNPs. (e) and (f) shows HEKa cells without any treatment with ICoNPs in white and violet light, respectively. (g) and (h) indicates the cells treated with 7.5 µM of ICoNPs; (i) and (j) show the cells after treatment with 30 µM of ICoNPs; (k) and (l) indicate the cells after treatment with 60 µM of ICoNPs at white and violet light respectively after a time duration of 3 hours which emits bright blue fluorescence.*

2.3.6.4 HEKa cell migration assay in diabetic and normal wound conditions

The core-shell metal protein nanoparticles induce cell migration after treatment with $CoCl_2$, insulin, insulin + $CoCl_2$ mixture, and ICoNPs in normal and diabetic wounds. However, the increase is more in normal injuries than in diabetic wounds. With increasing time, the rate of cell division and migration was enhanced when monitored at a specific concentration of 30 µM. For the change in scratch width, I have measured scratch width at three distinguished places for all the scratches made on an individual plate. I took the mean of all readings of scratch width for calculating the percentage alteration in scratchwidth with time. The change in scratch width of HEKa cells taken as control after 0, 6, 12, and 24 h is indicated in **Figure. 17(a) a-d**. In diabetic conditions, the cells treated with core-shell ICoNPs show the percentage change of the scratched wound after 6, 12, and 24 h as 41.4 ± 1.08 %, 54.94 ± 0.97 %, and 67.66 ± 0.28 %, respectively, and is shown in **Figure. 17(a) q-t**. A similar procedure was followed, and the % of a gap left in cells that were treated with $CoCl_2$, insulin, and insulin + $CoCl_2$ was calculated and showed significant migration when compared to control but less than that of core-shell ICoNPs. The % change in a migration after 6,

12, and 24 h is noticed in all samples and came out to be 27.12 ± 0.50 %, 45.58 ± 1.26 %, and 54.45 ± 0.35 % in cells incubated with a mixture of insulin + $CoCl_2$ (**Figure. 17(a) m-p**). In cells treated with insulin, the value of change in migration is 20.27 ± 0.35 %, 37.08 ± 0.35 %, and 43.29 ± 0.33 %, respectively (**Figure. 17(a) i-l**), while it is 7.88 ± 0.60 %, 21.09 ± 0.35 % and 24.83 ± 0.70 % in cells treated with $CoCl_2$ (**Figure. 17(a) e-h**). A comparative study of variation in scratch diameter of the diabetic wound after treating the cells with all four samples is shown graphically in **Figure. 17(a) u**.

Similarly, in the normal wound, the variation in scratch diameter for control cells is shown in **Figure. 17(b) a-d**. The % variation in scratch width is monitored after the same time interval in normal conditions and found to be 14.84 ± 0.60 %, 31.75 ± 0.35 %, and 34.7 ± 0.70 % in the cells treated with $CoCl_2$ (**Figure. 17(b) e-h**). In the cells treated with insulin, insulin + $CoCl_2$, the % variation in migration with time is more as compared to $CoCl_2$ and is equal to 30.33 ± 0.80 %, 41.27 ± 0.70 %, and 48.98 ± 0.35 % in insulin (**Figure. 17(b) i-l**), 40.65 ± 0.35 %, 50.8 ± 0.35 % and 59.19 ± 0.35 % in insulin + $CoCl_2$. (**Figure. 17(b) m-p**). The core-shell ICoNPs show the maximum migration, and the % scratch width changed is 56.13 ± 0.92 %, 63.50 ± 0.70%, and 71.43 ± 0.35 %, respectively, indicating the significance of prepared nanoparticles in the healing application of normal wounds (**Figure. 17(b) q-t**). The graph in **Figure. 17(b) u** shows the variation in normal scratch width as a comparative study of all the formulations after particular time intervals. A comparative data table of change in wound migration in normal and diabetic wounds is shown in **Table 6**. To find if the data is statistically significant, p values were determined for scratch assay using one-way ANOVA in diabetic and normal wound conditions, and the comparative data is shown in **Table 7**.

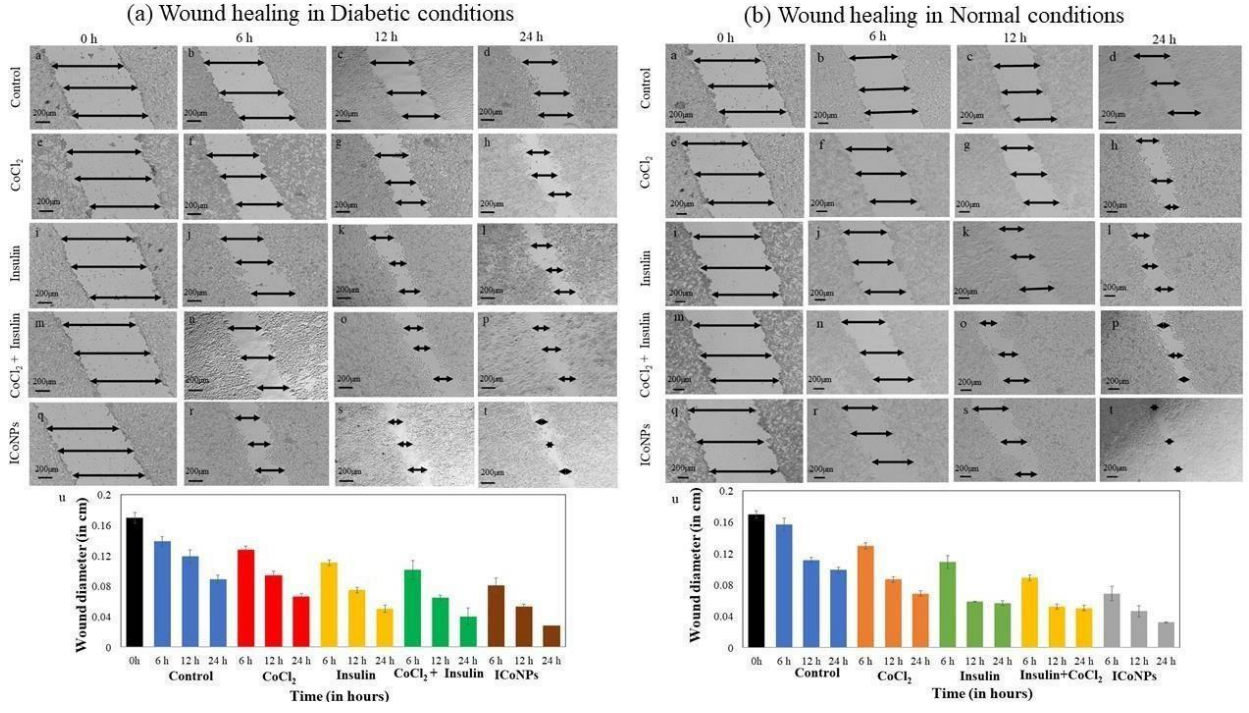

Figure. 17. Promotion and monitoring of in vitro wound recovery of the diabetic and normal wound using ICoNPs. *The nanoparticles induced better wound recovery in HEKa cells when compared with cobalt salt, insulin, or a mixture of both. The cells were treated using a particular concentration of all the solutions, that is, 30 µM. HEKa cells were taken as control (without any added formulations). (a) The figure shows diabetic wound healing using HEKa cells (a) 0h, (b) 6h, (c) 12h, (d) 24h; the cells treated with the salt solution of cobalt chloride after (e) 0h, (f) 6h, (g) 12h, (h) 24h; the HEKa cells after treatment with insulin protein (i) 0h, (j) 6h, (k) 12h, (l) 24h; the cells after treating them with a mixture of insulin and cobalt chloride are shown in figure (m) 0h, (n)*

6h, (o) 12h, (p) 24h; cells after treatment with ICoNPs after a duration of (q) 0h, (r) 6h, (s) 12h, (t) 24h; respectively. (u) The plot shows the relative change in scratch width in diabetic conditions after treatment with all the solutions respectively after specific time intervals. (b) The figure shows normal wound healing using HEKa cells (a) 0h, (b) 6h, (c) 12h, (d) 24 h; the cells treated with the salt solution of cobalt chloride after (e) 0h, (f) 6h (g) 12h (h) 24h; the HEKa cells after treatment with insulin protein (i) 0h (j) 6h (k) 12h (l) 24h; the cells after treating them with a mixture of insulin and cobalt chloride are shown in figure (m) 0h (n) 6h (o) 12h (p) 24 h; cells after treatment with ICoNPs after a duration of (q) 0h (r) 6h (s) 12h (t) 24h respectively. (u) The plot shows the relative change in scratch width in normal conditions after treatment with all the solutions respectively after specific time intervals.

Table 6. It shows the comparative data of variation in scratch width in diabetic and normal conditions after treatment with 30 µM of insulin, cobalt chloride, and the mixture of insulin and cobalt chloride and ICoNPs. The data was measured after a time duration of 6, 12, and 24 h.

% Change in diabetic scratch width with time				
Time	**$CoCl_2$**	**Insulin**	**Insulin +$CoCl_2$**	**ICoNPs**
6 h	7.88 ± 0.59 %	20.27 ± 0.35 %	27.12 ± 0.50 %	41.4 ± 1.08 %
12 h	21.09 ± 0.47 %	37.08 ± 0.35 %	45.58 ± 1.26 %	54.94 ± 0.97 %
24 h	24.83 ± 0.60 %	43.29 ± 0.33 %	54.45 ± 0.35 %	67.66 ± 0.28 %
% Change in normal scratch width with time				
Time	**$CoCl_2$**	**Insulin**	**Insulin +$CoCl_2$**	**ICoNPs**
6 h	14.84 ± 0.60 %	30.33 ± 0.80 %	40.65 ± 0.35 %	56.13 ± 0.92 %
12 h	31.75 ± 0.35 %	41.27 ± 0.70 %	50.8 ± 0.35 %	63.50 ± 0.70 %
24 h	34.7 ± 0.70 %	48.98 ± 0.35 %	59.19 ± 0.35 %	71.43 ± 0.35 %

Table 7. The table indicates the p values calculated for % alteration in scratch diameter in diabetic and normal conditions after treatment with 30 µM of insulin, cobalt chloride, the mixture of both insulin and cobalt chloride and ICoNPs. The statistical significance of data is considered when $p < 0.05$.

P value for checking the statistical significance of data for diabetic wound				
Time	**$CoCl_2$**	**Insulin**	**Insulin +$CoCl_2$**	**ICoNPs**
6 h	0.10824	0.003371	0.001639	0.001567
12 h	0.005436	0.000469	0.000585	0.000618
24 h	0.023327	0.002122	0.000904	0.00038
P value for checking the statistical significance of data for normal wound				
Time	**$CoCl_2$**	**Insulin**	**Insulin +$CoCl_2$**	**ICoNPs**
6 h	0.005648	0.001751	0.000152	0.000222
12 h	0.001058	1.33E-05	2.59E-05	0.000139
24 h	0.000447	0.00012	7.07E-05	5.44E-06

2.3.7 Combination index of cobalt and insulin

For calculating CI, Dm was determined using m and y from **Figure. 18a** for cobalt and **Figure. 18b** for insulin. It was found from the CI's calculated values that the cobalt chloride salt and insulin show a synergistic effect. The values determined for varying combinations of insulin and cobalt chloride concentrations come out to be less than one, indicating the synergism between the two, which work

together to enhance each other's activity. This is in accordance with the results obtained for cell viability and cell migration assay, indicating the significant role of insulin cobalt nanoparticles in faster wound healing applications. The data is shown in **Table 8.**

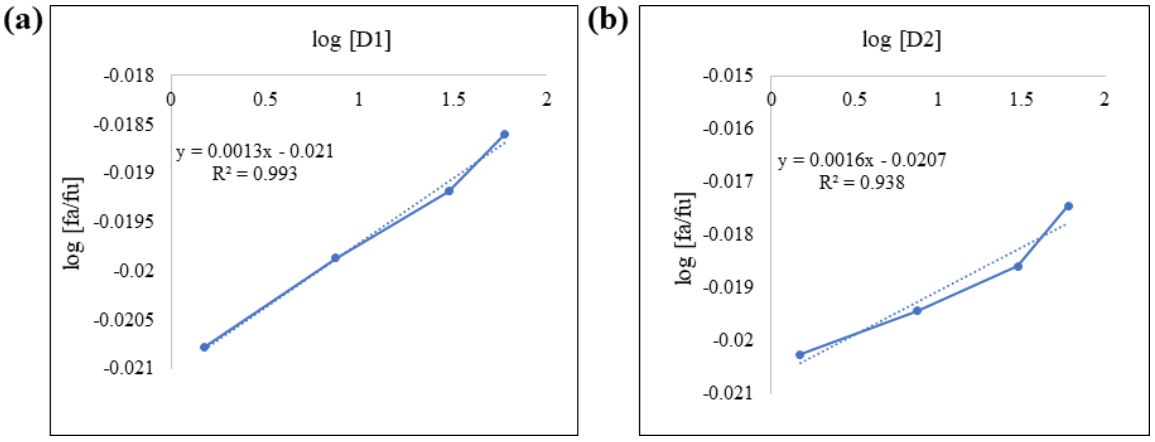

Figure. 18. Median plots of (a) Co salt and (b) Insulin *for finding the y-intercept and m values to calculate Dm to determine the combination index of cobalt and insulin.*

Table 8. The Combination Index (CI) values for the cell viability for varying combinations of cobalt salt with insulin protein were calculated, and the values come out to be less than 1, indicating the synergistic effect of drugs.

Combination Index (CI)			
The concentration of Co salt and insulin	(Dx)1 (Co salt) = Dm [fa/fu]$^{1/m}$	(Dx)2 (Insulin) = Dm [fa/fu]$^{1/m}$	CI = (D)1/(Dx)1 + (D)2/(Dx)2
1.5 µM	93118.86	171484.6	0.0000265
7.5 µM	71757.25	128844.6	0.00018188
30 µM	50284.49	96861.06	0.00098882
60 µM	29936.43	65800.79	0.00329352

2.4 Conclusion

To maintain the proper healing environment and eliminate any complications in the wound recovery process, the wounds were sometimes reopened, paving the way for improper healing, enhanced healthcare costs, and decreased life quality. Thus, suitable agents are always required, which assist in selectively binding to the wound site and guide in monitoring the progress of wound recovery. I have formulated novel core-shell ICoNPs containing insulin and cobalt and evaluated their role in wound healing activity. Insulin promotes cellular growth by modulating inflammation, reduces blood glucose concentration, and exhibits anti-inflammatory activity. Cobalt is known to reduce the microbial contamination load. Thus, the formulations were checked for a synergistic effect in wound treatment. Different techniques were used to confirm their formation, including TEM micrography, elemental analysis, FTIR, Raman spectroscopy, and Metal ion binding site prediction and docking server (MIB) to ensure Co-metal interaction with the insulin protein. From FTIR and Raman spectra, I got peaks showing the intermolecular interaction between Co and insulin and exhibiting moderate structural changes in amide regions of the protein. The metal-ion binding site prediction and docking server were used to find possible sites for the metal ion to bind with insulin amino acid chains A and B. No site was observed in chain A, while in chain B, there was a binding site for Co^{2+} ions, and the amino acids involved in groove formation were 8 GLY, 9 SER, and 10 HIS. The

loading efficiency and release kinetic studies were done to determine the effective loading of insulin drugs over the nanoparticles. The synthesized core-shell nanoparticles were tested for their effect on cell viability so they could be used further for diabetic and normal wound healing and bioimaging applications. The calculated values for the MTT assay and combination index values indicate the synergism between the cobalt chloride salt and insulin protein, making them suitable for further utilization in biological activities. The formed core-shell nanoparticles, ICoNPs, show excellent target-specificity. Due to the insulin consumption in their synthesis, they exhibit the property of binding to insulin receptors, making these particles unique from other particles in various respects, mainly in target-specificity properties. Further, they have enhanced fluorescent properties when compared with insulin alone, which can be easily detected using fluorescence microscopy and fluorescence bioimaging. They also possess an enormous tendency to heal both diabetic and normal wounds. Thus, it has multiple applications in healing, bioimaging, and material and biomaterial sciences. Therefore, it can be further explored for *in vivo* applications in diverse fields.

Chapter 3: Protection of lead-induced cytotoxicity using paramagnetic Nickel-Insulin quantum clusters

Abstract

Pb toxicity is associated with inflammation, which leads to a delay in wound healing. Pb^{2+} utilizes calcium ion channels to enter the cell. Therefore, to achieve adequate healing in the Pb-poisoned system, capturing Pb^{2+} from the circulation would be an effective approach without hampering the activity of the calcium ion channel. In this work, an insulin-nickel fluorescent quantum (INiQCs) cluster has been synthesized and used for specific detection of Pb^{2+} ions *in vitro* and cell-free systems. INiQCs (0.09µM) can detect Pb^{2+} as low as 10 pM effectively in a cell-free system using the fluorescence turn-off method. *In vitro* INiQCs (0.45µM) can detect Pb^{2+} as low as 1 µM. INiQCs also promote wound healing, which can easily be monitored using the bright fluorescence of INiQCs. INiQCs also help to overcome the wound recovery inhibitory effect of Pb^{2+} *in vitro* using lead nitrate. This work helps to generate effective biocompatible therapeutics for wound recovery in Pb^{2+} poisoned individuals (**Figure. 19**)

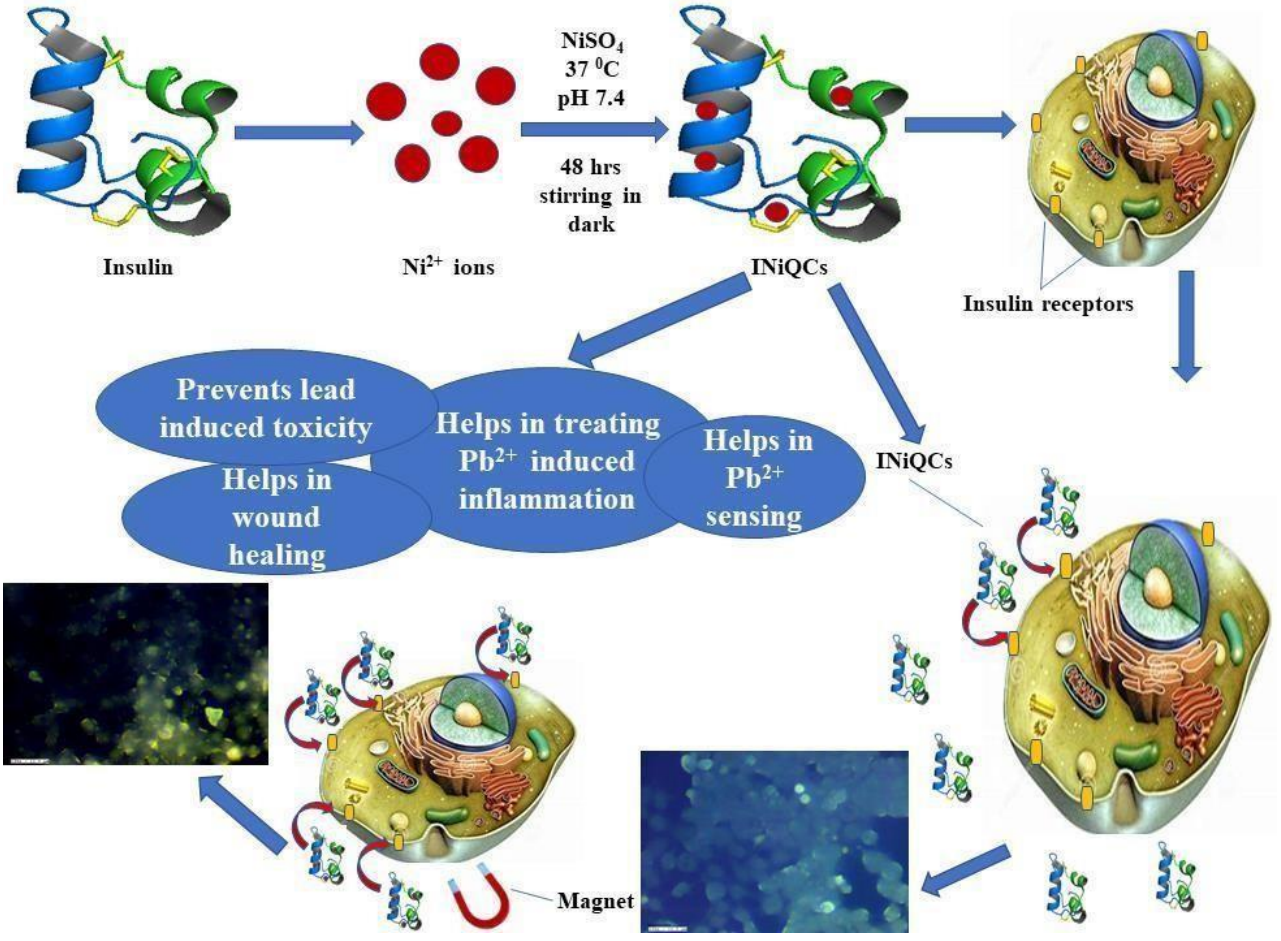

Figure. 19. The figure depicts the schematic representation of *the process involved in the synthesis of INiQCs, their biocompatible nature, and their applications as lead sensing agents, bioimaging agents, and wound healing-promoting agents.*

3.1 Introduction

Lead is a highly toxic, non-biodegradable element present ubiquitously in nature, causes environmental pollution, affects the human body to a large extent, and is among the 275 most hazardous substances listed by the Environmental Protection Agency (EPA), formulated by the Agency for Toxic Substances and Disease Registry (ATSDR) [282]. Lead affects around 0.6% of the population globally[1] and causes acute and chronic toxicity even in minute quantity. Certain heavy metals, including Pb^{2+}, Cd^{2+}, and $Hg^{2+,}$ can enter the body through food, water, smoking, industrial means, and even skin surfaces, leading to heavy metal poisoning [283],[284]. Lead at a level of 600 ppm is considered a "safe" level in the soil and would contribute under 5 ~g/dl to the total blood lead of children below 12 years [285]. There is no relaxation in the maximum permissible limit for lead in water, which was set at 0.05 ppm and is the highest desirable amount in drinking water in India. According to WHO, 1993, 25 μg/l lead per kg body weight is the maximum tolerable amount weekly [286]. Daily exposure to Pb^{2+} causes its deposition in body parts, including the liver, kidney, spleen, and brain, causing multiple tissue damage by inducing oxidative stress.

Moreover, long-term exposure to lead causes inflammatory infiltration, alterations in tissues of testicles, reduction in spermatocytes, necrosis of hepatocytes, degeneration of renal tubules, hypertrophy in the renal epithelium, and induces endoplasmic reticulum stress due to calcium imbalance in the liver and kidney [287],[288]. Kidneys are prone to the oxidative reaction of lead as lead intoxication sometimes causes dysfunctioning of the proximal tubule or irreversible nephropathy depending on exposure regimens, thus adversely affecting the health of kidney function along with cadmium and mercury [289],[290],[291] and can be excreted through urine and feces [292]. It affects the central nervous system, causes several neurological disturbances, and affects the blood-brain barrier, causing edema and loss of neurons. The astroglial activation in the brain leads to pathological processes which causes death of neuronal cells, that releases cytokines and chemokines, causing the inflammation [293]. Also, children, after exposure to lead in the environment, are more prone to toxicity due to the absorption of ingested lead from the gastrointestinal tract and nervous system [294]. Pb^{2+} has a carcinogenic effect by damaging the DNA and disrupting its repair system by generating ROS (reactive oxygen species). It can even impair memory and learning in the brain by disrupting NMDAR (N-methyl-d-aspartate receptors) [295]. Lead is found to be responsible for rashes, damaging the epithelial tissues, c, and accumulating on the epidermal layer [296],[297]. The toxicity due to lead is primarily dependent on the dosage and affects efficient wound healing by causing mechanical stiffness, slowing down cellular migration, and affecting the shape of cells [298],[299],[300].

Lead by modulating different inflammatory markers at the molecular level alters the humoral and cellular immune responses [301], such as cytokines (Interleukin-8, Tumor Necrosis Factor, etc.), acute phase proteins, enzymes known for causing inflammation like COX-2 and destroy intracellular molecules mediators and decreases immunoglobulin production, making individuals more prone to inflammation and other diseases [282],[302].

To cope with the toxic lead and its accumulation in the body, the quantum clusters are being used as one of the efficient ways for its detection up to a picomolar level in a cell-free system and can be detected well *in vitro* [303],[304]. For this purpose, insulin nickel quantum clusters were prepared as nickel metal promotes cell growth and healing activities [305]. Further, nickel is a micronutrient which is required for proper human body functioning by not only increasing the hormonal activity but by lipid metabolism as well. Nickel deficiency in mice is responsible for the significant decline in the action of lipogenic enzymes, such as, malic enzyme, and fatty acid synthase deficiency [306],[307]. Nowadays, QCs are gaining preference due to their luminescence emitting properties due to high photostability, emission rates, and large stokes shift [4],[308],[309]. QCs play the role of a connecting bridge between nanoparticles, atoms, and bulk molecules and, further because of

their size up to fermi wavelength, they significantly regulate different properties like optical, electronic, and chemical [310],[311]. QCs have few particles in the core as compared to the surface and are highly stable due to the presence of ligands with which surface atoms bind [312]. Different noble metals, including gold, silver, copper, and zinc, were used to make water-soluble QCs using mild reductants, including glutathione, alkyl thiol, and $NaBH_4$, along with different peptides, proteins, amino acids, dendrimers, and DNA which can be used as templates [313],[314],[315]. A variety of proteins, including proteins such as lacto-transferrin, hemoglobin, and BSA, has been used for making QCs with Au^+, Fe^{2+}, Cu^{2+}, Ca^{2+}, Ag^+ [228],[303],[316] which exhibited optical properties, catalytic activity and fluorescence thus, can be used in bio-imaging, natural marking, bio detecting of proteins, nucleic acids, and enzymes, and biological changes linked to them after translation or transcription [317],[318],[319],[320].

Insulin is widely used nowadays because the receptors for insulin are present over the mammalian cell membranes, and their amount varies greatly from 40 in erythrocytes to 200~300× 10^3 for adipocytes and hepatocytes. The number of insulin receptors in cancerous cells is much higher than in cells [321],[322],[323]. Insulin also plays the role of growth factor, which is responsible for facilitating chemotaxis and pinocytosis, increasing the secretion of inflammatory agents, and promoting re-epithelialization, that are essential for the efficient healing of wounds [233]. Multiple quantum clusters having distinct functions like drug delivery using silver QCs, super-resolution microscopy using gold, bioimaging using copper, and wound healing using zinc were synthesized using insulin.[49],[324],[14].

Here, insulin-nickel fluorescent quantum clusters are being synthesized and they have been utilized for sensing $Pb2^+$ in cell-free systems and countering its poisoning *in vitro*.

3.2 Materials and methods

3.2.1 Materials

Metal salts of analytical grade, including $NiSO_4$ (Nickel Sulphate) and Pb $(NO_3)_2$ (Lead Nitrate) were procured from Loba Chemie, India. Recombinant human insulin was purchased from (Elli Lilly, India). DMEM cell culture media, Fetal Bovine Serum (FBS), and penicillin-streptomycin were purchased from HiMedia, India. The rest of the chemicals were purchased from HiMedia and were of analytical grade.

3.2.2 Synthesis of Insulin Quantum clusters with Nickel metal salt

The nickel sulphate salt was converted into Insulin-protected quantum clusters following the standard synthesis protocol. The final concentration of insulin was set at 1.82 µM using distilled water as a medium. NaOH was used for adjusting the insulin pH up to 10.5. This is labeled as SOLUTION A and kept in the dark. After this, salt solutions having a molarity of 1.82 µM ($NiSO_4$) were prepared in a separate vial and labeled as SOLUTION B. After that, SOLUTION A and B were thoroughly mixed, followed by adjusting the pH by using HCl (0.1N) at 7.4. The final solution was placed in the incubator for 2 days at 37 ^oC at slow stirring (240 rpm)) [254],[325],[256].

3.2.3 Spectroscopic Characterization of INiQCs

3.2.3.1 UV-Visible spectroscopy

UV-visible absorbance of INiQCs was determined using instrument UV-2600 spectrophotometer Shimadzu and cuvette of quartz having a capacity of 4000µl and 1cm path length and scanned in the range 200 nm to 800 nm to monitor the interactions between insulin protein and $NiSO_4$ salt solution.

3.2.3.2 Fluorescence spectroscopy

Fluorescence data of INiQCs was measured using Agilent technologies Cary Eclipse fluorescence spectrophotometer. It helps to monitor the alteration in fluorescence intensity after the binding of

insulin to the metal salt solutions to form fluorescent protein-linked metal quantum clusters. It was done for INiQCs, insulin, and $NiSO_4$ solutions, all of which had similar concentrations. The fluorescence studies were done in the emission range 280 - 800 nm by exciting at a wavelength of 272 nm and an excitation and emission slit of 20 mm.

Along with this, a heavy metal sensing experiment was also performed using the following protocol. A 1 mM solution of Pb2+ metal ion was made using salt nitrates. After that, the solution undergoes ten folds of $1/10^{th}$ dilution. 1800 µl of the sample was taken from each of the solutions obtained in the above dilution series, 200 µl of INiQCs were added into each of the solutions, and luminescence was measured immediately after the addition of the heavy metal ions into quantum clusters. The data obtained were analyzed to check out if there was any quenching due to heavy metal ions in fluorescence. Also, a 1mM solution of other heavy metals and certain cationic and anionic species was made using the above-described method. As a result, a dilution series was obtained for each of the ions, including Cd^{2+}, Cu^{2+}, Hg^{2+}, Zn^{2+}, Ca^{2+}, K^{+}, Na^{+}, Cl^{-}, OH^{-}, HCO_3^{-}, SO_4^{2-}, S^{2-}. For each sample, 1800 µl of the solution of the ions mentioned above and 200 µl of INiQCs having pH 10 were added, followed by an instant measurement of fluorescence intensity to find out the specificity. The percentage increase in intrinsic fluorescence intensity was calculated and compared for both insulin and INiQCs using the given equation (a)

$$\% \text{ of change in emission intensity} = \frac{\text{F.I.(INiQCs)} - \text{F.I.(Insulin)} \times 100\%}{\text{F.I.(Insulin)}} \quad \ldots\ldots(a)$$

A similar formula was used to find out the % change in emission intensity after adding Pb^{2+} metal ions into INiQCs. For finding out the quantum yield of both insulin and INiQCs, the standard tyrosine fluorescence quantum yield was used as in equation (b)

$$Q.Y.(S) = \frac{Q.Y.(Tyr) \times I\,(S) \times 1\text{-}10^{-Al}\,(Tyr) \times n^2\,(S)}{I\,(Tyr) \times 1\text{-}10^{-Al}\,(S) \times n^2\,(Tyr)} \quad \ldots\ldots(b)$$

Here, Q.Y.is quantum yield; I is Integrated Emission Intensity; n is the Refractive Index of Solvent; A is the Absorbance at Excitation wavelength; l is the length of absorption cell; Tyr is Tyrosine (reference), and S is Sample.

3.2.4 FTIR Analysis

FTIR Spectrophotometer of Agilent Cary 600 series was used to identify the functional groups and insulin in the INiQCs mentioned above. After washing, the final product was dried on a glass side at 37 ˚C before being used. Then, the pellets were thoroughly mixed with KBr, and scanning was done from 400 cm^{-1} to 4000 cm^{-1}.

3.2.5 Morphological and Elemental Analysis using DLS and HRTEM

I have performed DLS (dynamic light scattering) to study the hydrodynamic size of INiQCs formed using a Malvern DLS-Zeta size analyzer. After that, to find out the morphology of insulin-linked Nickel quantum clusters, High-Resolution Transmission Electron Microscopy (HRTEM) Talos F200S G2, Thermo Scientific, and Selected Area Electron Diffraction (SAED) were used. For this, the samples were centrifuged at 240 rpm for nearly 10-15 minutes, after which a thorough washing of the pellet was done to get rid of unbound metal salt or impurities. Electron Dynamic Scattering (EDS) was done and the same pellet was monitored to get the percentage of elements present in the sample.

3.2.6 Stoichiometry ratio of Ni^{2+} ions: insulin protein

The stoichiometry of nickel ions to insulin protein is calculated using the following equation to study the interactions taking place between ligands, that is, metal ions and complex protein

Number of proteins bound to single Ni^{2+} ion = $\frac{\text{average number of bound proteins per ml}}{\text{average number of } Ni^{2+} \text{ ions per ml}}$

Further, for calculating the stoichiometry of INiQCs to Pb^{2+} ions present, I have done the Job's plot by maintaining the total concentration fixed and varying the individual concentration of ligand and complex.

3.2.7 *in silico* studies

To find the possible binding site for multiple transition metal ions with the help of the fragment transformation method, an online docking server tool called MIB can be used. To apply this method, two different protein chains were required, which were obtained from the protein data bank (PDB) and consisted of the template protein (T) of length m containing metal-ion and query protein (S) of length n. These chains were then arranged so that after proper alignment, the metal ion binding protein chain could be converted into the query protein structure. Various specifications were followed to obtain these protein structures. The most critical parameter is that there should be a binding site for any of the transition metals, including Ni^{2+}, Cu^{2+}, Mg^{2+}, Ca^{2+}, Co^{2+}, Zn^{2+}, Fe^{2+}, and Fe^{3+} metal ions. After that there should be at least 50 residues in the entire length of the protein chain; otherwise, it will be excluded [257]. For writing the residues of the query template and metal ion binding triplets, the notation N-Cα-C backbone atoms and as (xN, xCα, xC) and (yN, yCα, yC), where x and y are the coordinates of PDB can be used. S and T can be written as (τ1, τ2. τm) and (σ1, σ2. σm) in terms of triplets. Further, a minimum of two metal ion binding residues should be there, and the distance between the PDB coordinates and the metal center should be within 3.5 Aº. Proper alignment is possible only if the distance is less than 3.5 Aº [258]. Also, the binding score of the residue needs to be greater than a particular threshold value, and only then will the residue bind to particular transition metal ions. The binding score is written as Ci and depending on the target protein structure and sequence, binding score is assigned to all the residues of the target protein by using root mean square deviation of C-alpha carbons of structural local alignment as well as BLOSUM62 substitution matrix [259],[260].

Thus, MIB tool assits in finding out the binding site of metal ions on a specific protein chain. Human Insulin protein (PDB ID: 4EWW) was extracted from the PDB database. This polypeptide contains two chains mentioned as A and B. In MIB, the Ni^{2+} ion was docked with chains A and B of human insulin independently, followed by monitoring the possible amino acids responsible for binding to the metal ion. [261].

3.2.8 Cytotoxicity testing:

To check out the cell viability, the HEK 293 cell line (Human Embryonic Kidney Cells) was used, and MTT (3-(4,5-dimethylthiazol-2-yl)-2,5-diphenyltetrazolium bromide) assay was performed. For this purpose, HEK 293, with a per well density of 1×10^4, were grown in 96 well plates and was kept till 80-85% confluency. After that, incubation of cells with three distinct amounts (1.5, 7.5, and 30 µM) of INiQCs, insulin, and $NiSO_4$, along with the mixture of insulin and $NiSO_4$, was followed by incubating the cells for 24 h and 37 ˚C. Later on, the MTT (2mg/ml in 5% ethanol) was added and kept for 3 h, followed by its removal thereafter. Lastly, 200µl DMSO was added for dissolving the formazan crystals, and then the OD was monitored at 570 nm. For calculating the percentage inhibition, the given equation was used

$$\% \text{ inhibition} = [1-(A_t / A_c) \times 100] \%$$

Where A_t is the test substance absorbance and A_C control solvent absorbance. For each of the concentrations [265].

Then another MTT was performed. In this, I have add six different concentrations (0, 1, 10, 100, 500, 1000 µM) of Pb^{2+} in each of the initially incubated cell lines with INiQCs, insulin, $NiSO_4$,

and a mixture of insulin and $NiSO_4$ as described above. After incubation for 12 h, the MTT was added, and all the steps were followed, as mentioned above.
While performing the MTT assay, both in the presence and absence of heavy metal Pb^{2+}, three independent groups were taken for all concentrations, followed by calculating the average of all those readings and plotting them.

3.2.9 Fluorescence Bioimaging:

Fluorescence imaging was done using the Dewinter fluorescence microscope. For bioimaging, the samples were incubated for one hour under UV light in a UV laminar. Then, 100µl from the Insulin metal quantum clusters (INiQCs) was taken and added to the cell line opted for the experiment, that is 293. After one day, to remove any impurities, cells were washed using PBS buffer twice, and cell fixation was done by adding 2% of formaldehyde solution followed by having pictures of the incubated cells with and without using a magnet. It was a bar magnet of size 5 cm x 2 cm x 1 cm having a field strength of 0.5 T. Similarly, in the other six-well plates, the above samples were again made as such, followed by the addition of 6 different concentrations (0, 1, 10, 100, 500, 1000 µM) of Pb^{2+} in each of the initially incubated well to find out the variation in fluorescence emission intensity *in vitro*. After that, bioimaging was done using a microscope.

3.2.10 Effect of INiQCs on recovery of the wound in the presence of toxic element Pb^{2+} using phase contrast and fluorescence imaging:

The cells were grown in 60 mm plates using the high glucose DMEM-F12 FBS-free medium and incubated at 37 ˚C and 5% CO_2 till80-85% confluency. After that, the scratch assay was used to make a wound, followed by treating cells with distinct concentrations of INiQCs, insulin, Ni salt, and the mixture of insulin and Ni salt (I + Ni). In one more plate, cells were treated initially with lead, followed by treatment with INiQCs. Time-lapse imaging was done, and the variation in the width of the wound was monitored after 6 h, 12 h, and 24 h, respectively. The scratch width was observed at multiple positions in a random manner, and the mean of all readings was taken to determine the percentage change in scratch width.

3.3 Results and Discussions

3.3.1 Absorbance spectra:

After the synthesis of INiQCs, its characterization was done. I have obtained a sharp peak for insulin at 272.03 with an absorbance value of 0.249, whereas for INiQCs, an absorbance value of 0.135 was obtained, having a peak at 272 nm **Figure. 20a**. This confirms the synthesis of INiQCs.

3.3.2 Fluorescence spectra:

For INiQCs, after excitation at 270 nm, an emission peak ranging from 280-360 nm was obtained with maxima at ~300 nm with an intensity of 240.52 a.u when it was monitored from 200-800 nm as given in **Figure. 20b.**

3.3.3 Structure, Composition, and Stoichiometry of Metal Insulin Clusters: The spherical quantum clusters of INiQCs were formed and confirmed by Transmission electron microscopic images. The size of clusters, as shown by HRTEM, is ~ 5-6 nm. The SAED (selected area electron diffraction) pattern is attached at the top, which shows a ring-like pattern in **Figure. 20c**. The presence of different elements like Ni, C, O, N, and S is shown in the Elemental mapping of the area. The even distribution and percentage of Ni associated with protein come out to be 5.28 % and analyzed by EDS (inset of **Figure. 20c**). Further, the stoichiometric ratio between insulin protein and Ni^{2+} ions was calculated and found that one Ni^{2+} ion (163 pm in radius) is encapsulated by ~ 687 insulin protein.

3.3.4 Metal-ion Binding Residue Templates:

I have used MIB, to find the binding sites on insulin with which the transition metal Ni^{2+} can bind. The interaction between proteins and metals is primarily based on the structure and sequence of the amino acids in a protein. Firstly, from PDB, the structure of insulin was obtained (PDB ID: 4EWW) and then inserted in the MIB tool to dock the Ni^{2+} ions with both the chains (chain A & B) of insulin. As a result, each amino acid residue gets its binding score, and if it is more significant than a threshold, then that site is marked as a potential target site for that particular metal ion. (Ni^{2+} in this study). The data indicates that chain A does not show any template indicating the absence of binding sites of Ni^{2+} ions with chain A, whereas, in chain B, a binding site was found for Ni^{2+} ions. Then, I have worked with another software called Maestro. By using this, I have calculated the distance between Ni^{2+} and amino acids, namely 9 SER and 10 HIS, present on Chain B of insulin. The distance was found to be 5.87 and 6.24, respectively, as shown in **Figure. 20d**. The binding score was also determined using MIB with different amino acids present in chain B of Insulin with Ni^{2+} ions, thus finding the best possible sites for attachment. **Figure. 20e**.

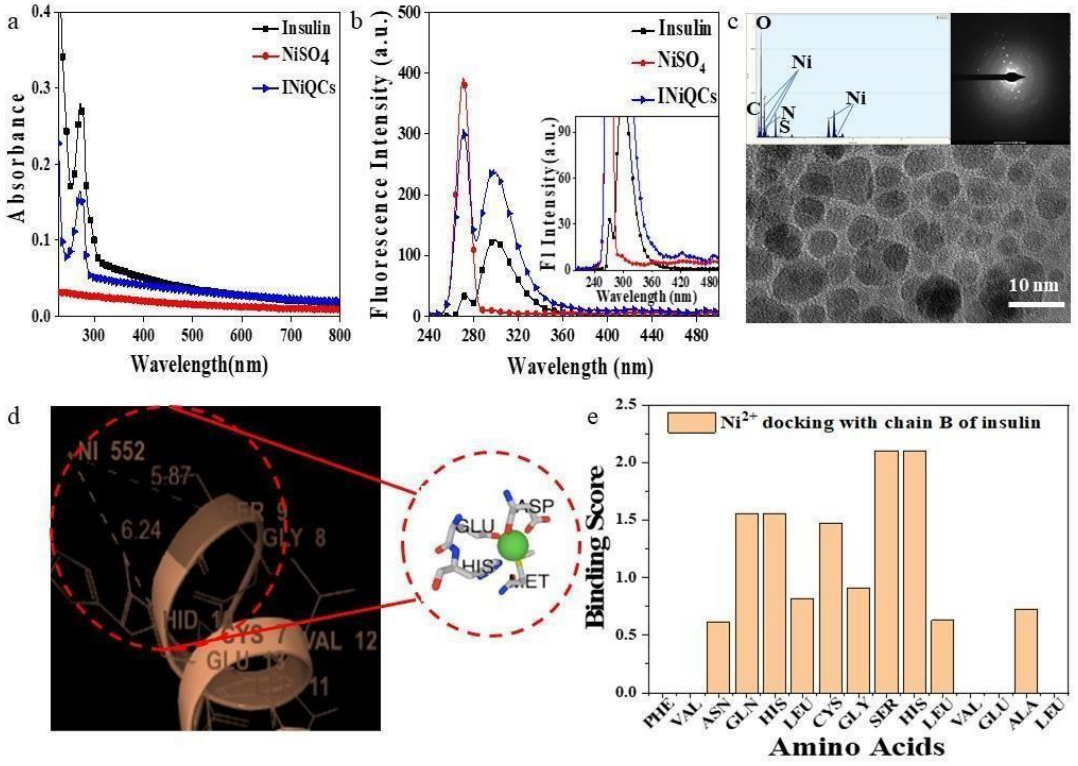

Figure. 20. Characterization of INiQCs *(a) The UV spectra indicate an excitation peak at 272 for INiQCs. (b) Shows the fluorescence spectra after exciting samples at 272 nm, and an emission spectra is obtained, which exhibits fluorescence maxima at 299.36 nm when scanned from 200-800 nm. Inset is the trailing of fluorescence from 380nm onwards. (c) HRTEM images on a 10 nm scale showing the ~ 5-6 nm size of INiQCs, Inset is the EDS showing that the Ni is present in the end product along with the selected area electron diffraction (SAED) (d) Metal ion binding residues: Depicts the binding site for Ni^{2+} with the amino acid residues within 3.55 Å diameter that can participate in binding on chain B of insulin (e) Binding potential of each amino acid with the Ni^{2+} ion.*

3.3.5 Quantum yield determination – Tyrosine was selected as the standard with which absorbance (**Figure. 21a)** and fluorescence spectra were compared. To find out the quantum yield of INiQCs, tyrosine was used as a standard as its quantum yield value is known. The % change in fluorescence was calculated. In comparison to insulin, the percentage change for INiQCs is 48.26%,

but when I add Pb^{2+} ions (10 pM) into INiQCs, the value decreases to 26.5%. The QY for Insulin was determined to be 0.1798, and of INiQCs was 0.7416. After adding Pb^{2+} into INiQCs, the quantum yield obtained was 0.4626. **Figure. 21b**.

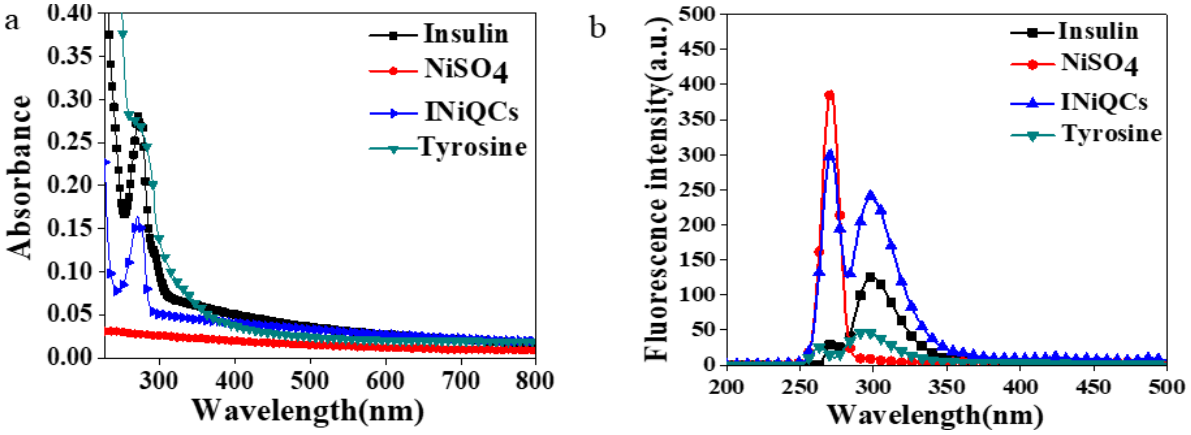

Figure. 21. Spectroscopic characterization of INiQCs *(a) It shows a comparison of absorbance value between Insulin, INiQCs, $NiSO_4$, and tyrosine (standard). (b) It shows a comparison of the fluorescence intensity value of Insulin, INiQCs, $NiSO_4$, and tyrosine (standard).*

3.3.6 FTIR Spectra

FTIR was used for NiSO4, insulin, and INiQCs to figure out the interactions involved in metal-protein binding. The peaks appeared due to intermolecular interactions of insulin and $NiSO_4$ at different wavenumbers. Firstly, the peak appeared at 670 cm^{-1}, which indicates formation of Ni-OH bending bond [326]. After that, at 742 cm^{-1} a peak was observed both in insulin and INiQCs, indicating NH_2 and NH wagging [228]. In addition to the first peak, a peak at 820 cm^{-1} shows the bond between Ni=O, which confirms the interaction between insulin and $NiSO_4$ [327]. A peak at 881 cm^{-1} in insulin shows C-O stretching. C-N stretching was observed both in insulin and INiQCs at 1046 cm^{-1}. Multiple S=O stretching peaks were observed, firstly at 1198 cm^{-1} in INiQCs and $NiSO_4$, followed by a peak at 1288cm^{-1} both in insulin and $NiSO_4$, and finally at 1415 cm^{-1} in INiQCs and $NiSO_4$ [14]. C-H bond was obtained in insulin at 1388.5 cm^{-1} [328]. Amide II is the NH_2 bond that was seen in insulin at 1528 cm^{-1} and 1590 cm^{-1} but only at 1590 cm^{-1} in INiQCs [329]. C-H stretching was observed at 2869.7 cm^{-1} in insulin only [257]. Intramolecular O-H stretching gives two peaks in INiQCs at 2958 cm^{-1} and 3187.6 cm^{-1}, respectively, but a single peak was observed at 3187.6 cm^{-1} in $NiSO_4$ [330]. A single peak was present in insulin, indicating amine N-H stretching at 3330 cm-1, which was absent in the other two [14]. For non-H-bonded O-H stretching, peaks were observed at 3682 cm^{-1} and 3782.5 cm^{-1} both in INiQCs and $NiSO_4$, but were absent in insulin [326]. This is shown in **Figure. 22**. and **Table 9**.

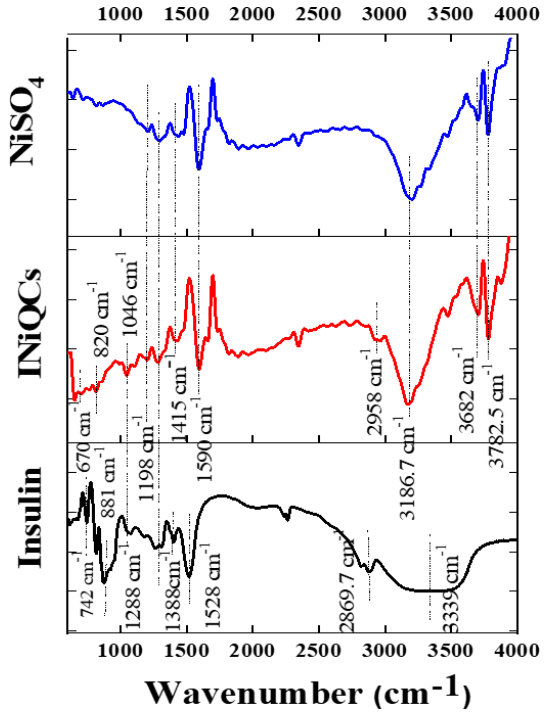

Figure. 22. FTIR spectroscopic studies to find the interaction between insulin protein and nickel metal ion. *The comparison shows the formation of new bonds between Ni-OH and Ni=O, which were otherwise not present.*

Table 9: The comparative wavenumber values of insulin, $NiSO_4$, and INiQCs show the position of multiple functional groups present, which confirms the interactions between insulin and $NiSO_4$ salt solution.

Functional group	**Insulin**	**$NiSO_4$**	**INiQCs**	**Ref.**
Ni-OH bending	-	-	670	[326]
NH_2 and NH wagging	742	-	742	[228]
Ni=O stretching	-	-	820	[327]
C-O stretching	881	-	-	[14]
C-N stretching	1046	-	1046	[14]
S=O stretching	- 1288 -	1198 1288 1415	1198 - 1415	[14]
C-H bond	1388.5	-	-	[328]
Amide C=O bond	1528 1590	- -	- 1590	[329]
C-H stretching vibrations	2869.7	-	-	[257]
O-H intramolecular stretching	- -	- 3187.6	2958 3187.6	[330]
Amine N-H stretching	3330	-	-	[14]
O-H stretching (non-H bonded)	- -	3682 3782.5	3682 3782.5	[326]

3.3.7 Heavy metal (Pb^{2+}) detection by luminescence quenching

The luminescence of INiQCs can be used as a highly selective and sensitive tool for detecting Pb^{2+} ions by a "turn-off" luminescent sensor. Fluorescence quenching is observed in the presence of Pb^{2+} ions, and it greatly varies with the amount of Pb^{2+} ions **Figure. 23a**. The more significant the concentration of heavy metal ions, the more is quenching, and the less is the fluorescence intensity, as shown in inset of **Figure. 23a**. Fluorescence quenching was maximum when the concentration of Pb^{2+} ions was maximum that is 10 millimolar in this case and declines gradually as concentration reaches up to 10 picomolar levels. Various other metal ions were also used to find out if fluorescence due to INiQCs decreases or increases in their presence, but no such effect was found for Cd^{2+}, Hg^{2+}, Cu^{2+}, Zn^{2+}, Ca^{2+}, K^{+}, Na^{+}, Cl^{-} OH^{-}, HCO_3^{-}, S^{2-}, $S\,O_4^{\ 2-}$ when I use their highest concentration similar to that of lead ions that is 10mM. Fluorescence was immediately measured after adding the QCs into the salt solutions of the highest concentration. However, no such effect was observed with any of the other metal ions **Figure. 23b**. Then the variation in fluorescence intensity of Insulin, INiQCs, $NiSO_4$, tyrosine, INiQCs + Pb^{2+} was measured to compare the differences between all and calculate quantum yield which comes out to be 0.7416 for INiQCs and 0.4626 when I add the Pb^{2+} ions **Figure. 23c**. Further, the stoichiometric ratio was computed using job's plot for INiQCs and Pb^{2+} and found to be 1:1 as shown in **Figure. 23d**.

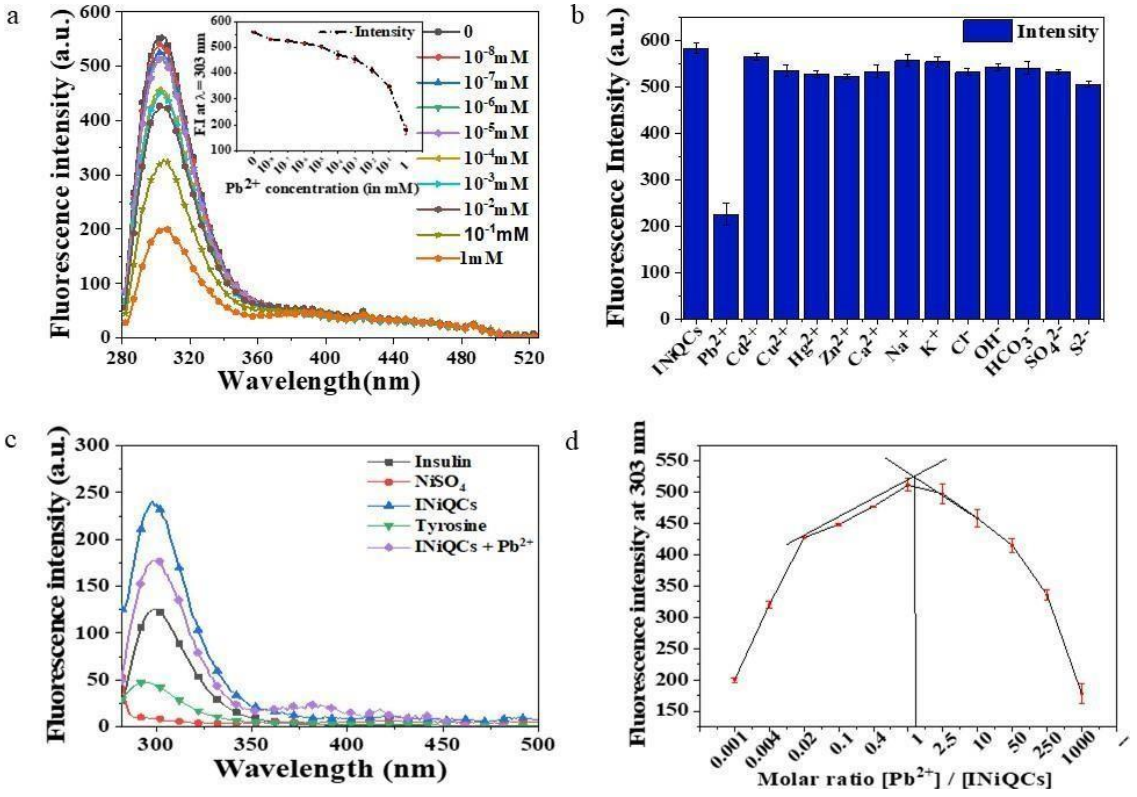

Figure. 23. Treatment of INiQCs with different concentrations of Pb^{2+} salt solution *(a) shows the variation in fluorescence spectra after excitation of all samples at 272 nm. An emission spectra was obtained showing a gradual decrease in fluorescence with increasing concentration of Pb^{2+} ions from 10^{-8}mM of Pb^{2+} to 0mM of Pb^{2+}. Inset is the decrease in fluorescence intensity at λ_{max} with varying concentrations of $Pb(NO_3)_2$. (b) Variation in fluorescence intensity at λ_{max} for different metal ions, including heavy metal ions and other cations and anions. (c) It shows the fluorescence spectra of INiQCs, INiQCs + Pb^{2+}, insulin, $NiSO_4$, and tyrosine, indicating variation in fluorescence intensity. (d) It shows the job plot for the determination of stoichiometry between INiQCs and Pb^{2+} ions.*

3.3.8 HEK 293 cell viability and migration assay

The MTT results, which are indicative of cell viability, mainly depend on the mitochondrial activity of cells. It is calculated for insulin, $NiSO_4$, a mixture of insulin, and $NiSO_4$ and INiQCs by using 1.5, 7.5, and 30 µM of concentrations, and the graph was plotted. While performing the MTT assay, both in the presence and absence of heavy metal Pb^{2+}, three separate groups were considered for every concentration, followed by taking an average of all those readings and plotting them. For $NiSO_4$ treated cells, cell viability shown is 102.94 ± 3.20% for 1.5 µM, 125.16 ± 1.27 % for 7.5 µM and 131.35 ± 10.96 % for 30 µM. Insulin shows 113.1± 4.60 % for 1.5 µM, 129.76 ± 0.49 % for7.5 µM, and 157.41 ± 18.47 % for 30 µM respectively. The cells treated with a combination of insulin and $NiSO_4$ showed more cell viability. It is 141.03 ± 3.03 % for 1.5 µM, 151.98 ± 2.46 % for7.5 µM and 162.3 ± 9.32 % for 30 µM respectively. Cell growth following the treatment with INiQCs exhibited considerable changes, which are 139.29 ± 1.13 % for 1.5 µM, 189.68 ± 1.64 % for7.5 µM, and 195.63 ± 7.36 % for 30 µM respectively, as compared with other samples. The results indicate the potential of these quantum clusters to promote cell growth and, hence, wound healing. The measurements were statistically significant. From the graph, it was demonstrated that no one is toxic in comparison to the control. With increasing concentration of samples added, the cell viability enhanced and was maximum for INiQCs formed, indicating that quantum clusters formed are not at all toxic; instead, they help in the cell division and multiplication and thus can be used for wound healing as well as shown in **Figure. 24a**.

Similarly, when I add different concentrations of Pb^{2+} ranging from 0, 1, 10, 100, 500, and 1000 µM, respectively, in the cells initially incubated with insulin, $NiSO_4$, a mixture of insulin and $NiSO_4$, and INiQCs, the MTT results show that the cell growth declined gradually with increasing concentration of lead metal ions in all the wells but in the presence of INiQCs, the cell growth is less impaired. The cell viability is calculated for all the samples. For cells incubated only with Pb^{2+}, the cell viability is 97.71 ± 4.46 % for 1 µM, 98.07 ± 1.85 % for 10 µM, 43.31 ± 17.26 % for 100 µM, 41.64 ± 5.11 % for 500 µM and 28.84 ± 0.92 % for 1000 µM. When I add the concentrations mentioned above of Pb^{2+} with a fixed concentration of $NiSO_4$, the cell viability comes out to be 100.84 ± 2.17 % for 1 µM, 103.31 ± 3.84 % for 10 µM, 61.58 ± 8.05 % for 100 µM, 65.43 ± 0.65 % for 500 µM and 46.49± 7.62 % for 1000 µM. A fixed concentration of insulin shows 107.15 ± 1.34 % for 1 µM, 100.53 ± 6.36 % for 10 µM, 79.59 ± 12.47 % for 100 µM, 50.03 ± 10.36 % for 500 µM and 27.40 ± 7.97 % for 1000 µM. The cells incubated with a mixture of insulin and $NiSO_4$ have cell viability as 92.76 ± 4.02 % for 1 µM, 91.30 ± 3.86 % for 10 µM, 49.88 ± 7.40 % for 100 µM, 46.80 ± 7.40 % for 500 µM, and 25.71 ± 2.54 % for 1000 µM. The cells exposed to INiQCS have the maximum cell viability out of all these, even in the presence of a varying concentration of Pb^{2+}, which is 103.38 ± 5.55 % for 1 µM, 104.92 ± 1.63 % for 10 µM, 79.95 ± 8.66 % for 100 µM, 80.16 ± 6.53 % for 500 µM and 61.63 ± 8.86 % for 1000 µM. The cells keep on growing without much effect of heavy metal ion even in the highest concentrations of Pb^{2+} ion, which are 100, 500, and 1000 µM, respectively. This indicates that INiQCs are not toxic themselves, overcome the effect of toxicity due to Pb^{2+}, and further result in improving cell multiplication and growth, as shown in **Figure. 24b.**

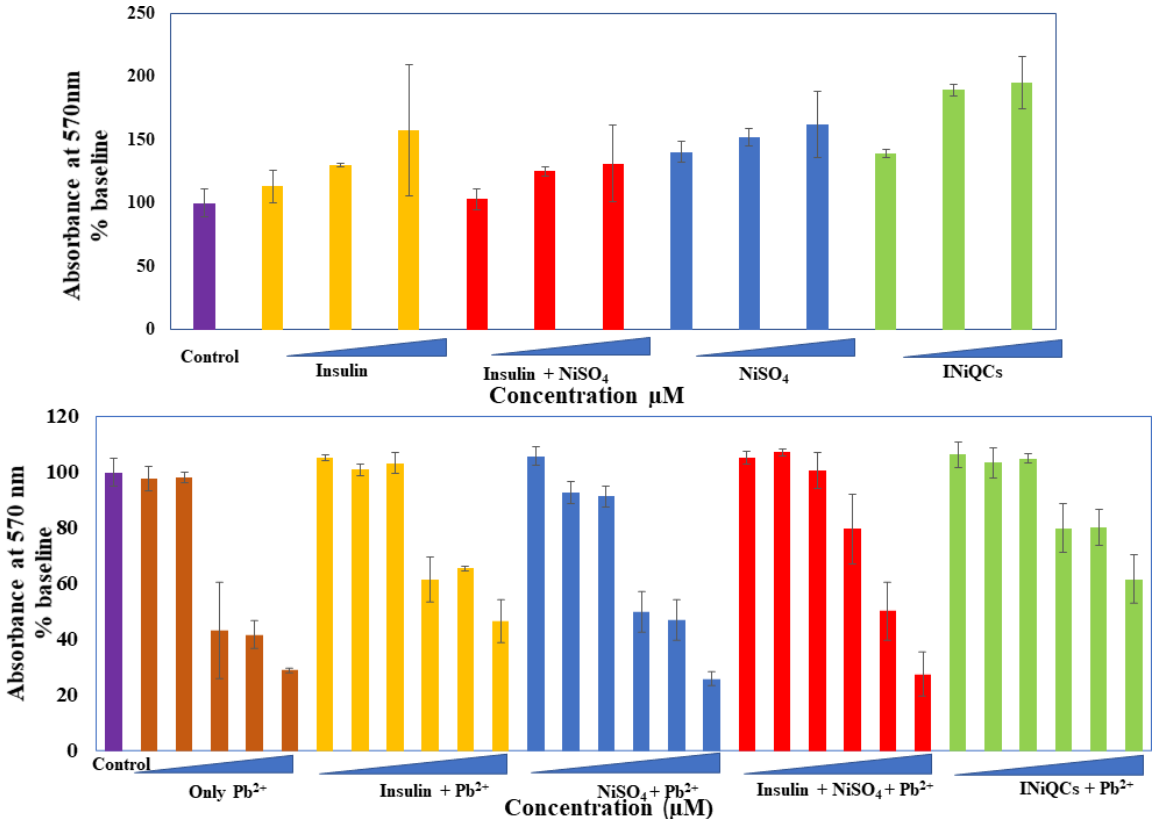

Figure. 24. MTT assay to determine the cell viability. *(a) Data shows treatment of HEK-293 cells with control, including insulin, $NiSO_4$, insulin + $NiSO_4$, and INiQCs ranging from 1.5, 7.5, and 30 µM concentration, respectively, of each sample. (b) Data shows the treatment of HEK-293 cells with 0.45 µM of insulin, $NiSO_4$, insulin + $NiSO_4$, and INiQCs. Then, the same cells were treated with 0, 1, 10, 100, 500, and 1000 (µM) concentrations of Pb^{2+} after three h, and data were plotted as the mean value of three independent experiments.*

INiQCs induced more cell migration than $NiSO_4$, insulin, and insulin + $NiSO_4$. With increasing time, the extent of cell division and migration increased at a fixed concentration that is 0.45µM. For the measurement of change in scratch width, I measured scratch width at six distinguished places for each scratch in all wells and determined the average of each well to obtain the percentage variation in scratch width. The cells treated with INiQCs show the percentage scratched width after 6, 12, and 24 h as 40.90 ± 4.54%, 27.62 ± 5.99%, and 8.51 ± 2.83% **Figure. 25 (m-o and r-t)** respectively **Figure. 25a–c** A similar procedure was followed and the % of a gap left in cells that were treated with $NiSO_4$, insulin, insulin + $NiSO_4$, were calculated and showed significant migration when compared to control. The cells treated with INiQCS + Pb^{2+} show 44.24 ± 1.04%, 37.74 ± 2.93%, and 27.42 ± 1.63% after 6, 12 and 24 h respectively as shown in **Figure. 25 (u-w)**. Similarly, the migration after 6, 12, and 24 h comes out to be 49.69 ± 4.29%, 52.52 ± 7.28%, and 35.46 ± 0% in cells incubated with insulin + $NiSO_4$ as can be seen in **Figure. 25 (j-l)**. In cells treated with insulin the value of migration is 64.24 ± 4.66%, 63.42 ± 4.71% and 62.83 ± 11.46% after the time duration of 6, 12 and 24 h **Figure. 25 (g-i)** while it is 82.72 ± 4.16%, 75.48 ± 4.85% and 71.63 ± 2.95% after the same time duration as above in cells treated with $NiSO_4$ as shown in **Figure. 25 (d-f)**.

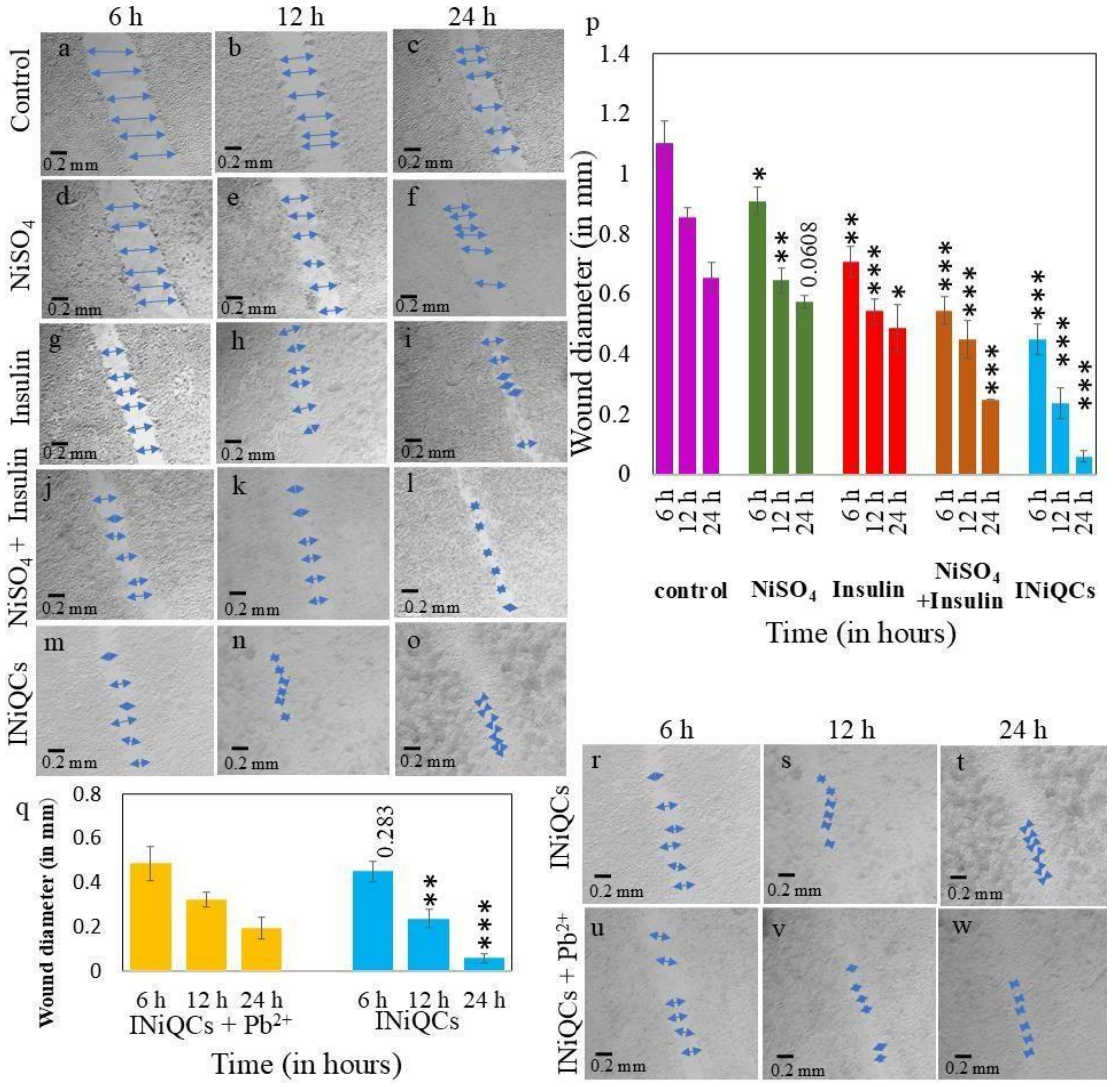

Figure. 25. Promotion and monitoring of in vitro wound recovery using INiQCs. *HEK-293 cells control (a) 6 h, (b) 12 h, and (c) 24 h, treated with 0.45 µM Ni salt for (d) 6 h, (e) 12 h, and (f) 24 h respectively, treated with insulin for (g) 6 h, (h) 12 h, and (i) 24 h respectively, treated with insulin + $NiSO_4$ (j) 6 h, (k) 12 h, and (l) 24 h respectively, treated with INiQCs for (m) 6 h, (n) 12 h and (o) 24 h (p) Plot shows the variation in scratch width after 6 h, 12 h, 24 h post-treatment with Ni salt, insulin, insulin + $NiSO_4$ and INiQCs respectively. (q) plot showing a comparison of variation in scratch width after treatment with INiQCs and INiQCs + Pb^{2+}. The statistical significance of data is shown in both the plots with "*," ***p < 0.001, **p<0.01, and *p<0.05, respectively. Change in diameter of the wound is shown after its treatment with INiQCs for (r) 6 h, (s) 12 h, and (t) 24 h, respectively, and after its treatment with INiQCs + Pb^{2+} for (u) 6h, (v) 12 h and (w) 24 h respectively.*

3.3.9 Fluorescence microscope bioimaging

For confirming the applications of INiQCs for imaging on cells, bioimaging was performed on HEK293 cell lines. Cells were treated with INiQCs and showed bright blue fluorescence after binding of INiQCs with the insulin receptors found on the cell wall of each cell, thus illuminating the cell walls and making cells look fluorescent. The imaging was performed on the HEK 293 cell line after treatment with INiQCs at both white and violet light, respectively, in the absence of a magnet **Figure. 26a, Figure. 26b.** The cells are showing bright blue-tinged fluorescence. Moreover, when the magnet was used while capturing the pictures, the fluorescence became much brighter,

indicating the paramagnetic effect of Ni^{2+} ions under white and violet light, respectively **Figure. 26c** and **Figure. 26d**. This shows the quantum clusters emit bright fluorescence and, therefore, can be utilized for bioimaging purposes. The same experiment was performed in the presence of Pb^{2+} ions. In this, the cells after treatment with INiQCs were treated with (0, 1, 10, 100, 500, 1000) µM Pb^{2+} ions, respectively, and incubated. After that, images were taken in white and violet light, and it was observed that as I went on increasing the concentration of Pb^{2+} ions, there was a gradual decline in the fluorescence of cells; that is, fluorescence quenching occurs with increased concentration of heavy metal even up to 1µM level indicating that even though the lead is toxic but still the INiQCs overcome its effect even at its highest concentrations and emit fluorescence thus can be used even in these conditions for bioimaging. The variation in fluorescence with different concentrations of heavy metal ions, that is (0, 1, 10, 100, 500, 1000) µM $Pb^{2+,}$ is shown in **Figure. 26 e, f, g, h, i,** and **j,** respectively.

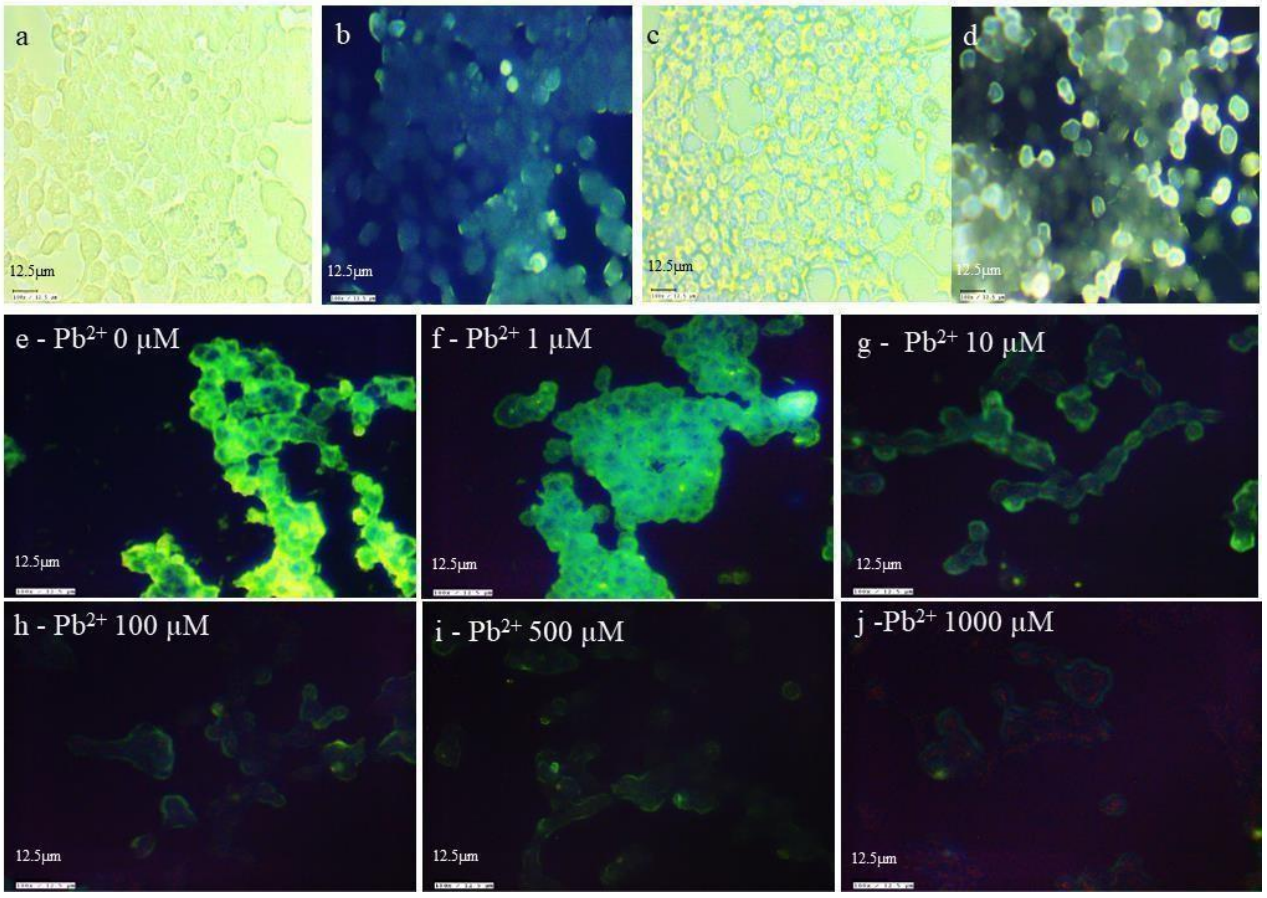

Figure. 26. HEK 293 cell line on treating with INiQCs *(a) in the absence of magnet at white light. (b) in the absence of a magnet at violet light, (c) in the presence of a magnet at white light, (d) in the presence of a magnet at violet light. Imaging of HEK 293 cell line on treatment with INiQCs (0.45 µM) followed by addition of different concentrations of Pb^{2+} ions as (e) 0 µM Pb^{2+} (f) 1 µM Pb^{2+} (g) 10 µM Pb^{2+} (h) 100 µM Pb^{2+} (i) 500µM Pb^{2+} (j) 1000 µM Pb^{2+} all under violet light respectively.*

3.4 Conclusion

Lead-induced toxicity has been very prevalent since earlier times. Although the overuse of lead is controlled in advanced countries like Canada, the USA, and the European Union, developing and underdeveloped countries are still excessively using it due to its specific physicochemical properties, which are of particular interest to humans. Lead affects all age groups, but infants are

more prone to lead toxicity. Lead accumulates slowly in all the organs and causes inflammation. Diabetic patients are severely affected due to its accumulation, leading to delays in wound recovery, thus needing to be taken care of efficiently. For this, I have prepared INiQCs, which contain insulin that has an anti-inflammatory effect. Both nickel and insulin also promote wound recovery. INiQCs were used to detect the heavy metal ion named Pb^{2+} in a cell-free system and *in vitro* up to certain minimum levels of picomolar range and that too by using low concentrations of INiQCs in the micromolar range, thus preventing its highly toxic effects. After that, INiQC's effect on wound healing was checked both in the presence and absence of lead. Different techniques were used to confirm their formation, including TEM micrography, elemental analysis, FTIR, and MIB, which confirmed the interaction of Ni-metal with the insulin protein. From FTIR, I got peaks that show intermolecular interaction between Ni and insulin, that is, a peak at 670 cm^{-1} and 820 cm^{-1} showing Ni-OH bending and bond between Ni=O, respectively. From MIB, the possible metal ion binding sites in chain B for Ni^{2+} ions were obtained, and amino acids 9 SER and 10 HIS were used to form the groove. The binding potential was maximum for serine and histidine.

Moreover, INiQCs are target-specific. They exhibit the potency to bind with insulin receptors present in the cells due to the use of insulin protein in their formation, indicating their target-specificity, which makes them unique from other particles in various respects. These particles exhibit fluorescence (blue fluorescence), which easily distinguishes them from control insulin. They have enhanced fluorescent properties, which can be easily detected using fluorescence microscopy. In the presence of a magnet, their fluorescence enhanced manifolds compared to those without a magnet. The INiQCs proved to be very specific for the particular lead metal ion, indicating their high selectivity which did not even get effected by other ions. This activity indicates its use as a fluorescence turn-off probe, which can be used in place of electronic and digital devices that have been used for several years for heavy metal detection. Thus, it has multiple applications not only in biolabeling and biosensing but also in material and biomaterial sciences and, therefore, can be further explored for *in vivo* applications.

Chapter 4: Insulin-Infused Bimetallic Nano-subclusters as Multifunctional Agents for ROS Scavenging, Antibacterial Resilience, and Accelerated in vitro cell migration

Abstract

This is the first report on the synthesis and wound healing application of green synthesized insulin-infused bimetallic (copper-silver) nano-subclusters (ICu-AgNSCs) with high stability, aqueous solubility, biocompatibility, and target specificity. HRTEM and SAED data confirm spherical particles (with a diameter of 9.6 ± 2.2 nm) composed of discrete copper clusters on the periphery and silver core that are further infused with insulin (0.5 ± 0.2 nm) corona, as confirmed by the characteristics of Cu-OH and Ag-O stretching bonds and alteration in insulin amide bonds. The ICu-AgNSCs had high insulin loading efficiency (93.90 ± 1.05 %) and drug release rate (92.69 ± 0.90 % within 40 h), allowing it to be ideal for sustained release applications. Wound healing in diabetic conditions gets delayed due to the prolonged proinflammatory phase and microbial infestation, which may lead to clinical amputation. Therefore, advanced therapeutics that promote cell growth by reducing inflammation and microbial growth are required. ICu-AgNSCs may satisfy all these criteria. Insulin and quercetin have ROS scavenging and anti-inflammatory properties. Insulin and copper have cellular growth-promoting activity; additionally, silver has antimicrobial properties. ICu-AgNSCs have been shown to accelerate diabetic cell migration *in vitro*, making them an ideal choice for pre-clinical and clinical applications (**Figure. 27**).

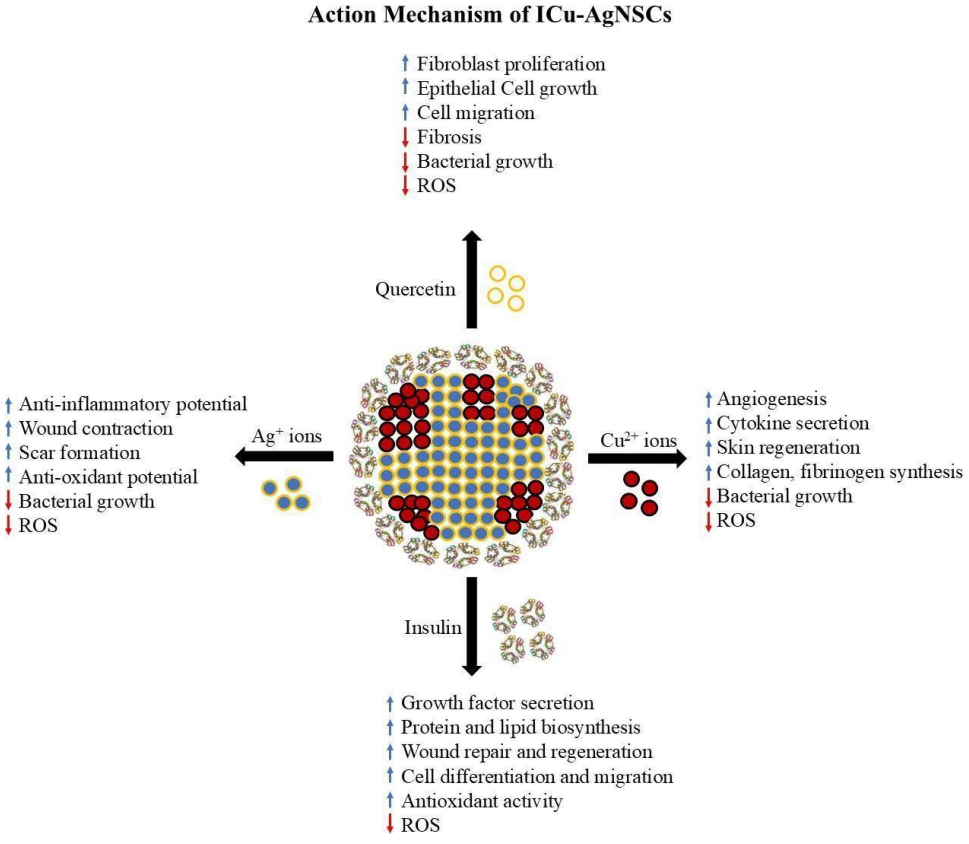

Figure 27: The figure shows the *potential role of four different components being used to synthesize bimetallic nano-subclusters in wound healing, antimicrobial, and antioxidant applications to cause efficient healing.*

4.1 Introduction

Wound healing is a significant challenge for the scientific community despite all the available treatments, and the global expenditure on healing wounds varies from $28.1 to $96.8 billion [331]. Healing is a complex event involving overlapping phases, which work together against the damage and restore the lost tissue or organ [203]. Healing begins with hemostasis, which consists of the activation of platelets, clot formation, and matrix organization. In proliferation, the gathering of growth factors, connective tissues, and angiogenesis factors occurs on the wound part. In the inflammatory phase, the proinflammatory cytokines promote vasodilation and activate the different signaling pathways. The extracellular matrix gets resynthesised in the remodeling phase to maintain the balance between dead and live cells [205], [332]. However, certain factors disrupt the normal physiological mechanism of wound healing, including microbial infection, trauma, ischemia, and diabetes mellitus [333],[209] which can be avoided by preventing bacterial infestation, removing the dead tissue and debris, and keeping the wound moist [210]. In diabetes, there is persistent release of proteases, proinflammatory cytokines, reactive oxygen species, and low secretion of anti-inflammatory cytokines [334]. Diabetic wounds are more susceptible to infection because of the body's immune response impairment [209]. The potential action of multiple antioxidant enzymes, like glutathione peroxidase and superoxide dismutase, is reduced, which leads to damage by free radical generation [218]. Diabetes also affects protein synthesis, re-epithelialization, cell migration, and fibroblast and keratinocyte proliferation by preventing the transport of nutrients to the wound site [215],[217]. Reactive oxygen species (ROS) are also a major issue, as their accumulation prevents the efficient working of macrophages and endogenous stem cells. Also, ROS causes dysfunctioning endothelial and restricts new blood vessel formation [335]. Additionally, ROS due to bacterial infection leads to chronic wound infection by damaging endothelial cells and blood vessels [336],[337].

To promote healing, tremendous research is going on to develop novel formulations that are biocompatible, efficient, environment-friendly, and cost-effective. Here, the role of nanoparticles comes into play as they possess massive potential in diverse fields ranging from drug delivery, bioimaging, wound healing, anticancer, antimicrobial, and antioxidant activity [338],[220]. Many nano-formulations using gold, silver, copper, zinc, and cobalt were developed to study wound healing antibacterial and antioxidant applications [225],[339],[42]. Nowadays, protein-based metallic nanoparticles have gained enormous interest because of their target specificity, biodegradability, ability to alter their surface for efficient attachment of the drugs, and easily metabolizable nature [132]. Protein-modified nanoformulations are developed using different proteins, including bovine serum albumin, insulin, transferrin, lactoferrin, and silk fibroin [340]. All these formulations possess single metal ions and, thus, obtain the property of that constituent metal ion only. It makes them less effective and unstable, and they tend to form aggregates, gradually decreasing their potential activities. However, the need of the hour is to develop formulations with multiple activities to increase their efficacy. Bimetallic formulations are preferred over monometallic because they can enhance multiple properties depending upon their surface effect, quantum tunneling effect, and quantum size effect [341]. They also possess outstanding potential in diverse biomedical applications [342],[343]. Based on the arrangement of the metal atoms, bimetallic particles can be classified into four major categories: alloyed, intermetallic, subclusters, and core-shell [344]. Bimetallic nano-subclusters (BNSCs) are a fascinating class of nanomaterials composed of two distinct metal atoms having two separate phases and a shared interface [345]. BNSCs exhibit features which make them attractive options for multiple uses, like in catalysis, sensing, and biomedicine. Their potential of encapsulating and delivering therapeutic agents directly

to targeted cells offers a new method to improve drug treatments' efficacy while minimizing side effects [346]. Additionally, BNSCs can be functionalized with targeting ligands for enhancing their specificity and selectivity towards specific cell types [347]. This work reports the synthesis of novel insulin-coated silver-copper bimetallic nano-subclusters and their potential role in promoting cell migration antioxidant and antibacterial activity.

Silver enhances the differentiation of fibroblasts into myofibroblasts, which promotes proliferation and keratinocyte relocation, which increases wound contraction. Silver activates macrophages, modulates the inflammatory response, reduces scar formation, and exhibits antimicrobial, anti-inflammatory, and antioxidant activity [348], [349]. Further, the oxidation of silver causes free radical generation and reactive oxygen species (ROS), which are capable of damaging the biomolecules, including DNA, lipids, and proteins, along with intracellular organelles, including mitochondria, ribosomes, vacuoles, etc. in the microbes [350]. Copper promotes wound recovery by regulating the secretion of various cytokines and growth factors. It stimulates the expression of fibrinogen, collagen, and integrin, which are found in the extracellular matrix and are essential for the attachment of cells to the extracellular matrix. It also exhibits biocidal action [351], [352]. Copper regulates vascular endothelial growth factor (VEGF), that is required for forming new blood vessels [353]. It enhances the expression of hypoxia-induced factor-1-alpha (HIF-1α), which promotes angiogenesis and skin regeneration [354]. Further, quercetin has a massive role in wound healing as it promotes fibroblast proliferation and migration, decreases the proinflammatory cytokines, reduces the immune cell infiltration, increases the collagen fiber accumulation, and improves the GSH level along with vascular endothelial growth factor, fibroblast growth factor, and alpha-smooth muscle actin levels. Quercetin itself works in the reduction and stabilization of nanoparticles [355],[356]. Insulin is gaining colossal interest from researchers for its ability as a growth factor and transition the proinflammatory cytokines to anti-inflammatory, which are essential for inflammation, re-epithelialization, wound repair, and regeneration [227],[273]. It promotes protein and lipid biosynthesis, stimulates cell glucose uptake, increases cellular differentiation, and promotes cellular migration [268]. After binding to the receptors, insulin activates different pathways like Akt, Erk, and NRF-2 pathways to promote wound healing [47],[357]. The insulin-templated nanoformulations have promising potential for bioimaging, super-resolution microscopy, and wound healing [273], [324].

Here, I have synthesized the bimetallic nanosubclusters to check the synergism between silver nanoparticles and insulin-loaded copper quantum clusters for healing wounds when linked together to yield formulations in the nano range. To maintain the affected individual's quality of life, there is a need to explore the potent and effective agents that not only have effective drug delivery potential but also have antimicrobial and antioxidant potency to yield better outcomes without making the process cumbersome, costly, and risky for the patient's life.

4.2 Materials and Methods

4.2.1 Chemicals and cell line

Silver nitrate ($AgNO_3$), Copper sulfate ($CuSO_4$), formaldehyde, HCl, NaOH, and H_2O_2 were of analytical grade and bought from HiMedia, India. Recombinant human insulin was purchased from Elli Lilly, India. For cell culture, DMEM cell culture media, Fetal Bovine Serum (FBS), 100X Penicillin-streptomycin, and Phosphate buffer solution (PBS) having pH 7.4 were procured from HiMedia, India. Human Primary Epithelial Keratinocytes (HEKa cells) ATCC-PCS-200-011 were procured from Himedia, India. The cells were cultured, maintained, and treated using DMEM containing 5% FBS at 37 $^{\circ}$C and 5% CO_2. The bacterial strains used for antibacterial activity include *Escherichia coli* (MTCC no. 448), *Bacillus subtilis* (MTCC no. 441), *Acinetobacter calcoaceticus*

(MTCC no. 1948), and *Staphylococcus aureus* (MTCC no. 902) which were procured from IMTech, Chandigarh, India.

4.2.2 Synthesis of bimetallic nano subclusters

At first, the insulin-protected copper quantum clusters (ICuQCs) were prepared by following a previously reported one-pot method. The insulin solution with a final concentration of 1.82 mM was prepared, and with the help of NaOH solution (0.1M), its pH was adjusted to 10.5 and kept in the dark. Afterward, a salt solution ($CuSO_4.5H_2O$) of the same concentration was prepared, followed by mixing insulin and salt solution in 1:1, which was further followed by adjustment of the pH of the final solution to a pH of 7.4, using HCl (0.1N). The final solution was kept in the incubator at slow stirring (240 rpm) for 24 h at 37 $^{\circ}$C and was dialyzed using a 10KDa cut-off dialysis membrane, stored at 4 $^{\circ}$C. After that, silver nanoparticles (AgNPs) were prepared to have the same concentration using quercetin and by slightly modifying the previously reported method [358] and incubated in the dark with the earlier formed insulin copper quantum clusters for 24 h at 37 $^{\circ}$C to obtain the bimetallic nano subclusters (ICu-AgNSCs) as shown in **Figure. 28a**. Then, the final solution was again dialyzed using a 10 kDa cut-off dialysis membrane, stored at 4 $^{\circ}$C, and used further for characterization and biological studies.

4.2.3 Study of Interactions using spectroscopic techniques

Initially, to monitor the interactions between the AgNPs and ICuQCs to form ICu-AgNSCs, UV-Visible absorbance studies were done by using the UV-2600 spectrophotometer (Shimadzu), which was operated between 200-800 nm, and a 4000 µl quartz cuvette having a path length of 1 cm was utilized to determine the absorbance for both the salt solutions ($CuSO_4$ and $AgNO_3$), AgNPs, insulin, ICuQCs, and Insulin linked bimetallic nano subclusters (ICu-AgNSCs) were measured.

To study the metal-protein interactions in the ICu-AgNSCs, FTIR was done with the help of an Agilent Cary 600 series Spectrophotometer. The potassium bromide (KBr) method was used to prepare the sample pellets. The sample scanning was done from 400 cm^{-1} to 4000 cm^{-1} to monitor the changes in certain specific bonds.

Furthermore, the same samples were analyzed using Surface Enhanced Raman Scattering (SERS) Spectra to study the modification in the structure of insulin protein. All the samples were prepared on a silicon wafer ten minutes prior to the experiment. The samples were scanned from 500 cm^{-1} to 1800 cm^{-1}. The LabRam Hr Evolution Horiba, was utilized to record the Raman spectra of insulin and ICu-AgNSCs at 785 nm.

Further, the most reliable technique (Circular Dichroism (CD)) was used to monitor the stability of secondary protein structures after the interactions between protein molecules and metallic nanoparticles. The CD experimentation was done at 25 ˚C with 1 ml of sample and scanned in the 200-260 nm wavelength range for pure insulin and ICu-AgNSCs using phosphate buffer (pH 7.4) as a solvent with the help of Mos500 CD biologic instrument.

4.2.4 Study of particle size, morphology, and elemental analysis

The DLS analysis (dynamic light scattering) was done using a Malvern DLS-Zeta size analyzer for determining the hydrodynamic size of synthesized ICu-AgNSCs. After that, for finding the morphology and size of bimetallic nanosubclusters, HRTEM (Talos F200S G2, Thermo Scientific) was used. For this, the samples were centrifuged at 240 rpm for 15 minutes, and then a thorough washing was done on the pellet to get rid of unbound metal salt or impurities present in the sample. Furthermore, the sample pellet was monitored for the elemental mapping to find the distribution of metal salts in the sample and to find out the percentage of the elements present by using the Energy dispersive X-ray Spectrometer (EDS) (Bruker QUANTAX 200).

4.2.5 Drug loading and release kinetics

To monitor the drug loading in the nanosubclusters, centrifugation of 1 ml of the synthesized ICu-AgNSCs was done for 15 min at 6000 rpm. The supernatant and the pellet were collected to determine the amount of bind and free drug and, thus, determine the drug loading capacity of the formulations. After that, the release kinetics were performed to determine the amount of insulin released from the nanosubclusters and, thus, determine the drug delivery efficiency. 1 ml of the synthesized nanosubclusters were taken, placed in a dialysis membrane, and kept at slow stirring conditions (250 - 300 rpm). The drug release was measured at specific time intervals for 40 hours at physiological conditions that are pH 7.4 and 37 °C. The absorption values (at 595 nm) were later plotted to note the trend of drug release by exploiting BSA standard curves.

4.2.6 *in vitro studies*

4.2.6.1 Cell viability

For evaluating the cell viability of synthesized nanosubclusters, the MTT (3-(4,5-dimethylthiazol-2-yl)-2,5-diphenyltetrazolium bromide) assay was performed by using the HEKa cell line (Human Epidermal Keratinocytes, adult). The cells were grown in a cell culture plate and let to be confluent till 80-85%, followed by their splitting and seeded into 96 well plates, with each well having the density of cells as 1×10^4. After that, the cells were incubated for further cell growth and confluence till 80-85%, and the media was regularly changed after specific time intervals. When the plate became confluent, the different samples, including salt solutions, AgNPs, ICuQCs, and ICu-AgNSCs having distinct concentrations (5, 10, 20, and 40 µM) were added in sets of 3 to get three concordant readings. The plate was later placed for 24 hours at 37 °C and 5% CO_2. After 24 h, the media in the MTT plate was replaced with fresh media with MTT (2mg/ml in 5% ethanol) and incubated for another 3 h. Following the specified time interval, the media was again discarded and replaced with 200µl dimethyl sulfoxide (DMSO) for the proper dissolution of the formazan crystals. Lastly, the OD was checked at a wavelength of 575 nm. The equation used to calculate the percentage of cell viability is as follows.

$$\%\, cell\ viability = [(A_t / A_c) \times 100]\,\% \qquad \ldots\ldots(1)$$

Here, A_t is the absorbance of the test substance, and A_C is the absorbance of the control solvent for each concentration.

4.2.6.2 Effect of ICu-AgNSCs on the cell migration, *in vitro,* using phase contrast imaging

To monitor the impact of synthesized particles on cellular migration *in vitro*, the HEKa cell line was used and grown in 60 mm plates both in the absence and presence of glucose (360mg/dl) to monitor the changes in normal and diabetic conditions. The cells were grown in the DMEM-F12 media (FBS-free medium) and kept in a humidized incubator at 37 °C and 5% CO_2 level. The cells were grown till they became 80-85% confluent, followed by creating a scratch in the confluent plate with the help of a pointed object, such as the sterile 200 µl tip, to analyze the effect on cell migration using the scratch assay. The plates were later incubated with fixed concentrations (5, 10, 20, and 40 µM) of different samples, including salt solutions, AgNPs, ICuQCs, and ICu-AgNSCs. Time-lapse imaging was done to observe the variations in scratch width after 6 h, 12 h, and 24 h, respectively. The width was measured at multiple places of the scratch-made in each plate, followed by taking the mean of those individual readings of scratch diameter is taken to determine the percentage variation in cell migration in the normal and diabetic conditions individually.

4.2.6.3 Antioxidant activity against H_2O_2-induced cytotoxicity

To perform the antioxidant activity, HEKa cells were grown in 96 well plates and kept at 37 °C and 5% CO_2 for 24 hours in DMEM medium supplemented with 10% FBS and left till 85-90% confluency. Afterward, the cells were segregated into two groups and treated with varying concentrations of H_2O_2 (0, 50, 100, 200, 400, 800, 1200, 1600, 2000 µM) in DMEM for 1-hour

duration, followed by washing them twice using PBS to obliterate the H_2O_2. The cells in one of the sets were incubated with fresh DMEM media alone, and in the other set, the cells were treated with bimetallic nanosubclusters of fixed concentrations alongside DMEM (40 µM) and kept in the incubator for 24 hours. Following this, an MTT assay was followed for determining the effect on cell viability following the treatment with H_2O_2 and to study the antioxidant effect of the synthesized nanosubclusters on cell viability. The media was discarded, and cells were washed with PBS before adding fresh media containing MTT and kept for a 3-hour incubation period, followed by DMSO to measure the absorbance at 570 nm [359].

4.2.6.4 Detection of ROS measurement using DCFDA

ROS generation was determined by flow cytometry using DCF-DA staining. The Heka cells were grown in DMEM media and treated with varying concentrations of H_2O_2 (200, 1000, 4000 µM) for a brief period of 1 hour. Then, the media containing H_2O_2 was discarded, and cells were treated with bimetallic nanosubclusters (40 µM) for 12 hours after adding fresh media. Following this, the cell detachment was done using trypsin-EDTA solution and suspended in 0.5 ml of PBS, to which DCFDA (10 µM) was added 10 minutes before performing the flow cytometric analysis.

4.2.7 Antibacterial activity of synthesized ICu-AgNSCs

To determine the antibacterial potential of the synthesized nanoformulations, the Minimum Inhibitory Concentration (MIC) which is the minimal concentration up to which an antibacterial agent retains the bacterial growth inhibition for the defined period. The Gram-negative (*Escherichia coli, Acinetobacter calcoaceticus*) and Gram-positive (*Bacillus subtilis, Staphylococcus aureus*) bacteria were utilized for the determination of the MIC of formulations using a growth curve experiment. The microdilution method was followed to determine the antimicrobial activity using 96 well plates. Initially, the bacteria were cultivated in the LB broth medium at 37 ˚C, and after 24 hours, the bacteria were taken in the LB media, and the concentration was adjusted to 10^{-8} CFU/ml. To evaluate the antimicrobial potential of nanosubclusters, 20 µl of bacteria, 20 µl of nanosubclusters (ranging from 0.5 µM to 64 µM), and 160 µl of luria broth was added in each well of 96 well plates. The negative control is taken as inoculated broth without nanosubclusters. The plates were placed in a microplate shaker for 24 hours and 37 ˚C at slow shaking conditions. Following this, the best concentration of synthesized nanosubclusters against different bacteria is determined by the MIC method. Further, the IC_{50} values were determined along with the MIC value for each bacteria [360].

4.2.8 Determination of combination index (CI) for $AgNO_3$ and ICuQCs

The combination index (CI) is one of the quantitative measures followed for calculating the effect of multiple drugs in combination with one another. The drug combination index was estimated when investigating synergistic or antagonistic drug combinations to quantify the level of synergism or antagonism. Suppose the value of the combination index comes out to be less than 1 (CI < 1). In that case, it indicates that different drugs, when administered together, work together to promote the activity of one another, called the synergistic effect. When the CI values come out to be equal to 1 (CI = 1), it indicates that none of the two drugs interfere with each other's action, hence exhibiting the additive effect, and a CI value of greater than 1 (CI >1) shows the inhibitory activity of one drug on the other drug, thus called the antagonistic effect. To calculate the combination index, the cell viability of HEKa cells was determined at different concentrations of $AgNO_3$ and ICuQCs, and then calculations were done using the following equation (e).

$$CI = {}^{(D)1}/_{(Dx)1} + {}^{(D)2}/_{(Dx)2} \quad \ldots\ldots(2)$$

Where, $D_x = D_m {}^{[f_a/f_u]}{}^{1/m}$ ……(3)

Here, (D)1 and (D)2 denote the respective concentrations of silver nitrate and insulin copper quantum clusters, respectively. The median effect equation (f) is used for the determination of single drug concentrations giving the same effect (Dx)1 and (Dx)2. Here, fa and fu denote the cell fractions that are affected and unaffected, respectively, and are equal to $10^{(y\text{-intercept})/m,}$ where m represents the slope median in the median effect plot of log (D) vs. log (fa/fu) [266].

4.2.9 Statistical Analysis

The data here is represented as the mean ± SD of at least three separate experiments. The statistical data analysis was done in MS Excel using one-way ANOVA. The corresponding p-values were calculated to find out if the data was statistically significant or not.

4.3 Results and Discussions

4.3.1 Spectroscopic analysis

4.3.1.1 Spectroscopic changes using absorbance spectra after synthesis of ICu-AgNSCs

After synthesizing ICu-AgNSCs, its spectroscopic characterization was done to observe the absorbance spectra of the formed nanosubclusters. After analysis of AgNPs and insulin, the absorbance spectra for AgNPs indicate a peak-maxima at 412 nm having an absorbance value of 0.145, and for insulin without any added salt solution, I have obtained a sharp peak at 271.61 nm with an absorbance value of 0.262 both of which are in accordance with the work reported. The absorbance spectra obtained for ICuQCs exhibit an absorption maxima at 271.31 nm, having an absorbance value of 0.23. Whereas, after incubating the AgNPs with ICuQCs for 48 h, two distinct absorption maxima were obtained at 271.31 nm and 412.86 nm, having absorbance values of 0.16 and 0.10, respectively, showing the interaction between the two, which indicates towards the possibility of ICu-AgNSCs synthesis as shown in **Figure. 28b**.

4.3.1.2 FTIR and Raman Spectra for monitoring the interactions between protein and metal ions after the formation of nano subclusters

To monitor the variation in the functional groups of insulin after interactions between the insulin copper quantum clusters and silver nanoparticles, the FTIR was performed for $CuSO_4$, $AgNO_3$, AgNPs, insulin, ICuQCs, and ICu-AgNSCs. The slight variation in major protein peaks appeared at different wavenumbers due to intermolecular interactions of ICuQCs and AgNPs and are shown in **Figure. 28c**. The peak at 791.29 cm^{-1} and 651.23 cm^{-1} indicates the NH_2 stretching and C=S stretching, respectively, in AgNPs, insulin, ICuQCs, and ICu-AgNSCs [268]. Then, a peak at 724.96 cm^{-1} in $CuSO_4$ and 718.19 cm^{-1} in ICuQCs and ICu-AgNSCs indicates Cu-OH stretch [361]. Ag-O stretching was observed in $AgNO_3$, AgNPs, and ICu-AgNSCs at 946.16 cm^{-1}, 986.79 $cm^{-1,}$ and 980.25 cm^{-1} respectively [362]. In addition to these, a peak at 912.31 cm^{-1} and 845.34 cm^{-1} in AgNPs, at 925.85 cm^{-1} in insulin, at 912.31 cm^{-1} and 838.57 cm^{-1} in ICuQCs and 912.31 cm^{-1} in ICu-AgNSCs shows the C-O stretching, confirming the interaction between AgNPs and ICuQCs [273]. A peak at 1113.20 cm^{-1} in insulin and 1048.23 cm^{-1} in ICu-AgNSCs shows C-N stretching [268]. Amide III stretching was observed in insulin and ICuQCs and ICu-AgNSCs at 1207.25 cm^{-1} and 1240.23 $cm^{-1,}$ respectively. NO_3 symmetric and asymmetric stretch was observed in $AgNO_3$ at 1320.86 cm^{-1}, in AgNPs at 1341.17 cm^{-1}, in insulin at 1307.31 cm^{-1}, in ICuQCs at 1347.51 cm^{-1} and at 1394.59 cm^{-1} in ICu-AgNSCs respectively [363]. C-OH stretching was observed at 1448.32 cm^{-1} in AgNPs and ICuQCs, at 1420.83 cm^{-1} in insulin, and at 1441.24 cm^{-1} in ICu-AgNSCs [227]. Amide II, C=O stretch was observed at 1535.29 cm^{-1} in insulin and at 1541.31 cm^{-1} in ICu-AgNSCs [227]. N=O stretching was observed at 1755.74 cm^{-1} in $AgNO_3$ and 1642.13 cm^{-1} in ICu-AgNSCs [363]. Nitrile stretch was marked at 2247.81 cm^{-1}, 2160.53 cm^{-1}, and 2351.64 cm^{-1} in insulin, ICuQCs, and ICu-AgNSCs, respectively [268]. A broad peak of -OH stretch was observed in all the formulations between 2760.42 cm^{-1} and 2867.03 cm^{-1} [227]. Amide B C-H stretch was observed at

2827.15 cm^{-1} and 2960.32 $cm^{-1,}$ respectively, in insulin and ICu-AgNSCs[268]. The amine N-H stretch was observed in insulin, ICuQCs, and ICu-AgNSCs at 3281.16 cm^{-1} [273]. The comparative wavenumbers of each solution are given in **Table 10**.

Table 10: The comparative wavenumber values indicated by FTIR in the range 400-4000 cm^{-1} of $CuSO_4$, $AgNO_3$, AgNPs, insulin, ICuQCs, and ICu-AgNSCs showing the position of different functional groups present, which coins the interaction amongst AgNPs and ICuQCs indicating the formation of bimetallic nanoparticles

Functional group	**$CuSO_4$**	**$AgNO_3$**	**AgNPs**	**Insulin**	**ICuQCs**	**ICu-AgNSCs**	**Ref.**
Amine NH stretch	-	-	-	3281.16	3281.16	3281.16	[273]
Amide-B -CH stretch	-	-	-	2827.15	-	2960.32	[268]
-OH stretch	2860.25	2760.42	2760.42	2760.42	2760.42	2867.03	[227]
Nitrile stretch	-	-	-	2247.81	2160.53	2351.64	[268]
N=O stretching	-	1755.74	-	-	-	1642.13	[363]
Amide II C=O stretch	-	-	-	1535.29	-	1541.31	[227]
C-OH stretch	-	-	1448.32	1420.93	1448.32	1441.24	[227]
NO_3 symmetric and asymmetric stretch	-	1320.86	1341.17	1307.31	1347.51	1394.59	[363]
Amide III stretching	-	-	-	1207.25	1207.25	1240.35	[363]
C-N stretch	-	-	-	1113.20	-	1048.23	[268]
Ag-O stretching	-	946.16	986.79	-	-	980.25	[362]
-CO stretch	-	-	912.31 845.34	925.85	912.31 838.57	912.31	[273]
NH_2 stretch	-	791.29	791.29	791.29	791.29	791.29	[268]
-Cu-OH stretch	724.96	-	-	-	718.19	718.19	[361]
C=S stretch	-	-	651.23	651.23	651.23	651.23	[268]

Similarly, Raman spectral analysis was used to study the significant conformational changes in insulin after interaction with metal ions. The S-S stretch was observed at 598.10 cm^{-1}, 584.76 $cm^{-1,}$ and 554.24 $cm^{-1,}$ respectively, in AgNPs, ICuQCs and ICu-AgNSCs [364]. The bond at 662.45 cm^{-1} is present in $AgNO_3$, AgNPs, ICuQCs, and ICu-AgNSCs, indicating a C-S-C bond [365]. The bond at 793.13 cm^{-1} in $CuSO_4$ and ICuQCs and at 794.12 cm^{-1} in ICu-AgNSCs indicates the Cu-

OH stretching [361]. The C-H out-of-plane wagging was observed at 847.81 cm^{-1} in $CuSO_4$ and insulin, at 841.74 cm^{-1} in $AgNO_3$ and ICuQCs, at 828.70 cm^{-1} in AgNPs and 849.74 cm^{-1} in ICu-AgNSCs [365]. The Ag-O stretching was observed at 947.26 cm^{-1} in AgNPs and ICu-AgNSCs and 931.12 cm^{-1} in $AgNO_3$ [362]. The C-O-C bond was observed at 986.23 cm^{-1} in insulin and ICu-AgNSCs [268]. The peaks at 995.87 cm^{-1}, 970.38 $cm^{-1,}$ and 1002.69 cm^{-1} in insulin, ICuQCs, and ICu-AgNSCs, respectively, indicate the C-C stretching [366]. C-N stretching was observed in AgNPs, insulin, ICuQCs, and ICu-AgNSCs, respectively, at 1086.86 cm^{-1}, 1071.15 cm^{-1}, 1072.34 cm^{-1} and 1097.53 cm^{-1} [367]. Amide III (α-helix) was observed at 1229.43 cm^{-1} in insulin and ICu-AgNSCs.[278] Band for Amide III random coils was observed at 1283.37 cm^{-1} in insulin, 1301.75 cm^{-1} in ICuQCs, 1311.24 $cm^{-1,}$ and 1340.28 cm^{-1} in ICu-AgNSCs [279]. The C-H bend was observed at 1364.12 cm^{-1} in ICu-AgNSCs [268]. The peak for Amide II was observed at 1442.80 cm^{-1} and 1445.50 $cm^{-1,}$ respectively, in insulin and ICu-AgNSCs [132]. The peak at 1516.32 in insulin, ICuQCs, and ICu-AgNSCs indicates the C-C stretch [268]. The peak for Amide I was observed at 1658.21 cm^{-1} in insulin and ICu-AgNSCs and at 1606.23 cm^{-1} in ICu-AgNSCs alone [132] and is shown in **Figure. 28d**. The comparative wavenumbers of each solution are mentioned in **Table 11**.

Table 11: The comparative wavenumber values indicated by Raman spectra in the range 500-1800 cm^{-1} of $CuSO_4$, $AgNO_3$, AgNPs, insulin, ICuQCs, and ICu-AgNSCs showing the position of different functional groups present, which coins the interaction amongst AgNPs and ICuQCs indicating the formation of bimetallic nanoparticles.

Functional group	**$CuSO_4$**	**$AgNO_3$**	**AgNPs**	**Insulin**	**ICuQCs**	**ICu-AgNSCs**	**Ref.**
Amide - I	-	-	-	1658.21	-	1606.23 1658.21	[132]
C-C stretch	-	-	-	1516.32	1516.32	1516.32	[268]
Amide – II	-	-	-	1442.80	-	1445.50	[132]
C-H bend	-	-	-	-	-	1364.12	[268]
Amide – III (random coils)	-	-	-	1283.37	1301.75	1311.24 1340.28	[279]
Amide III (α – helix)	-	-	-	1229.43	-	1229.43	[278]
C-N stretching	-	-	1086.86	1071.15	1072.34	1097.53	[367]
C-C stretching	-	-	-	995.87	970.38	1002.69	[366]
C-O-C	-	-	-	986.23	-	986.23	[268]
Ag-O stretching	931.12	-	947.26	-	-	947.26	[362]
C-H out of plane wagging	847.08	841.74	828.70	847.81	841.74	849.74	[365]
Cu-OH stretch	793.13	-	-	-	793.13	794.12	[361]
C-S-C stretching vibrations	-	662.45	662.45	-	662.45	662.45	[365]
S-S stretch	-	-	598.10	-	584.76	554.24	[364]

Circular Dichroism was performed using insulin protein and ICu-AgNSCs to monitor the stability of the secondary structure of protein after interaction with metal ions from silver nanoparticles and insulin copper quantum clusters. The three significant far UV signals were observed in both solutions. A positive peak was observed at ~ 194 nm (representative of β-sheet), and two negative peaks, one at ~ 208 nm and the other at ~ 217 nm, were observed (representative of α-helix), indicating the secondary structure of insulin protein [368]. Slight variations in all three peaks were observed in ICu-AgNSCs, that is, 5.57%, 3.75%, and 5.15%, respectively, and is shown in **Figure. 28e**. The % variation is much less when compared with pure insulin, confirming protein stability with no significant observable structural changes.

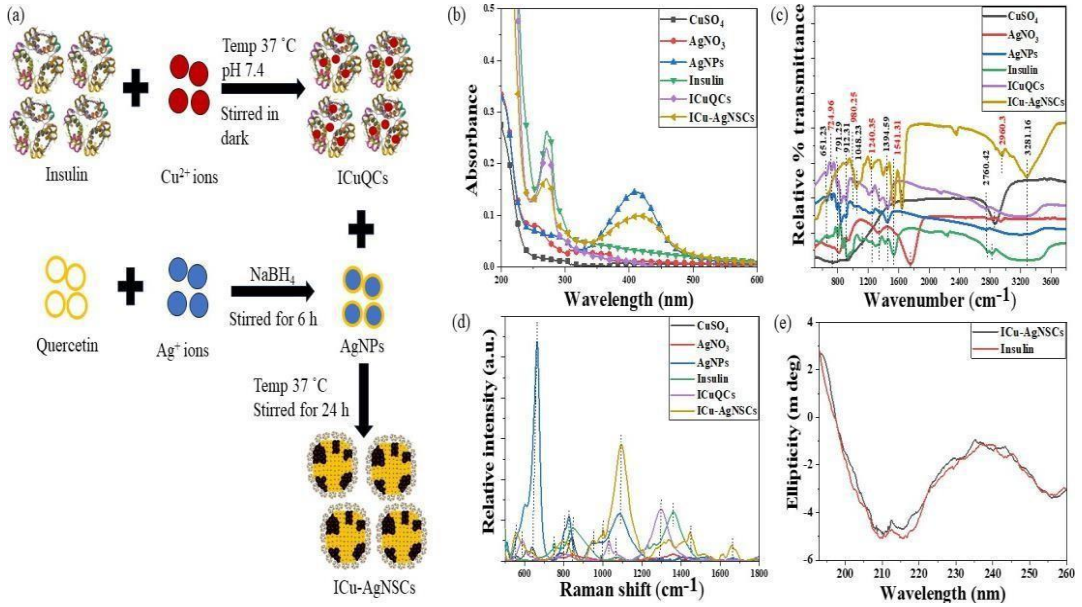

Figure. 28. Synthesis and spectroscopic studies confirming the interactions between ICuQCs and AgNPs for synthesizing ICu-AgNSCs. *(a) It shows a schematic representation of the synthesis protocol being followed for formulating bimetallic nanosubclusters. (b) UV-Visible absorption spectra showing the peak of pure insulin, ICuQCs, and ICu-AgNSCs at ~ 272 nm and peak at ~ 412 nm in AgNPs and ICu-AgNSCs confirming the interaction between the two (c) FTIR spectra of $CuSO_4$, $AgNO_3$, AgNPs, insulin, ICuQCs and ICu-AgNSCs in the range 400-4000 cm^{-1} indicating the formation of new bonds; Cu-OH stretching and Ag-O bond which were otherwise not present in pure insulin (d) Raman spectra of $CuSO_4$, $AgNO_3$, AgNPs, insulin, ICuQCs and ICu-AgNSCs indicate the involvement of different functional groups of insulin in synthesizing ICu-AgNSCs (e) Circular Dichroism confirms the stability of secondary protein structure with minimal changes even after the synthesis of ICu-AgNSCs.*

4.3.2 Structure, Composition, and stoichiometry of metal insulin nano subclusters

The hydrodynamic size of AgNPs, ICuQCs, and ICu-AgNSCs was measured and found to be 25 ± 5 nm, 35 ± 5 nm, and 40 ± 5 nm, respectively, and shown in **Figure. 29a-c** respectively.

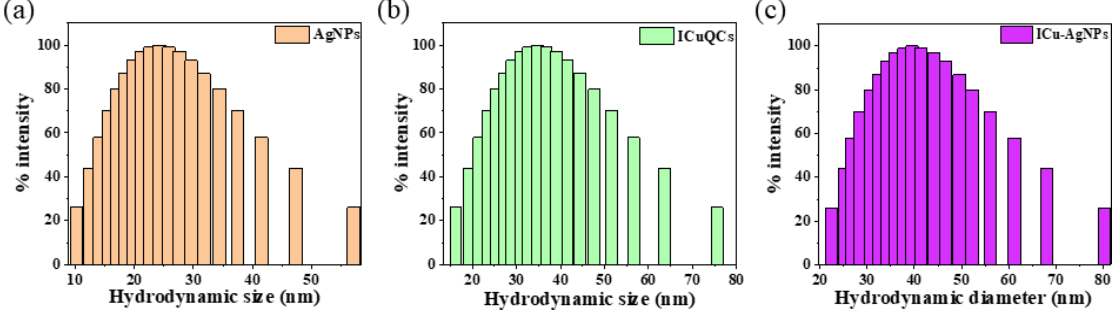

Figure. 29: The DLS spectra show the hydrodynamic size of *(a) AgNPs, (b) ICuQCs, and (c) ICu-AgNSCs, respectively.*

Further, the formation of nearly spherical bimetallic nano-subclusters (ICu-AgNSCs) having size 9.6 ± 2.2 nm and outer insulin layer (0.5 ± 0.2 nm) was confirmed by transmission electron microscopic images (at a scale of 20 and 2 nm) as shown in **Figure. 30a-b respectively,** and SAED pattern obtained is shown in **Figure. 30c**. Additionally, the lattice fringes in HRTEM were spaced apart by 0.23 nm and 0.17 nm and were indexed with Ag (111) and Cu (200) respectively. It was found that copper is mainly present in the peripheral region, and silver is inside, forming distinct phases with copper. Further, it was evident from the percentage obtained for Ag and Cu in the nanoparticles (7.63 % and 6.17%) that silver is in higher amounts, which is further confirmed from the TEM image where the electron-dense portion indicating the copper and the rest of the part is for silver having lower electron density. The energy-dispersive X-ray spectroscopy was utilized for the determination of different elements, including C, O, Cu, and Ag, in the bimetallic nano subclusters as shown in spectra given in **Figure. 30d**. The elemental mapping was done to verify the presence of both silver and copper in the synthesized bimetallic nano subclusters, and it confirms the presence of carbon (**Figure. 30e**), oxygen (**Figure. 30f**), silver (**Figure. 30g**), copper (**Figure. 30h**) and combined of all elements in **Figure. 30i**.

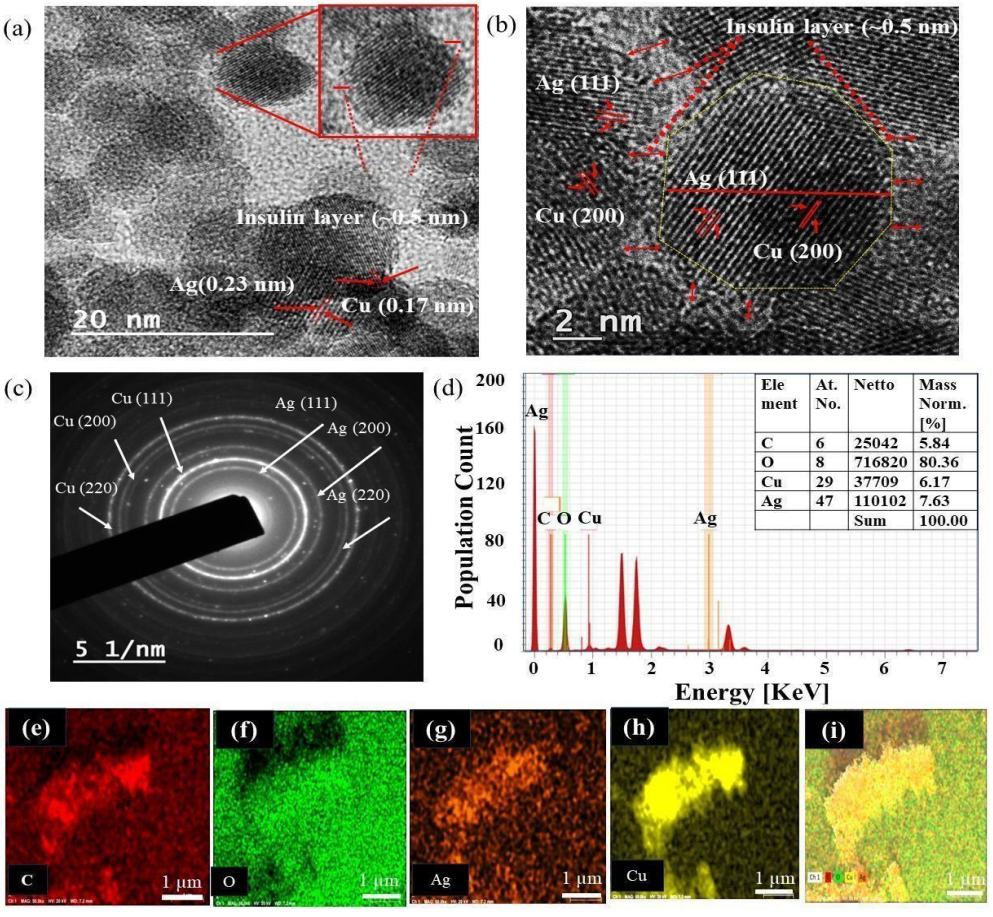

Figure. 30. Structural, morphological, and elemental characterization of ICu-AgNSCs. *TEM micrographs of ICu-AgNSCs show the nanoparticle size to be ~9.6 ± 2.2 nm at a scale of (a) 20 nm (b) 2 nm (inset shows the insulin layer of (0.5 ± 0.2 nm) around individual bimetallic cluster) (c) SAED confirms the crystalline structure of bimetallic nanosubclusters. (d) EDS spectra show the presence of both silver and copper (inset shows the relative percentage of each element). Elemental mapping showing the different elements in ICu-AgNSCs (e) Carbon (f) Oxygen (g) Silver (h) Copper (i) combined image showing all elements.*

4.3.3 Drug loading and release kinetic studies

The synthesized bimetallic nanosubclusters were studied for their drug loading and release kinetics, and the encapsulation efficiency of insulin in the bimetallic nanosubclusters was determined to be 88.54 ± 0.40 %. For the initial 8 h, burst drug release was observed, followed by sustained drug release after that, with most of the drug being released in the 40 h. Further, the percentage of drug released from ICu-AgNSCs by the end of 40 hours was found to be 93.90 ± 0.90 %, making it an efficient drug delivery system and is shown in **Figure. 31a** and the drug released per hour in mg/ml is shown in **Figure. 31b**.

4.3.4 *in vitro* cell studies

4.3.4.1 HEKa cell viability assay

Cell viability analysis was performed using HEKa cells and an MTT assay to monitor the biocompatibility of the synthesized formulations. The study was performed using salt solutions, silver nanoparticles, insulin, insulin copper quantum clusters, and bimetallic nanoformulations using four different concentrations of each (5, 10, 20, and 40 µM). The cell viability of untreated cells (control) is taken as 100, and the values for other samples are compared with that of the control. The cells treated with $CuSO_4$ exhibit the cell viability as 100.57 ± 1.77 %, 102.22 ± 3.74 %, 105.58 ± 3.81 %, and 107.05 ± 5.09 % and the cells treated with $AgNO_3$ have the cell viability as 100.85 ± 6.73 %, 102.45 ± 1.39 %, 106.37 ± 1.38 %, and 108.07 ± 4.12 % for 5, 10, 20, and 40 µM respectively. The cells treated with AgNPs have cell viability in the order 109.12 ± 6.01 %, 115.07 ± 3.93 %, 117.89 ± 1.66 %, and 119.78 ± 2.48 %. The cells after treatment with insulin show viability as 121.29 ± 3.74% for 5 µM, 124.72 ± 2.06 % for 10 µM, 128.45 ± 5.35 % for 20 µM and 132.39 ± 2.47 % for 40 µM respectively. The cells exposed to ICuQCs have higher viability than those of insulin alone and are 124.47 ± 2.78 %, 127.18 ± 1.04 %, 131.96 ± 5.11 %, and 135.18 ± 2.96 %, respectively, for 5, 10, 20, and 40 µM respectively. Cell viability after treatment with bimetallic ICu-AgNSCs showed much more significant changes, which are 133.07 ± 1.18 % for 5 µM, 150.37 ± 1.04 % for 10 µM, 163.92 ± 3.76 % for 20 µM and 169.72 ± 0.38 % for 40 µM respectively and is shown in **Figure. 31c** and comparative data is shown in **Table 12**. From the graph, it was demonstrated that none of the samples was toxic to the cells. Moreover, as the concentration of added samples increases, the cell viability increases and was found to be maximum for synthesized bimetallic ICu-AgNSCs, indicating that nano subclusters formed to promote cell division and growth and thus can be examined further through different *in vitro* and *in vivo* studies for confirming its role in wound healing.

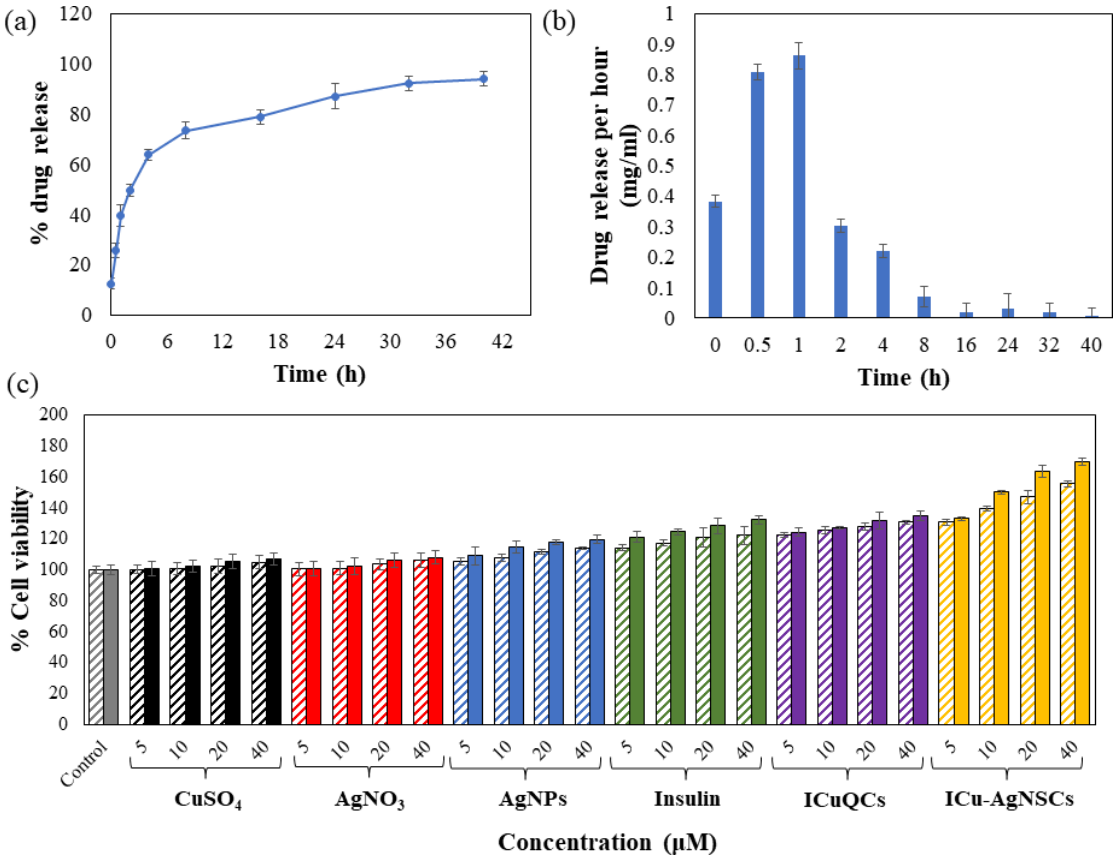

Figure. 31. Drug release kinetics and cell viability assay *(a) the plot shows the release kinetic studies to determine the % drug released from the bimetallic nanosubclusters (b) it shows the drug released per hour in mg/ml from ICu-AgNSCs (c) MTT assay to determine the effect of synthesized formulations on the cell viability to determine their potential role in cell growth and wound healing. The data were plotted as the mean value of three independent experiments, and the solid bars indicate normal conditions while the patterned bars indicate diabetic conditions in the graph.*

Table 12. The table indicates the % change in mitochondrial reductase activity in the MTT assay for finding out the cellular metabolism rate using HEKa cells after treating cells with varying concentrations of control ($CuSO_4$, $AgNO_3$, AgNPs, insulin, ICuQCs) and ICu-AgNSCs, that is, 5 µM, 10 µM, 20 µM, and 40 µM respectively, for 24 hours. The data were plotted as mean value ± SD of three independent experiments.

% Of change in mitochondrial reductase activity						
Dose	**$CuSO_4$**	**$AgNO_3$**	**AgNPs**	**Insulin**	**ICuQCs**	**ICu-AgNSCs**
5 µM	100.57 ± 1.77 %	100.85 ± 6.73 %	109.12 ± 6.01 %	121.29 ± 3.74 %	124.47 ± 2.78 %	133.07 ± 1.18 %
10 µM	102.22 ± 3.74 %	102.45 ± 1.39 %	115.07 ± 3.93 %	124.72 ± 2.06 %	127.18 ± 1.04 %	150.37 ± 1.04 %
20 µM	105.58 ± 3.81 %	106.37 ± 1.38 %	117.89 ± 1.66 %	128.45 ± 5.35 %	131.96 ± 5.11 %	163.92 ± 3.76 %
40 µM	107.05 ± 5.09 %	108.07 ± 4.12 %	119.78 ± 2.42 %	132.39 ± 2.47 %	135.18 ± 2.96 %	169.72 ± 0.38 %

4.3.4.2 HEKa cell migration assay in diabetic and normal conditions

The synthesized bimetallic nanoformulations, along with silver nitrate salt solution, copper sulfate solution, silver nanoparticles, insulin, and insulin quantum clusters, were tested for their potential role in cell migration in normal and diabetic conditions on HEKa cells by treating them with a fixed concentration of each one of them (40 µM). The bimetallic nano subclusters demonstrate excellent migration abilities in both conditions but have more migration impact in normal conditions than diabetic ones. As time passes, a significant increase in cell division eventually leads to enhanced migration rates when monitored after specific time intervals. Initially, the percentage change in scratch diameter is measured in HEKa cells taken as control (without any treatment) after 6, 12, and 24 h and is shown in **Figure. 32(a) a-c**. Following this, I have observed the changes in cells grown in diabetic conditions. The percentage change in scratch diameter of cells treated with $CuSO_4$ after 6, 12, and 24 h is 0.56 ± 0.39 %, 1.40 ± 0.46 %, and 1.30 ± 0.37 %, respectively, and is shown in **Figure. 32(a) d-f**. Similarly, the % of a gap left in cells that were treated with $AgNO_3$ comes out to be 0.28 ± 0.43 %, 0.35 ± 0.50 %, and 0.86 ± 0.44 %, respectively, after fixed intervals (**Figure. 32(a) g-i**). The % change in migration after 6, 12, and 24 h in AgNPs and Insulin is even higher and came out to be 25.30 ± 1.35 %, 45.18 ± 0.63 %, and 46.29 ± 0.43 % in AgNPs (**Figure. 32(a) j-l**) and 39.81 ± 0.37 %, 50.87 ± 0.18 %, and 52.17 ± 0.51 % in cells incubated with insulin (**Figure. 32(a) m-o**). In cells after treatment with ICuQCs, the value of % change in scratch is 44.75 ± 0.25 %, 56.14 ± 0.35 %, and 58.69 ± 0.35 %, respectively (**Figure. 32(a) p-r**). The maximum change in scratch diameter as compared with control is observed in cells treated with the synthesized bimetallic formulations, where the value comes to be 65.52 ± 0.51 %, 72.28 ± 0.01 %, and 75.21 ± 0.44 % after 6, 12, and 24 h (**Figure. 32(a) s-u**). A comparative study of variation in scratch diameter of the diabetic cells after treating the cells with all samples is shown graphically in **Figure. 32(a) v**.

The exact concentration and time intervals were followed to monitor the scratch diameter variation under normal conditions. The percentage variation in scratch diameter in control cells is shown in (**Figure. 32(b) a-c**). The % change in scratch diameter after treatment with $CuSO_4$ is 1.54 ± 0.46 %, 2.59 ± 0.46 %, and 1.38 ± 0.44 % **Figure. 32(b) d-f** and after treatment with $AgNO_3$ is 1.85 ± 0.32 %, 2.22 ± 0.49 %, and 1.85 ± 0.55 % respectively (**Figure. 32(b) g-i**). In the cells treated with AgNPs, insulin, and ICuQCs, the % variation in migration with time is more as compared to the salt solutions alone and is equal to 29.91 ± 0.44 %, 49.47 ± 0.64 %, and 51.73 ± 0.42 % in AgNPs (**Figure. 32(b) j-l**), 43.87 ± 0.35 %, 52.59 ± 0.14 % and 54.62 ± 0.50 % in insulin alone (**Figure. 32(b) m-o**) and 48.43 ± 0.37 %, 57.40 ± 0.25 % and 58.33 ± 0.21 % in ICuQCs (**Figure. 32(b) p-r**). The bimetallic nanosubclusters exhibit the maximum % change in scratch diameter, which is 66.04 ± 0.61 %, 76.66 ± 0.31 %, and 79.62 ± 0.31 %, respectively, indicating the enormous potential of prepared nanosubclusters in the enhanced cell migration in normal conditions (**Figure. 32(b) s-u**). The graph in **Figure. 32(b) v** shows the variation in normal scratch diameter as a comparative study of all the formulations after particular time intervals. A comparative data table of change in cell migration in normal and diabetic cells is shown in **Table 13**. To find the statistical significance of data, p values were calculated for scratch assay in diabetic and normal conditions, and the comparative data is shown in **Table 14**.

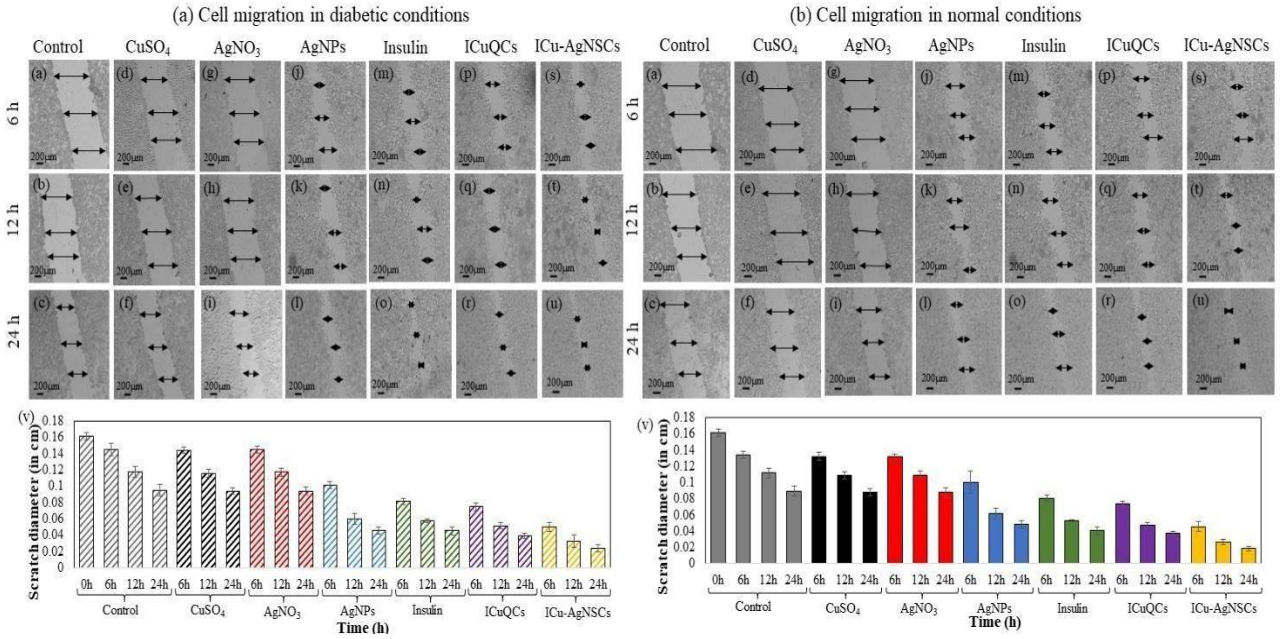

Figure. 32. Promotion and monitoring of in vitro cell migration in the diabetic and normal cells using ICu-AgNSCs. *The bimetallic nano subclusters induced better cell migration in HEKa cells compared to salt solutions, insulin, AgNPS, and ICuQCs. The cells were treated using a fixed concentration of all the solutions, that is, 40 µM. HEKa cells were taken as control (without any added formulations). (a) The figure shows cell migration in diabetic conditions using HEKa cells without any treatment (a) 6 h, (b) 12 h, (c) 24 h; the cells treated with the salt solution of copper sulfate after (d) 6 h (e) 12 h (f) 24 h; the HEKa cells after treatment with silver nitrate (g) 6 h (h) 12 h (i) 24 h; the cells after treating them with silver nanoparticles (j) 6 h (k) 12 h (l) 24 h; cells after treatment with insulin after a duration of (m) 6 h (n) 12 h (o) 24 h respectively; cells treated with ICuQCs after (p) 6 h (q) 12 h (r) 24 h and cells after treatment with ICu-AgNSCs after (s) 6 h (t) 12 h (u) 24 h. (v) The plot shows the relative change in cell migration in diabetic conditions after treatment with all the solutions respectively after specific time intervals. (b) The figure shows cell migration in normal conditions using HEKa cells without any treatment (a) 6 h, (b) 12 h, (c) 24 h; the cells treated with the salt solution of copper sulfate after (d) 6 h (e) 12 h (f) 24 h; the HEKa cells after treatment with silver nitrate (g) 6 h (h) 12 h (i) 24 h; the cells after treating them with silver nitrate are shown in figure (j) 6 h (k) 12 h (l) 24 h; cells after treatment with insulin after a duration of (m) 6 h (n) 12 h (o) 24 h respectively; cells treated with ICuQCs after (p) 6 h (q) 12 h (r) 24 h and cells after treatment with ICu-AgNSCs after (s) 6 h (t) 12 h (u) 24 h. (v) The plot shows the relative change in cell migration in normal conditions after treatment with all the solutions respectively after specific time intervals.*

Table 13. It shows the comparative data of variation in scratch width in diabetic and normal conditions after treatment with 40 µM of $CuSO_4$, $AgNO_3$, AgNPs, insulin, ICuQCs, and ICu-AgNSCs. The data was measured after a time duration of 6, 12, and 24 h.

% Change in diabetic scratch width with time						
Time	**$CuSO_4$**	**$AgNO_3$**	**AgNPs**	**Insulin**	**ICuQCs**	**ICu-AgNSCs**
6 h	0.56 ± 0.39 %	0.28 ± 0.43 %	25.30 ± 1.35 %	39.81 ± 0.37 %	44.75 ± 0.25 %	65.52 ± 0.51 %
12 h	1.40 ± 0.46 %	0.35 ± 0.50 %	45.18 ± 0.63 %	50.87 ± 0.18 %	56.14 ± 0.35 %	72.28 ± 0.01 %
24 h	1.30 ± 0.37 %	0.86 ± 0.44 %	46.29 ± 0.43 %	52.17 ± 0.51 %	58.69 ± 0.35 %	75.21 ± 0.44 %
% Change in normal scratch width with time						
Time	**$CuSO_4$**	**$AgNO_3$**	**AgNPs**	**Insulin**	**ICuQCs**	**ICu-AgNSCs**
6 h	1.54 ± 0.46 %	1.85 ± 0.32 %	29.91 ± 0.44 %	43.87 ± 0.35 %	48.43 ± 0.37 %	66.04 ± 0.61 %
12 h	2.59 ± 0.46 %	2.22 ± 0.49 %	49.47 ± 0.64 %	52.59 ± 0.14 %	57.40 ± 0.25 %	76.66 ± 0.31 %
24 h	1.38 ± 0.44 %	1.85 ± 0.55 %	51.73 ± 0.42 %	54.62 ± 0.50 %	58.33 ± 0.21 %	79.62 ± 0.31 %

Table 14: It shows the p values determined for % variation in scratch width in diabetic and normal conditions after treatment 40 µM of $CuSO_4$, $AgNO_3$, AgNPs, insulin, ICuQCs, and ICu- AgNSCs. The statistical significance of data is considered when $p < 0.05$.

P value for diabetic wound						
Time	**$CuSO_4$**	**$AgNO_3$**	**AgNPs**	**Insulin**	**ICuQCs**	**ICu-AgNSCs**
6 h	0.874856	0.938437	0.001017	0.000198	0.000177	5.58E-05
12 h	0.731361	0.932761	0.000351	8.89E-05	8.92E-05	2.21E-05
24 h	0.803987	0.873529	0.00052	0.000624	0.00027	0.000126
P value for normal wound						
Time	**$CuSO_4$**	**$AgNO_3$**	**AgNPs**	**Insulin**	**ICuQCs**	**ICu-AgNSCs**
6 h	0.610239	0.481817	0.014853	9.19E-05	3.61E-05	1.16E-05
12 h	0.554408	0.617227	0.0006	8.97E-05	7.86E-05	0.000219
24 h	0.774738	0.731361	0.000499	0.000331	0.000101	3.89E-05

4.3.4.3 Antioxidant activity against H_2O_2 induced cytotoxicity

H_2O_2, when present in biological samples or cells, is widely responsible for its cytotoxic effect. As per previous studies, the H_2O_2 is toxic to the cells (HEKa) at a concentration of 400 µM or higher and decreases the cell viability with increasing concentration. The same effect was observed in this study. When treated only with H_2O_2 with a concentration of 400 µM or higher, cell viability was decreased due to the cytotoxic nature of H_2O_2 responsible for the free radical generation is shown in **Figure. 33a**. Alternatively, when the cells initially treated with 1000 µM H_2O_2 were incubated with varying concentrations (5, 10, 20, 40 µM) of synthesized bimetallic formulations, an antioxidant effect was observed because of the scavenging of H_2O_2-induced reactive oxygen species

responsible for cell death and is shown in **Figure. 33b**. The ICu-AgNSCs increase the scavenging of ROS and the % scavenging goes on increasing with increase in the concentration of ICu-AgNSCs, making them potent H_2O_2 scavengers essential for promoting the antioxidant activity of nano subclusters. The % ROS scavenging after treatment with 5, 10, 20, 40 µM of ICu-AgNSCs is 6.76 ± 1.98%, 14.85 ± 1.40%, 21.72 ± 3.56 %, and 28.37 ± 1.31% respectively.

4.3.4.4 Intracellular ROS measurement

Flow cytometry was performed to examine the ROS scavenging activity of synthesized nanoformulations. Briefly, the non-fluorescent DCFDA dye exhibits green fluorescence when it comes in contact with ROS-generating species and is determined by measuring the fluorescence at 572 nm using flow cytometry. To begin with, the analysis was performed on control cells and cells containing only DCFDA dye. After that, the ROS scavenging activity of bimetallic nanosubclusters was determined, for which initially, the fluorescence was measured for the cells treated with varying concentrations of H_2O_2, followed by the cells treated with bimetallic nanosubclusters. The results show prominent scavenging of H_2O_2-induced ROS in the presence of ICu-AgNSCs. The percentage variation in fluorescence is measured with respect to DCFDA control cells. The percentage enhancement in ROS after treatment with 4000, 1000, and 200 µM of H_2O_2 is found to be 22.81%, 38.56%, and 47.05%, respectively. The cells, after treatment with ICu-AgNSCs (40 µM), showed a sharp decline in the fluorescence intensity, which is 28.40% and 21.78 %, respectively, for 1000 and 4000 µM of H_2O_2, which is in relevance to the ROS scavenging data obtained in the previous section and a higher decrease was monitored in cells treated with lowest concentration of H_2O_2 that is 200 µM of which is even 1.76% less than DCFDA control itself which shows the strong ROS scavenging potential of synthesized formulations which is very beneficial to promote the wound healing by overcoming the ROS as demonstrated in **Figure. 33c**.

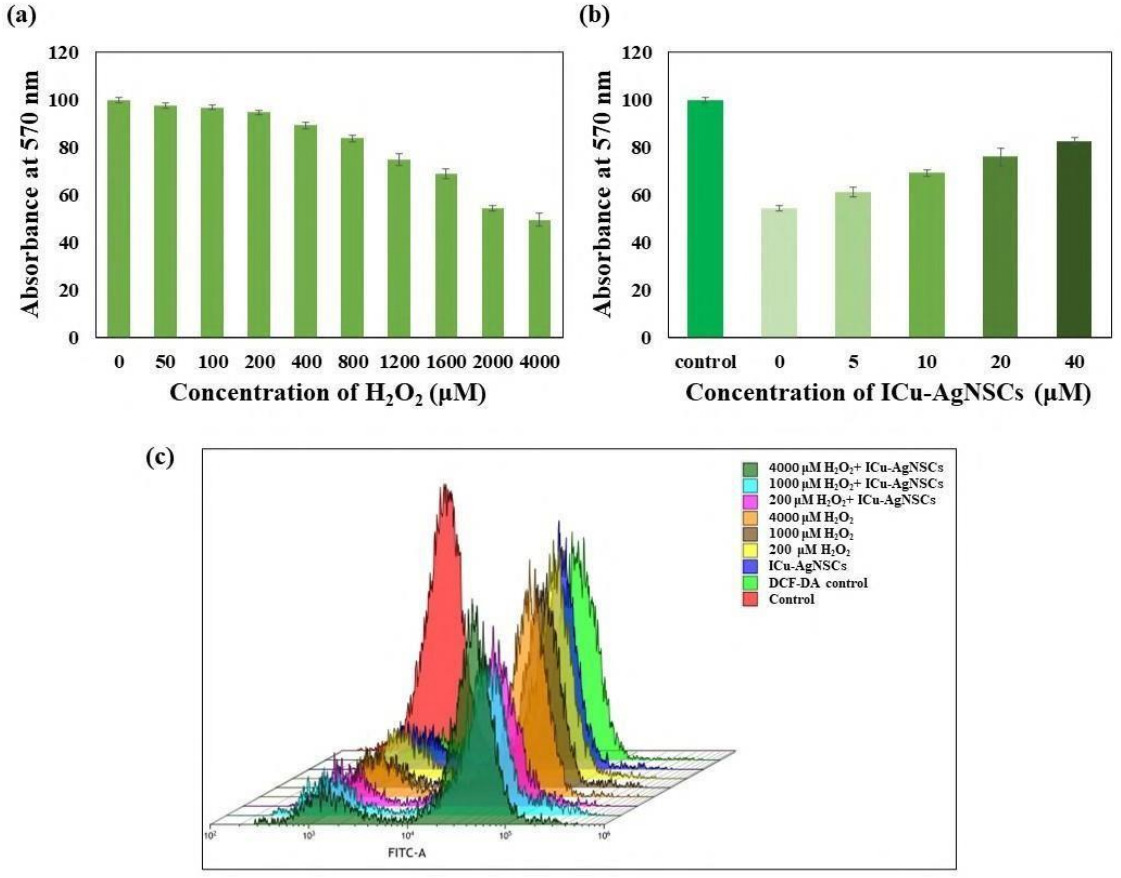

Figure. 33. Reactive Oxygen Species scavenging potential of ICu-AgNSCs *(a) Effect of varying concentrations of H_2O_2 mediated ROS on the cell viability of HEKa cells (b) ROS scavenging effect of varying concentrations of ICu-AgNSCs against H_2O_2 mediated ROS. Fluorescence microscopy*

to monitor the intracellular ROS scavenging by ICu-AgNSCs in HEKa cells (c) It indicates the flow cytometry analysis of ROS scavenging due to varying concentrations of bimetallic nanosubclusters.

4.3.5 Antibacterial effect on Gram-positive and Gram-negative strains

The antibacterial testing was done using the broth dilution method, and the MIC and IC_{50} values against each bacteria were calculated. The MIC values for both Gram-negative bacteria, *Escherichia coli*, and *Acinetobacter calcoaceticus* are 16 µM and are shown in **Figure. 34a-b**, and for Gram-positive bacteria, including *Bacillus subtilis* and *Staphylococcus aureus* the MIC value is 64 µM which is shown in **Figure. 34c-d**. The possible reason behind this is due to the easy influx of small nanoparticles through the cell wall of Gram-negative bacteria, which is comprised of a unique outer membrane alongside a single peptidoglycan layer in comparison with the Gram-positive bacteria having multiple peptidoglycan layers, which makes the entry of nanoparticles difficult into the bacterial membrane. The IC_{50} values for *E. coli, A. calcoaceticus, B. subtilis, and S. aureus* are 5.11 ± 1.52 µM, 4.85 ± 0.43 µM, 5.153 ± 1.25 µM, and 4.91 ± 1.75 µM respectively indicating the influential role of nanosubclusters in the antibacterial activity and is shown in **Figure. 34e-f**.

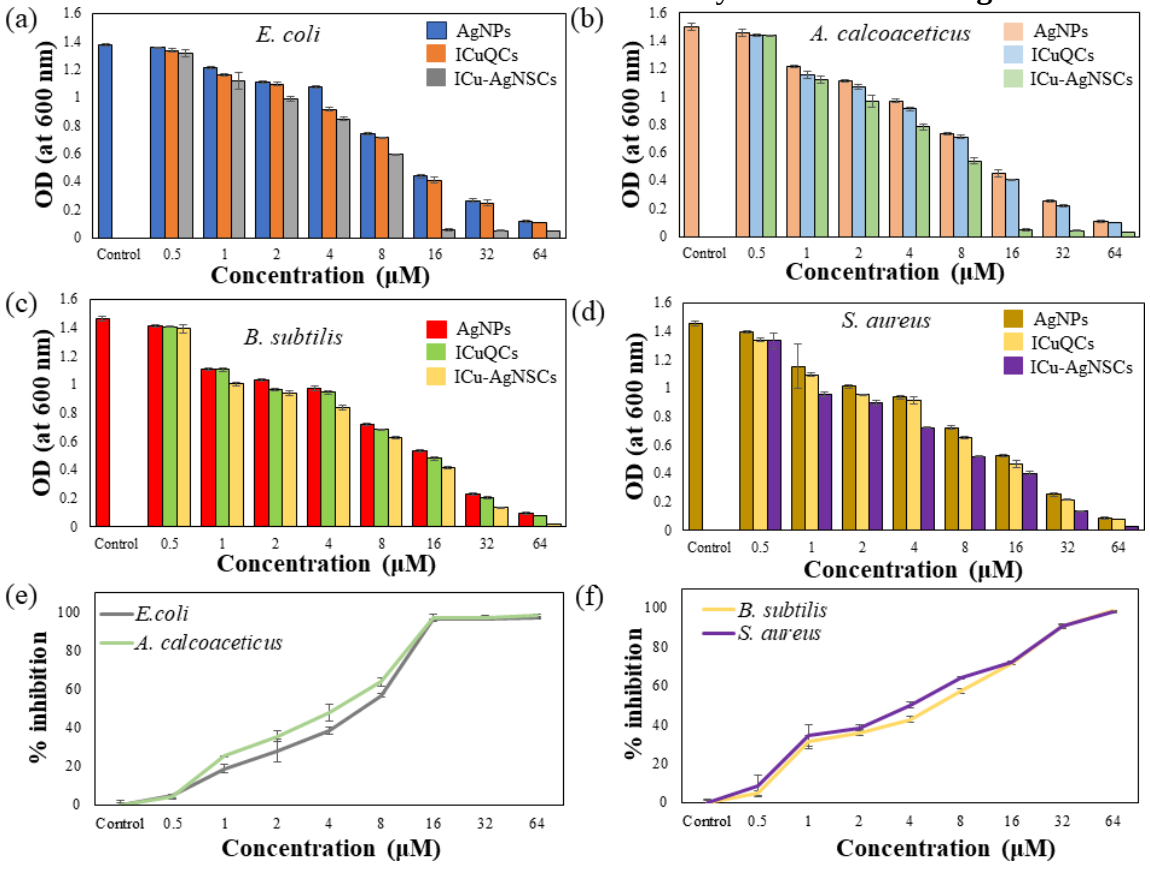

Figure. 34. Monitoring the antibacterial potential against Gram-negative and Gram-positive bacteria by incubating with AgNPs, ICuQCs, and ICu-AgNSCs. *(a) E. coli (b) A. calcoaceticus (c) B. subtilis (d) S. aureus (e) % bacterial inhibition against Gram-negative E. coli and A. calcoaceticus using ICu-AgNSCs (f) % bacterial inhibition against Gram-positive B. subtilis and S. aureus using ICu-AgNSCs.*

4.3.6 Combination index of silver nanoparticles and insulin copper quantum clusters

To calculate CI, Dm was determined using m and y from **Figure. 35a** for AgNPs and **Figure. 35b** for ICuQCs. The calculated CI values for AgNPs and ICuQCs indicate a synergistic effect between the two as the calculated values by varying the concentrations of two are found to be less than one, which confirms that the two formulations promote each other's activity when combined. These results are in accordance with the ones obtained from MTT assay for cell viability and scratch assay

for cell migration studies, indicating their potential role in wound healing applications. The data is shown in **Table 15**.

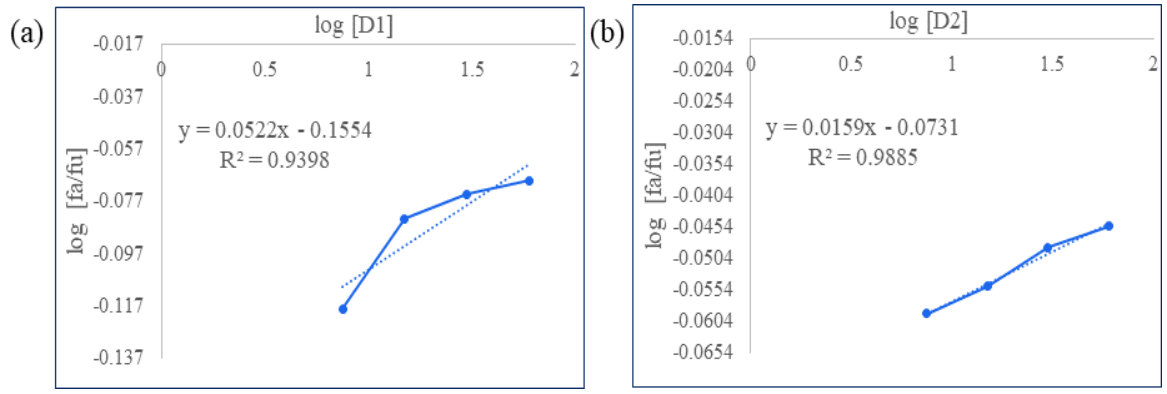

Figure. 35. Median plots of (A) AgNPs and (B) ICuQCs *for determining the y-intercept and m values to calculate Dm to calculate the combination index of AgNPs and ICuQCs.*

Table 15. The CI values for the cell viability for varying amounts of cobalt salt with insulin protein were calculated to monitor the combined effect of two, and the value is observed to be less than 1, indicating the synergism of drugs.

Combination Index (CI)			
The concentration of AgNPs and ICuQCs	**(Dx)1 (AgNPs) = Dm [fa/fu]$^{1/m}$**	**(Dx)2 (ICuQCs) = Dm [fa/fu]$^{1/m}$**	**CI = (D)1/(Dx)1 + (D)2/(Dx)2**
7.5 µg/ml	26610.47166	868.8462276	0.008913981
15 µg/ml	1411.979766	668.4709171	0.033062653
30 µg/ml	707.4789328	469.4895702	0.106303273
60 µg/ml	498.5425244	390.9564944	0.273820578

4.4 Conclusion

Maintaining an efficient microenvironment across the wound site is critical to avoid microbial contamination and eliminate all possible complications that can hinder wound recovery, thus lowering healthcare costs and increasing life quality. Effective wound healing agents that are biocompatible, target-specific, and have a high drug delivery rate are always required. I have synthesized the bimetallic nano subclusters by combining the silver nanoparticles and insulin copper quantum clusters to study their potential role in accelerating cell migration in normal and diabetic conditions, antioxidant role, and antimicrobial activity. Insulin is widely known for its role in promoting cellular growth by decreasing the blood glucose level, exhibiting the antioxidant effect, and modulating the inflammatory responses by replacing the proinflammatory cytokines with the anti-inflammatory cytokines. Silver and copper have been explored for decades for their antimicrobial potential, which is essential for faster and contamination-free wound healing. Insulin and quercetin possess anti-inflammatory and antioxidant potentials. Depending upon these features, the formulations were synthesized and checked for synergistic effects in normal and diabetic conditions.

The synthesized nanosubclusters are the first of their kind, having two distinct metal ions embedded in protein corona and exhibited a desirable HRTEM size of about 9.6 ± 2.2 nm and demonstrated notable encapsulation efficiency and drug release profile. By efficiently conjugating the insulin copper quantum clusters and silver nanoparticles, the targeted delivery was obtained due to the

enormous presence of insulin receptors across the human cells, which gives them an upper hand over general formulations. The FTIR and Raman spectra show the intermolecular interactions between metal ions and insulin and exhibit minimal structural variations in the amide regions of the protein. Also, the stability of the protein secondary structure was maintained throughout the synthesis, which is confirmed by CD spectroscopy. The MTT assay and the combination index performed on the silver nanoparticles and insulin copper quantum clusters emphasized the significant synergistic effect between the two, eventually resulting in better cell migration abilities with antioxidant and antibacterial potential in synthesized subclusters. Furthermore, the synthesized bimetallic nanosubclusters exhibited accelerated cell migration properties in normal and diabetic conditions, even at very low concentrations. Apart from this, the subclusters possess antioxidant and antibacterial properties, which are essential for promoting microbial infection-free wound recovery.

Thus, the remarkable cell migration potential, antibacterial activity, and antioxidant properties of these novel bimetallic nanosubclusters have enormous potential to be used further in biomedical applications and exploration for *in vivo* applications. Hopefully, the outcomes of this article will promote enormous research in the development of bimetallic nanosubclusters, which have enormous potential in normal and diabetic wound healing and can be further explored for *in vivo*, pre-clinical, and clinical studies.

Chapter 5: Chitosan-insulin nano-formulations as critical modulators of inflammatory cytokines and Nrf-2 pathway to accelerate burn wound healing

Abstract

Burn injuries are characterized by prolonged inflammatory phases, neurovascular damage, and hypermetabolism, eventually causing improper tissue regeneration. Insulin has gained considerable attention in normal and diabetic wound healing, yet its role in burn wounds remains poorly understood. In this study, insulin-chitosan nano-formulations (ICNP) were synthesized using a simple and robust mechanism and characterized to monitor specific interactions between insulin and chitosan, and the particles measuring approximately 30 nm in size exhibited mild alterations in the amide I, II, and III bonds of the insulin protein along with impressive insulin loading efficiency of 88.725 ± 0.295% under physiological conditions, and significantly improved burn wound healing *in vitro* (HEKa cells) and *in vivo* (murine third-degree burn model). The underlying mechanism behind superior wound closure and tissue remodeling was attributed to significant early phase reduction of pro-inflammatory cytokine IL-6 levels in ICNP-treated mice, while anti-inflammatory cytokine IL-10 levels became markedly elevated, resulting in enhanced re-epithelialization and collagen deposition. Furthermore, treatment of ICNP was associated with unregulated expression of Nrf-2, a key regulator of oxidative stress and inflammation, indicating their molecular crosstalk. These findings highlight the potential of ICNP as a promising therapeutic formulation for burn wound healing, promoting wound closure by modulating inflammatory phases, making it a valuable candidate for further clinical development in burn care (**Figure. 36**).

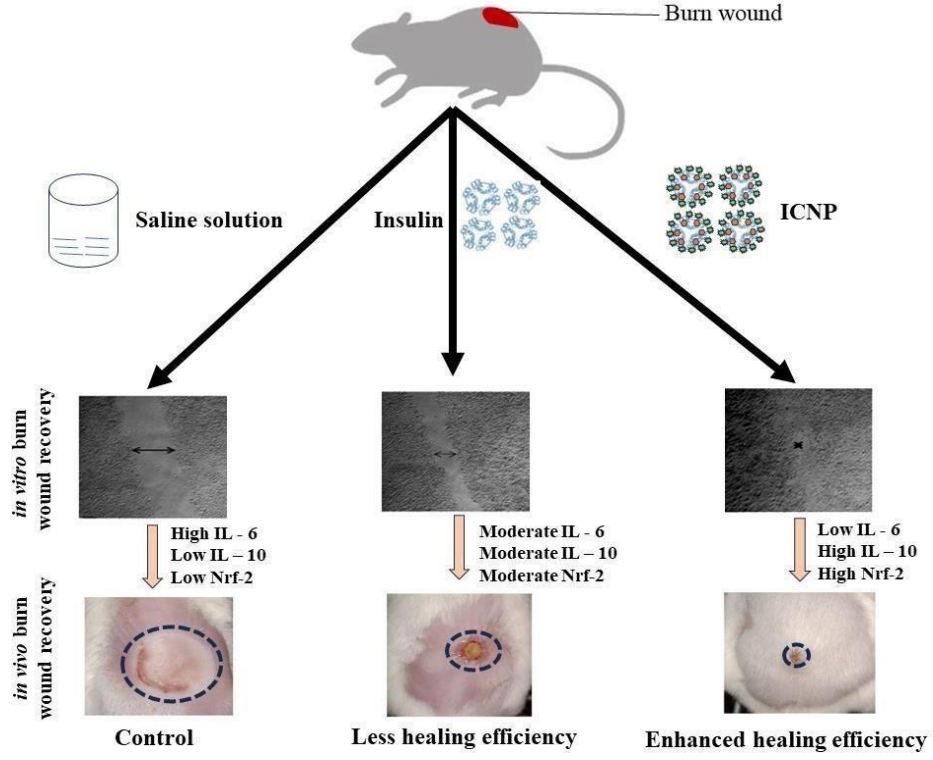

Figure. 36. The graphical abstract depicts the *simple and robust synthesis of empty and insulin-loaded chitosan nanoparticles for their potent application as burn wound healing agents. The wound healing efficiency of these particles was tested on both in vitro and in vivo models. The*

outcome depicts the much higher efficiency of insulin-loaded chitosan nanoparticles compared to empty chitosan nanoparticles.

5.1 *Introduction*

Wound healing involves sequential phases, including inflammation, proliferation, and remodeling, to maintain tissue integrity [369],[370]. The expenditure being spent on healing acute and chronic wounds ranges from $28.1 to $96.8 billion, with surgical wounds and diabetic ulcers incurring the highest expenses [331]. Burn injuries are particularly debilitating and painful, leading to increased morbidity and mortality rates. As per the World Health Organization (WHO), burn injuries cause 180,000 deaths annually, with approximately 11 million people requiring medical assistance globally, as per the report of 2018. The number of patients affected in India was around 1 million, whereas in the USA, the number is nearly half a million [371]. Thermal burns, which can result from dry (fire/flame) or wet (scald) sources, account for approximately 80% of all burns and are classified based on wound depth [372]. When a thermal injury covers over 20% of the body's surface area, it is called a burn shock [373].

Burn injuries are divided into three distinct categories: First-degree (damaged epidermis), Second-degree (damaged epidermis and part of dermis), and Third-degree (damage extended up to hypodermis) based on the severity of the injury [374]. Third-degree burns, histologically distinct from superficial burns, are characterized by destruction of the epidermis, dermis, and part of hypodermis, coagulative necrosis, absence of epidermal regeneration, and pronounced inflammatory response. These burns necessitate surgical intervention, such as skin grafts, due to their inability to self-regenerate. Histological analysis may reveal granulation tissue formation in later stages, often leading to hypertrophic or keloid scarring. Wound healing involves a balance between pro-inflammatory and anti-inflammatory pathways, but burn injuries disrupt this process [49]. Burn injuries are distinct from other wounds in some respects, such as the degree of systemic inflammation [375], electrolyte and fluid loss, compromised or necrotized wound edges, and tendency towards shock or coma [376]. They are characterized by enhanced capillary permeableness, greater systemic vascular resistance, reduced cardiac output, increased hydrostatic pressure across microvasculature, and movement of proteins and fluids to the interstitial space from intravascular space [377]. The altered immune system increases the susceptibility to infection, eventually leading to sepsis and thus aggravating systemic inflammation [378]. Microbial infection arising from multi-drug resistant bacteria and fungi is becoming the primary cause of mortality in patients with burn wounds [379],[42]. Further, the extent and depth of the burn are directly proportional to the extent of hypermetabolism and inflammation, which are responsible for impaired wound healing by delaying re-epithelialization [380],[381]. These changes in the pathophysiology have a more significant impact on the pharmacodynamics and pharmacokinetics of the drugs used for healing burn wounds. The major challenge before the researchers is burn management due to its slow healing rate, pain, higher infection susceptibility, and hypertrophic scarring [382]. Clinical practices, including skin grafting, skin substitutes, wound dressings, and negative pressure wound therapy, are being explored for burn healing. Apart from them, various other treatments are under consideration for the treatment of burn pain (Ketamine, sedatives, anxiolytics, pruritus, and neuropathic drugs) and scar management (mesenchymal stem cells and adipose-derived stem cells) along with pharmacological approaches (silicone, corticosteroids, transforming growth factor-β modulators) and surgical approaches (fat grafting, laser therapy for scars, ablative and non-ablative fractional lasers) [383],[384],[385],[386]. Although these methods have huge potential, they have limited usefulness as they primarily focus on promoting the closure of wounds rather than addressing the underlying pathophysiology [384]. Limitations include delayed healing, low mechanical strength, and reduced aeration [49]. These factors lead to prolonged recovery, increased recurrence rates, treatment failure, amputations, and higher costs for patients [384],[387],[388],[389].

Keratinocytes play a crucial role by immediately reaching the wound site and starting their healing function, which further leads to alterations in gene expression profiles. They stimulate the growth of myofibroblast-like cells responsible for wound contraction and also secrete signaling molecules that act either in an autocrine or paracrine manner, causing the pleiotropic effect on various cell types, which in turn promote the activation of keratinocytes during wound closure by secreting signaling molecules [390],[391].

Achieving a balance between pro-inflammatory and anti-inflammatory cytokines is crucial for effective burn wound healing. Pro-inflammatory cytokines, such as tumor necrosis factor-alpha (TNF-α), interleukin-1 beta (IL-1β), and interleukin-6 (IL-6), are released in burn wounds, leading to tissue damage and delayed healing. Anti-inflammatory signaling pathways, like the Nrf-2 (Nuclear factor erythroid 2-related factor 2) pathway, counteract inflammation and promote tissue repair by increasing anti-inflammatory cytokines, like interleukin-10 (IL-10) that help to resolve inflammation and promote tissue repair [392],[393]. Nrf-2 is a cytosolic transcription factor that has enormous potential in cellular defense by activating antioxidant and detoxifying enzymes [394], [395]. It helps prevent excessive reactive oxygen species (ROS) production in inflamed and wounded tissues, suppressing chronic inflammation. Nrf-2 expression is significant in keratinocytes and macrophages, promoting matrix and granulation tissue formation [396],[397]. It also activates the production of TGF-β (Transforming Growth Factor- beta) and protects cells from ROS-induced damage. The Nrf-2 antioxidant pathway is vital for cellular protection against inflammation and environmental stressors [398]. Bone marrow mesenchymal stem cells are found to promote burn wound healing by activating the Akt/mTOR (protein kinase B/ mammalian Target of Rapamycin) pathway [399].

Recently, proteins and growth factors, including insulin, have become common and effective therapeutic choices for tissue regeneration and wound healing [400]. Insulin regulates various cytokines, growth factors, and hormones through selective mechanisms. It reduces inflammation by inactivating NF-kβp50/p65 (Nuclear factor kappa-light-chain- enhancer of activated B cells) and TNFα-mediated inflammatory pathways [400]. Insulin modulates protein synthesis, promoting cell growth and differentiation and enhancing cell survival by inhibiting proteolysis via FOXO (Forkhead Box O) inactivation [49]. Additionally, insulin stimulates the secretion of anti-inflammatory cytokines and reduces the secretion of pro-inflammatory cytokines, thereby modulating wound inflammation [314]. Nanoparticle-based insulin delivery has shown enhanced selectivity, sensitivity, and effectiveness compared to free insulin [401],[402],[132]. These nanocarriers improve the therapeutic potential of the drug manifold by acting as site-specific delivery agents due to their functionalization with specific moieties, which add to their efficacy [403],[404],[338]. This caused the development of various insulin-based and other antidiabetic protein-based drugs that either improve insulin sensitivity or stimulate increased insulin secretion from the pancreas to treat wounds under normal or diabetic conditions [227],[405],[232],[340]. Insulin-loaded Poly-DL-lactide/glycolide nanoparticles were developed for topical delivery of insulin to treat skin burn wounds by regeneration of skin [406]. Other proteins like silk fibroin are found to be effective against burn wounds when delivered in combination with gelsevirine as a multilayer dressing [407].

Nanotherapeutics involving metals and polymers has enormous potential in treating burn wounds [408]. Different naturally occurring biopolymers have emerged as potent agents for controlled drug delivery. One such biodegradable polymer is chitosan [409]. Chitosan is a cationic heteropolymer derived from chitin, that is commonly obtained from exoskeleton of shrimp, fungi, and yeasts [410]. In wound healing, chitosan plays a crucial role by providing a matrix for three-dimensional tissue growth, stimulating tissue organization and cell proliferation. It also activates macrophages and enhances their tumoricidal activity. Additionally, chitosan assists in natural blood clotting and reduces pain at the wound site by blocking nerve endings [411]. It promotes hemostasis,

keratinocyte proliferation, and improved adhesion. Furthermore, chitosan can be easily modified to be efficiently degraded by body enzymes, making it a promising candidate for burn wounds [412], [413],[414]. Chitosan nanoparticles are found to be preventive against collagen-induced severe arthritis in Wistar rats when loaded with zinc gluconate [415]. The hydrogel films were developed using carboxy methyl chitosan and hydroxyethyl cellulose for potent fibroblast growth factor-2 (FGF-2) delivery to the dermal tissue injury site [416]. Similarly, chitosan/alginate nanoparticles were used to heal burn wounds by delivering Esculentoside A at the burn site [417]. The present study aims to synthesize insulin-loaded chitosan nano-formulations and investigate human insulin's structural and functional changes after interaction with chitosan under various physiological conditions. The effectiveness and efficiency of these formulations will be evaluated using in vitro and in vivo models in terms of tissue healing activity, with a focus on mechanistic aspects.

5.2 Materials and Methods

5.2.1 Materials

The required materials were sourced as follows: sodium triphosphate, chitosan, NaOH, and HCl were ordered from Loba Chemie, India, while recombinant human insulin was procured from Elli Lilly, India. DMEM (Dulbecco's Modified Eagle Medium) cell culture media, Fetal Bovine Serum (FBS), and penicillin-streptomycin were acquired from HiMedia, India. Other chemicals used in the study were of research grade and obtained from HiMedia.

5.2.2 Synthesis of ECNP and ICNP nanoparticles

The formation of TPP (Tripolyphosphate) mediated ECNP (empty chitosan-TPP nanoparticles) and ICNP (insulin-loaded chitosan-TPP nanoparticles) nanoparticles was achieved through a straightforward procedure. Initially, chitosan (10 mg) was dissolved in double distilled water, and the pH was maintained at 6 by adding the acetic acid solution to facilitate the proper dissolution of chitosan. A solution of TPP previously suspended in 4 ml deionized water was prepared separately and kept at stirring for 10 min at 37 ˚C. This TPP solution was later on added drop by drop to the chitosan solution, followed by stirring the final sample at 37 ˚C for one h. The resulting solution was labeled as ECNP (empty chitosan-TPP nanoparticles) nanoparticles. To synthesize ICNP (insulin-loaded chitosan-TPP nanoparticles) nanoparticles, the TPP solution described above was mixed with 40 µl of insulin and stirred for 10 min at low rpm and room temperature. Subsequently, dropwise addition of this solution was done to the chitosan solution and kept on stirring for an hour at room temperature. Different solutions were prepared by adjusting the pH of the chitosan solution to obtain solutions with pH values of 6, 7.4, 8, and 9. **(Figure. 37a)**.

5.2.3 Particle size and morphological analysis

I have performed DLS to find out the average hydrodynamic size of ECNP and ICNP using a Malvern DLS-Zeta size analyzer. Also, the zeta potential was measured to check out the stability of the formed samples using the same instrument. After that, FE-SEM (Field Emission-Scanning Electron Microscopy) analysis was done to determine the ICNP’s morphology. For this, the samples were centrifuged at 240 rpm for nearly 10-15 min, and thoroughly washed to remove unbound salt or impurities associated with the sample.

5.2.4 FTIR Analysis

To identify the functional group alterations in chitosan, TPP, ECNP, insulin, and ICNP, an Agilent Cary 600 series FTIR (Fourier-Transform Infrared Spectroscopy) Spectrophotometer was employed. Before analysis, the samples were washed to eliminate impurities and were subsequently dried at 37 ˚C. Next, the dried samples were mixed withKBr to create pellets, which were then subjected to scanning in the spectral range of 500 cm-1 to 4000 cm-1. This allowed for the comprehensive examination of the samples' infrared absorption characteristics and the determination of their respective functional groups [418].

5.2.5 Protein loading and release kinetics

The chitosan nanoparticles were utilized for loading human insulin, and their drug-loading capacity and release kinetics were investigated. The particles were suspended in 30 ml of PBS buffer of pH 7.4, and kept at 37 ˚C while subjecting it to a rotational speed ranging between 130-150 rpm. At regular periods, a 2 ml sample was taken from the suspension, and their OD was monitored. A UV-2600 spectrophotometer (Shimadzu) having a 4000µl quartz cuvette with a path length of 1 cm was employed for the measurements, operating within 200 nm to 800 nm. The obtained absorbance was then plotted against time to analyze the drug release trend over time [419].

5.2.6 Cell viability studies

To determine cell viability, the HEKa cell line (Human Epidermal Keratinocytes (adult)) was utilized, and an MTT (3-(4,5-dimethylthiazol-2-yl)-2,5-diphenyltetrazolium bromide) assay was conducted. HEKa cells were seeded in 96-well and grown till they reach a confluency of 75-80%. Subsequently, the cells were incubated with four distinct concentrations (1.5, 7.5, 30, and 60 µM) of ECNP, insulin, and ICNP, followed by keeping them at 37 ˚C for 24 h. Following the incubation period, the media was discarded, and MTT solution (2mg/ml in 5% ethanol) was added, followed by keeping it for 3 h in an incubator, after which the media-MTT mixture was discarded, and 200µl of dimethyl sulfoxide (DMSO) was added for dissolving the formazan crystals. The OD value was monitored at 570 nm.

For finding the inhibition percentage, the given equation was employed:

$$\% \text{ inhibition} = [1 - (At / Ac)] \times 100 \text{-------- (a)}$$

Here At represents the absorbance of the test substance, and Ac represents the absorbance of the control solvent. The experiment was performed three times for each concentration, and the average values were used to generate the corresponding graphs.

5.2.7 *in vitro* wound healing assay

Human epidermal keratinocyte (HEKa) cells were employed to conduct the *in vitro* wound healing assay using the prepared nanoparticles. The cells were cultured in 35mm plates using DMEM media supplemented with antibiotics. Following this, the cells incubated at 37 ˚C with a 5% CO_2 supply, providing an optimal environment for cell growth. Once the cells reached a 90-95% confluency, the scratch method was employed to create wounds. Varying concentrations (1.5, 7.5, 30, and 60 µM) of ECNP, insulin, ICNP, and media were added to the cells and incubated. The scratch width were measured at specific time intervals, including 6 h, 12 h, and 24 h, to assess the changes in diameter over time and evaluate the effects of the nanoformulations on the wound healing progress.

5.2.8 Determination of combination index (CI) for chitosan-insulin

The quantitative measurement of getting the combinatorial potential of two individual drugs is called the Combination Index (CI). Whether the two different drugs will exhibit synergism or antagonism is determined by calculating the drug combination index. A synergistic effect is observed if the different drugs administered together act together to increase each other's activity and are given a value of less than 1 (CI < 1). Whereas, if the CI value comes out to be more than 1 (CI >1), the antagonistic effect is shown, which shows that another inhibits the action of one drug. And, if the CI value is equal to 1 (CI = 1), the additive effect is indicated, which shows that no one of the two drugs interferes with each other's action. To calculate the combination index, the cell migration assay was performed using varying concentrations of chitosan and insulin on HEKa cells, and further calculations were done using the given equation.

$$CI = (D)1/(Dx)1 + (D)2/ (Dx)2 \quad \text{(b)}$$

$$\text{Where, } Dx = Dm [fa/fu]^{1/m} \text{---------- (c)}$$

Here, (D)1 represents the chitosan concentration, whereas (D)2 denotes insulin concentration. The median effect equation (f) was used for the determination of single drug concentrations, which gave the same effect (Dx)1 and (Dx)2. The fa and fu give affected and unaffected cell fractions in the median dose, respectively, and are equal to $10^{(y\text{-intercept})/m,}$ where m indicates the slope median in the median effect plot of log (D) vs. log (fa/fu)

5.2.9 *in vivo* experiment

5.2.9.1 Experimental animal accusation and maintenance:

Five-week-old female Swiss albino mice were procured from the Animal Care facility of Chittaranjan National Cancer Institute. All animals were carefully maintained at 25 ˚C and a daily supply of healthy food and water according to the instruction of the Institutional Animal Ethics Committee and entire experimentation was done as per guidelines and regulations approved by the Institutional Animal Ethics Committee of Chittaranjan National Cancer Institute (IAEC approved proposal no: IAEC-1774/BB-2/2018/10).

5.2.9.2 Third-degree Burn wound induction in mice

Five-week-old 40 female Swiss albino mice were chosen and acclimatized for one week in a new animal house. Before induction of the burn wound, hairs from the dorsal side of each animal were removed carefully. For giving mice anesthesia, intraperitoneal (IP) injections of Ketamine (87 mg/kg b.w) and xylazine (13 mg/kg b.w) were given in accordance with individual weight. Distilled water was boiled at 100 ˚C, and a 13 mm metal rod was placed on it for 1 min. A hot metal rod was placed on the shaved dorsal surface of each anesthetized mouse for 10 sec.

5.2.9.3 Treatment and measurement of burn wound healing

All mice were caged individually after burn wound induction. After burn induction, the mice were randomly segregated into five groups, i.e., Control, ECNP, Insulin, ICNP, and Standard, each containing eight mice, and all experiments were repeated twice. All treatments were applied topically over the wound area for up to 20 days. Control groups were treated with saline, and the standard group received commercially available ointment Silverex. 100 µl of ECNP, insulin, and ICNP (each 60 µM) were applied topically over the wound. All groups received treatment up to the day of sacrifice.

The wound area was measured at regular intervals with a digital caliper, which measured the length (L) and width (W) of the wound. The wound area was analyzed by the formula Area (A) = $\pi/4\ LW$. The formula analyzed the percentage of wound reduction. Wound reduction (%) = $[(A_0 - A_t)/A_0]x100$, where A_0 is the initial wound area, and A_t is the final wound area.

5.2.9.4 Wound tissue collection and histological staining

Half of each group was randomly selected and sacrificed after 10 days of treatment, and the other half was sacrificed after 20 days. Wound tissue samples and plasma were collected from the freshly sacrificed animals. Mice were sacrificed by overdose of Ketamine (160mg/kg) with xylazine (20mg/kg) via intraperitoneal injection. Wound skin tissues were washed gently in PBS and submerged in 10% neutral-buffered formalin (NBF) overnight. Before block preparation, tissue sections were processed in 70% alcohol for 2 h, then in 90% alcohol for 1 h, acetone for 1 h, Xylene for 30 min, and finally in liquid paraffine overnight at 65 ˚C. Tissue blocks were prepared and sectioned into 5 µm thick slices. Tissue sections were mounted over Poly-L-Lysine coated slides for histological staining. For Hematoxylin and Eosin staining, tissue sections containing slides were deparaffinized in Xylene for 15 min. Rehydration of slides was done by following sequential incubation in 100%, 90%, 70%, and 50% alcohol for staining with hematoxylin and eosin. Then, the slides were dehydrated in increasing alcohol concentration and mounted with a DPX (Dibutylphthalate Polystyrene Xylene) mounting medium. Finally, stained slides were observed under a microscope and photographed.

5.2.9.5 Masson's trichrome staining for collagen

In Masson's trichrome staining procedure performed after the sacrifice of the animals on the 20th day, deparaffinization of skin tissue sections was done using Xylene and sequentially rehydrated through incubations in 100%, 90%, 70%, and 50% alcohol for 5 min each. Following this, staining of the sections with Weigert's iron hematoxylin was done for 10 min and subsequently subjected to Biebrich scarlet-acid fuchsin staining for 5 min, followed by treatment with phosphomolybdic–-phosphotungstic acid solution for 10 min and aniline blue staining for 10 min. Afterward, the slides were dehydrated, mounted, and observed under a microscope. This staining method enabled the visualization of collagen synthesis, with collagen fibers appearing blue, and allowed for the evaluation of the effects of chitosan insulin nano-formulations on collagen deposition in the skin tissues, contributing to the understanding of wound healing mechanisms.

5.2.9.6 Collection of plasma and analysis of cytokine

After 10 and 20 days of burn injury, blood was collected from each group of mice in EDTA (Ethylene diamine tetraacetate) coated vials. Collected blood was centrifuged at 1500 rpm for 10 min to separate the plasma and stored at -80 ˚C until use. IL-6 and IL-10 ELISA (Enzyme-Linked Immunosorbent Assay) kits (BioLegend) were used to analyze the Pro and Anti-inflammatory cytokine levels. Before running the ELISA, the coating of the captured antibody was done in a 96-well plate overnight at 4 ˚C. Blocking was performed, and standard solutions were prepared along with plasma samples, incubated for 1 h, and washing was done using wash buffer. Then, wells were sequentially incubated with detection antibody and Avidin-HRP (Avidin-Horseradish Peroxidase) solution. Wells were thoroughly washed after every incubation. A TMB (Tetramethylbenzidine) substrate solution was added in the dark for 20 minutes, and the reaction was stopped using a stop solution. Finally, the OD value was taken in a spectrophotometer at 450 nm within 15 min. The standard curve was prepared, and unknown concentrations were analyzed from OD (Optical Density) values.

5.2.9.7 Immunohistochemical staining of burn wound skin tissues

Skin tissue samples were collected from the burn wounds of experimental animals at 10 days post-injury. Tissue samples from different treated groups were obtained, including the control, chitosan nano-formulation (ECNP), insulin, standard drug, and chitosan insulin nano-formulation (ICNP) groups. The collected skin tissue samples fixation was done using 10% formalin for 24 h and processed for paraffin embedding. Microtome was used for sectioning the paraffin-embedded tissue blocks into 5 μm thick slices. The tissue sections were placed on glass slides and subjected to deparaffinization and rehydration.

The tissue sections underwent antigen retrieval by heat-induced epitope retrieval using citrate buffer (pH-6.0) at 85 ˚C for 30 min. Endogenous peroxidase activity was blocked with hydrogen peroxide treatment. The Nrf-2 primary antibody (R&D Systems) was used in 1:200 dilution and kept in incubator for 12 h at 4 ˚C. There after washing was done followed by incubating slides with HRP-tagged secondary antibody (Santa Cruz Biotechnology) for 30 min at room temperature. The sections were treated with a DAB (3,3'-diaminobenzidine) substrate, resulting in a brown color reaction at the site of Nrf-2 expression. This allowed for the visualization of Nrf-2-positive cells and tissues.

The stained tissue sections were observed under a light microscope. The staining intensity and distribution of Nrf-2 immunoreactivity were assessed and documented. ImageJ performed quantitative or qualitative analysis, and statistical analyses were conducted to find out significant variations between the treated groups.

5.2.10 Statistical analysis

Data are plotted as mean ± SE. Statistical values were calculated using analysis of variance (ANOVA) and multiple comparison tests using GraphPad Prism version 7.0 (GraphPad Software, La Jolla, CA, United States). When p-value is <0.05 data was considered significant.

5.3 Results and Discussions

5.3.1 Structure and Morphological Studies

FE-SEM and Dynamic light scattering studies were used to study nanoparticle morphology and hydrodynamic size. The size of ECNP nanoparticles comes out to be ~ 25 nm **(Figure. 37b),** while that of ICNP nanoparticles is ~ 30 nm **(Figure. 37c),** and the particles come out to be spherical in FE-SEM. The hydrodynamic diameter of ECNP alone was slightly different from that of ICNP. At pH 6, the size of ECNP was 180.88 ± 20 nm, while ICNP was 187.47 ± 20 nm. At pH 7.4, ECNP was found to be 255.44 ± 20 nm, while for ICNP, the size was 289.20 ± 20 nm. The size comes out to be 133.27 ± 20 nm and 214.57 ± 20 nm for ECNP and ICNP, respectively, at a pH of 8. The size is 174.44 ± 20 nm for ECNP **(Figure. 37d)** and 119. 50 ± 40 nm for ICNP at pH 9 **(Figure. 37e)**.

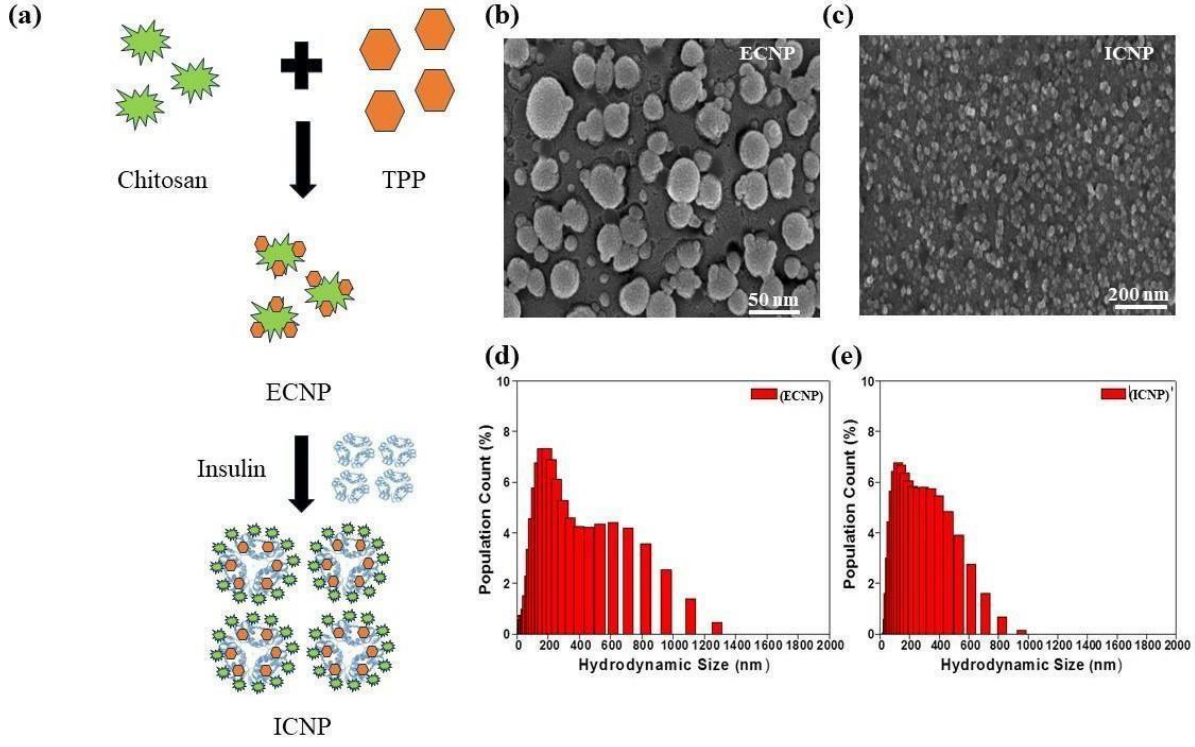

Figure. 37. The figure shows the schematic synthesis and morphological studies of synthesized ICNPs *(a) a brief synthesis procedure for making the ICNP nanoparticles. FE-SEM image of (b) ECNP particles and (c) ICNP nanoparticles at pH 9 indicating the synthesis of spherical particles of size 160 nm and 30 nm, respectively, at a scale of 500nm and 200 nm. Dynamic light scattering is used for getting the hydrodynamic size of (d) ECNP particles and (e) ICNP particles at a pH of 9.*

A comparative DLS data at different pH is shown in **(Figure. 38 a-h)**. There is also a change in Zeta potential with a change in pH. For ECNP, zeta potential comes out to be 10.9 ± 2.74 mV, 25.9 ± 3.39 mV, 26.7 ± 2.63 mV, and 24.6 ± 3.1 mV at pH 6, 7.4, 8, and 9, respectively. Similarly, there is variation in zeta potential values of ICNP. It was found to be 28.8 ± 3.08 mV, 23.2 ± 2.9 mV, 23.4 ± 3.12 mV, and 14.7 ± 2.5 mV, respectively, indicating the formation of desired nanoparticles as mentioned in **Table 16**.

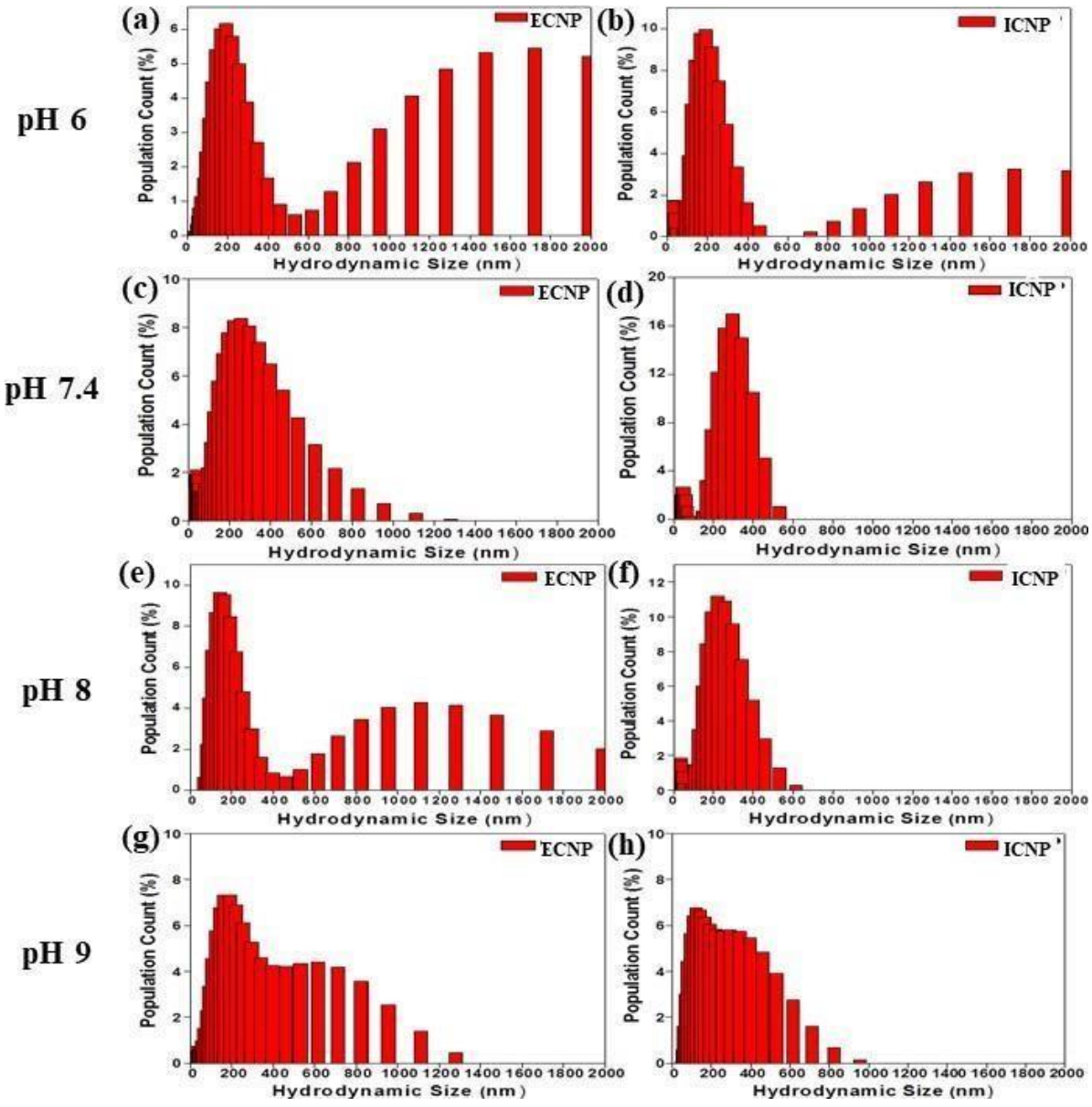

Figure. 38. The figure represents the variation in size of nanoparticles *(both empty chitosan nanoparticles (ECNP) and insulin-loaded chitosan nanoparticles (ICNP)) with slight variation in pH (a) ECNP and (b) ICNP at pH 6, (c) ECNP and (d) ICNP at pH 7.4, (e) ECNP and (f) ICNP at pH 8 and (g) ECNP and (h) ICNP at pH 9 respectively.*

Table 16: The table below depicts the zeta potential variation of ECNP and ICNP with varying pH conditions, including pH 6, 7.4, 8, and 9, respectively.

pH	Zeta potential (mV) ECNP	Zeta potential (mV) ICNP
6	10.9 ± 2.74	28.8 ± 3.08
7.4	25.9 ± 3.39	23.2 ± 2.9
8	26.7 ± 2.63	23.4 ± 3.12
9	24.6 ± 3.1	14.7 ± 2.5

5.3.2 FTIR Spectra to monitor the changes in conformation at the protein level because of chitosan-insulin interactions

FTIR was used to determine the interactions between TPP, chitosan, and insulin, and studies were done for TPP, chitosan, insulin, ECNP, and ICNP. Firstly, the peak indicating N-H stretch observed at 3294 cm^{-1} and 3282 cm^{-1} in chitosan and ECNP, respectively, whereas for ICNP, it was found at 3272 cm^{-1} and 3282 cm^{-1} [420]. Then, a peak appeared at 3054 cm^{-1} in ECNP and ICNP, indicating aromatic C-H stretching [421]. Similarly, for aliphatic C-H stretching, the peak was at 2878 cm^{-1} in chitosan, 2867 cm^{-1}, 2950 cm^{-1} in ECNP, 2826 cm^{-1} in insulin, and 2878 cm^{-1} and 2950 cm^{-1} in ICNP [421]. The peak indicating C=O stretch (Amide-I, O=C-NHR) was found at 1642 cm^{-1} in chitosan, ECNP, ICNP, and 1641.99 cm^{-1} in insulin [422], while for N-H bend (Amide-II) it appears at 1561 cm^{-1} for chitosan, 1533.65 cm^{-1} for insulin and at 1536 cm^{-1} for both ECNP and ICNP [423]. In addition to these peaks, a peak at 1431 cm^{-1} in insulin and 1447 cm^{-1} in ECNP and ICNP was observed exhibiting the S=O bond [232]. O-H bending was obtained at 1323 cm^{-1} and 1375 cm^{-1} in chitosan, 1399 cm^{-1} in ECNP, 1336 cm^{-1} in insulin, and 1393 cm^{-1} in ICNP [424]. The peak at 1241 cm^{-1} in ECNP and ICNP while at 1215 cm^{-1} and 1294 cm^{-1} shows the bond for C-O stretching [425]. Similarly, C-N stretching was observed only in insulin at 1104 cm^{-1} [426]. The symmetric and asymmetric vibrations for O-P=O were found only in TPP at 1167 $cm^{-1,}$ and the PO_3 symmetric and asymmetric stretching vibrations were observed at 1046 cm^{-1} in chitosan, ECNP, and ICNP [427]. For C-O bending, the peak appeared at 930 cm^{-1} in ECNP, 930 cm-1 and 973 cm-1 in insulin, and 25 cm^{-1} and 988 cm^{-1} in ICNP [425]. The stretching vibration of the P-O-P bridge was observed alone in TPP at 887 cm^{-1} [427]. NH_2 bending vibration was at 803 cm^{-1} and 872 $cm^{-1,}$ while C-O-O bending was at 746 cm^{-1} only in insulin. Similarly, both the C=S stretch and S-S stretch were observed at 651 cm^{-1}, 682 $cm^{-1,}$ and 551 $cm^{-1,}$ respectively [49] as shown in (**Figure. 39a and Figure. 39b)**. A comparative FTIR data of TPP, chitosan, insulin, ECNP, and ICNP is given in **Table 17**.

Table 17: The comparative wavenumber values indicated by FTIR (in the range 400-4000 cm^{-1}) of TPP, chitosan, ECNP, insulin, and ICNP determine the position of different functional groups present, which coins the interaction amongst these solutions indicating the formation of insulin loaded chitosan nanoparticles.

Functional Groups	TPP	Chitosan	ECNP	Insulin	ICNP	Ref.
N-H stretch (Amide-I, O=C-NHR)	-	3294	3282	-	3282 3272	[420]
Aromatic C-H stretching	-	-	3054	-	3054	[421]
Aliphatic C-H stretching	-	2878	2950 2867	2826	2950 2878	[421]
C=O stretch (Amide-I, O=C-NHR)	-	1642	1642	1641	1642	[422]
N-H bend (Amide-II NH_2)	-	1561	1536	1533.65	1536	[423]
S=O bond	-	-	1447	1431	1447	[232]

O-H bending	-	1375 1323	1399	1336	1393	[424]
C-O stretching	-	-	1241	1294 1215	1241	[425]
O-P=O Symmetric and asymmetric stretching vibrations	1167	-	-	-	-	[427]
C-N stretching	-	-	-	1104	-	[426]
PO_3 Symmetric and asymmetric stretching vibrations	-	1046	1046	-	1046	[427]
C-O bending	-	-	930	973 930	988 925	[425]
Stretching vibrations of P-O-P bridge	887	-	-	-	-	[427]
NH_2 bending vibrations	-	-	-	872 803	-	[49]
C-O-O bending				746		[49]
C=S (stretch)	-	-	-	651 682	-	[49]
S-S stretch	-	-	-	551	-	[49]

5.3.3 Protein loading and release kinetics studies

The insulin protein loading and release kinetics of ICNP were studied, where the amount of insulin loaded was 88.725 ± 0.295% in the ECNP particles. The release kinetics of insulin were studied from ICNP particles at the physiological pH of 7.4 and 37 $^{\circ}$C. The particles were loaded into the dialysis membrane, and the release kinetics was observed by taking the OD values at 595 nm after particular time intervals for a period of 36 h. Burst drug release was observed in the initial 2 h, followed by a sustained drug release till 12 h. Most of the insulin was released within 36 h. The percentage of insulin released during the first 2 h is 73.98 ± 0.019 %, while by the end of 36 h, the total insulin released was 89.84 ± 0.01 % of the loaded one, and the data is shown in **(Figure. 39 c-d).** This indicates the high drug delivery potential of ICNP nano-formulations within less time intervals, making them efficient and effective drug delivery agents.

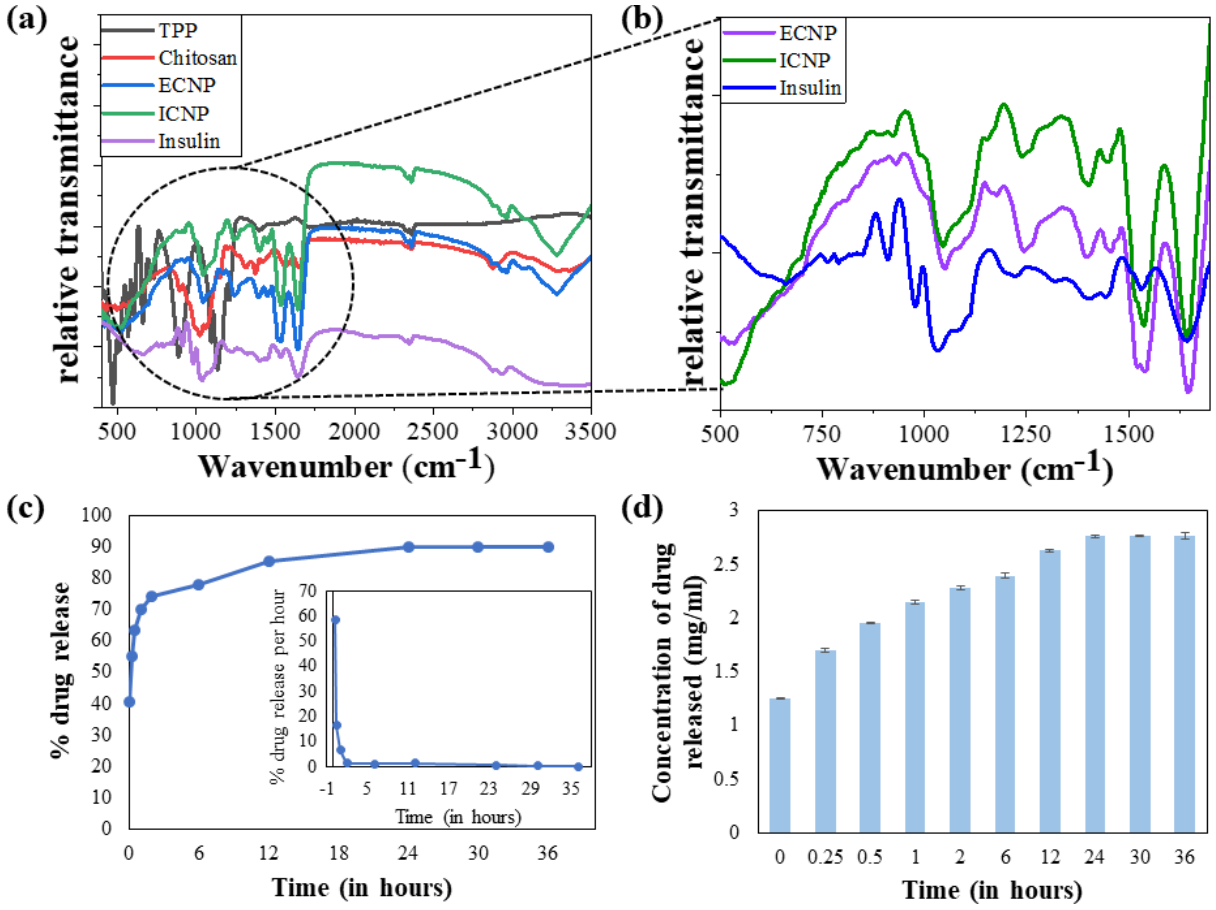

Figure. 39. The figure shows the spectroscopic studies to determine variation in insulin protein structure after interaction with chitosan and the drug release studies from ICNPs*. The plots show the FTIR spectroscopic studies of TPP, chitosan, ECNP, insulin, and ICNP, indicating the changes in the wavenumber of characteristic bonds, confirming the interactions between ECNP and insulin at different scale bar (a) 500-4000 cm^{-1} and (b) 500-1500 cm^{-1} (fingerprint region). The release kinetic studies from ICNP nanoparticles (c) Plot for the % of total drug release during the time span of 36h from ICNP (Inlet shows the plot for the release kinetics indicating the % drug release per h). (d) The graph provides information on the amount of drug released in mg/ml from ICNP.*

5.3.4 Cell viability studies

After incubating the HEKa cells with varying concentrations (1.5, 7.5, 30, 60 µM**)** of ECNP, Insulin, and ICNP for 24 h, 48 h, and 72 h, the cell viability was obtained using an MTT assay. As is known, the cell viability using MTT assay depends upon the mitochondrial activity of the cells. The results show that none of the three components, including ECNP, insulin, and ICNP, are toxic to the HEKa cell line; instead, they can potentially enhance the cell division of normal human epidermal keratinocyte cells and thus can be used for wound healing applications. As I go on increasing the concentration and time duration of incubation for all samples, there is a tremendous improvement in the rate of cell growth, and it was maximum for the highest concentration, that is, 60 µM and maximum after 72 h incubation period. The % increase in cell growth is 143.807 ± 3.75, 146.71 ± 5.86, and 185.14 ± 12.17 after 24, 48, and 72 h as compared to the control, which is assumed to be 100% for each time point with varying absorbance values, and the studies are done in relevance to it. The variation in OD value for different concentrations of each compound was plotted against the time and is shown in **Figure. 40a**. A comparative table for varying values of OD is given in **Table 18**.

Table 18. Table indicates changes in mitochondrial reductase activity in the MTT assay for determining % change in cell viability after treating cells with different amounts of ECNP, insulin, and ICNP, that is, 1.5 µM, 7.5 µM, 30 µM, and 60 µM respectively, for a duration of 24, 48 and 72 hours. The OD values for control after 24, 48, and 72 hours are 0.255 ± 0.020, 0.606 ± 0.036, and 0.850 ± 0.007, respectively. The data for the rest of the samples is presented below in a comparative manner and given as mean value ± SD of 3 different experiments.

Variation in mitochondrial reductase activity (OD value at 575 nm)				
Dose	**Time**	**ECNP**	**Insulin**	**ICNP**
1.5 µM	24 h	0.263 ± 0.040	0.271 ± 0.017	0.287 ± 0.033
	48 h	0.606 ± 0.036	0.634 ± 0.062	0.741 ± 0.050
	72 h	0.869 ± 0.066	0.940 ± 0.056	1.156 ± 0.081
7.5 µM	24 h	0.269 ± 0.037	0.286 ± 0.037	0.336 ± 0.097
	48 h	0.624 ± 0.048	0.659 ± 0.051	0.782 ± 0.043
	72 h	0.872 ± 0.141	1.201 ± 0.098	1.371 ± 0.084
30 µM	24 h	0.279 ± 0.010	0.288 ± 0.021	0.348 ± 0.026
	48 h	0.634 ± 0.062	0.745 ± 0.048	0.847 ± 0.077
	72 h	1.0167 ± 0.125	1.407 ± 0.154	1.46 ± 0.026
60 µM	24 h	0.284 ± 0.012	0.331 ± 0.067	0.367 ± 0.037
	48 h	0.678 ± 0.077	0.741 ± 0.082	0.875 ± 0.058
	72 h	0.957 ± 0.059	1.439 ± 0.067	1.575 ± 0.121

5.3.5 *in vitro* HEKa cell migration studies

ICNP-treated cells show enhanced HEKa cell migration in comparion with control cells without any treatment, ECNP, and insulin-treated cells. An enhancement in the rate of cell division and growth with an increase in time and concentration was observed. After treatment with ICNP for 6, 12, and 24 h, the cells show a gradual decrease in the scratch diameter with increased time duration. The percentage of the gap left after 6, 12, and 24 h of treatment with ICNP is 76.63 ± 2.30 %, 64.45 ± 2.88 %, and 96.13 ± 2.30 %, respectively, at 1.5 µM; 57.732 ± 2.30 %, 57.03 ± 3.46 % and 75.13 ± 4.61 % respectively at 7.5 µM; 47.07 ± 1.73 %, 49.21 ± 3.46 % and 46.96 ± 2.88 % respectively at 30 µM; 36.76 ± 4.04 %, 29.68 ± 2.30 % and 28.17 ± 4.04 % respectively at 60 µM. In the case of insulin, the % of the gap left between the scratch is more in comparison to that of ICNP. The HEKa cells after treatment with insulin show the percentage change in scratch diameter after 6, 12, and 24 h as 52.92 ± 5.77 %, 45.70 ± 2.88 %, and 45.30 ± 1.15 %, respectively, at a concentration of 1.5 µM; 42.26 ± 1.73 %, 40.62 ± 2.30 %, and 34.25 ± 1.15 % respectively at 7.5 µM. The variation in wound scratch diameter is found to be 34.70 ± 1.73 %, 33.20 ± 1.73 %, and 29.28 ± 1.73 %, respectively, for 30 µM concentration; and 26.80 ± 1.15 %, 26.17 ± 1.73 % and 20.99 ± 1.15 %

respectively for 60 µM of insulin. In the case of ECNP, the migration of cells is observed compared to that of untreated cells. ECNP-treated cells at a concentration of 1.5 µM show the % change in scratch width after 6, 12, and 24 h as 70.99 ± 5.77 %, 76.95 ± 2.30 %, and 96.13 ± 5.77 respectively. At 7.5 µM concentration, the change with increasing time interval is 67.69 ± 1.73 %, 67.57 ± 1.73 %, and 75.69 ± 1.73 %, respectively. The values come out to be 67.69 ± 1.73 %, 67.57 ± 1.73 %, and 56.35 ± 1.15, respectively, after 6, 12, and 24 h, while for 60 µM concentration % change is 67.01 ± 8.66 %, 57.81 ± 1.15 % and 57.40 ± 2.30 % respectively. The comparative data of wound migration for control and under the influence of varying concentrations of ECNP, insulin, and ICNP is shown in **(Figure. 40 b-e)** and **(Figure. 41-43).** For evaluating if data is statistically significant, the p values were determined for % variation in scratch width followed by treating using different amounts of ECNP, insulin, and ICNP (1.5, 7.5, 30 and 60 µM) after 6h, 12 h, and 24h respectively and when $p < 0.05$, data is considered significant and is given in **Table 19**.

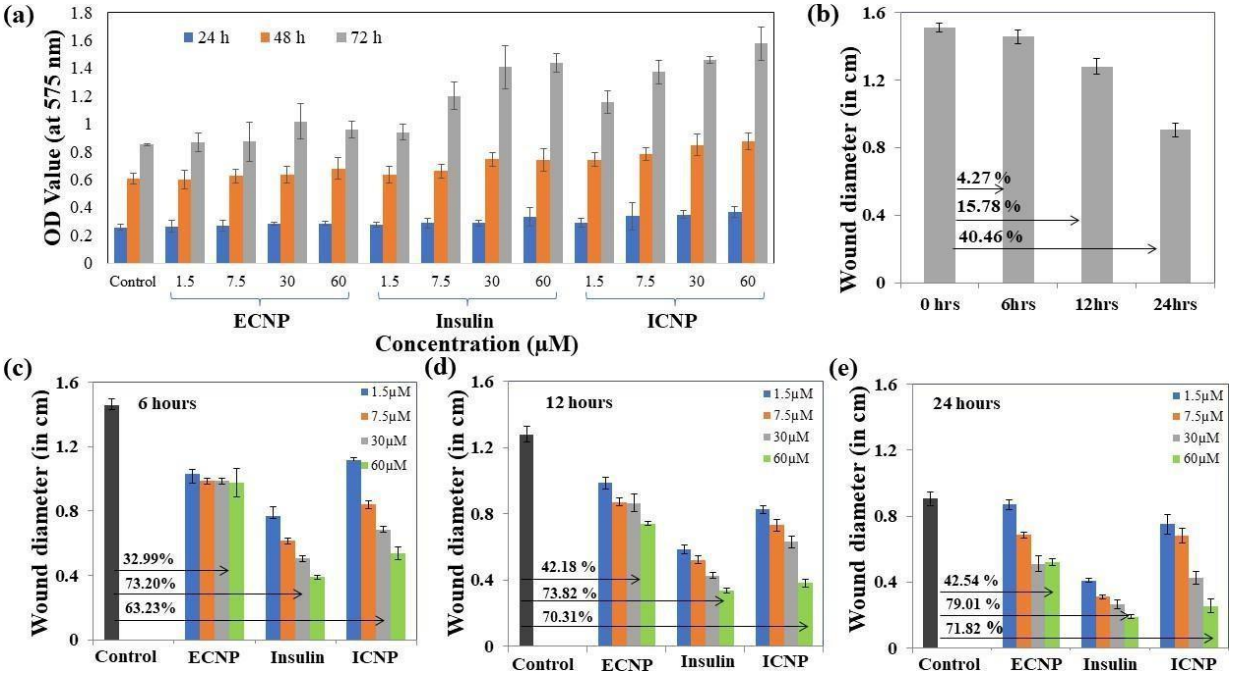

Figure. 40. This figure indicates the cell viability studies and migration studies (in vitro) for confirming the wound healing abilities of ICNP *(a) The graph shows the treatment of HEKa cells for different intervals with 1.5 µM, 7.5 µM, 30 µM, and 60 µM of ECNP, insulin, and ICNP to check their biocompatibility, and the data indicates that they are not toxic to the normal skin cells. Enhanced in vitro wound healing after treatment with ECNP, insulin, and ICNP at different concentrations and time intervals, indicating the ICNP nanoparticles are efficient wound healing agents, and the healing effect increases with concentration and time. The figures show a comparative study of all three formulations of varying concentrations of 1.5 µM, 7.5 µM, 30 µM, and 60 µM after (b) 6h of treatment, (c) 12h of treatment, and (d) 24h of treatment to determine the effect in wound healing with time and concentration.*

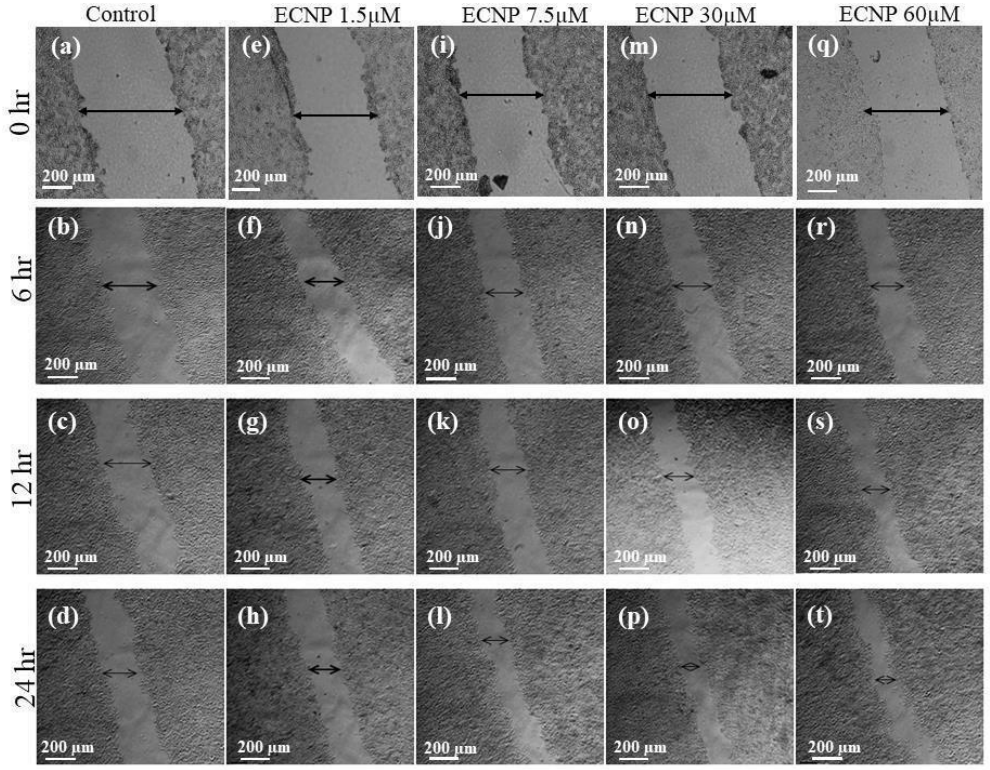

Figure. 41. The given figure shows the effect of change in concentration of ECNP in the process of wound healing with change in time using migration assay. *Cells were incubated uisng varying amounts of ECNP (e), (f), (g), and (h) 1.5 μM (i), (j), (k), and (l) with 7.5 μM, (m), (n), (o), and (p) with 30 μM and (q), (r), (s), and (t) with 60 μM respectively for 6, 12 and 24 h duration to observe the cell migration.*

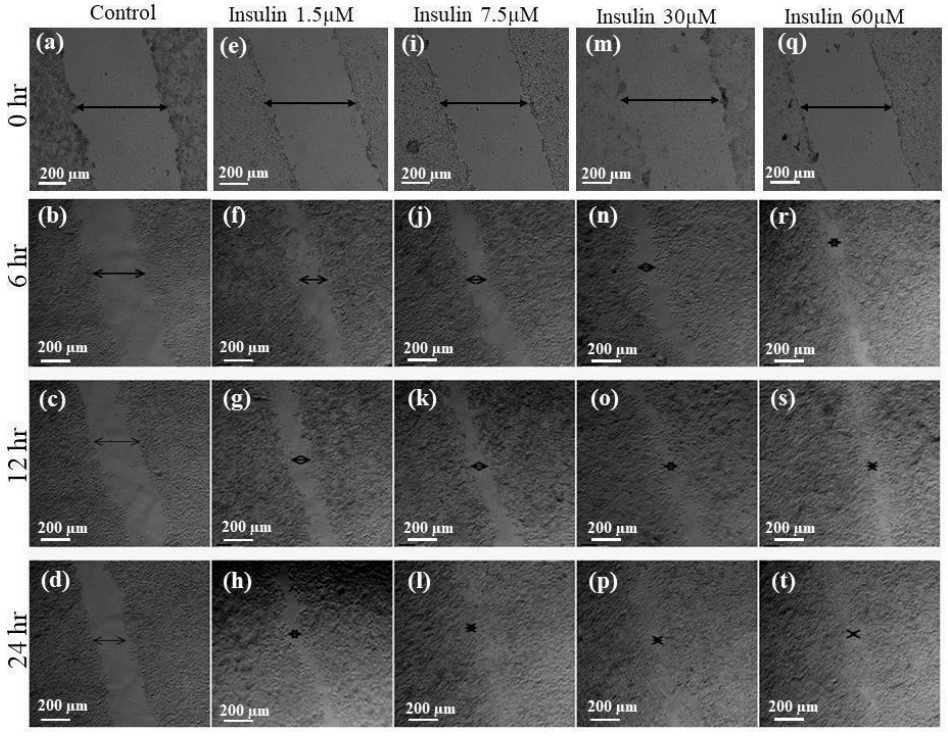

Figure. 42. The given figure shows the role of change in insulin concentration in the process of wound healing with change in time using migration assay*. Cells were incubated uisng varying*

amounts of insulin (e), (f), (g), and (h) 1.5 μM (i), (j), (k), and (l) with 7.5 μM, (m), (n), (o), and (p) with 30 μM and (q), (r), (s), and (t) with 60 μM respectively for 6, 12 and 24 h duration to observe the cell migration.

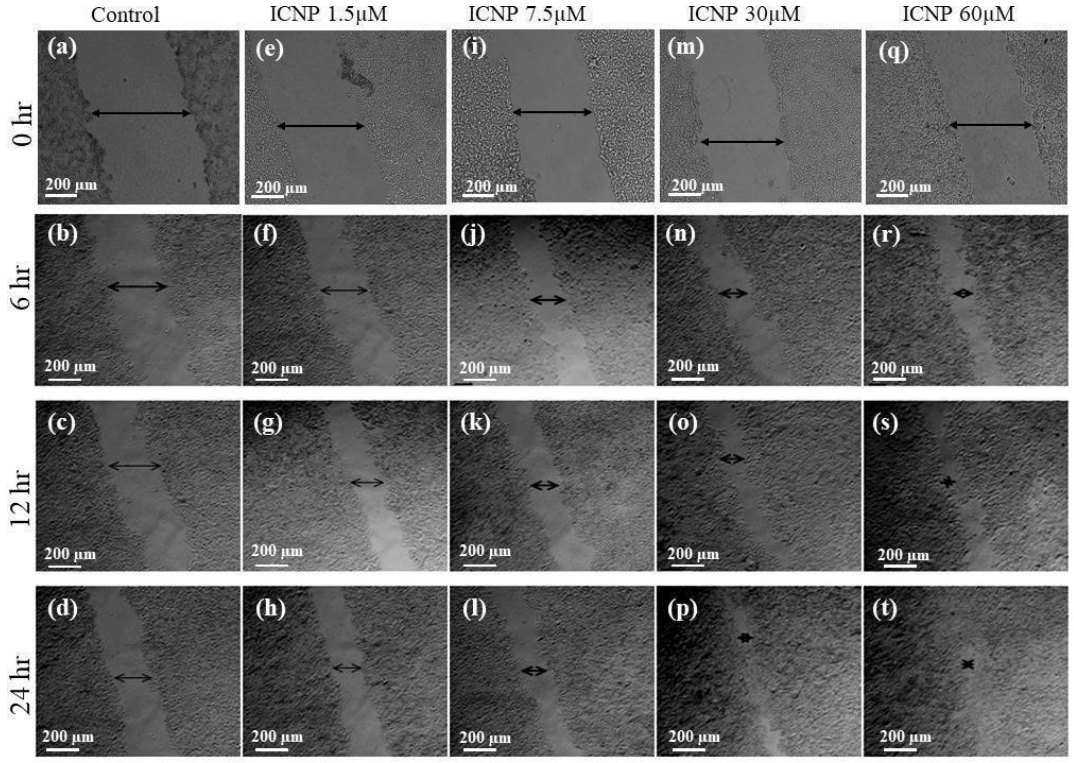

Figure. 43. The given figure shows the effect of change in concentration of ICNP in the process of wound healing with change in time using migration assay*. Cells were incubated with varying amount of ICNP (e), (f), (g), and (h) 1.5 μM (i), (j), (k), and (l) with 7.5 μM, (m), (n), (o), and (p) with 30 μM and (q), (r), (s), and (t) with 60 μM respectively for 6, 12 and 24 h duration to observe the cell migration.*

Table 19: It demonstrates the p values obtained for percentage variation in scratch width following treatment with distinct concentrations of ECNP, insulin, and ICNP (1.5, 7.5, 30, and 60 μM) after 6h, 12 h, and 24h, respectively. The statistical significance of data is considered when $p < 0.05$.

P value for determining if data for scratch assay is significant or not				
Time	**Concentration**	**ECNP**	**Insulin**	**ICNP**
6 h	1.5 μM	0.002317	5.68E-05	0.013705
	7.5 μM	9.94E-05	7.9E-05	9.53E-05
	30 μM	8.97E-05	1.55E-05	6.51E-05
	60 μM	8.5E-05	7.11E-06	4.13E-05
12 h	1.5 μM	0.000624	4.03E-05	0.000861
	7.5 μM	0.001332	3.61E-05	0.000219
	30 μM	0.000174	2.09E-05	6.11E-05
	60 μM	0.000165	1.86E-05	2.88E-05
24 h	1.5 μM	0.321863	0.00015	0.019979
	7.5 μM	0.015416	4.51E-05	0.001427
	30 μM	0.000193	1.05E-05	0.000112
	60 μM	6.91E-05	9.11E-06	0.000156

5.3.6 Combination index of chitosan and insulin

For the calculation of the CI, Dm was determined by using m and y from **(Figure. 44 a)** for chitosan and **(Figure. 44 b)** for insulin after 6 hours, **(Figure. 44 c)** for chitosan and **(Figure. 44 d)** for insulin after 12 hours, and **(Figure. 44 e)** for chitosan and **(Figure. 44 f)** for insulin after 24 hours. The calculated combination index values for the chitosan and insulin show a synergistic effect. After calculating the combination index by changing the concentrations of both chitosan and insulin, the values come out to be less than one, representing the synergism between the two drugs; that is, they increase each other's activity by working cordially. These results are in resemblance with the ones obtained earlier from cell viability and cell migration assays performed *in vitro*, indicating the potent therapeutic role of chitosan and insulin in enhanced wound healing applications. The data is shown in **Table 20**.

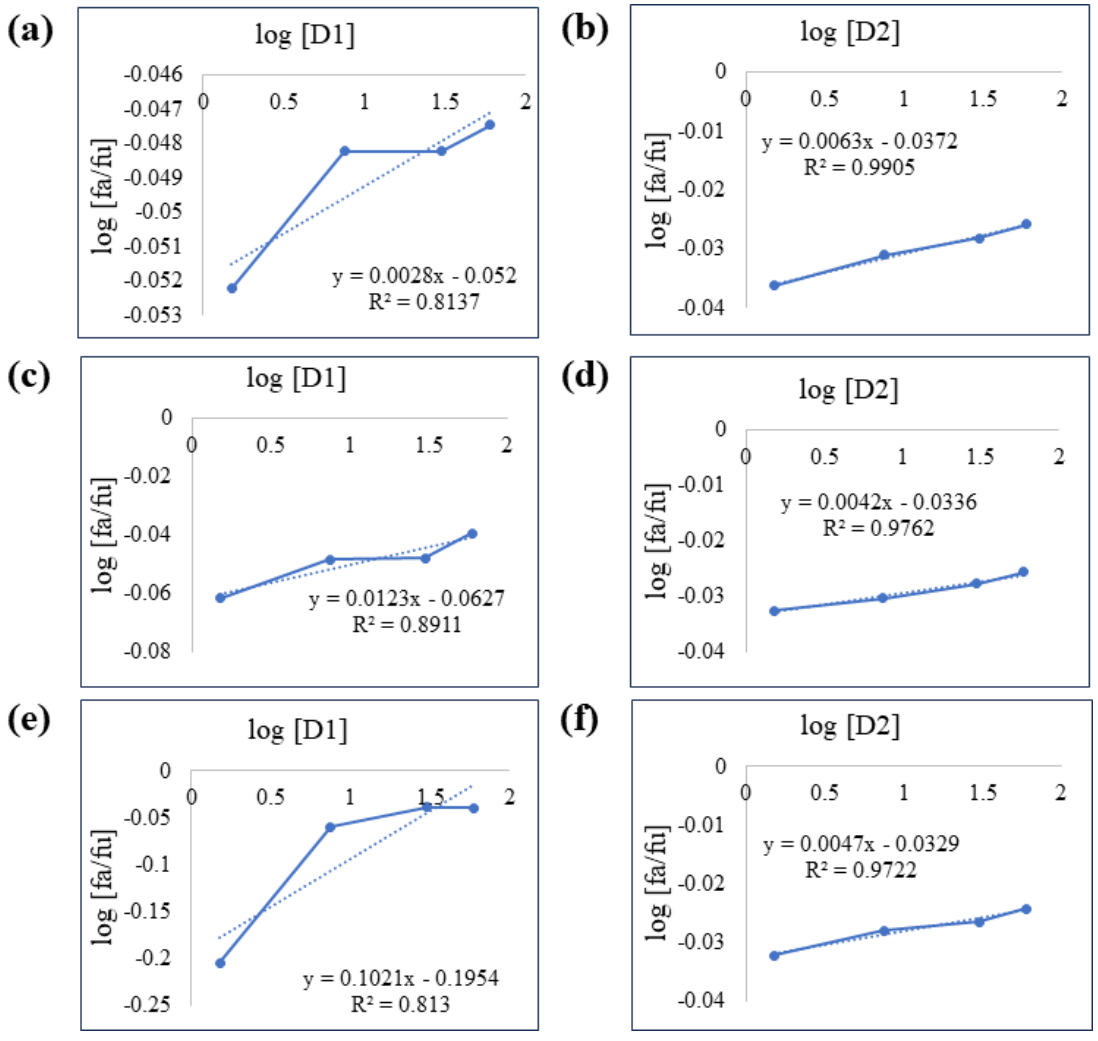

Figure. 44. Median plots of (a) Chitosan, (b) Insulin *after 6 hours, (c) Chitosan, (d) Insulin after 12 hours, and (e) Chitosan and (f) Insulin after 24 hours for determining the y-intercept and m values to obtain Dm to find out the CI of chitosan and insulin.*

Table 20: CI values for the cell viability after varying % of chitosan with insulin protein were calculated to check synergistic or antagonistic effect of drugs.

Combination Index (CI)			
The concentration of Chitosan and Insulin	(Dx)1 (Chitosan) = Dm [fa/fu]$^{1/m}$	(Dx)2 (Insulin) = Dm [fa/fu]$^{1/m}$	CI = (D)1/(Dx)1 + (D)2/(Dx)2
6 hours			
1.5 µM	536974719	6906.95751	0.000217
7.5 µM	124279920	3473.38471	0.002159
30 µM	124279920	2445.95753	0.012265
60 µM	95113804.3	1832.71399	0.032739
12 hours			
1.5 µM	6081.89	31223.2	0.00029
7.5 µM	1853.28	20645	0.00441
30 µM	1786.88	12640	0.01916
60 µM	896.3	8703.2	0.07384
24 hours			
1.5 µM	1918.72	2159.44	0.00148
7.5 µM	588.579	1368.32	0.01822
30 µM	304.722	1167.8	0.12414
60 µM	317.224	937.648	0.25313

5.3.7 Chitosan insulin nano-formulation accelerates burn wound healing through collagen deposition and tissue remodeling

Burn wound closure was monitored over 20 days starting from wound induction (Day 0) (**Figure. 45a)** shows representative images of the wounds during the treatment period in different groups, following confirmation of third-degree burn wound histology with healthy mice skin histology on day 0 (**Figure. 45b**). No significant wound closure was observed among the treatment groups for up to 5 days, but only ICNP treated group significantly reduced the wound by 29.3 ± 4.63 % **(Figure. 45c).** Significant wound closure was obtained in all treatment groups when compared with the control from 10 days of treatment. The degree of wound closure was less in the control and ECNP groups, whereas insulin, standard, and ICNP-treated groups reduced the wound area by 50.26 ± 7.65 %, 49.39 ± 5.29 %, and 55.66 ± 4.17 %. A similar pattern was observed after 20 days of treatment. The ICNP-treated group displays more significant wound contraction of 95.77 ± 4.26 % than the insulin and standard group, i.e., 68.38 ± 6.62 % and 76.57 ± 4.14 %. Control and ECNP groups showed less wound reduction, about 43.25 ± 6.56 % and 50.13 ± 5.39 %.

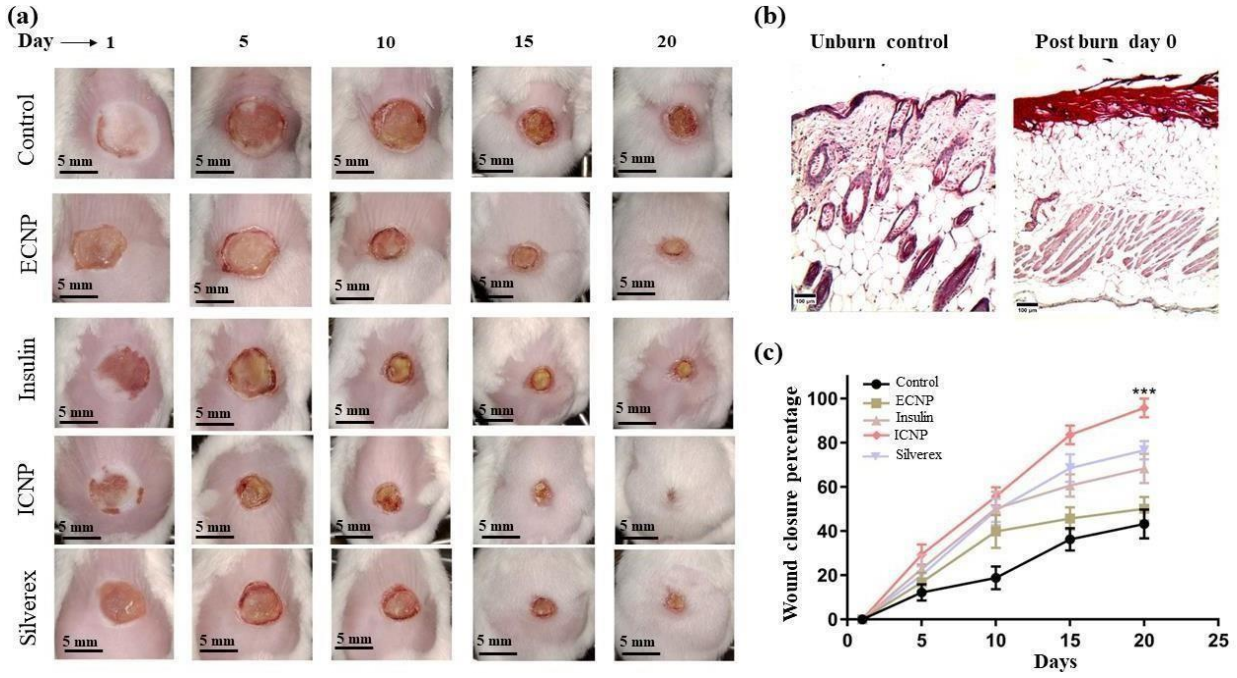

Figure. 45. Representative images of day-wise burn wound closure images of control and all treated groups *(a) Percentage of burn wound closure up to 20 days. (b) Hematoxylin and Eosin staining of post-burn day 0 and unburn control mice skin. Day 0 burn wound skin showing the development of third-degree burn wound indicated by completely damaged epidermis, dermis, and hypodermis (c) Data represents as mean ± SEM; ***p<0.001; * indicates statistically significant values from the control)*

10-day post burn own skin tissue histology images **(Figure. 46a)** showed control and ECNP group dominated with inflammatory cell-rich tissue. Wound eschar started to separate from the wound bed in Insulin and standard groups, and epidermal keratinocyte migration started beneath the eschar to re-epithelize the wound area. The ICNP-treated group was observed to have less inflammatory cell infiltration, a complete absence of wound eschar, and moderate reepithelization. On day 20, the control group still exhibited wound eschar, enhanced inflammatory cells, and re-epithelization in a small area **(Figure. 46b)**; however, ECNP, insulin, and the standard group were characterized by increasing epidermal thickness. Moreover, Well-repaired hair follicles were observed in the ICNP-treated group, indicating accelerated wound healing and re-epithelization.
In Masson's trichrome collagen staining, collagens are stained blue, whereas muscle and cytoplasm are stained red. The staining assessed the collagen deposition during the granulation tissue formation. The intensity of blue staining corresponds to the relative quantity of new collagen fiber deposition. On 20-day skin tissue collagen staining, less blue stained area and intensity were observed in control and ECNP groups **(Figure. 46c).** The rate of collagen formation was comparatively higher in insulin and standard-treated groups, but the presence of reddish areas in collagen indicates burn-induced denatured collagen fibers. The highest new collagen fiber deposition was observed in the ICNP-treated group, marked by a high-intensity blue-stained area. This suggests that new collagen was rearranged during wound healing, and the ICNP-treated group showed this in the shortest time.

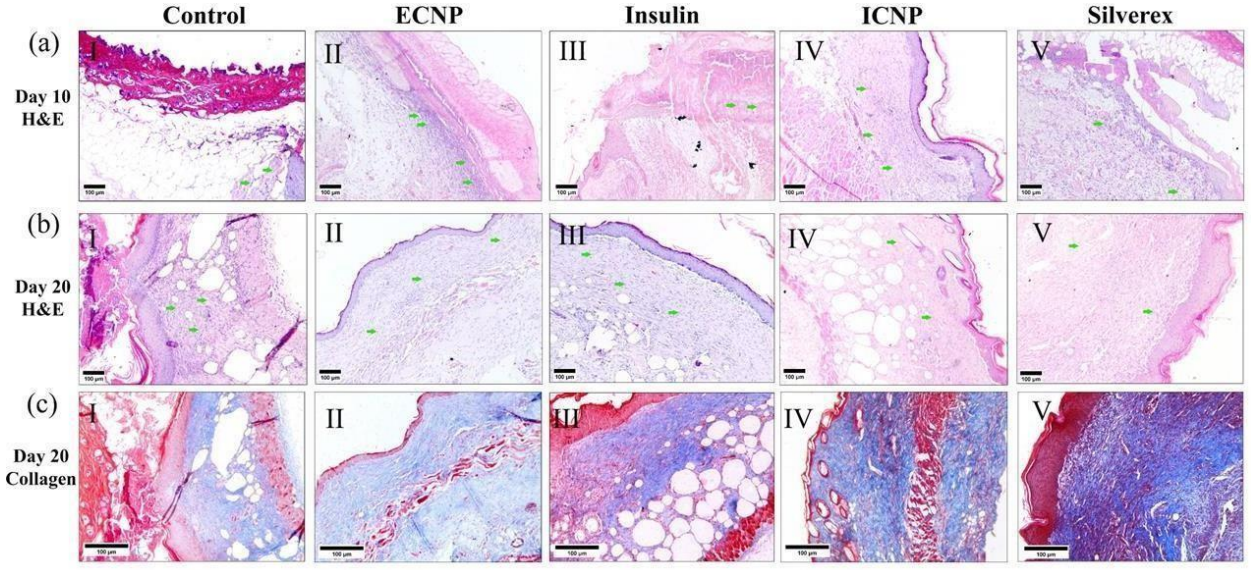

Figure. 46. The figure depicts tissue histology and collagen deposition during burn wound healing *Hematoxylin and eosin-stained post-burn (a) day 10, (b) day 20, and (c) collagen-stained day 20 wound skin histology images. Green arrows indicate inflammatory cell infiltration. All H&E images were taken at 100X magnification, and collagen staining images at 200X magnification (Scale bar 100 µm).*

5.3.8 Chitosan insulin nano-formulation regulates pro and anti-inflammatory cytokines

Pro-inflammatory and anti-inflammatory cytokine levels in plasma were evaluated 10 days after burn injury. The control and chitosan nano-formulation (ECNP)-treated groups exhibited high levels of plasma IL-6 (620.60 ± 41.58 pg/ml and 534.35 ± 27.37 pg/ml) and relatively low levels of plasma IL-10 (172.50 ± 31.82 pg/ml and 190.00 ± 14.14 pg/ml). Treatment with insulin and a standard drug significantly reduced IL-6 levels (397.50 ± 42.43 pg/ml and 352.50 ± 60.10 pg/ml) while increasing plasma IL-10 levels (227.50 ± 31.82 pg/ml and 282.75 ± 18.03 pg/ml). Furthermore, topical administration of the chitosan insulin nano-formulation (ICNP) markedly decreased IL-6 levels to 185.00 ± 7.07 pg/ml, accompanied by an elevated IL-10 plasma content of 389.95 ± 35.28 pg/ml. The elevated IL-6 levels observed in the control and ECNP-treated groups indicate an ongoing pro-inflammatory response. However, treatment with insulin or the standard drug showed a significant reduction in IL-6 levels and an enhanced IL-10, indicating the ability of these interventions to suppress excessive inflammation. The changes in mean plasma IL-10 levels for ECNP, Insulin, and Silverex groups were not significant, but the ICNP group showed considerable change compared to the control group. ICNP showed better efficacy than insulin or the standard drug by significantly reducing IL-6 levels and elevating IL-10 levels, showing the best modulation of pro-inflammatory and anti-inflammatory cytokine profiles **(Figure. 47a).**

Compared to control, which had IL-6 levels of 267 ± 35.7 pg/ml, the ECNP group exhibited a slightly lower concentration at 221 ± 29.9 pg/ml. However, it's noteworthy that insulin and the standard drug group significantly reduced IL-6 levels, recording values of 139.7 ± 22.4 pg/ml and 112.3 ± 27.3 pg/ml, respectively. Remarkably, the ICNP-treated group demonstrated the most substantial decrease in IL-6 levels, reaching as low as 107.4 ± 25.4 pg/ml. Also, the plasma IL-10, the control group, had levels of 152.3 ± 22.6 pg/ml, and the ECNP group showed a similar concentration at 145.7 ± 19.3 pg/ml. Once again, both insulin and the standard drug group displayed decreased IL-10 levels, measuring 101.1 ± 21.6 pg/ml and 95.4 ± 30.5 pg/ml, respectively. In stark

contrast, the ICNP-treated group exhibited the most remarkable drop in IL-10 levels, registering as low as 89.8 ± 20.8 pg/ml.

The observations at day 20 point towards a notable trend in the cytokine levels across all treatment groups. The IL-6 levels in the insulin, Silverex, and ECNP groups have decreased to what can be considered normal levels, signifying the resolution of the earlier pro-inflammatory response. Correspondingly, the levels of IL-10, which had been balancing the pro-inflammatory effects of IL-6, have also decreased notably in these groups. Interestingly, the control and ECNP groups still exhibit relatively higher IL-6 levels at day 20. However, these elevated IL-6 levels are somewhat compensated for by a slight increase in IL-10 levels. This might suggest a normal systemic response that occurs independently of any treatment and could be attributed to the ongoing wound-healing process. The comparison of plasma IL-6 and IL-10 levels among the treatment groups at day 20 reveals the efficacy of various interventions (**Figure. 48**).

5.3.9 Chitosan insulin nano-formulation regulates Nrf-2 expression

Immunohistochemical (IHC) staining analysis revealed distinct Nrf-2 expression patterns among the treated groups **(Figure. 47b)**. Quantification of positive Nrf-2 staining areas in burn wound tissues was performed using ImageJ software. Multiple images were captured at a high-power field from each treatment group, and the positive staining areas were calculated. The data were plotted in a bar diagram to illustrate the comparative Nrf-2 expression levels among the groups **(Figure. 47c).** In the control and ECNP groups, Nrf-2 expression levels in the IHC staining was very low in comparison with other groups. This suggests that the control and ECNP treatments had a limited impact on activating the Nrf-2 pathway. In contrast, the insulin and standard drug groups exhibited moderate Nrf-2 expression in the IHC staining analysis. The ICNP-treated group displayed a significantly higher Nrf-2 expression in the IHC staining than all other groups. This suggests that the chitosan insulin nano-formulation, ICNP, effectively upregulates Nrf-2 expression, potentially enhancing the cellular defense mechanisms against oxidative stress and countering inflammation.

Insulin possess anti-inflammatory properties and can modulate the inflammatory response. Similarly, Nrf-2 suppresses inflammation by controlling the expression of antioxidant and detoxifying enzymes. The increased expression of Nrf-2 in the ICNP-treated group, as demonstrated by IHC staining, suggests that ICNP may regulate inflammation by activating Nrf-2. The table for checking the statistical significance of IL-6, IL-10, and Nrf-2 data is given in **Table 21**.

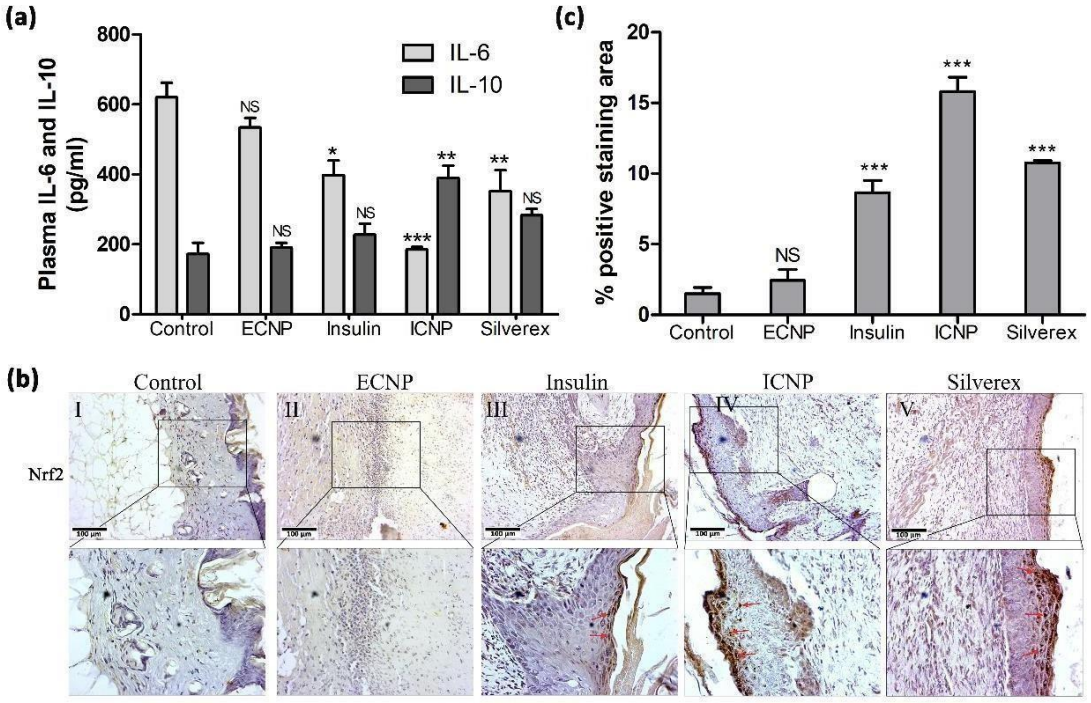

Figure. 47. The figure provides information about the regulation of inflammatory cytokines during burn wound healing along with Immunohistochemical (IHC) staining of Nrf-2 expression in 10-day post-burn wound tissue sections *(a) Post-burn injury plasma IL-6 and IL-10 levels were collected on day 10 to analyze the inflammatory phases. (b) Immunohistochemical (IHC) staining of Nrf-2 expression in 10-day post-burn wound tissue sections. Representative images show Nrf-2 immunoreactivity in different treatment groups, including control, chitosan insulin nano-formulation (ECNP), insulin, standard drug, and chitosan insulin nano-formulation (ICNP). The ICNP-treated group displays significantly higher Nrf-2 expression compared to other groups. Red arrows indicate positive Nrf-2 staining, (c) Quantitative analysis of positive stained areas was performed using ImageJ software for Nrf-2 immunohistochemical staining in burn wound tissues. Data represented as mean ± SEM; *p<0.05, **p<0.01, ***p<0.001; * are representing a significant variation from the control taken; NS (Nonsignificant); Scale bar 100 µm.*

Table 21. It shows the p values calculated for checking the IL-6 data's statistical significance for IL-6, IL-10, and Nrf-2 % alteration in scratch width following the treatment with ECNP, insulin, and ICNP (60 µM), respectively. The statistical significance of data is considered when $p < 0.05$.

P value for checking the statistical significance of data for IL-6, IL-10, and Nrf-2				
	ECNP	**Insulin**	**ICNP**	**Silverex**
IL-6	0.0678	0.0481	0.000612	0.00457
IL-10	0.0751	0.0547	0.0081	0.0518
Nrf-2	0.0524	0.00042	0.000181	0.000524

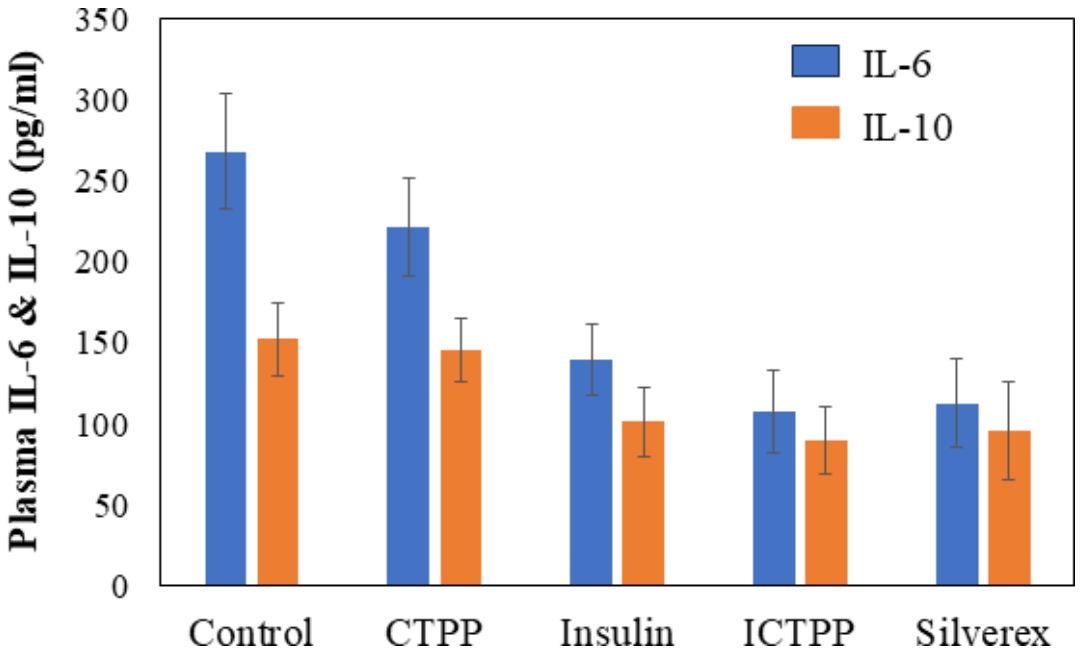

Figure. 48. The figure shows the post-burn injury plasma IL-6 and IL-10 levels *collected on day 20 to analyze the inflammatory phases. Data are mean ± SEM; n=3/group.*

5.4 Conclusion

Burn wound healing poses a significant challenge in healthcare due to slow re-epithelialization and high susceptibility to microbial infection, ultimately affecting over 10 million people annually, as per the WHO report. Addressing this issue is crucial to alleviate the burden on the health sector, and protein-based nano-formulations are gaining attention depending on their characteristic features and potential to cure injuries. Insulin promotes healing in normal and diabetic conditions, but the potential and mechanism behind burn wound healing are yet to be explored. Insulin-based nano-formulations outperform conventional insulin due to high stability, enhanced solubility, improved bioavailability, high entrapment efficiency, and controlled release. This study highlights a potential nano-formulation involving chitosan-insulin nanoparticles as advanced therapeutic agents for burn wound healing and tissue regeneration.

Different techniques were used to monitor insulin and chitosan interactions, followed by their biocompatibility and wound healing studies *in vitro* and *in vivo* systems. The enhanced cell migration observed in ICNP-treated cells suggests their role in promoting cell proliferation, which is critical for the recovery of wounds. The combination index calculations affirmed the synergistic effect of chitosan and insulin. In the animal burn wound model, the ICNP-treated group exhibited a remarkable 29.3% decrease in the wound area when compared to other groups in the initial days of treatment, signifying its early efficacy. Subsequently, all treatment groups displayed differential wound closure in comparison with control following 10 days of treatment, while the ICNP-treated group demonstrated the highest rate of wound contraction of 95.77% after 20 days. Histological examinations after 10 and 20 days showed the least inflammatory cell infiltration, the complete absence of wound eschar, and significant reepithelization in the treated group. Masson's trichrome collagen staining indicated enhanced collagen fiber deposition in the ICNP-treated group, as shown by the intensive blue-stained area, indicating its potential in collagen synthesis during wound healing.

Further, the cytokine analysis on day 10 demonstrated that ICNP effectively suppressed pro-inflammatory cytokine IL-6 while elevating anti-inflammatory cytokine IL-10, and this trend persisted till day 20, showing its superior modulation of pro-inflammatory and anti-inflammatory cytokine profiles, while control and ECNP groups at day 20 indicated an ongoing pro-inflammatory response. Immunohistochemical staining revealed that ICNP significantly upregulated Nrf-2 expression compared to all other groups on day 10 of treatment, suggesting enhanced cellular defense against oxidative stress and inflammation. Nrf-2 is pivotal in regulating intracellular redox homeostasis by increasing cytoprotective gene expression, and its activation accelerates diabetic wound healing by facilitating diabetes-mediated oxidative stress and inflammation [393]. Considering that insulin possesses anti-inflammatory properties, the increased Nrf-2 expression in the ICNP-treated group indicated that ICNP regulates inflammation through Nrf-2 activation. Few studies show the protective roles of Nrf-2 in burn trauma-induced intestinal injury and burn-induced cardiac dysfunction [428],[429] as well as the role of topical insulin [34] or insulin nanoparticles [37] in burn wound healing, but none has implicated the role of insulin in activation of Nrf-2 pathway. Further, different formulations are being developed for burn wound healing, including the topical application of simvastatin on the burn wound Wistar rat model, and it was found to promote healing by modulating Akt/mTOR signaling pathway along with increased CD31 VEGF levels. Similarly, when the simvastatin was incorporated with bone marrow-derived mesenchymal stem cells, the outcomes showed synergistic effect in enhanced re-epithelialization, higher wound closure area, enhanced collagen deposition, and epidermal regeneration and followed the same Akt/mTOR pathway for healing burn injuries [374],[399].

Our study showed effective modulation of inflammatory phases by activating the Nrf-2 pathway, underscoring its promise as a therapeutic intervention in burn care and management. This field holds remarkable potential to improve the lives of burn injury sufferers. The excellent drug loading and release efficiency and their potential in treating burn wounds *in vitro* and *in vivo* hold great value and can serve as a catalyst in burn wound healing research. Further, the global market of protein-based nanoformulations is rapidly expanding and is projected to double from $14 billion in 2020 to $28 billion by 2025, indicating its vast potential in the near future [430]. I firmly believe that the injury healing and anti-inflammatory properties of these particles and the key findings of this report will have a lasting impact, fostering innovation and ability to inspire future research in the field of burn wounds across the research community, ultimately improving and saving the lives of patients fighting against burn injuries.

Chapter 6: Conclusion and Future Perspectives

6.1 Conclusion

Protein-based nanoformulations offer a potent combination of biocompatibility, efficiency, and precision in targeted drug delivery, thus leading to groundbreaking advancements in the field of wound healing. These formulations enhance the protein's biological activity, ensuring that they remain active and effective over extended periods and stabilize the proteins. Additionally, these formulations exhibit a sustained release mechanism, which is crucial in accelerating the healing process and preventing complications such as infections, which are common in chronic wounds and burn injuries. By integrating proteins into distinct delivery formulations—like ointments, dressings, scaffolds, hydrogels, and electrospun fibers—these nanoformulations showcase their remarkable versatility and ability to address different wound types and healing requirements. The increasing demand for protein-functionalized nanomaterials is a testament to their potential to revolutionize wound care. However, to fully harness this potential, it is essential to streamline the synthesis processes, making them more efficient and scalable. This would not only enhance the applicability of these nanoformulations in therapeutic and theranostic fields but also pave the way for their widespread use in personalized medicine. Personalized wound care, particularly for chronic conditions like diabetic ulcers, could benefit immensely from these advancements. By tailoring the nanoformulations to the specific needs of individual patients, healthcare providers can achieve more effective and rapid healing, reducing the overall burden of chronic wounds.

The research that I have done in this field has underscored the significant potential of insulin and metal-based nanoparticles in the realm of wound healing, especially in managing complex scenarios like diabetic and burn wounds. For instance, studies that I have carried forward in this thesis have demonstrated that insulin, when combined with metals such as cobalt, nickel, silver, and copper in nanoformulations, can work synergistically to promote cellular growth, reduce inflammation, and enhance antimicrobial activity. These nanoformulations are particularly effective in targeting specific wound sites, thereby improving healing rates and reducing the risk of infection. Additionally, their applications extend beyond wound healing to include bioimaging and biosensing, offering a multifunctional approach to wound management. The development of novel protein-based nanoformulations, including core-shell nanoparticles and bimetallic nanosubclusters, has further expanded the possibilities in wound care. These advanced formulations are designed to tackle the unique challenges posed by conditions like diabetes, where impaired tissue recovery becomes a significant concern. By leveraging the antioxidant, anti-inflammatory, and antimicrobial activities of these formulations, I have achieved contamination-free recovery and improved healing outcomes. Furthermore, the ability of insulin-loaded chitosan nanoformulations to modulate cellular responses through key pathways such as Nrf-2 highlights their potential as therapeutic agents that can address not only the symptoms but also the underlying mechanisms of delayed wound healing.

In conclusion, protein-based nanoformulations hold immense promise for the future of wound healing. Their ability to revolutionize treatment approaches in both medical and commercial contexts cannot be overstated. As research and innovation in this field continue to advance, the full range of their capabilities will likely be explored, leading to improved outcomes for millions of patients worldwide. The expanding global market for these formulations, coupled with the encouraging results from recent studies, suggests that protein-based nanoformulations are poised to act as vital agents in the field of wound care. These formulations give new hope to patients infected with chronic or burn injuries, along side different challenging conditions, potentially transforming the landscape of wound management and significantly enhancing the quality of life for those

affected.

6.2 Future Perspectives of Protein-based metallic nanoformulations in wound healing

The future of protein-based nanoformulations in wound healing is poised for significant advancements, with several key areas of development likely to shape their impact:

1. With the recent developments in the field of personalized medicine, protein-based nanoformulations could be modified as per an individual's requirement. The need of the hour is to customize nanoformulations for promoting the efficiency and speed of wound healing by analyzing a patient's unique wound characteristics and underlying conditions, such as diabetes or autoimmune disorders. This individualized approach may lead to more precise and effective treatments, reducing healing times and minimizing the risk of complications.

2. More research needs to be focused on discovering the *in vivo* injury healing and anti-inflammatory abilities of ICoNPs, ICu-AgNSCs, and INiQCs. *in vivo,* bioimaging using ICoNPs and INiQCs also needs to be explored.

3. It is also necessary to translate the synthesized four nanoformulations into pre-clinical and clinical models. These formulations have a bright future in therapeutic and theranostics, and they can be used as promising drug carriers, making the delivery targeted and effective. Clinical trials will be crucial in validating the efficacy and safety of protein-based nanoformulations. These trials will provide the data necessary to refine formulations, determine optimal dosages, and identify any potential long-term effects. The translation of research findings into clinical practice will be a key focus, ensuring that the benefits of these innovations reach patients as quickly and safely as possible.

4. Future research is expected to focus on refining the drug delivery systems associated with protein-based nanoformulations by incorporating new innovations such as stimuli-responsive nanoparticles, which release therapeutic agents after getting exposed to some external factor like pH, temperature, or some enzymes to significantly improve the therapeutic outcomes and decreasing the potential negative aspects through limiting drug release at specific targeted site.

5. Apart from the basic wound healing application, protein-based nanoformulations are likely to see expanded applications in bioimaging and biosensing, which could lead to the development of multifunctional platforms that not only diagnose and monitor but treat wounds simultaneously. For instance, nanoformulations could be designed to change color or fluorescence in response to infection, providing real-time feedback to healthcare providers and enabling prompt intervention.

6. The intersection of protein-based nanoformulations with regenerative medicine and tissue engineering offers exciting possibilities by integrating them with biomaterials like scaffolds or matrices used in tissue regeneration, which promotes not only wound healing but also the regeneration of damaged tissues which could be of specific interest in case of severe burns or chronic ulcers where traditional healing processes are insufficient.

7. The next step is to meet the increased demand for these nanoformulations, for which the focus will shift toward making synthesis processes more scalable and cost-effective. Advances in manufacturing techniques, including the use of green chemistry and sustainable

materials, could drive down costs and make these treatments more accessible to a broader range of patients. Also, due to the growing occurrence of chronic wounds and the increasing aging population, the global market for protein-based nanoformulations is expected to expand rapidly. Future developments will likely see these treatments becoming a standard part of wound care protocols worldwide, particularly in regions with high incidences of diabetes and other chronic conditions that impair wound healing.

8. As these nanoformulations evolve, researchers will need to address emerging challenges such as nanoparticle toxicity, long-term stability, and potential immune responses. Advances in nanotechnology and protein engineering will likely results in developing safer and more efficient formulations capable of overcoming these hurdles.

6.3 Multiple ways by which nanoformulations can be modified as per the needs of the patient.

1. **Selection of metal-ion** – The metal-ion can be selected based on the patients need and type of wound (chronic, diabetic, or infective wound) as metal ions determine the biological activity of formulation. For instance, if the patient is suffering from infection in wounds, silver ion can be used. Similarly, copper is useful for promoting angiogenesis and collagen synthesis. Zinc oxide enhances epithelialization by promoting cell proliferation and support.
2. **Selection of protein** – Proteins can be selected based on an individual's healing deficiencies. For instance, insulin can be used in patients suffering from diabetic wounds as it enhances the conversion of M1 macrophages to M2 macrophages. Similarly, collagen can be used in old age patients who face decreased collagen secretion with age, and collagen itself is critical for healing as it acts as a scaffold for cell growth and supports tissue repair.
3. **Size and shape of nanoparticles** – The size and shape need to be determined beforehand as they influence the bioavailability and cellular interactions. The smaller the particle (less than 10 nm) size, the better the penetration, the better antibacterial efficacy, and exhibit the rapid action; thus, it can be used in acute wounds. On the other hand, particles with large sizes (more than 50 nm) are used for sustained drug release for a prolonged period and thus can be used in patients suffering from chronic wounds.
4. **Surface Functionalization** – The therapeutic efficacy of nanoparticles is enhanced manifolds by surface functionalization. The surface can be modified in different manners like antimicrobial peptides can be used to coat nanoparticles and make them effective against infected wounds by increasing antimicrobial potential. Also, the utilization of polymeric coatings like chitosan provides sustained release and helps in moisture retention. The use of growth factors to promote cell proliferation and angiogenesis can be helpful in ischemic wounds.
5. **Integration with Biomaterials** – The synthesized formulations can be integrated into wound dressings or scaffolds. Bandages can be coated with nanoparticles to increase wound healing and antimicrobial efficacy. Hydrogels can be loaded with nanoparticles to get prolonged drug release with moisture retention.

In summary, the future of protein-based nanoformulations in wound healing is incredibly promising, with the potential to revolutionize how wounds are treated. Continued research and innovation will be essential in unlocking their full potential, ultimately leading to more effective, personalized, and accessible wound care solutions which will improve the life quality for patients globally.

References

[1] Z. Wang, Z. Wang, W.W. Lu, W. Zhen, D. Yang, S. Peng, Novel biomaterial strategies for controlled growth factor delivery for biomedical applications, NPG Asia Materials 9 (2017) e435–e435. https://doi.org/10.1038/am.2017.171.

[2] S.F. Oliveira, G. Bisker, N.A. Bakh, S.L. Gibbs, M.P. Landry, M.S. Strano, Protein functionalized carbon nanomaterials for biomedical applications, Carbon NY 95 (2015) 767–779. https://doi.org/10.1016/J.CARBON.2015.08.076.

[3] K. Liu, L. Han, J. Zhuang, D.P. Yang, Protein-directed gold nanoparticles with excellent catalytic activity for 4-nitrophenol reduction, Mater Sci Eng C Mater Biol Appl 78 (2017) 429–434. https://doi.org/10.1016/J.MSEC.2017.04.052.

[4] F. Wang, W.B. Tan, Y. Zhang, X. Fan, M. Wang, Luminescent nanomaterials for biological labelling, Nanotechnology 17 (2006) R1-R3. https://doi.org/10.1088/0957-4484/17/1/R01.

[5] J.L. Swift, D.T. Cramb, Nanoparticles as fluorescence labels: is size all that matters?, Biophys J 95 (2008) 865–876. https://doi.org/10.1529/BIOPHYSJ.107.127688.

[6] S.L. Gawali, S.B. Shelar, J. Gupta, K.C. Barick, P.A. Hassan, Immobilization of protein on Fe 3 O 4 nanoparticles for magnetic hyperthermia application, Int J Biol Macromol 166 (2021) 851–860. https://doi.org/10.1016/J.IJBIOMAC.2020.10.241.

[7] X. Liu, H. Zhang, L. Chang, B. Yu, Q. Liu, J. Wu, Y. Miao, P. Ma, D. Fan, H. Fan, Human-like collagen protein-coated magnetic nanoparticles with high magnetic hyperthermia performance and improved biocompatibility, Nanoscale Res Lett 10 (2015) 28-36. https://doi.org/10.1186/S11671-015-0752-3.

[8] S. Vieira, S. Vial, R.L. Reis, J.M. Oliveira, Nanoparticles for bone tissue engineering, Biotechnol Prog 33 (2017) 590–611. https://doi.org/10.1002/BTPR.2469.

[9] W. Lohcharoenkal, L. Wang, Y.C. Chen, Y. Rojanasakul, Protein nanoparticles as drug delivery carriers for cancer therapy, Biomed Res Int 2014 (2014) 180459. https://doi.org/10.1155/2014/180549.

[10] Y. Dang, J. Guan, Nanoparticle-based drug delivery systems for cancer therapy, Smart Mater Med 1 (2020) 10–19. https://doi.org/10.1016/J.SMAIM.2020.04.001.

[11] A.M.M. Brito, E. Belleti, L.R. Menezes, A.J.C. Lanfredi, I.L. Nantes-Cardoso, Proteins and Peptides at the Interfaces of Nanostructures., An Acad Bras Cienc 91 (2019) e20181236–e20181236. https://doi.org/10.1590/0001-3765201920181236.

[12] K. Siriwardana, A. Wang, M. Gadogbe, W.E. Collier, N.C. Fitzkee, D. Zhang, Studying the Effects of Cysteine Residues on Protein Interactions with Silver Nanoparticles, J Phys Chem C Nanomater Interfaces 119 (2015) 2910–2916. https://doi.org/10.1021/JP512440Z.

[13] R. Subbiah, M. Veerapandian, K. S. Yun, Nanoparticles: functionalization and multifunctional applications in biomedical sciences, Curr Med Chem 17 (2010) 4559–4577. https://doi.org/10.2174/092986710794183024.

[14] P. Kaur, S. Sharma, S.D. Choudhury, D. Singh, S. Sharma, K. Gadhave, N. Garg, D. Choudhury, Insulin-copper quantum clusters preparation and receptor targeted bioimaging, Colloids Surf B Biointerfaces 188 (2020) 110875. https://doi.org/10.1016/J.COLSURFB.2020.110785.

[15] P. Kaur, D. Choudhury, Functionality of receptor targeted zinc-insulin quantum clusters in skin tissue augmentation and bioimaging, J Drug Target 29 (2021) 541–550. https://doi.org/10.1080/1061186X.2020.1864740.

[16] D. Sharda, K. Attri, P. Kaur, D. Choudhury, Protection of lead-induced cytotoxicity using paramagnetic nickel-insulin quantum clusters, RSC Adv 11 (2021) 24656–24668. https://doi.org/10.1039/D1RA03597E.

[17] A. Tofanello, É.G.A. Miranda, I.W.R. Dias, A.J.C. Lanfredi, J.T. Arantes, M.A. Juliano, I.L. Nantes, pH-Dependent Synthesis of Anisotropic Gold Nanostructures by Bioinspired Cysteine-Containing Peptides, ACS Omega 1 (2016) 424–434. https://doi.org/10.1021/ACSOMEGA.6B00140.

[18] M. Yu, J. Wu, J. Shi, O.C. Farokhzad, Nanotechnology for protein delivery: Overview and perspectives, J Con Rel 240 (2016) 24–37. https://doi.org/10.1016/j.jconrel.2015.10.012.
[19] X. Zhu, J. Wu, W. Shan, W. Tao, L. Zhao, J. Lim, M. D'Ortenzio, R. Karnik, Y. Huang, J. Shi, Polymeric nanoparticles amenable to simultaneous installation of exterior targeting and interior therapeutic proteins, Angew Chem Int Ed Engl. 128 (2016) 3309–3312. https://doi.org/10.1002/anie.201509183.
[20] J. Wu, N. Kamaly, J. Shi, L. Zhao, Z. Xiao, G. Hollett, R. John, S. Ray, X. Xu, X. Zhang, Development of multinuclear polymeric nanoparticles as robust protein nanocarriers, Angew Chem Int Ed Engl. 53 (2014) 8975–8979. https://doi.org/10.1002/anie.201404766.
[21] X. Chen, X. Ling, L. Zhao, F. Xiong, G. Hollett, Y. Kang, A. Barrett, J. Wu, Biomimetic shells endow sub-50 nm nanoparticles with ultrahigh paclitaxel payloads for specific and robust chemotherapy, ACS Appl Mater Interfaces 10 (2018) 33976–33985. https://doi.org/10.1021/acsami.8b11571.
[22] R. Hama, J.W. Reinhardt, A. Ulziibayar, T. Watanabe, J. Kelly, T. Shinoka, Recent tissue engineering approaches to mimicking the extracellular matrix structure for skin regeneration, Biomimetics 8 (2023) 130. https://doi.org/10.3390/biomimetics8010130.
[23] G. Ghosh, L. Panicker, Protein-nanoparticle interactions and a new insight, Soft Matter 17 (2021) 3855–3875. https://doi.org/10.1039/D0SM02050H.
[24] F. Strodtbeck, Physiology of wound healing, Newborn Infant Nurs Rev 1 (2001) 43–52. https://doi.org/10.1053/NBIN.2001.23176.
[25] E.M. Golebiewska, A.W. Poole, Platelet secretion: From haemostasis to wound healing and beyond, Blood Rev 29 (2015) 153–162. https://doi.org/10.1016/j.blre.2014.10.003.
[26] D. Scully, P. Sfyri, H.N. Wilkinson, A. Acebes-Huerta, S. Verpoorten, M.C. Muñoz-Turrillas, A. Parnell, K. Patel, M.J. Hardman, L. Gutierrez, Optimising platelet secretomes to deliver robust tissue-specific regeneration, J Tissue Eng Regen Med 14 (2020) 82–98. . https://doi.org/10.1002/term.2965.
[27] E. Kolaczkowska, P. Kubes, Neutrophil recruitment and function in health and inflammation, Nat Rev Immunol 13 (2013) 159–175. https://doi.org/10.1038/nri3399.
[28] M. Phillipson, P. Kubes, The healing power of neutrophils, Trends Immunol 40 (2019) 635–647. https://doi.org/10.1016/j.it.2019.05.001.
[29] M. Xue, C.J. Jackson, Extracellular matrix reorganization during wound healing and its impact on abnormal scarring, Adv Wound Care (New Rochelle) 4 (2015) 119–136. https://doi.org/10.1089/wound.2013.0485.
[30] P. Rousselle, F. Braye, G. Dayan, Re-epithelialization of adult skin wounds: Cellular mechanisms and therapeutic strategies, Adv Drug Deliv Rev 146 (2019) 344–365. https://doi.org/10.1016/j.addr.2018.06.019.
[31] T.M. Honnegowda, P. Kumar, E.G.P. Udupa, S. Kumar, U. Kumar, P. Rao, Role of angiogenesis and angiogenic factors in acute and chronic wound healing, Plast Aesthet Res 2 (2015) 243–249. https://doi.org/10.4103/2347-9264.165438.
[32] R.A. Poché, C.-W. Hsu, M.L. McElwee, A.R. Burns, M.E. Dickinson, Macrophages engulf endothelial cell membrane particles preceding pupillary membrane capillary regression, Dev Biol 403 (2015) 30–42. https://doi.org/10.1016 /j.ydbio.2015.03.017.
[33] I.A. Darby, B. Laverdet, F. Bonté, A. Desmoulière, Fibroblasts and myofibroblasts in wound healing, Clin Cosmet Investig Dermatol (2014) 301–311. https://doi.org/ 10.2147/CCID.S50046.
[34] S.S. Mathew-Steiner, S. Roy, C.K. Sen, Collagen in wound healing, Bioengineering 8 (2021) 63. https://doi.org/ 10.3390/bioengineering8050063.
[35] H.N. Wilkinson, M.J. Hardman, Wound healing: Cellular mechanisms and pathological outcomes, Open Biol 10 (2020) 200223. https://doi.org/ 10.1098/rsob.200223.
[36] B. Kahle, H.-J. Hermanns, G. Gallenkemper, Evidence-based treatment of chronic leg ulcers, Dtsch Arztebl Int 108 (2011) 231-237. https://doi.org/10.3238/ARZTEBL.2011.0231.
[37] S. Guo, L.A. DiPietro, Factors affecting wound healing, J Dent Res 89 (2010) 219–229.

https://doi.org/10.1177/0022034509359125.
[38] J. Larouche, S. Sheoran, K. Maruyama, M.M. Martino, Immune Regulation of Skin Wound Healing: Mechanisms and Novel Therapeutic Targets, Adv Wound Care (New Rochelle) 7 (2018) 209–231. https://doi.org/10.1089/WOUND.2017.0761.
[39] P. Kaur, D. Choudhury, Insulin Promotes Wound Healing by Inactivating NFkβP50/P65 and Activating Protein and Lipid Biosynthesis and alternating Pro/Anti-inflammatory Cytokines Dynamics, Biomol Concepts 10 (2019) 11–24. https://doi.org/10.1515/BMC-2019-0002.
[40] S.M. McCormick, N.M. Heller, Regulation of Macrophage, Dendritic Cell, and Microglial Phenotype and Function by the SOCS Proteins, Front Immunol 6 (2015) 549. https://doi.org/10.3389/FIMMU.2015.00549.
[41] A. Kasuya, Y. Tokura, Attempts to accelerate wound healing, J Dermatol Sci 76 (2014) 169–172. https://doi.org/10.1016/J.JDERMSCI.2014.11.001.
[42] D. Sharda, K. Attri, D. Choudhury, Future research directions of antimicrobial wound dressings, Antimicrobial Dressings (2023) 229–246. https://doi.org/10.1016/B978-0-323-95074-9.00007-5.
[43] S.K. Gupta, Impact of ulceration, Ulcers of the Lower Extremity (2016) 9–14. https://doi.org/10.1007/978-81-322-2635-2_2/COVER.
[44] L.M. Martins, A.R.S. Oliveira, K.J.C. Cruz, F.L. Orres-Leal, D. do N. Marreiro, Obesity, inflammation, and insulin resistance, Braz J Pharm Sci 50 (2014) 677–692. https://doi.org/10.1590/S1984-82502014000400003.
[45] S. Apikoglu-Rabus, F. V. Izzettin, P. Turan, F. Ercan, Effect of topical insulin on cutaneous wound healing in rats with or without acute diabetes, Clin Exp Dermatol 35 (2010) 180–185. https://doi.org/10.1111/J.1365-2230.2009.03419.X.
[46] C. Watters, J.A. Everett, C. Haley, A. Clinton, K.P. Rumbaugh, (C Watters, K. Deleon, U. Trivedi, J.A. Gris-Wold, M. Lyte, K.J. Hampel, M.J. Wargo, K.P. Rumbaugh, Insulin treatment modulates the host immune system to enhance Pseudomonas aeruginosa wound biofilms., Infect Immun 82 (2013) 92–100. https://doi.org/10.1128/IAI.00651-13.
[47] M. Hrynyk, R.J. Neufeld, Insulin and wound healing, Burns 40 (2014) 1433–1446. https://doi.org/10.1016/J.BURNS.2014.03.020.
[48] A. Oryan, E. Alemzadeh, Effects of insulin on wound healing: A review of animal and human evidences., Life Sci 174 (2017) 59–67. https://doi.org/10.1016/J.LFS.2017.02.015.
[49] P. Kaur, A.K. Sharma, D. Nag, A. Das, S. Datta, A. Ganguli, V. Goel, S. Rajput, G. Chakrabarti, B. Basu, D. Choudhury, Novel nano-insulin formulation modulates cytokine secretion and remodeling to accelerate diabetic wound healing, Nanomedicine 15 (2019) 47–57. https://doi.org/10.1016/J.NANO.2018.08.013.
[50] H.W. Ju, O.J. Lee, J.M. Lee, B.M. Moon, H.J. Park, Y.R. Park, M.C. Lee, S.H. Kim, J.R. Chao, C.S. Ki, C.H. Park, Wound healing effect of electrospun silk fibroin nanomatrix in burn-model, Int J Biol Macromol 85 (2016) 29–39. https://doi.org/10.1016/J.IJBIOMAC.2015.12.055.
[51] T.P. Nguyen, Q.V. Nguyen, V.-H. Nguyen, T.-H. Le, V.Q.N. Huynh, D.-V.N. Vo, Q.T. Trinh, S.Y. Kim, Q. Van Le, Silk fibroin-based biomaterials for biomedical applications: A review, Polymers (Basel) 11 (2019) 1933. https://doi.org/ 10.3390/polym11121933.
[52] C. Martínez-Mora, A. Mrowiec, E.M. García-Vizcaíno, A. Alcaraz, J.L. Cenis, F.J. Nicolás, Fibroin and sericin from Bombyx mori silk stimulate cell migration through upregulation and phosphorylation of c-Jun, PLoS One 7 (2012) e42271. https://doi.org/10.1371/JOURNAL.PONE.0042271.
[53] Y. Kambe, Functionalization of silk fibroin-based biomaterials for tissue engineering, Polym J 53 (2021) 1345–1351. https://doi.org/10.1038/s41428-021-00536-5.
[54] Y.R. Park, M.T. Sultan, H.J. Park, J.M. Lee, H.W. Ju, O.J. Lee, D.J. Lee, D.L. Kaplan, C.H. Park, NF-κB signaling is key in the wound healing processes of silk fibroin, Acta Biomater 67 (2018) 183–195. https://doi.org/10.1016/J.ACTBIO.2017.12.006.
[55] R. Wu, H. Li, Y. Yang, Q. Zheng, S. Li, Y. Chen, Bioactive Silk Fibroin-Based Hybrid Biomaterials for Musculoskeletal Engineering: Recent Progress and Perspectives, ACS Appl Bio Mater 4 (2021)

6630–6646. https://doi.org/10.1021/ACSABM.1C00654.
[56] J. Wang, S. Hao, T. Luo, Z. Cheng, W. Li, F. Gao, T. Guo, Y. Gong, B. Wang, Feather keratin hydrogel for wound repair: Preparation, healing effect and biocompatibility evaluation, Colloids Surf B Biointerfaces 149 (2017) 341–350. https://doi.org/10.1016/J.COLSURFB.2016.10.038.
[57] S. Feroz, N. Muhammad, J. Ratnayake, G. Dias, Keratin-Based materials for biomedical applications, Bioact Mater 5 (2020) 496–509. https://doi.org/ 10.1016/j.bioactmat.2020.04.007.
[58] X. Chen, D. Zhai, B. Wang, S. Hao, J. Song, Z. Peng, Hair keratin promotes wound healing in rats with combined radiation-wound injury, J Mater Sci Mater Med 31 (2020) 28. https://doi.org/10.1007/S10856-020-06365-X.
[59] L.R. Burnett, M.B. Rahmany, J.R. Richter, T.A. Aboushwareb, D. Eberli, C.L. Ward, G. Orlando, R.R. Hantgan, M.E. Van Dyke, Hemostatic properties and the role of cell receptor recognition in human hair keratin protein hydrogels, Biomaterials 34 (2013) 2632–2640. https://doi.org/10.1016/J.BIOMATERIALS.2012.12.022.
[60] M.B. Rahmany, R.R. Hantgan, M. Van Dyke, A mechanistic investigation of the effect of keratin-based hemostatic agents on coagulation, Biomaterials 34 (2013) 2492–2500. https://doi.org/10.1016/J.BIOMATERIALS.2012.12.008.
[61] S. Xu, L. Sang, Y. Zhang, X. Wang, X. Li, Biological evaluation of human hair keratin scaffolds for skin wound repair and regeneration, Mater Sci Eng C Mater Biol Appl 33 (2013) 648–655. https://doi.org/10.1016/J.MSEC.2012.10.011.
[62] S. Wang, Z. Wang, S.E.M. Foo, N.S. Tan, Y. Yuan, W. Lin, Z. Zhang, K.W. Ng, Culturing fibroblasts in 3D human hair keratin hydrogels, ACS Appl Mater Interfaces 7 (2015) 5187–5198. https://doi.org/10.1021/ACSAMI.5B00854.
[63] I.M. Freedberg, M. Tomic-Canic, M. Komine, M. Blumenberg, Keratins and the keratinocyte activation cycle, J Invest Dermatol 116 (2001) 633–640. https://doi.org/10.1046/J.1523-1747.2001.01327.X.
[64] X. Zhang, M. Yin, L.J. Zhang, Keratin 6, 16 and 17—Critical Barrier Alarmin Molecules in Skin Wounds and Psoriasis, Cells 8 (2019) 807. https://doi.org/10.3390/CELLS8080807.
[65] D.M. Reilly, J. Lozano, Skin collagen through the lifestages: Importance for skin health and beauty, Plast. Aesthetic Res 8 (2021). https://doi.org/ 10.20517/2347-9264.2020.153.
[66] S. Chattopadhyay, R.T. Raines, Collagen-based biomaterials for wound healing, Biopolymers 101 (2014) 821–833. https://doi.org/10.1002/BIP.22486.
[67] S.S. Mathew-Steiner, S. Roy, C.K. Sen, Collagen in Wound Healing, Bioengineering (Basel) 8 (2021) 63. https://doi.org/10.3390/BIOENGINEERING8050063.
[68] R.A. Hatz, N.C.S. von Jan, F.-W. Schildberg, Mechanisms of Action of Collagenase in Wound Repair, Wound Healing and Skin Physiology (1995) 227–237. https://doi.org/10.1007/978-3-642-77882-7_20.
[69] T. Sekine, T. Nakamura, Y. Shimizu, H. Ueda, K. Matsumoto, Y. Takimoto, T. Kiyotani, A new type of surgical adhesive made from porcine collagen and polyglutamic acid, J Biomed Mater Res 54 (2001) 305-310. https://doi.org/10.1002/1097-4636(200102)54:2<305::aid-jbm18>3.0.co;2-b.
[70] C. Hao, H. Xu, L. Yu, L. Zhang, Heparin: an essential drug for modern medicine, Prog Mol Biol Transl Sci 163 (2019) 1–19. https://doi.org/ 10.1016/bs.pmbts.2019.02.002.
[71] M.C. Goh, Y. Hwang, G. Tae, Epidermal growth factor loaded heparin-based hydrogel sheet for skin wound healing, Carbohydr Polym 147 (2016) 251–260. https://doi.org/10.1016/J.CARBPOL.2016.03.072.
[72] L. GALVAN, Effects of heparin on wound healing, Journal of WOCN 23 (1996) 224–226. https://doi.org/10.1016/S1071-5754(96)90095-9.
[73] P. Olczyk, Ł. Mencner, K. Komosinska-Vassev, Diverse Roles of Heparan Sulfate and Heparin in Wound Repair, Biomed Res Int 2015 (2015) 549417. https://doi.org/10.1155/2015/549417.
[74] A. Nawaz, S. Zaman Safi, S. Sikandar, R. Zeeshan, S. Zulfiqar, N. Mehmood, H.M. Alobaid, F. Rehman, M. Imran, M. Tariq, A. Ali, T. Bin Emran, M. Yar, Heparin-Loaded Alginate Hydrogels: Characterization and Molecular Mechanisms of Their Angiogenic and Anti-Microbial Potential,

Materials (Basel) 15 (2022) 6683. https://doi.org/10.3390/MA15196683.
[75] J. Zheng, W. Zhang, L. Li, Y. He, Y. Wei, Y. Dang, S. Nie, Z. Guo, Signaling pathway and small-molecule drug discovery of FGFR: A comprehensive review, Front Chem 10 (2022) 860985. https://doi.org/ 10.3389/fchem.2022.860985.
[76] L. Benington, G. Rajan, C. Locher, L.Y. Lim, Fibroblast growth factor 2—A review of stabilisation approaches for clinical applications, Pharmaceutics 12 (2020) 508. https://doi.org/ 10.3390/pharmaceutics12060508.
[77] K. Takaya, N. Aramaki-Hattori, S. Sakai, K. Okabe, T. Asou, K. Kishi, Fibroblast growth factor 7 suppresses fibrosis and promotes epithelialization during wound healing in mouse fetuses, Int J Mol Sci 23 (2022) 7087. https://doi.org/ 10.3390/ijms23137087.
[78] W. Xiaojie, J. Banda, H. Qi, A.K. Chang, C. Bwalya, L. Chao, X. Li, Scarless wound healing: Current insights from the perspectives of TGF-β, KGF-1, and KGF-2, Cytokine Growth Factor Rev 66 (2022) 26–37. https://doi.org/ 10.1016/j.cytogfr.2022.03.001.
[79] M. Monavarian, S. Kader, S. Moeinzadeh, E. Jabbari, Regenerative scar-free skin wound healing, Tissue Eng Part B Rev 25 (2019) 294–311. https://doi.org/ 10.1089/ten.TEB.2018.0350.
[80] A.G. Goswami, S. Basu, F. Huda, J. Pant, A. Ghosh Kar, T. Banerjee, V.K. Shukla, An appraisal of vascular endothelial growth factor (VEGF): The dynamic molecule of wound healing and its current clinical applications, Growth Factors 40 (2022) 73–88. https://doi.org/ 10.1080/08977194.2022.2074843.
[81] C. Mohanty, J. Pradhan, A human epidermal growth factor-curcumin bandage bioconjugate loaded with mesenchymal stem cell for in vivo diabetic wound healing, Mater Sci Eng C Mater Biol Appl 111 (2020) 110751. https://doi.org/ 10.1016/j.msec.2020.110751.
[82] F. Xu, H. Wang, J. Zhang, L. Jiang, W. Zhang, Y. Hu, A facile design of EGF conjugated PLA/gelatin electrospun nanofibers for nursing care of in vivo wound healing applications, JInd Text 51 (2022) 420S-440S. https://doi.org/ 10.1177/1528083720976348.
[83] K. Jian, C. Yang, T. Li, X. Wu, J. Shen, J. Wei, Z. Yang, D. Yuan, M. Zhao, J. Shi, PDGF-BB-derived supramolecular hydrogel for promoting skin wound healing, J Nanobiotechnology 20 (2022) 1–9. https://doi.org/ 10.1186/s12951-022-01390-0.
[84] X. Gong, Self-Assembly Technique for Biomedical Applications, Nano Life 05 (2015) 1542002. https://doi.org/10.1142/S1793984415420027.
[85] X. Liu, X. Gong, Q. Hu, Y. Li, Ion-modulated flow behavior of layer-by-layer fabricated polymer thin films, RSC Adv 5 (2015) 64192–64195. https://doi.org/10.1039/C5RA11734H.
[86] N. Desai, Challenges in development of nanoparticle-based therapeutics, AAPS J 14 (2012) 282–295. https://doi.org/10.1208/S12248-012-9339-4.
[87] R. Bawa, Nanoparticle-based Therapeutics in Humans: A Survey, Nanotechnol Law Bus. 5 (2008) 135-155.
[88] G. Goncalves, P.A.A.P. Marques, C.M. Granadeiro, H.I.S. Nogueira, M.K. Singh, J. Grácio, Surface modification of graphene nanosheets with gold nanoparticles: The role of oxygen moieties at graphene surface on gold nucleation and growth, Chemistry of Materials 21 (2009) 4796–4802. https://doi.org/10.1021/CM901052S.
[89] M. Mahmoudi, S. Sant, B. Wang, S. Laurent, T. Sen, Superparamagnetic iron oxide nanoparticles (SPIONs): development, surface modification and applications in chemotherapy, Adv Drug Deliv Rev 63 (2011) 24–46. https://doi.org/10.1016/J.ADDR.2010.05.006.
[90] D. Cheng, X. Yong, T. Zhu, Y. Qiu, J. Wang, H. Zhu, B. Ma, J. Xie, Synthesis of protein nanoparticles for drug delivery, Eur J BioMed Res 2 (2016) 8. https://doi.org/10.18088/EJBMR.2.2.2016.PP8-11.
[91] F. Fehse, M. Trautmann, J.J. Holst, A.E. Halseth, N. Nanayakkara, L.L. Nielsen, M.S. Fineman, D.D. Kim, M.A. Nauck, Exenatide augments first- and second-phase insulin secretion in response to intravenous glucose in subjects with type 2 diabetes, J Clin Endocrinol Metab 90 (2005) 5991–5997. https://doi.org/10.1210/JC.2005-1093.
[92] S.K. Jain, Y. Gupta, A. Jain, A.R. Saxena, P. Khare, A. Jain, Mannosylated gelatin nanoparticles

bearing an anti-HIV drug didanosine for site-specific delivery, Nanomedicine 4 (2008) 41–48. https://doi.org/10.1016/J.NANO.2007.11.004.
[93] S. Balthasar, K. Michaelis, N. Dinauer, H. Von Briesen, J. Kreuter, K. Langer, Preparation and characterisation of antibody modified gelatin nanoparticles as drug carrier system for uptake in lymphocytes, Biomaterials 26 (2005) 2723–2732. https://doi.org/10.1016/J.BIOMATERIALS.2004.07.047.
[94] M.T. Neves-Petersen, Z. Gryczynski, J. Lakowicz, P. Fojan, S. Pedersen, E. Petersen, S. Bjørn Petersen, High probability of disrupting a disulphide bridge mediated by an endogenous excited tryptophan residue, Protein Sci 11 (2002) 588–600. https://doi.org/10.1110/PS.06002.
[95] A.O. Elzoghby, W.M. Samy, N.A. Elgindy, Protein-based nanocarriers as promising drug and gene delivery systems, J Control Release 161 (2012) 38–49. https://doi.org/10.1016/J.JCONREL.2012.04.036.
[96] S. Cui, Z. Yang, D.J. McClements, X. Xu, X. Qiao, L. Zhou, Q. Sun, B. Jiao, Q. Wang, L. Dai, Stability mechanism of Pickering emulsions co-stabilized by protein nanoparticles and small molecular emulsifiers by two-step emulsification with different adding sequences: From microscopic to macroscopic scales, Food Hydrocoll 137 (2023) 108372. https://doi.org/10.1016/j.foodhyd.2022.108372.
[97] F. Crisante, I. Francolini, M. Bellusci, A. Martinelli, L. D'Ilario, A. Piozzi, Antibiotic delivery polyurethanes containing albumin and polyallylamine nanoparticles, Eur JPharm Sci 36 (2009) 555–564. https://doi.org/ 10.1016/j.ejps.2008.12.006.
[98] M.S.M. Meiguni, M. Salami, K. Rezaei, M.A. Aliyari, S.-B. Ghaffari, Z. Emam-Djomeh, J.F. Kennedy, A. Ghasemi, Fabrication and characterization of a succinyl mung bean protein and arabic gum complex coacervate for curcumin encapsulation, Int J Biol Macromol 224 (2023) 170–180. https://doi.org/ 10.1016/j.ijbiomac.2022.10.113.
[99] C. Yan, W. Zhang, Coacervation processes, in: Microencapsulation in the Food Industry,, (2014) 125–137. https://doi.org/ 10.1016/B978-0-12-404568-2.00012-1.
[100] K. Parveen, V. Banse, L. Ledwani, Green synthesis of nanoparticles: Their advantages and disadvantages, in: AIP Conf Proc, 1724 (2016) 020048. https://doi.org/ 10.1063/1.4945168.
[101] V. Bourganis, T. Karamanidou, O. Kammona, C. Kiparissides, Polyelectrolyte complexes as prospective carriers for the oral delivery of protein therapeutics, Eur J Pharm Biopharm111 (2017) 44–60. https://doi.org/ 10.1016/j.ejpb.2016.11.005.
[102] N. Habibi, A. Mauser, Y. Ko, J. Lahann, Protein nanoparticles: uniting the power of proteins with engineering design approaches, Adv Sci 9 (2022) 2104012. https://doi.org/ 10.1002/advs.202104012.
[103] L.P.H. Estrada, J.A. Champion, Protein nanoparticles for therapeutic protein delivery, Biomater Sci 3 (2015) 787–799. https://doi.org/ 10.1039/c5bm00052a.
[104] M. Fathi, F. Donsi, D.J. McClements, Protein-based delivery systems for the nanoencapsulation of food ingredients, Compr Rev Food Sci Food Saf 17 (2018) 920–936. https://doi.org/ 10.1111/1541-4337.12360.
[105] F. Hua, Y.M. Lvov, Layer-by-layer assembly, The New Frontiers of Organic and Composite Nanotechnology (2008) 1–44. https://doi.org/10.1016/B978-008045052-0.50003-8.
[106] S. Zhang, F. Xia, S. Demoustier-Champagne, A.M. Jonas, Layer-by-layer assembly in nanochannels: assembly mechanism and applications, Nanoscale 13 (2021) 7471–7497. https://doi.org/10.1039/D1NR01113H.
[107] G.L. Butterfield, M.J. Lajoie, H.H. Gustafson, D.L. Sellers, U. Nattermann, D. Ellis, J.B. Bale, S. Ke, G.H. Lenz, A. Yehdego, Evolution of a designed protein assembly encapsulating its own RNA genome, Nature 552 (2017) 415–420. https://doi.org/ 10.1038/nature25157.
[108] S. Zhao, C. Huang, X. Yue, X. Li, P. Zhou, A. Wu, C. Chen, Y. Qu, C. Zhang, Application advance of electrosprayed micro/nanoparticles based on natural or synthetic polymers for drug delivery system, Mater Des 220 (2022) 110850. https://doi.org/ 10.1016/j.matdes.2022.110850.
[109] D.F. Quevedo, N. Habibi, J. V Gregory, Y. Hernandez, T.D. Brown, R. Miki, B.N. Plummer, S.

Rahmani, J.E. Raymond, S. Mitragotri, Multifunctional Synthetic Protein Nanoparticles via Reactive Electrojetting, Macromol Rapid Commun 41 (2020) 2000425. https://doi.org/10.1002/marc.202000425.
[110] K. Bulaklak, C.A. Gersbach, The once and future gene therapy, Nature Communications 11 (2020) 1–4. https://doi.org/10.1038/s41467-020-19505-2.
[111] H. Li, Y. Yang, W. Hong, M. Huang, M. Wu, X. Zhao, Applications of genome editing technology in the targeted therapy of human diseases: mechanisms, advances and prospects, Signal Transduct Target Ther 5 (2020) 1–23. https://doi.org/10.1038/s41392-019-0089-y.
[112] U. Arif, S. Haider, A. Haider, N. Khan, A.A. Alghyamah, N. Jamila, M.I. Khan, W.A. Almasry, I.-K. Kang, Biocompatible Polymers and their Potential Biomedical Applications: A Review, Curr Pharm Des 25 (2019) 3608–3619. https://doi.org/10.2174/1381612825999191011105148.
[113] E.M. Elmowafy, M. Tiboni, M.E. Soliman, Biocompatibility, biodegradation and biomedical applications of poly(lactic acid)/poly(lactic-co-glycolic acid) micro and nanoparticles, J Pharm Investig 49 (2019) 347–380. https://doi.org/10.1007/S40005-019-00439-X.
[114] D. Kothale, U. Verma, N. Dewangan, P. Jana, A. Jain, D. Jain, Alginate as Promising Natural Polymer for Pharmaceutical, Food, and Biomedical Applications, Curr Drug Deliv 17 (2020) 755–775. https://doi.org/10.2174/1567201817666200810110226.
[115] F. Fang, I. Szleifer, Kinetics and thermodynamics of protein adsorption: A generalized molecular theoretical approach, Biophys J 80 (2001) 2568–2589. https://doi.org/10.1016/S0006-3495(01)76228-5.
[116] J.M. Mollerup, A review of the thermodynamics of protein association to ligands, protein adsorption, and adsorption isotherms, Chem Eng Technol 31 (2008) 864–874. https://doi.org/10.1002/CEAT.200800082.
[117] F. Goudarzi, P. Hejazi, Comprehensive study on the effects of total monomers' content and polymerization temperature control on the formation of the polymer-layer in preparation of insulin-imprinted magnetic nanoparticles, Eur Polym J 126 (2020) 109541. https://doi.org/10.1016/J.EURPOLYMJ.2020.109541.
[118] P. Kaur, A.K. Sharma, D. Nag, A. Das, S. Datta, A. Ganguli, V. Goel, S. Rajput, G. Chakrabarti, B. Basu, D. Choudhury, Novel nano-insulin formulation modulates cytokine secretion and remodeling to accelerate diabetic wound healing, Nanomedicine 15 (2019) 47–57. https://doi.org/10.1016/j.nano.2018.08.013.
[119] S. Fan, Y. Zhang, H. Shao, X. Hu, Electrospun regenerated silk fibroin mats with enhanced mechanical properties, Int J Biol Macromol 56 (2013) 83–88. https://doi.org/10.1016/J.IJBIOMAC.2013.01.033.
[120] R. Zhang, T. Zhang, Y. Lv, P. Qin, H. Li, J. ping Li, T. Tan, Selective binding of heparin oligosaccharides in a magnetic thermoresponsive molecularly imprinted polymer, Talanta 201 (2019) 441–449. https://doi.org/10.1016/J.TALANTA.2019.04.050.
[121] N. Kianvash, A. Bahador, M. Pourhajibagher, H. Ghafari, V. Nikoui, S.M. Rezayat, A.R. Dehpour, A. Partoazar, Evaluation of propylene glycol nanoliposomes containing curcumin on burn wound model in rat: biocompatibility, wound healing, and anti-bacterial effects, Drug Deliv Transl Res 7 (2017) 654–663. https://doi.org/10.1007/S13346-017-0405-4.
[122] Y.P. Zhu, J.R. Brown, D. Sag, L. Zhang, J. Suttles, Adenosine 5'-monophosphate-activated protein kinase regulates IL-10-mediated anti-inflammatory signaling pathways in macrophages, J Immunol 194 (2015) 584–594. https://doi.org/10.4049/JIMMUNOL.1401024.
[123] A.M. Miller, M.J. Nolan, J. Choi, T. Koga, X. Shen, B.Y.J.T. Yue, P.A. Knepper, Lactate treatment causes NF-kappaB activation and CD44 shedding in cultured trabecular meshwork cells., Invest Ophthalmol Vis Sci 48 (2007) 1615–1621. https://doi.org/10.1167/IOVS.06-1086.
[124] T. Hosoyama, M.I. Aslam, J. Abraham, S.I. Prajapati, K. Nishijo, J.E. Michalek, L.A. Zarzabal, L.D. Nelon, D.C. Guttridge, B.P. Rubin, C. Keller, IL-4R drives dedifferentiation, mitogenesis, and metastasis in rhabdomyosarcoma, Clin Cancer Res 17 (2011) 2757–2766. https://doi.org/10.1158/1078-0432.CCR-10-3445.

[125] S.B. Weisser, K.W. McLarren, E. Kuroda, L.M. Sly, Generation and characterization of murine alternatively activated macrophages, Methods Mol Biol 946 (2013) 225–239. https://doi.org/10.1007/978-1-62703-128-8_14.
[126] A. Fraternale, S. Brundu, M. Magnani, Polarization and Repolarization of Macrophages, J Clin Cell Immunol 6 (2015) 1-10. https://doi.org/10.4172/2155-9899.1000319.
[127] X. Li, Y. Liu, J. Zhang, R. You, J. Qu, M. Li, Functionalized silk fibroin dressing with topical bioactive insulin release for accelerated chronic wound healing., Mater Sci Eng C Mater Biol Appl 72 (2016) 394–404. https://doi.org/10.1016/J.MSEC.2016.11.085.
[128] A. Ehterami, M. Salehi, S. Farzamfar, A. Vaez, H. Samadian, H. Sahrapeyma, M. Mirzaii, S. Ghorbani, A. Goodarzi, In vitro and in vivo study of PCL/COLL wound dressing loaded with insulin-chitosan nanoparticles on cutaneous wound healing in rats model, Int J Biol Macromol 117 (2018) 601–609. https://doi.org/10.1016/J.IJBIOMAC.2018.05.184.
[129] D.H. Abdelkader, M.M. Tambuwala, C.A. Mitchell, M.A. Osman, S.A. El-Gizawy, A.M. Faheem, M. El-Tanani, P.A. McCarron, Enhanced cutaneous wound healing in rats following topical delivery of insulin-loaded nanoparticles embedded in poly(vinyl alcohol)-borate hydrogels, Drug Deliv Transl Res 8 (2018) 1053–1065. https://doi.org/10.1007/S13346-018-0554-0.
[130] M.C. Ribeiro, V.L.R. Correa, F.K.L. da Silva, A.A. Casas, A. de L. das Chagas, L.P. de Oliveira, M.P. Miguel, D.G.A. Diniz, A.C. Amaral, L.B. de Menezes, Wound healing treatment using insulin within polymeric nanoparticles in the diabetes animal model, Eur J Pharm Sci 150 (2020) 105330. https://doi.org/10.1016/J.EJPS.2020.105330.
[131] J. Lee, M. Blaber, Increased Functional Half-life of Fibroblast Growth Factor-1 by Recovering a Vestigial Disulfide Bond, J Protein proteomics 1 (2010), 37-42.
[132] D. Sharda, D. Choudhury, Insulin–cobalt core–shell nanoparticles for receptor-targeted bioimaging and diabetic wound healing, RSC Adv 13 (2023) 20321–20335. https://doi.org/ 10.1039/d3ra01473h.
[133] T. Ponrasu, P.K. Veerasubramanian, R. Kannan, S. Gopika, L. Suguna, V. Muthuvijayan, Morin incorporated polysaccharide–protein (psyllium–keratin) hydrogel scaffolds accelerate diabetic wound healing in Wistar rats, RSC Adv 8 (2018) 2305–2314. https://doi.org/10.1039/C7RA10334D.
[134] W. Wan, F. Cai, J. Huang, S. Chen, Q. Liao, A skin-inspired 3D bilayer scaffold enhances granulation tissue formation and anti-infection for diabetic wound healing, J Mater Chem B 7 (2019) 2954–2961. https://doi.org/10.1039/C8TB03341B.
[135] Y. Agarwal, P.S. Rajinikanth, S. Ranjan, U. Tiwari, J. Balasubramnaiam, P. Pandey, D.K. Arya, S. Anand, P. Deepak, Curcumin loaded polycaprolactone-/polyvinyl alcohol-silk fibroin based electrospun nanofibrous mat for rapid healing of diabetic wound: An in-vitro and in-vivo studies, Int J Biol Macromol 176 (2021) 376–386. https://doi.org/10.1016/J.IJBIOMAC.2021.02.025.
[136] B. Maity, S. Alam, S. Samanta, R.G. Prakash, T. Govindaraju, Antioxidant Silk Fibroin Composite Hydrogel for Rapid Healing of Diabetic Wound, Macromol Biosci 22 (2022) 2200097. https://doi.org/10.1002/MABI.202200097.
[137] M. Tariq, H.M. Tahir, S.A. Butt, S. Ali, A.B. Ahmad, C. Raza, M. Summer, A. Hassan, J. Nadeem, Silk derived formulations for accelerated wound healing in diabetic mice, PeerJ 9 (2021) e10232. https://doi.org/10.7717/PEERJ.10232/SUPP-2.
[138] N. Özen, Z. Özbaş, B. İzbudak, S. Emik, B. Özkahraman, A. Bal-Öztürk, Boric acid-impregnated silk fibroin/gelatin/hyaluronic acid-based films for improving the wound healing process, J Appl Polym Sci 139 (2022) 51715. https://doi.org/10.1002/APP.51715.
[139] F. Zhang, C. Yin, X. Qi, C. Guo, X. Wu, Silk Fibroin Crosslinked Glycyrrhizic Acid and Silver Hydrogels for Accelerated Bacteria-Infected Wound Healing, Macromol Biosci 22 (2022) 2100407. https://doi.org/10.1002/MABI.202100407.
[140] A.H. Karaly, W.A. Sarhan, I.M. El-Sherbiny, Development of a silk fibroin-based multitask aerosolized nanopowder formula for efficient wound healing, Int J Biol Macromol 182 (2021) 413–424. https://doi.org/10.1016/J.IJBIOMAC.2021.03.178.

[141] Y.Y. Wu, Y.P. Jiao, L.L. Xiao, M.M. Li, H.W. Liu, S.H. Li, X. Liao, Y.T. Chen, J.X. Li, Y. Zhang, Experimental Study on Effects of Adipose-Derived Stem Cell–Seeded Silk Fibroin Chitosan Film on Wound Healing of a Diabetic Rat Model, Ann Plast Surg 80 (2018) 572. https://doi.org/10.1097/SAP.0000000000001355.
[142] S. Sen, P. Basak, B. Prasad Sinha, P. Maurye, K. Kumar Jaiswal, P. Das, T. Kumar Mandal, Anti-inflammatory effect of epidermal growth factor conjugated silk fibroin immobilized polyurethane ameliorates diabetic burn wound healing, Int J Biol Macromol 143 (2020) 1009–1032. https://doi.org/10.1016/J.IJBIOMAC.2019.09.219.
[143] Q. Yao, Q.H. Lan, X. Jiang, C.C. Du, Y.Y. Zhai, X. Shen, H.L. Xu, J. Xiao, L. Kou, Y.Z. Zhao, Bioinspired biliverdin/silk fibroin hydrogel for antiglioma photothermal therapy and wound healing, Theranostics 10 (2020) 11719. https://doi.org/10.7150/THNO.47682.
[144] Q. Wang, S. Zhou, L. Wang, R. You, S. Yan, Q. Zhang, M. Li, Bioactive silk fibroin scaffold with nanoarchitecture for wound healing, Compos B Eng 224 (2021) 109165. https://doi.org/10.1016/j.compositesb.2021.109165.
[145] K. Huang, Z. Jinzhong, T. Zhu, Y. Morsi, A. Aldalbahi, M. El-Newehy, X. Yan, X. Mo, Exploration of the antibacterial and wound healing potential of a PLGA/silk fibroin based electrospun membrane loaded with zinc oxide nanoparticles, J Mater Chem B 9 (2021) 1452–1465. https://doi.org/10.1039/d0tb02822c.
[146] P.K. Veerasubramanian, P. Thangavel, R. Kannan, S. Chakraborty, B. Ramachandran, L. Suguna, V. Muthuvijayan, An investigation of konjac glucomannan-keratin hydrogel scaffold loaded with Avena sativa extracts for diabetic wound healing, Colloids Surf B Biointerfaces 165 (2018) 92–102. https://doi.org/10.1016/J.COLSURFB.2018.02.022.
[147] F. Gao, W. Li, J. Deng, J. Kan, T. Guo, B. Wang, S. Hao, Recombinant Human Hair Keratin Nanoparticles Accelerate Dermal Wound Healing, ACS Appl Mater Interfaces 11 (2019) 18681–18690. https://doi.org/10.1021/ACSAMI.9B01725.
[148] P. Kumaran, A. Gupta, S. Sharma, Synthesis of wound healing keratin hydrogels using chicken feathers proteins and its properties, 9 (2017) https://doi.org/10.22159/ijpps.2017v9i2.15620.
[149] D.C. Roy, S. Tomblyn, D.M. Burmeister, N.L. Wrice, S.C. Becerra, L.R. Burnett, J.M. Saul, R.J. Christy, Ciprofloxacin-Loaded Keratin Hydrogels Prevent Pseudomonas aeruginosa Infection and Support Healing in a Porcine Full-Thickness Excisional Wound, 4 (2015) 457–468. https://doi.org/10.1089/WOUND.2014.0576.
[150] K. Zuniga, A. Isaac, S. Christy, N. Wrice, L. Mangum, S. Natesan, L. Burnett, R. Christy, C. Kowalczewski, Characterization of a Human Platelet Lysate-Loaded Keratin Hydrogel for Wound Healing Applications In Vitro, Int J Mol Sci 23 (2022) 4100. https://doi.org/10.3390/IJMS23084100.
[151] R.S. Kirsner, S. Cassidy, C. Marsh, A. Vivas, R.J. Kelly, Use of a keratin-based wound dressing in the management of wounds in a patient with recessive dystrophic epidermolysis bullosa, Adv Skin Wound Care 25 (2012) 400–403. https://doi.org/10.1097/01.ASW.0000419404.44947.DE.
[152] S. Su, T. Bedir, C. Kalkandelen, A. Ozan Başar, H. Turkoğlu Şaşmazel, C. Bulent Ustundag, M. Sengor, O. Gunduz, Coaxial and emulsion electrospinning of extracted hyaluronic acid and keratin based nanofibers for wound healing applications, Eur Polym J 142 (2021) 110158. https://doi.org/10.1016/J.EURPOLYMJ.2020.110158.
[153] S. Sharma, H. Rostamabadi, S. Gupta, A.K. Nadda, M.S. Kharazmi, S.M. Jafari, Nano/micro-formulations of keratin in biocomposites, wound healing and drug delivery systems; recent advances in biomedical applications, Eur Polym J 180 (2022) 111614. https://doi.org/10.1016/j.eurpolymj.2022.110614.
[154] M.M. Rana, M.S. Rahman, M.A. Ullah, A. Siddika, M.L. Hossain, M.S. Akhter, M.Z. Hasan, S.M. Asaduzzaman, Amnion and collagen-based blended hydrogel improves burn healing efficacy on a rat skin wound model in the presence of wound dressing biomembrane, Biomed Mater Eng 31 (2020) 1–17. https://doi.org/10.3233/BME-201076.
[155] I.B. Pathan, S.J. Munde, S. Shelke, W. Ambekar, C. Mallikarjuna Setty, Curcumin loaded fish scale

collagen-HPMC nanogel for wound healing application: Ex-vivo and In-vivo evaluation, 68 (2018) 165–174. https://doi.org/10.1080/00914037.2018.1429437.
[156] A.A. Mahmoud, A.H. Salama, Norfloxacin-loaded collagen/chitosan scaffolds for skin reconstruction: Preparation, evaluation and in-vivo wound healing assessment, Eur J Pharm Sci 83 (2016) 155–165. https://doi.org/10.1016/J.EJPS.2015.12.026.
[157] L. Sun, W. Gao, X. Fu, M. Shi, W. Xie, W. Zhang, F. Zhao, X. Chen, Enhanced wound healing in diabetic rats by nanofibrous scaffolds mimicking the basketweave pattern of collagen fibrils in native skin, Biomater Sci 6 (2018) 340–349. https://doi.org/10.1039/C7BM00545H.
[158] E.H. Gokce, S. Tuncay Tanrıverdi, I. Eroglu, N. Tsapis, G. Gokce, I. Tekmen, E. Fattal, O. Ozer, Wound healing effects of collagen-laminin dermal matrix impregnated with resveratrol loaded hyaluronic acid-DPPC microparticles in diabetic rats, Eur J Pharm Biopharm 119 (2017) 17–27. https://doi.org/10.1016/J.EJPB.2017.04.027.
[159] J. Natarajan, B.K.R. Sanapalli, M. Bano, S.K. Singh, M. Gulati, V.V.S.R. Karri, Nanostructured Lipid Carriers of Pioglitazone Loaded Collagen/Chitosan Composite Scaffold for Diabetic Wound Healing, Adv Wound Care (New Rochelle) 8 (2019) 499–513. https://doi.org/10.1089/WOUND.2018.0831.
[160] L.I.F. Moura, A.M.A. Dias, E. Suesca, S. Casadiegos, E.C. Leal, M.R. Fontanilla, L. Carvalho, H.C. de Sousa, E. Carvalho, Neurotensin-loaded collagen dressings reduce inflammation and improve wound healing in diabetic mice, Biochim Biophys Acta 1842 (2014) 32–43. https://doi.org/10.1016/J.BBADIS.2013.10.009.
[161] L.J. Pruett, C.H. Jenkins, N.S. Singh, K.J. Catallo, D.R. Griffin, Heparin Microislands in Microporous Annealed Particle Scaffolds for Accelerated Diabetic Wound Healing, Adv Funct Mater 31 (2021) 2104337. https://doi.org/10.1002/ADFM.202104337.
[162] H.L. Xu, J. Xu, B.X. Shen, S.S. Zhang, B.H. Jin, Q.Y. Zhu, D.L. ZhuGe, X.Q. Wu, J. Xiao, Y.Z. Zhao, Dual Regulations of Thermosensitive Heparin-Poloxamer Hydrogel Using ϵ-Polylysine: Bioadhesivity and Controlled KGF Release for Enhancing Wound Healing of Endometrial Injury, ACS Appl Mater Interfaces 9 (2017) 29580–29594. https://doi.org/10.1021/ACSAMI.7B10211/ASSET/IMAGES/LARGE/AM-2017-10211P_0011.JPEG.
[163] B. Maatouk, M.A. Jaffa, M. Karam, D. Fahs, W. Nour-Eldine, A. Hasan, A.A. Jaffa, R. Mhanna, Sulfated alginate/polycaprolactone double-emulsion nanoparticles for enhanced delivery of heparin-binding growth factors in wound healing applications, Colloids Surf B Biointerfaces 208 (2021) 112105. https://doi.org/10.1016/J.COLSURFB.2021.112105.
[164] L. Shahzadi, A. Ramzan, A. Anjum, F. Jabbar, A.F. Khan, F. Manzoor, S.A. Shahzad, A.A. Chaudhry, I. ur Rehman, M. Yar, An efficient new method for electrospinning chitosan and heparin for the preparation of pro-angiogenic nanofibrous membranes for wound healing applications, J Appl Polym Sci (2022) e53212. https://doi.org/10.1002/APP.53212.
[165] B. Senturk, S. Mercan, T. Delibasi, M.O. Guler, A.B. Tekinay, Angiogenic Peptide Nanofibers Improve Wound Healing in STZ-Induced Diabetic Rats, ACS Biomater Sci Eng 2 (2016) 1180–1189. https://doi.org/10.1021/ACSBIOMATERIALS.6B00238.
[166] Y. Peng, D. He, X. Ge, Y. Lu, Y. Chai, Y. Zhang, Z. Mao, G. Luo, J. Deng, Y. Zhang, Construction of heparin-based hydrogel incorporated with Cu5. 4O ultrasmall nanozymes for wound healing and inflammation inhibition, Bioact Mater 6 (2021) 3109–3124. https://doi.org/ 10.1016/j.bioactmat.2021.02.006.
[167] Y. Lu, H. Li, J. Wang, M. Yao, Y. Peng, T. Liu, Z. Li, G. Luo, J. Deng, Engineering bacteria-activated multifunctionalized hydrogel for promoting diabetic wound healing, Adv Funct Mater 31 (2021) 2105749. https://doi.org/ 10.1002/adfm.202105749.
[168] R. Shi, H. Li, X. Jin, X. Huang, Z. Ou, X. Zhang, G. Luo, J. Deng, Promoting Re-epithelialization in an oxidative diabetic wound microenvironment using self-assembly of a ROS-responsive polymer and P311 peptide micelles, Acta Biomater 152 (2022) 425–439. https://doi.org/ 10.1016/j.actbio.2022.09.017.

[169] X. Ge, J. Hu, Y. Peng, Z. Zeng, D. He, X. Li, Y. Chen, G. Luo, J. Deng, Z. Xu, Atmosphere-inspired multilayered nanoarmor with modulable protection and delivery of Interleukin-4 for inflammatory microenvironment modulation, Biomaterials 301 (2023) 122254. https://doi.org/ 10.1016/j.biomaterials.2023.122254.
[170] Y. Shang, P. Wang, X. Wan, L. Wang, X. Liu, J. Yuan, B. Chi, J. Shen, Chlorhexidine-loaded polysulfobetaine/keratin hydrogels with antioxidant and antibacterial activity for infected wound healing, Int J Biol Macromol 242 (2023) 124754. https://doi.org/ 10.1016/j.ijbiomac.2023.124754.
[171] C. Valentino, B. Vigani, G. Zucca, M. Ruggeri, C. Boselli, A.I. Cornaglia, L. Malavasi, G. Sandri, S. Rossi, Formulation development of collagen/chitosan-based porous scaffolds for skin wounds repair and regeneration, Int J Biol Macromol 242 (2023) 125000. https://doi.org/ 10.1016/j.ijbiomac.2023.125000.
[172] M. Budhiraja, S. Zafar, S. Akhter, M. Alrobaian, M.A. Rashid, M.A. Barkat, S. Beg, F.J. Ahmad, Mupirocin-loaded chitosan microspheres embedded in Piper betle extract containing collagen scaffold accelerate wound healing activity, AAPS PharmSciTech 23 (2022) 77. https://doi.org/ 10.1208/s12249-022-02233-9.
[173] M. Li, X. Li, Y. Gao, Y. Yang, C. Yi, W. Huang, B. Shen, D. Qi, Z. Mao, J. Wu, Composite nanofibrous dressing loaded with Prussian blue and heparin for anti-inflammation therapy and diabetic wound healing, Int J Biol Macromol 242 (2023) 125144. https://doi.org/ 10.1016/j.ijbiomac.2023.125144.
[174] P. Du, L. Diao, Y. Lu, C. Liu, J. Li, Y. Chen, J. Chen, G. Lv, X. Chen, Heparin-based sericin hydrogel–encapsulated basic fibroblast growth factor for in vitro and in vivo skin repair,9 Heliyon (2023) e13554. https://doi.org/ 10.1016/j.heliyon.2023.e13554.
[175] X. Meng, I. Zare, X. Yan, K. Fan, Protein-protected metal nanoclusters: An emerging ultra-small nanozyme, Wiley Interdiscip Rev Nanomed Nanobiotechnol 12 (2020) e1602. https://doi.org/10.1002/WNAN.1602.
[176] L. Fan, L. Ding, J. Lan, J. Niu, Y. He, L. Song, Fibroblast Growth Factor-1 Improves Insulin Resistance via Repression of JNK-Mediated Inflammation, Front Pharmacol 10 (2019) 01478. https://doi.org/10.3389/FPHAR.2019.01478.
[177] D.M. Ornitz, N. Itoh, The Fibroblast Growth Factor signaling pathway, Wiley Interdiscip Rev Dev Biol 4 (2015) 215–266. https://doi.org/10.1002/WDEV.176.
[178] C.T. Nguyen, T.T. Nguyen, T.T. Nguyen, P.P.T. Nguyen, A.D. Nguyen, L.T. Tran, H. Tran-Van, Preparation and in vitro evaluation of FGF-2 incorporated carboxymethyl chitosan nanoparticles, Carbohydr Polym 173 (2017) 114–120. https://doi.org/10.1016/J.CARBPOL.2017.05.080.
[179] A. Butko, G. Bonat Celli, A. Paulson, A. Ghanem, Entrapment of basic fibroblast growth factor (bFGF) in a succinylated chitosan nanoparticle delivery system and release profile, J Biomater Sci Polym Ed 27 (2016) 1045–1057. https://doi.org/10.1080/09205063.2016.1178519.
[180] M. Cetin, Y. Aktas, I. Vural, Y. Capan, L.A. Dogan, M. Duman, T. Dalkara, Preparation and in vitro evaluation of bFGF-loaded chitosan nanoparticles, Drug Deliv 14 (2007) 525–529. https://doi.org/10.1080/10717540701606483.
[181] P. Losi, E. Briganti, C. Errico, A. Lisella, E. Sanguinetti, F. Chiellini, G. Soldani, Fibrin-based scaffold incorporating VEGF- and bFGF-loaded nanoparticles stimulates wound healing in diabetic mice, Acta Biomater 9 (2013) 7814–7821. https://doi.org/10.1016/J.ACTBIO.2013.04.019.
[182] L. Claesson-Welsh, Signal transduction by vascular endothelial growth factor receptors, Biochem Soc Trans 31 (2003) 20–24. https://doi.org/10.1042/BST0310020.
[183] S. Reddy, M. Raffin, V. Kaklamani, Targeting angiogenesis in metastatic breast cancer, Oncologist 17 (2012) 1014–1026. https://doi.org/10.1634/THEONCOLOGIST.2012-0043.
[184] K.K. Chereddy, A. Lopes, S. Koussoroplis, V. Payen, C. Moia, H. Zhu, P. Sonveaux, P. Carmeliet, A. des Rieux, G. Vandermeulen, V. Préat, Combined effects of PLGA and vascular endothelial growth factor promote the healing of non-diabetic and diabetic wounds, Nanomedicine 11 (2015) 1975–1984. https://doi.org/10.1016/J.NANO.2015.07.006.
[185] W.L. Murphy, M.C. Peters, D.H. Kohn, D.J. Mooney, Sustained release of vascular endothelial

growth factor from mineralized poly(lactide-co-glycolide) scaffolds for tissue engineering, Biomaterials 21 (2000) 2521–2527. https://doi.org/10.1016/S0142-9612(00)00120-4.
[186] A. Mohandas, B.S. Anisha, K.P. Chennazhi, R. Jayakumar, Chitosan-hyaluronic acid/VEGF loaded fibrin nanoparticles composite sponges for enhancing angiogenesis in wounds, Colloids Surf B Biointerfaces 127 (2015) 105–113. https://doi.org/10.1016/J.COLSURFB.2015.01.024.
[187] W. Zha, J. Wang, Z. Guo, Y. Zhang, Y. Wang, S. Dong, C. Liu, H. Xing, X. Li, Efficient delivery of VEGF-A mRNA for promoting diabetic wound healing via ionizable lipid nanoparticles, Int J Pharm 632 (2023) 122565. https://doi.org/ 10.1016/j.ijpharm.2022.122565.
[188] Y.-H. Lee, Y.-L. Hong, T.-L. Wu, Novel silver and nanoparticle-encapsulated growth factor co-loaded chitosan composite hydrogel with sustained antimicrobility and promoted biological properties for diabetic wound healing, Mater Sci Eng: C Mater Biol Appl 118 (2021) 111385. https://doi.org/ 10.1016/j.msec.2020.111385.
[189] R. Augustine, A. Hasan, Y.B. Dalvi, S.R.U. Rehman, R. Varghese, R.N. Unni, H.C. Yalcin, R. Alfkey, S. Thomas, A.-E. Al Moustafa, Growth factor loaded in situ photocrosslinkable poly (3-hydroxybutyrate-co-3-hydroxyvalerate)/gelatin methacryloyl hybrid patch for diabetic wound healing, Mater Sci Eng: C Mater Biol Appl 118 (2021) 111519. https://doi.org/ https://doi.org/ 10.1016/j.msec.2020.111519.
[190] A. Pan, M. Zhong, H. Wu, Y. Peng, H. Xia, Q. Tang, Q. Huang, L. Wei, L. Xiao, C. Peng, Topical Application of Keratinocyte Growth Factor Conjugated Gold Nanoparticles Accelerate Wound Healing, Nanomedicine 14 (2018) 1619–1628. https://doi.org/10.1016/J.NANO.2018.04.007.
[191] Y. Xie, N. Su, J. Yang, Q. Tan, S. Huang, M. Jin, Z. Ni, B. Zhang, D. Zhang, F. Luo, H. Chen, X. Sun, J.Q. Feng, H. Qi, L. Chen, FGF/FGFR signaling in health and disease, Signal Transduct Target Ther 5 (2020) 181. https://doi.org/10.1038/S41392-020-00222-7.
[192] S. Li, Q. Tang, H. Xu, Q. Huang, Z. Wen, Y. Liu, C. Peng, Improved stability of KGF by conjugation with gold nanoparticles for diabetic wound therapy, Nanomedicine (Lond) 14 (2019) 2909–2923. https://doi.org/10.2217/NNM-2018-0487.
[193] I. Muhamed, E.P. Sproul, F.S. Ligler, A.C. Brown, Fibrin Nanoparticles Coupled with Keratinocyte Growth Factor Enhance the Dermal Wound-Healing Rate, ACS Appl Mater Interfaces 11 (2019) 3771–3780. https://doi.org/10.1021/ACSAMI.8B21056.
[194] A. Béduneau, P. Saulnier, J.P. Benoit, Active targeting of brain tumors using nanocarriers, Biomaterials 28 (2007) 4947–4967. https://doi.org/10.1016/J.BIOMATERIALS.2007.06.011.
[195] E. Mortaz, M. Reza Masjedi, A. Allameh, I. M. Adcock, Inflammasome signaling in pathogenesis of lung diseases, Curr Pharm Des 18 (2012) 2320–2328. https://doi.org/10.2174/138161212800166077.
[196] P. Zhang, C. Liu, Enhancement of Skin Wound Healing by rhEGF-Loaded Carboxymethyl Chitosan Nanoparticles, Polymers (Basel) 12 (2020) 1612. https://doi.org/10.3390/POLYM12071612.
[197] G. Gainza, M. Pastor, J.J. Aguirre, S. Villullas, J.L. Pedraz, R.M. Hernandez, M. Igartua, A novel strategy for the treatment of chronic wounds based on the topical administration of rhEGF-loaded lipid nanoparticles: In vitro bioactivity and in vivo effectiveness in healing-impaired db/db mice, J Control Release 185 (2014) 51–61. https://doi.org/10.1016/J.JCONREL.2014.04.032.
[198] Y. Chu, D. Yu, P. Wang, J. Xu, D. Li, M. Ding, Nanotechnology promotes the full-thickness diabetic wound healing effect of recombinant human epidermal growth factor in diabetic rats, Wound Repair Regen 18 (2010) 499–505. https://doi.org/10.1111/J.1524-475X.2010.00612.X.
[199] M. Rajam, S. Pulavendran, C. Rose, A.B. Mandal, Chitosan nanoparticles as a dual growth factor delivery system for tissue engineering applications, Int J Pharm 410 (2011) 145–152. https://doi.org/10.1016/J.IJPHARM.2011.02.065.
[200] Z. Xie, C.B. Paras, H. Weng, P. Punnakitikashem, L.C. Su, K. Vu, L. Tang, J. Yang, K.T. Nguyen, Dual growth factor releasing multi-functional nanofibers for wound healing, Acta Biomater 9 (2013) 9351–9359. https://doi.org/10.1016/J.ACTBIO.2013.07.030.
[201] A. Circolo, G.F. Pierce, Y. Katz, R.C. Strunk, Antiinflammatory effects of polypeptide growth factors. Platelet-derived growth factor, epidermal growth factor, and fibroblast growth factor inhibit

the cytokine-induced expression of the alternative complement pathway activator factor B in human fibroblasts., J Biol Chem 265 (1990) 5066–5071. https://doi.org/10.1016/S0021-9258(19)34085-2.
[202] M. Piran, S. Vakilian, M. Piran, A. Mohammadi-Sangcheshmeh, S. Hosseinzadeh, A. Ardeshirylajimi, In vitro fibroblast migration by sustained release of PDGF-BB loaded in chitosan nanoparticles incorporated in electrospun nanofibers for wound dressing applications, Artif Cells Nanomed Biotechnol 46 (2018) 511–520. https://doi.org/10.1080/21691401.2018.1430698.
[203] I. Pastar, O. Stojadinovic, N.C. Yin, H. Ramirez, A.G. Nusbaum, A. Sawaya, S.B. Patel, L. Khalid, R.R. Isseroff, M. Tomic-Canic, Epithelialization in Wound Healing: A Comprehensive Review, Adv Wound Care (New Rochelle) 3 (2014) 445–464. https://doi.org/10.1089/WOUND.2013.0473.
[204] G.A. Duque, A. Descoteaux, Macrophage cytokines: involvement in immunity and infectious diseases, Front Immunol 5 (2014) 491. https://doi.org/10.3389/FIMMU.2014.00491.
[205] J.E. Janis, B. Harrison, Wound Healing: Part I. Basic Science, Plast Reconstr Surg 138 (2016) 9S-17S. https://doi.org/10.1097/PRS.0000000000002773.
[206] W. PH, H. BS, H. HC, Y. CC, C. YJ, Wound healing, J Chin Med Assoc 81 (2018) 94–101. https://doi.org/10.1016/J.JCMA.2017.11.002.
[207] L. Teot, N. Ohura, Challenges and management in wound care, Plast Reconstr Surg 147 (2021) 9S-15S.
[208] L.H. K, I. M, S.-V. E, H. RM, Chronic wounds: Current status, available strategies and emerging therapeutic solutions, J Control Release 328 (2020) 532–550. https://doi.org/10.1016/J.JCONREL.2020.09.039.
[209] T.N. Demidova-Rice, M.R. Hamblin, I.M. Herman, Acute and impaired wound healing: pathophysiology and current methods for drug delivery, part 1: normal and chronic wounds: biology, causes, and approaches to care, Adv Skin Wound Care 25 (2012) 304–314. https://doi.org/10.1097/01.ASW.0000416006.55218.D0.
[210] A. Sood, M.S. Granick, N.L. Tomaselli, Wound Dressings and Comparative Effectiveness Data, Adv Wound Care (New Rochelle) 3 (2014) 511–529. https://doi.org/10.1089/WOUND.2012.0401.
[211] J.L. Burgess, W.A. Wyant, B. Abdo Abujamra, R.S. Kirsner, I. Jozic, Diabetic wound-healing science, Medicina (B Aires) 57 (2021) 1072. https://doi.org/ 10.3390/medicina57101072.
[212] R.G. Frykberg, J. Banks, Challenges in the Treatment of Chronic Wounds, Adv Wound Care (New Rochelle) 4 (2015) 560–582. https://doi.org/10.1089/WOUND.2015.0635/ASSET/IMAGES/LARGE/FIGURE4.JPEG.
[213] J.A. Beckman, M.A. Creager, P. Libby, Diabetes and atherosclerosis: epidemiology, pathophysiology, and management, JAMA 287 (2002) 2570–2581. https://doi.org/10.1001/JAMA.287.19.2570.
[214] A. Koïtka, P. Abraham, B. Bouhanick, D. Sigaudo-Roussel, C. Demiot, J.L. Saumet, Impaired pressure-induced vasodilation at the foot in young adults with type 1 diabetes, Diabetes 53 (2004) 721–725. https://doi.org/10.2337/DIABETES.53.3.721.
[215] A. Lima, T. Illing, S. Schliemann, P.E.-A.J. of Clinical, undefined 2017, Cutaneous manifestations of diabetes mellitus: a review, Springer 18 (2017) 541–553. https://doi.org/10.1007/s40257-017-0275-z.
[216] T.A.M. Andrade, D.S. Masson-Meyers, G.F. Caetano, V.A. Terra, P.P. Ovidio, A.A. Jordão-Júnior, M.A.C. Frade, Skin changes in streptozotocin-induced diabetic rats, Biochem Biophys Res Commun 490 (2017) 1154–1161. https://doi.org/10.1016/J.BBRC.2017.06.166.
[217] J.H. Kim, N.Y. Yoon, D.H. Kim, M. Jung, M. Jun, H.Y. Park, C.H. Chung, K. Lee, S. Kim, C.S. Park, K.H. Liu, E.H. Choi, Impaired permeability and antimicrobial barriers in type 2 diabetes skin are linked to increased serum levels of advanced glycation end-product, Exp Dermatol 27 (2018) 815–823. https://doi.org/10.1111/EXD.13466.
[218] J. Dworzański, M. Strycharz-Dudziak, E. Kliszczewska, M. Kiełczykowska, A. Dworzańska, B. Drop, M. Polz-Dacewicz, Glutathione peroxidase (GPx) and superoxide dismutase (SOD) activity in patients with diabetes mellitus type 2 infected with Epstein-Barr virus, PLoS One 15 (2020). https://doi.org/10.1371/JOURNAL.PONE.0230374.

[219] S. Matoori, A. Veves, D.J. Mooney, Advanced bandages for diabetic wound healing, Sci Transl Med 13 (2021) eabe4839. https://doi.org/ 10.1126/scitranslmed.abe4839.
[220] N. Naderi, D. Karponis, A. Mosahebi, A.M. Seifalian, Nanoparticles in wound healing; from hope to promise, from promise to routine, Frontiers in Bioscience-Landmark 23 (2018) 1038–1059 https://doi.org/ 10.2741/4632.
[221] E.T. Goh, G. Kirby, R. Jayakumar, X.-J. Liang, A. Tan, Accelerated wound healing using nanoparticles, in: Nanoscience in Dermatology, 2016: pp. 287–306. https://doi.org/ 10.1016/B978-0-12-802926-8.00023-9.
[222] N.K. Rajendran, S.S.D. Kumar, N.N. Houreld, H. Abrahamse, A review on nanoparticle based treatment for wound healing, J Drug Deliv Sci Technol 44 (2018) 421–430. https://doi.org/10.1016/J.JDDST.2018.01.009.
[223] B. Blanco-Fernandez, O. Castaño, M.Á. Mateos-Timoneda, E. Engel, S. Pérez-Amodio, Nanotechnology Approaches in Chronic Wound Healing, Adv Wound Care (New Rochelle) 10 (2021) 234. https://doi.org/10.1089/WOUND.2019.1094.
[224] C. Mendes, A. Thirupathi, M.E.A.B. Corrêa, Y. Gu, P.C.L. Silveira, The Use of Metallic Nanoparticles in Wound Healing: New Perspectives, Int J Mol Sci 23 (2022) 15376. https://doi.org/10.3390/IJMS232315376.
[225] S.K. Nethi, S. Das, C.R. Patra, S. Mukherjee, Recent advances in inorganic nanomaterials for wound-healing applications, Biomater Sci 7 (2019) 2652–2674. https://doi.org/10.1039/C9BM00423H.
[226] J.S. Mohanty, P.L. Xavier, K. Chaudhari, M.S. Bootharaju, N. Goswami, S.K. Pal, T. Pradeep, Luminescent, bimetallic AuAg alloy quantum clusters in protein templates, Nanoscale 4 (2012) 4255–4262. https://doi.org/10.1039/c2nr30729d.
[227] P. Kaur, D. Choudhury, Functionality of receptor targeted zinc-insulin quantum clusters in skin tissue augmentation and bioimaging, J Drug Target 29 (2021) 541–550. https://doi.org/10.1080/1061186X.2020.1864740.
[228] P.L. Xavier, K. Chaudhari, P.K. Verma, S.K. Pal, T. Pradeep, Luminescent quantum clusters of gold in transferrin family protein, lactoferrin exhibiting FRET, Nanoscale 2 (2010) 2769–2776. https://doi.org/10.1039/c0nr00377h.
[229] M. Tarhini, H. Greige-Gerges, A. Elaissari, Protein-based nanoparticles: From preparation to encapsulation of active molecules, Int J Pharm 522 (2017) 172–197. https://doi.org/10.1016/J.IJPHARM.2017.01.067.
[230] K. Chaudhari, P.L. Xavier, T. Pradeep, Understanding the evolution of luminescent gold quantum clusters in protein templates, ACS Nano 5 (2011) 8816–8827. https://doi.org/10.1021/nn202901a.
[231] I. Negut, V. Grumezescu, A.M. Grumezescu, Treatment Strategies for Infected Wounds, Molecules 23 (2018) 2392. https://doi.org/10.3390/MOLECULES23092392.
[232] D. Sharda, K. Attri, P. Kaur, D. Choudhury, Protection of lead-induced cytotoxicity using paramagnetic nickel–insulin quantum clusters, RSC Adv 11 (2021) 24656–24668. https://doi.org/ 10.1039/d1ra03597e.
[233] A. Oryan, E. Alemzadeh, Effects of insulin on wound healing: A review of animal and human evidences, Life Sci 174 (2017) 59–67. https://doi.org/10.1016/J.LFS.2017.02.015.
[234] P.-F. Chen, C.-L. Liu, W.-K. Lin, K.-C. Chen, P.-T. Chou, S.-W. Chu, Fluorescence depletion properties of insulin–gold nanoclusters, Biomed Opt Express 6 (2015) 3066. https://doi.org/10.1364/boe.6.003066.
[235] C.-H. Lee, K.-C. Hung, M.-J. Hsieh, S.-H. Chang, J.-H. Juang, I.-C. Hsieh, M.-S. Wen, S.-J. Liu, Core-shell insulin-loaded nanofibrous scaffolds for repairing diabetic wounds, Nanomedicine 24 (2020) 102123. https://doi.org/ 10.1016/j.nano.2019.102123.
[236] W. Li, F. Gao, J. Kan, J. Deng, B. Wang, S. Hao, Synthesis and fabrication of a keratin-conjugated insulin hydrogel for the enhancement of wound healing, Colloids Surf B Biointerfaces 175 (2019) 436–444. https://doi.org/ 10.1016/j.colsurfb.2018.12.020.
[237] Z. Zhang, L. Lv, Effect of local insulin injection on wound vascularization in patients with diabetic

foot ulcer, Exp Ther Med 11 (2016) 397–402. https://doi.org/ 10.3892/etm.2015.2917.
[238] M.K. Bhittani, M. Rehman, H.N. Altaf, O.S. Altaf, Effectiveness of topical insulin dressings in management of diabetic foot ulcers, World J Surg 44 (2020) 2028–2033. https://doi.org/ 10.1007/s00268-019-05321-3.
[239] M.H.S. Dawoud, G.E. Yassin, D.M. Ghorab, N.M. Morsi, Insulin mucoadhesive liposomal gel for wound healing: a formulation with sustained release and extended stability using quality by design approach, AAPS PharmSciTech 20 (2019) 1–15. https://doi.org/ 10.1208/s12249-019-1363-6.
[240] A. Ćwiertnia, M. Kozłowski, A. Cymbaluk-Płoska, The role of iron and cobalt in gynecological diseases, Cells 12 (2022) 117. https://doi.org/ 10.3390/cells12010117.
[241] K. Yamada, Cobalt: its role in health and disease, Met Ions Life Sci 13 (2013) 295–320. https://doi.org/ 10.1007/978-94-007-7500-8_9.
[242] A.K. Solanki, F. V. Lali, H. Autefage, S. Agarwal, A. Nommeots-Nomm, A.D. Metcalfe, M.M. Stevens, J.R. Jones, Bioactive glasses and electrospun composites that release cobalt to stimulate the HIF pathway for wound healing applications, Biomater Res 25 (2021) 1–16. https://doi.org/10.1186/S40824-020-00202-6/FIGURES/3.
[243] L.O. Simonsen, H. Harbak, P. Bennekou, Cobalt metabolism and toxicology—A brief update, Science of The Total Environment 432 (2012) 210–215. https://doi.org/10.1016/J.SCITOTENV.2012.06.009.
[244] M.A.C. Déry, M.D. Michaud, D.E. Richard, Hypoxia-inducible factor 1: regulation by hypoxic and non-hypoxic activators, Int J Biochem Cell Biol 37 (2005) 535–540. https://doi.org/10.1016/J.BIOCEL.2004.08.012.
[245] J. Li, F. Lv, J. Li, Y. Li, J. Gao, J. Luo, F. Xue, Q. Ke, H. Xu, Cobalt-based metal–organic framework as a dual cooperative controllable release system for accelerating diabetic wound healing, Nano Res 13 (2020) 2268–2279. https://doi.org/10.1007/S12274-020-2846-1.
[246] J. Zhou, L. Zhao, Multifunction Sr, Co and F co-doped microporous coating on titanium of antibacterial, angiogenic and osteogenic activities, Sci Rep 6 (2016) 1–14. https://doi.org/10.1038/srep29069.
[247] C. Wu, Y. Zhou, W. Fan, P. Han, J. Chang, J. Yuen, M. Zhang, Y. Xiao, Hypoxia-mimicking mesoporous bioactive glass scaffolds with controllable cobalt ion release for bone tissue engineering, Biomaterials 33 (2012) 2076–2085. https://doi.org/10.1016/J.BIOMATERIALS.2011.11.042.
[248] Q. Shi, X. Luo, Z. Huang, A.C. Midgley, B. Wang, R. Liu, D. Zhi, T. Wei, X. Zhou, M. Qiao, J. Zhang, D. Kong, K. Wang, Cobalt-mediated multi-functional dressings promote bacteria-infected wound healing, Acta Biomater 86 (2019) 465–479. https://doi.org/10.1016/J.ACTBIO.2018.12.048.
[249] A. Hoppe, A. Brandl, O. Bleiziffer, A. Arkudas, R.E. Horch, B. Jokic, D. Janackovic, A.R. Boccaccini, In vitro cell response to Co-containing 1393 bioactive glass, Mater Sci Eng: C 57 (2015) 157–163. https://doi.org/10.1016/J.MSEC.2015.07.014.
[250] M.M. Azevedo, O. Tsigkou, R. Nair, J.R. Jones, G. Jell, M.M. Stevens, Hypoxia inducible factor-stabilizing bioactive glasses for directing mesenchymal stem cell behavior, Tissue Eng Part A 21 (2015) 382–389. https://doi.org/10.1089/TEN.TEA.2014.0083.
[251] A.K. Solanki, H. Autefage, A.R. Rodriguez, S. Agarwal, J. Penide, M. Mahat, T. Whittaker, A. Nommeots-Nomm, E. Littmann, D.J. Payne, Cobalt containing glass fibres and their synergistic effect on the HIF-1 pathway for wound healing applications, Front Bioeng Biotechnol 11 (2023) 1125060. https://doi.org/ 10.3389/fbioe.2023.1125060.
[252] D. Moura, M.T. Souza, L. Liverani, G. Rella, G.M. Luz, J.F. Mano, A.R. Boccaccini, Development of a bioactive glass-polymer composite for wound healing applications, Mater Sci Eng: C 76 (2017) 224–232. https://doi.org/ 10.1016/j.msec.2017.03.037.
[253] Y. Chen, Q. Zhao, X. Yang, X. Yu, D. Yu, W. Zhao, Effects of cobalt chloride on the stem cell marker expression and osteogenic differentiation of stem cells from human exfoliated deciduous teeth, Cell Stress Chaperones 24 (2019) 527–538. https://doi.org/ 10.1007/s12192-019-00981-5.

[254] J. Xie, Y. Zheng, J.Y. Ying, Protein-directed synthesis of highly fluorescent gold nanoclusters, J Am Chem Soc 131 (2009) 888–889. https://doi.org/10.1021/ja806804u.
[255] J. Lin, Z. Zhou, Z. Li, C. Zhang, X. Wang, K. Wang, G. Gao, P. Huang, D. Cui, Biomimetic one-pot synthesis of gold nanoclusters/nanoparticles for targeted tumor cellular dual-modality imaging, Nanoscale Res Lett 8 (2013) 1–7. https://doi.org/10.1186/1556-276X-8-170.
[256] C.-L. Liu, H.-T. Wu, Y.-H. Hsiao, C.-W. Lai, C.-W. Shih, Y.-K. Peng, K.-C. Tang, H.-W. Chang, Y.-C. Chien, J.-K. Hsiao, J.-T. Cheng, P.-T. Chou, Insulin-Directed Synthesis of Fluorescent Gold Nanoclusters: Preservation of Insulin Bioactivity and Versatility in Cell Imaging, Angew Chem Int Ed Engl 50 (2011) 7056–7060. https://doi.org/10.1002/anie.201100299.
[257] A.G. Murzin, S.E. Brenner, T. Hubbard, C. Chothia, SCOP: A structural classification of proteins database for the investigation of sequences and structures, J Mol Biol 247 (1995) 536–540. https://doi.org/10.1016/S0022-2836(05)80134-2.
[258] G. Monnier, E. Frahm, B. Luo, K. Missal, Developing FTIR microspectroscopy for analysis of plant residues on stone tools, J Archaeol Sci 78 (2017) 158–178. https://doi.org/10.1016/j.jas.2016.12.004.
[259] C.-H. Citation: Lu, Y.-F. Lin, J.-J. Lin, C.-S. Yu, Prediction of Metal Ion-Binding Sites in Proteins Using the Fragment Transformation Method, PLoS One 7 (2012) 39252. https://doi.org/10.1371/journal.pone.0039252.
[260] J.C. Gower, G.J.S. Ross, Minimum Spanning Trees and Single Linkage Cluster Analysis, Appl Stat 18 (1969) 54. https://doi.org/10.2307/2346439.
[261] C.-H. Lu, Y.-S. Lin, Y.-C. Chen, C.-S. Yu, S.-Y. Chang, J.-K. Hwang, The fragment transformation method to detect the protein structural motifs, Proteinss 63 (2006) 636–643. https://doi.org/10.1002/prot.20904.
[262] D. Choudhury, P.L. Xavier, K. Chaudhari, R. John, A.K. Dasgupta, T. Pradeep, G. Chakrabarti, Unprecedented inhibition of tubulin polymerization directed by gold nanoparticles inducing cell cycle arrest and apoptosis, Nanoscale 5 (2013) 4476–4489. https://doi.org/10.1039/C3NR33891F.
[263] S. Razavi, R. Seyedebrahimi, M. Jahromi, Biodelivery of nerve growth factor and gold nanoparticles encapsulated in chitosan nanoparticles for schwann-like cells differentiation of human adipose-derived stem cells, Biochem Biophys Res Commun 513 (2019) 681–687. https://doi.org/10.1016/J.BBRC.2019.03.189.
[264] M.J. Oviedo, K. Quester, G.A. Hirata, R. Vazquez-Duhalt, Determination of conjugated protein on nanoparticles by an adaptation of the Coomassie blue dye method, MethodsX 6 (2019) 2134. https://doi.org/10.1016/J.MEX.2019.09.015.
[265] Y. Shi, C. Tian, X. Yu, Y. Fang, X. Zhao, X. Zhang, D. Xia, Protective Effects of Smilax glabra Roxb. Against Lead-Induced Renal Oxidative Stress, Inflammation and Apoptosis in Weaning Rats and HEK-293 Cells, Front Pharmacol 11 (2020) 556248. https://doi.org/10.3389/fphar.2020.556248.
[266] O.M. Ali, A.A. Bekhit, S.N. Khattab, M.W. Helmy, Y.S. Abdel-Ghany, M. Teleb, A.O. Elzoghby, Synthesis of lactoferrin mesoporous silica nanoparticles for pemetrexed/ellagic acid synergistic breast cancer therapy, Colloids Surf B Biointerfaces 188 (2020) 110824. https://doi.org/10.1016/J.COLSURFB.2020.110824.
[267] D. Choudhury, A. Ganguli, D.G. Dastidar, B.R. Acharya, A. Das, G. Chakrabarti, Apigenin shows synergistic anticancer activity with curcumin by binding at different sites of tubulin, Biochimie 95 (2013) 1297–1309. https://doi.org/10.1016/J.BIOCHI.2013.02.010.
[268] P. Kaur, A.K. Sharma, D. Nag, A. Das, S. Datta, A. Ganguli, V. Goel, S. Rajput, G. Chakrabarti, B. Basu, D. Choudhury, Novel nano-insulin formulation modulates cytokine secretion and remodeling to accelerate diabetic wound healing, Nanomedicine 15 (2019) 47–57. https://doi.org/10.1016/j.nano.2018.08.013.
[269] C.W. Tang, C. Bin Wang, S.H. Chien, Characterization of cobalt oxides studied by FT-IR, Raman, TPR and TG-MS, Thermochim Acta 473 (2008) 68–73. https://doi.org/10.1016/J.TCA.2008.04.015.

[270] M.H. Habibi, Z. Rezvani, Nanostructure copper oxocobaltate fabricated by co-precipitation route using copper and cobalt nitrate as precursors: Characterization by combined diffuse reflectance and FT infrared spectra, Spectrochim Acta A Mol Biomol Spectrosc 130 (2014) 309–312. https://doi.org/10.1016/J.SAA.2014.04.057.
[271] O. V. Netskina, A.A. Pochtar, O. V. Komova, V.I. Simagina, Solid-State NaBH4 Composites as Hydrogen Generation Material: Effect of Thermal Treatment of a Catalyst Precursor on the Hydrogen Generation Rate, Catalysts 10 (2020) 201. https://doi.org/10.3390/CATAL10020201.
[272] F. Zhang, C. Yuan, X. Lu, L. Zhang, Q. Che, X. Zhang, Facile growth of mesoporous Co 3O 4 nanowire arrays on Ni foam for high performance electrochemical capacitors, J Power Sources 203 (2012) 250–256. https://doi.org/10.1016/J.JPOWSOUR.2011.12.001.
[273] D. Sharda, K. Attri, P. Kaur, D. Choudhury, Protection of lead-induced cytotoxicity using paramagnetic nickel–insulin quantum clusters, RSC Adv 11 (2021) 24656–24668. https://doi.org/10.1039/D1RA03597E.
[274] P. Kaur, S. Sharma, S.D. Choudhury, D. Singh, S. Sharma, K. Gadhave, N. Garg, D. Choudhury, Insulin-copper quantum clusters preparation and receptor targeted bioimaging, Colloids Surf B Biointerfaces 188 (2020) 110785. https://doi.org/10.1016/j.colsurfb.2020.110785.
[275] O. V. Netskina, A.A. Pochtar, O. V. Komova, V.I. Simagina, Solid-State NaBH4 Composites as Hydrogen Generation Material: Effect of Thermal Treatment of a Catalyst Precursor on the Hydrogen Generation Rate, Catalysts 10 (2020) 201. https://doi.org/10.3390/CATAL10020201.
[276] C. Joseph, A. Daniels, S. Singh, M. Singh, Histidine-Tagged Folate-Targeted Gold Nanoparticles for Enhanced Transgene Expression in Breast Cancer Cells In Vitro, Pharmaceutics 14 (2021) 53. https://doi.org/10.3390/PHARMACEUTICS14010053.
[277] P. Maloň, L. Bedna´rova´, B. Bedna´rova, B. Bedna´rova´, M. Straka, L. Krejč I ´, L. Luka´, L. Kumprecht, T. Toma´, T. Kraus, M. Ta, K. Kuba´, K. Ova´, O. Ova´, V. Vladimi´, V. Baumruk, Disulfide chromophore and its optical activity, Wiley Online Library 22 (2010) 20851. https://doi.org/10.1002/chir.20851.
[278] S. Luber, Solvent effects in calculated vibrational Raman optical activity spectra of α-helices, J Phys Chem A 117 (2013) 2760–2770. https://doi.org/10.1021/JP400105U.
[279] M. Beg, Anukul Maji, Amit, K. Mandal, S. Das, Mt, N. Aktara, Pradeep, K. Jha, M. Hossain, Green synthesis of silver nanoparticles using Pongamia pinnata seed: Characterization, antibacterial property, and spectroscopic investigation of interaction with, J Mol Recognit 30 (2016) 2565. https://doi.org/10.1002/jmr.2565.
[280] C.M.V. Stålhandske, C.I. Stålhandske, I. Persson, M. Sandström, F. Jalilehvand, Crystal and solution structures of N,N-dimethylthioformamide-solvated copper(I), silver(I), and gold(I) ions studied by X-ray diffraction, X-ray absorption, and vibrational spectroscopy, Inorg Chem 40 (2001) 6684–6693. https://doi.org/10.1021/IC010226I.
[281] S.J. Roeters, C.N. Van Dijk, A. Torres-Knoop, E.H.G. Backus, R.K. Campen, M. Bonn, S. Woutersen, Determining in situ protein conformation and orientation from the amide-I sum-frequency generation spectrum: theory and experiment, ACS Publications 117 (2013) 6311–6322. https://doi.org/10.1021/jp401159r.
[282] E. Metryka, K. Chibowska, I. Gutowska, A. Falkowska, P. Kupnicka, K. Barczak, D. Chlubek, I. Baranowska-Bosiacka, Lead (Pb) exposure enhances expression of factors associated with inflammation, Int J Mol Sci 19 (2018) 19061813. https://doi.org/10.3390/ijms19061813.
[283] F. Zhou, G. Yin, Y. Gao, D. Liu, J. Xie, L. Ouyang, Y. Fan, H. Yu, Z. Zha, K. Wang, L. Shao, C. Feng, G. Fan, Toxicity assessment due to prenatal and lactational exposure to lead, cadmium and mercury mixtures, Environ Int 133 (2019) 105192. https://doi.org/10.1016/j.envint.2019.105192.
[284] N. Idrees, R. Sarah, B. Tabassum, E.F. Abd_Allah, Evaluation of some heavy metals toxicity in Channa punctatus and riverine water of Kosi in Rampur, Uttar Pradesh, India, Saudi J Biol Sci 27 (2020) 1191–1194. https://doi.org/10.1016/j.sjbs.2020.03.002.
[285] S. Madhavan, K.D. Rosenman, T. Shehata, Lead in soil: Recommended maximum permissible levels, Environ Res 49 (1989) 136–142. https://doi.org/10.1016/S0013-9351(89)80028-3.

[286] M. Kumar, A. Puri, A review of permissible limits of drinking water, Indian J Occup Environ Med 16 (2012) 40–44. https://doi.org/10.4103/0019-5278.99696.
[287] M.E. Abd El-Hack, S.A. Abdelnour, A.E.M.E. Abd El-Moneim, M. Arif, A. Khafaga, H. Shaheen, D. Samak, A.A. Swelum, Putative impacts of phytogenic additives to ameliorate lead toxicity in animal feed, Environ Sci Pollut Res Int. 26 (2019) 23209–23218. https://doi.org/10.1007/s11356-019-05805-8.
[288] G. Wang, J. Tang, Q. Song, Q. Yu, C. Yao, P. Li, Y. Ding, M. Lin, D. Cheng, Malus micromalus Makino phenolic extract preserves hepatorenal function by regulating PKC-α signaling pathway and attenuating endoplasmic reticulum stress in lead (II) exposure mice, J Inorg Biochem 203 (2020) 110925. https://doi.org/10.1016/j.jinorgbio.2019.110925.
[289] A. Soussi, M. Gargouri, A. Akrouti, A. El Feki, Antioxidant and nephro-protective effect of Juglans Regia vegetable oil against lead-induced nephrotoxicity in rats and its characterization by GC-MS, EXCLI J 17 (2018) 492–504. https://doi.org/10.17179/excli2018-1235.
[290] R.B. Jain, Co-exposures to toxic metals cadmium, lead, and mercury and their impact on unhealthy kidney function, Environ Sci Pollut Res Int. 26 (2019) 30112–30118. https://doi.org/10.1007/s11356-019-06182-y.
[291] J.J. Carmouche, J.E. Puzas, X. Zhang, P. Tiyapatanaputi, D.A. Cory-Slechta, R. Gelein, M. Zuscik, R.N. Rosier, B.F. Boyce, R.J. O'Keefe, E.M. Schwarz, Lead exposure inhibits fracture healing and is associated with increased chondrogenesis, delay in cartilage mineralization, and a decrease in osteoprogenitor frequency, Environ Health Perspect 113 (2005) 749–755. https://doi.org/10.1289/ehp.7596.
[292] M.S. de Oliveira, W.A. da Costa, D.S. Pereira, J.R.S. Botelho, T.O. de Alencar Menezes, E.H. de Aguiar Andrade, S.H.M. da Silva, A.P. da Silva Sousa Filho, R.N. de Carvalho, Chemical composition and phytotoxic activity of clove (Syzygium aromaticum) essential oil obtained with supercritical CO2, J Supercritl Fluids 118 (2016) 185–193. https://doi.org/10.1016/j.supflu.2016.08.010.
[293] L. Struzyńska, B. Dą browska-Bouta, K. Koza, G. Sulkowski, Inflammation-like glial response in lead-exposed immature rat brain, Tox Sci 95 (2007) 156–162. https://doi.org/10.1093/toxsci/kfl134.
[294] R.L. Ruebner, S.R. Hooper, C. Parrish, S.L. Furth, J.J. Fadrowski, Environmental lead exposure is associated with neurocognitive dysfunction in children with chronic kidney disease, Pediatr Nephrol 34 (2019) 2371–2379. https://doi.org/10.1007/s00467-019-04306-7.
[295] G. Azeh Engwa, P. Udoka Ferdinand, F. Nweke Nwalo, M. N. Unachukwu, Mechanism and Health Effects of Heavy Metal Toxicity in Humans, in: Poisoning in the Modern World - New Tricks for an Old Dog?, , (2019) 1-23. https://doi.org/10.5772/intechopen.82511.
[296] B. Kaličanin, D. Velimirović, A Study of the Possible Harmful Effects of Cosmetic Beauty Products on Human Health, Biol Trace Elem Res 170 (2016) 476–484. https://doi.org/10.1007/s12011-015-0477-2.
[297] T.L. Pan, P.W. Wang, S.A. Al-Suwayeh, C.C. Chen, J.Y. Fang, Skin toxicology of lead species evaluated by their permeability and proteomic profiles: A comparison of organic and inorganic lead, Toxicol Lett 197 (2010) 19–28. https://doi.org/10.1016/j.toxlet.2010.04.019.
[298] P. Zhu, J. Hawkins, W.H. Linthicum, M. Wang, N. Li, N. Zhou, Q. Wen, A. Timme-Laragy, X. Song, Y. Sun, Heavy Metal Exposure Leads to Rapid Changes in Cellular Biophysical Properties, ACS Biomater Sci Eng 6 (2020) 1965–1976. https://doi.org/10.1021/acsbiomaterials.9b01640.
[299] S. Pérez-Debén, R. Gonzalez-Martin, A. Palomar, A. Quiñonero, S. Salsano, F. Dominguez, Copper and lead exposures disturb reproductive features of primary endometrial stromal and epithelial cells, Reprod Toxicol 93 (2020) 106–117. https://doi.org/10.1016/j.reprotox.2020.01.008.
[300] Y. Fujiwara, T. Kaji, S. Sakurai, M. Sakamoto, H. Kozuka, Inhibitory effect of lead on the repair of wounded monolayers of cultured vascular endothelial cells, Toxicology 117 (1997) 193–198. https://doi.org/10.1016/S0300-483X(96)03575-5.
[301] L. Tutkun, M. Gunduzoz, O. Oztan, V. Ali Turksoy, M. Erdem Alaguney, S. Birgin Iritas, The relation between lead exposure and inflammation / endothelial dysfunction, Med Science 9 (2020)

468. https://doi.org/10.5455/medscience.2020.08.9249.
[302] M. Boskabady, N. Marefati, T. Farkhondeh, F. Shakeri, A. Farshbaf, M.H. Boskabady, The effect of environmental lead exposure on human health and the contribution of inflammatory mechanisms, a review, Environ Int 120 (2018) 404–420. https://doi.org/10.1016/j.envint.2018.08.013.
[303] N. Goswami, A. Giri, M.S. Bootharaju, P.L. Xavier, T. Pradeep, S.K. Pal, Copper quantum clusters in protein matrix: Potential sensor of Pb 2+ ion, Anal Chem 83 (2011) 9676–9680. https://doi.org/10.1021/ac202610e.
[304] B. Das, D. Bodhisatwa, C.P. Sharma, Heavy Metal Sensing by Protein Stabilized Gold Quantum Clusters: A Quantitative Approach , Trends Biomater Artif Organs 26 (2012) 130-138.
[305] V. D'Antò, R. Valletta, M. Amato, H. Schweikl, M. Simeone, S. Paduano, S. Rengo, G. Spagnuolo, Effect of Nickel Chloride on Cell Proliferation, Open Dent J 6 (2012) 177–181. https://doi.org/10.2174/1874210601206010177.
[306] G.I. Stangl, M. Kirchgessner, Nickel deficiency alters liver lipid metabolism in rats, J Nutr 126 (1996) 2466–2473. https://doi.org/10.1093/jn/126.10.2466.
[307] J. Ding, G.H. #1, W. Gong, W. Wen, W. Sun, B. Ning, S. Huang, K. Wu, C. Huang, M. Wu, W. Xie, H. Wang, Effects of Nickel on Cyclin Expression, Cell Cycle Progression and Cell Proliferation in Human Pulmonary Cells, Cancer Epidemiol Biomarkers Prev 18 (2009) 3874128. https://doi.org/10.1158/1055-9965.EPI-09-0115.
[308] C. Li, W. Chen, D. Wu, D. Quan, Z. Zhou, J. Hao, J. Qin, Y. Li, Z. He, K. Wang, Large Stokes Shift and High Efficiency Luminescent Solar Concentrator Incorporated with CuInS2/ZnS Quantum Dots, Sci Rep 5 (2015) 1–9. https://doi.org/10.1038/srep17777.
[309] Y.J. Jin, D. Araki, M. Teraguchi, T. Aoki, G. Kwak, Dimesitylboryl-containing polydiphenylacetylene with a large Stokes shift, high fluorescence efficiency, and fluoride ion sensing ability, Polymer (Guildf) 148 (2018) 310–315. https://doi.org/10.1016/J.POLYMER.2018.06.044.
[310] J. Zheng, P.R. Nicovich, R.M. Dickson, Highly fluorescent noble-metal quantum dots, Annu Rev Phys Chem 58 (2007) 409–431. https://doi.org/10.1146/ANNUREV.PHYSCHEM.58.032806.104546.
[311] H. Cha, J.H. Yoon, S. Yoon, Probing quantum plasmon coupling using gold nanoparticle dimers with tunable interparticle distances down to the subnanometer range, ACS Nano 8 (2014) 8554–8563. https://doi.org/10.1021/NN5032438.
[312] M.A. Habeeb Muhammed, S. Ramesh, S.S. Sinha, S.K. Pal, T. Pradeep, Two distinct fluorescent quantum clusters of gold starting from metallic nanoparticles by pH-dependent ligand etching, Nano Res 1 (2008) 333–340. https://doi.org/10.1007/s12274-008-8035-2.
[313] X. Le Guevel, Recent advances on the synthesis of metal quantum nanoclusters and their application for bioimaging, IEEE J Sel Top Quantum Electron 20 (2014) 45-56. https://doi.org/10.1109/JSTQE.2013.2282275.
[314] P. Kaur, D. Choudhury, Insulin Promotes Wound Healing by Inactivating NFkβP50/P65 and Activating Protein and Lipid Biosynthesis and alternating Pro/Anti-inflammatory Cytokines Dynamics., Biomol Concepts 10 (2019) 11–24. https://doi.org/10.1515/BMC-2019-0002.
[315] A.T. Lusk, G.K. Jennings, Characterization of self-assembled monolayers formed from sodium S-alkyl thiosulfates on copper, Langmuir 17 (2001) 7830–7836. https://doi.org/10.1021/la010816t.
[316] J.M. Liu, L.P. Lin, X.X. Wang, S.Q. Lin, W.L. Cai, L.H. Zhang, Z.Y. Zheng, Highly selective and sensitive detection of Cu2+ with lysine enhancing bovine serum albumin modified-carbon dots fluorescent probe, Analyst 137 (2012) 2637–2642. https://doi.org/10.1039/c2an35130g.
[317] R. Mehta, P. Kaur, D. Choudhury, K. Paul, V. Luxami, Al 3+ induced hydrolysis of rhodamine-based Schiff-base: Applications in cell imaging and ensemble as CN - sensor in 100% aqueous medium, J Photochem Photobiol A Chem 380 (2019) 111851. https://doi.org/10.1016/j.jphotochem.2019.05.014.
[318] K. Chaudhari, T. Pradeep, Initial growth kinetics of luminescent quantum clusters of silver within albumin family protein templates, J Phys Chem C 119 (2015) 9988–9994.

https://doi.org/10.1021/acs.jpcc.5b00496.
[319] V. Poderys, M. Matulionytė-Safinė, D. Rupšys, R. Rotomskis, Baltymu stabilizuoti aukso nanoklasteriai: Spektrinių savybių IR fotostabilumo tyrimai, Lith J Phys 56 (2016) 55–65. https://doi.org/10.3952/physics.v56i1.3277.
[320] V.F. Razumov, S.A. Tovstun, Features of luminescence of colloidal quantum dot clusters, High Energy Chem 49 (2015) 44–47. https://doi.org/10.1134/S0018143915010117.
[321] N. Roohani, R. Hurrell, R. Kelishadi, R. Schulin, Zinc and its importance for human health: An integrative review, J Res Med Sci 18 (2013) 144–157. https://doi.org/10.1016/j.foodpol.2013.06.008.
[322] M. Watanabe, H. Hayasaki, T. Tamayama, M. Shimada, Histologic distribution of insulin and glucagon receptors, Braz J Med Biol Res 31 (1998) 243–256. https://doi.org/10.1590/S0100-879X1998000200008.
[323] V. Papa, V. Pezzino, A. Costantino, A. Belfiore, D. Giuffrida, L. Frittitta, G.B. Vannelli, R. Brand, I.D. Goldfine, R. Vigneri, Elevated insulin receptor content in human breast cancer, J Clin Investig 86 (1990) 1503–1510. https://doi.org/10.1172/JCI114868.
[324] P.-F. Chen, C.-L. Liu, W.-K. Lin, K.-C. Chen, P.-T. Chou, S.-W. Chu, Fluorescence depletion properties of insulin-gold nanoclusters, Biomed Opt Express 6 (2015) 3066. https://doi.org/10.1364/BOE.6.003066.
[325] M. Li, D.P. Yang, X. Wang, J. Lu, D. Cui, Mixed protein-templated luminescent metal clusters (Au and Pt) for H2O2 sensing, Nanoscale Res Lett 8 (2013) 1–5. https://doi.org/10.1186/1556-276X-8-182.
[326] J. Li, M. Wei, W. Chu, N. Wang, High-stable A-phase NiCo double hydroxide microspheres via microwave synthesis for supercapacitor electrode materials, Chem Eng J 316 (2017) 277–287. https://doi.org/10.1016/j.cej.2017.01.057.
[327] Z. Wei, H. Qiao, H. Yang, L. Zhu, X. Yan, Preparation and characterization of NiO nanoparticles by anodic arc plasma method, J Nanomater 2009 (2009) 795928. https://doi.org/10.1155/2009/795928.
[328] S. Bhakya, S. Muthukrishnan, M. Sukumaran, M. Muthukumar, Biogenic synthesis of silver nanoparticles and their antioxidant and antibacterial activity, Applied Nanoscience (Switzerland) 6 (2016) 755–766. https://doi.org/10.1007/s13204-015-0473-z.
[329] B. De Campos Vidal, M.L.S. Mello, Collagen type I amide I band infrared spectroscopy, Micron 42 (2011) 283–289. https://doi.org/10.1016/j.micron.2010.09.010.
[330] A. Mitsuzuka, A. Fujii, T. Ebata, N. Mikami, Infrared spectroscopy of intramolecular hydrogen-bonded OH stretching vibrations in jet-cooled methyl salicylate and its clusters, J Phys Chem A 102 (1998) 9779–9784. https://doi.org/10.1021/jp9830934.
[331] C.K. Sen, Human Wounds and Its Burden: An Updated Compendium of Estimates, Adv Wound Care (New Rochelle) 8 (2019) 39–48. https://doi.org/10.1089/WOUND.2019.0946.
[332] P.H. Wang, B.S. Huang, H.C. Horng, C.C. Yeh, Y.J. Chen, Wound healing, J Chin Med Assoc 81 (2018) 94–101. https://doi.org/10.1016/J.JCMA.2017.11.002.
[333] Y. Yang, J. Wang, S. Huang, M. Li, J. Chen, D. Pei, Z. Tang, B. Guo, Bacterial responsive programmed self-activating antibacterial hydrogel to remodel regeneration microenvironment for infected wound healing, Natl Sci Rev (2024) nwae044. https://doi.org/ 10.1093/nsr/nwae044.
[334] R.G. Frykberg, J. Banks, Challenges in the Treatment of Chronic Wounds, Adv Wound Care (New Rochelle) 4 (2015) 560. https://doi.org/10.1089/WOUND.2015.0635.
[335] H. Wu, F. Li, W. Shao, J. Gao, D. Ling, Promoting angiogenesis in oxidative diabetic wound microenvironment using a nanozyme-reinforced self-protecting hydrogel, ACS Cent Sci 5 (2019) 477–485. https://doi.org/ 10.1021/acscentsci.8b00850.
[336] Y.-K. Wu, N.-C. Cheng, C.-M. Cheng, Biofilms in chronic wounds: pathogenesis and diagnosis, Trends Biotechnol 37 (2019) 505–517. https://doi.org/ 10.1016/j.tibtech.2018.10.011.
[337] Y. Yang, M. Li, G. Pan, J. Chen, B. Guo, Multiple stimuli-responsive nanozyme-based cryogels with controlled NO release as self-adaptive wound dressing for infected wound healing, Adv Funct

Mater 33 (2023) 2214089. https://doi.org/ 10.1002/adfm.202214089.
[338] K. Attri, D. Sharda, B.N. Chudasama, R. Mahajan, D. Choudhury, A Review on Terpenes for Treatment of Gastric Cancer: Current Status and Nanotechnology-enabled Future, RSC Sustainability (2023). https://doi.org/ 10.1039/D2SU00137C.
[339] W. Qin, Y. Wu, J. Liu, X. Yuan, J. Gao, A comprehensive review of the application of nanoparticles in diabetic wound healing: Therapeutic potential and future perspectives, Int J Nanomedicine (2022) 6007–6029. https://doi.org/ 10.2147/IJN.S386585.
[340] D. Sharda, P. Kaur, D. Choudhury, Protein-modified nanomaterials: emerging trends in skin wound healing, Discover Nano 18 (2023) 127. https://doi.org/ 10.1186/s11671-023-03903-8.
[341] A. Behera, B. Mittu, S. Padhi, N. Patra, J. Singh, Bimetallic nanoparticles: Green synthesis, applications, and future perspectives, in: Multifunctional Hybrid Nanomaterials for Sustainable Agri-Food and Ecosystems, (2020) 639–682. https://doi.org/ 10.1016/B978-0-12-821354-4.00025-X.
[342] C. Singh, A.K. Mehata, V. Priya, A.K. Malik, A. Setia, M.N.L. Suseela, Vikas, P. Gokul, Samridhi, S.K. Singh, Bimetallic Au–Ag nanoparticles: advanced nanotechnology for tackling antimicrobial resistance, Molecules 27 (2022) 7059. https://doi.org/ 10.3390/molecules27207059.
[343] A. Sathiyaseelan, K. Saravanakumar, M.-H. Wang, Bimetallic silver-platinum (AgPt) nanoparticles and chitosan fabricated cotton gauze for enhanced antimicrobial and wound healing applications, Int J Biol Macromol 220 (2022) 1556–1569. https://doi.org/ 10.1016/j.ijbiomac.2022.09.045.
[344] A. Zaleska-Medynska, M. Marchelek, M. Diak, E. Grabowska, Noble metal-based bimetallic nanoparticles: the effect of the structure on the optical, catalytic and photocatalytic properties, Adv Colloid Interface Sci 229 (2016) 80–107. https://doi.org/ 10.1016/j.cis.2015.12.008.
[345] H. Fan, Z. Tong, Z. Ren, K. Mishra, S. Morita, E. Edouarzin, L. Gorla, B. Averkiev, V.W. Day, D.H. Hua, Synthesis and Characterization of Bimetallic Nanoclusters Stabilized by Chiral and Achiral Polyvinylpyrrolidinones. Catalytic C (sp3)–H Oxidation, J Org Chem 87 (2022) 6742–6759. https://doi.org/ 10.1021/acs.joc.2c00449.
[346] X. Yuan, X. Dou, K. Zheng, J. Xie, Recent advances in the synthesis and applications of ultrasmall bimetallic nanoclusters, Part Part Syst Charact 32 (2015) 613–629. https://doi.org/ 10.1002/ppsc.201400212.
[347] A. Sannigrahi, S. Chowdhury, I. Nandi, D. Sanyal, S. Chall, K. Chattopadhyay, Development of a near infrared Au–Ag bimetallic nanocluster for ultrasensitive detection of toxic Pb 2+ ions in vitro and inside cells, Nanoscale Adv 1 (2019) 3660–3669. https://doi.org/ 10.1039/c9na00459a.
[348] F. Paladini, M. Pollini, Antimicrobial silver nanoparticles for wound healing application: progress and future trends, Materials 12 (2019) 2540. https://doi.org/ 10.3390/ma12162540.
[349] S.H. Lee, B.-H. Jun, Silver nanoparticles: synthesis and application for nanomedicine, Int J Mol Sci 20 (2019) 865. https://doi.org/ 10.3390/ijms20040865.
[350] G. Sandri, D. Miele, A. Faccendini, M.C. Bonferoni, S. Rossi, P. Grisoli, A. Taglietti, M. Ruggeri, G. Bruni, B. Vigani, Chitosan/glycosaminoglycan scaffolds: the role of silver nanoparticles to control microbial infections in wound healing, Polymers (Basel) 11 (2019) 1207. https://doi.org/ 10.3390/polym11071207.
[351] S. Alizadeh, B. Seyedalipour, S. Shafieyan, A. Kheime, P. Mohammadi, N. Aghdami, Copper nanoparticles promote rapid wound healing in acute full thickness defect via acceleration of skin cell migration, proliferation, and neovascularization, Biochem Biophys Res Commun 517 (2019) 684–690. https://doi.org/ 10.1016/j.bbrc.2019.07.110.
[352] J. Salvo, C. Sandoval, Role of copper nanoparticles in wound healing for chronic wounds: literature review, Burns Trauma 10 (2022) tkab047. https://doi.org/ 10.1093/burnst/tkab047.
[353] A.P. Kornblatt, V.G. Nicoletti, A. Travaglia, The neglected role of copper ions in wound healing, J Inorg Biochem 161 (2016) 1–8. https://doi.org/ 10.1016/j.jinorgbio.2016.02.012.
[354] A. Das, V. Sudhahar, G.-F. Chen, H.W. Kim, S.-W. Youn, L. Finney, S. Vogt, J. Yang, J. Kweon, B. Surenkhuu, Endothelial antioxidant-1: a key mediator of copper-dependent wound healing in vivo, Sci Rep 6 (2016) 33783. https://doi.org/ 10.1038/srep33783.

[355] Y. Mi, L. Zhong, S. Lu, P. Hu, Y. Pan, X. Ma, B. Yan, Z. Wei, G. Yang, Quercetin promotes cutaneous wound healing in mice through Wnt/β-catenin signaling pathway, J Ethnopharmacol 290 (2022) 115066. https://doi.org/ 10.1016/j.jep.2022.115066.
[356] G. Yin, Z. Wang, Z. Wang, X. Wang, Topical application of quercetin improves wound healing in pressure ulcer lesions, Exp Dermatol 27 (2018) 779–786. https://doi.org/ 10.1111/exd.13679.
[357] D. Sharda, S. Ghosh, P. Kaur, B. Basu, D. Choudhury, Chitosan-insulin nano-formulations as critical modulators of inflammatory cytokines and Nrf-2 pathway to accelerate burn wound healing, 18 (2023) 154. https://doi.org/ 10.1186/s11671-023-03941-2.
[358] F. Tasca, R. Antiochia, Biocide activity of green quercetin-mediated synthesized silver nanoparticles, Nanomaterials 10 (2020) 909. https://doi.org/ 10.3390/nano10050909.
[359] T. Odatsu, S. Kuroshima, A. Shinohara, A. Valanezhad, T. Sawase, Lactoferrin with Zn-ion protects and recovers fibroblast from H2O2-induced oxidative damage, Int J Biol Macromol 190 (2021) 368–374. https://doi.org/ 10.1016/j.ijbiomac.2021.08.214.
[360] A.K. Keshari, R. Srivastava, P. Singh, V.B. Yadav, G. Nath, Antioxidant and antibacterial activity of silver nanoparticles synthesized by Cestrum nocturnum, J Ayurveda Integr Med 11 (2020) 37–44. https://doi.org/ 10.1016/j.jaim.2017.11.003.
[361] S. Moniri, M. Ghoranneviss, M.R. Hantehzadeh, M.A. Asadabad, Synthesis and optical characterization of copper nanoparticles prepared by laser ablation, Bull Mater Sci 40 (2017) 37–43. https://doi.org/ 10.1007/s12034-016-1348-y.
[362] G.I.N. Waterhouse, G.A. Bowmaker, J.B. Metson, The thermal decomposition of silver (I, III) oxide: A combined XRD, FT-IR and Raman spectroscopic study, Phys Chem Chem Phys 3 (2001) 3838–3845. https://doi.org/ 10.1039/B103226G.
[363] M. Trivedi, A. Branton, D. Trivedi, G. Nayak, K. Bairwa, S. Jana, Spectroscopic characterization of disodium hydrogen orthophosphate and sodium nitrate after biofield treatment, Chromatography Separation Techniques 5 (2015) 1000282. https://doi.org/ 10.4172/2157-7064.1000282.
[364] M.H. Habibi, Z. Rezvani, Nanostructure copper oxocobaltate fabricated by co-precipitation route using copper and cobalt nitrate as precursors: Characterization by combined diffuse reflectance and FT infrared spectra, Spectrochim Acta A Mol Biomol Spectrosc 130 (2014) 309–312. https://doi.org/ 10.1016/j.saa.2014.04.057.
[365] A.J. Kora, J. Arunachalam, Green fabrication of silver nanoparticles by gum tragacanth (Astragalus gummifer): A dual functional reductant and stabilizer, J Nanomater 2012 (2012) 1–8. https://doi.org/ 10.1155/2012/869765.
[366] D. Li, Z. Zhang, X. Wang, Y. Wang, X. Gao, Y. Li, A direct method for detecting proteins in body fluids by Surface-Enhanced Raman Spectroscopy under native conditions, Biosens Bioelectron 200 (2022) 113907. https://doi.org/ 10.1016/j.bios.2021.113907.
[367] A. Bankapur, R.S. Krishnamurthy, E. Zachariah, C. Santhosh, B. Chougule, B. Praveen, M. Valiathan, D. Mathur, Micro-Raman spectroscopy of silver nanoparticle induced stress on optically-trapped stem cells, PLoS One 7 (2012) e35075. https://doi.org/ 10.1371/journal.pone.0035075.
[368] M. Correia, M.T. Neves-Petersen, P.B. Jeppesen, S. Gregersen, S.B. Petersen, UV-light exposure of insulin: pharmaceutical implications upon covalent insulin dityrosine dimerization and disulphide bond photolysis, PLoS One 7 (2012) e50733. https://doi.org/ 10.1371/journal.pone.0050733.
[369] P.H. Wang, B.S. Huang, H.C. Horng, C.C. Yeh, Y.J. Chen, Wound healing, J Chin Med Assoc 81 (2018) 94–101. https://doi.org/10.1016/J.JCMA.2017.11.002.
[370] P. Martin, R. Nunan, Cellular and molecular mechanisms of repair in acute and chronic wound healing, Br J Dermatol 173 (2015) 370–378. https://doi.org/10.1111/bjd.13954.
[371] Y. Wang, J. Beekman, J. Hew, S. Jackson, A.C. Issler-Fisher, R. Parungao, S.S. Lajevardi, Z. Li, P.K.M. Maitz, Burn injury: Challenges and advances in burn wound healing, infection, pain and scarring, Adv Drug Deliv Rev 123 (2018) 3–17. https://doi.org/10.1016/J.ADDR.2017.09.018.
[372] R.J. Kagan, M.D. Peck, D.H. Ahrenholz, W.L. Hickerson, J. Holmes IV, R. Korentager, J. Kraatz, K. Pollock, G. Kotoski, Surgical management of the burn wound and use of skin substitutes: an expert panel white paper, J Burn Care Res 34 (2013) e60–e79. https://doi.org/

10.1097/BCR.0b013e31827039a6.
[373] T.N. Pham, L.C. Cancio, N.S. Gibran, American Burn Association practice guidelines burn shock resuscitation, J Burn Care Res 29 (2008) 257–266. https://doi.org/ 10.1097/BCR.0b013e31815f3876.
[374] P. Ramhormozi, J.M. Ansari, S. Simorgh, H.R. Asgari, M. Najafi, M. Barati, A. Babakhani, M. Nobakht, Simvastatin accelerates the healing process of burn wound in Wistar rats through Akt/mTOR signaling pathway, AnnAnat 236 (2021) 151652. https://doi.org/ 10.1016/j.aanat.2020.151652.
[375] V.K. Tiwari, Burn wound: How it differs from other wounds?, Indian J Plast Surg 45 (2012) 364–373. https://doi.org/ 10.4103/0970-0358.101319.
[376] A. Oryan, E. Alemzadeh, A. Moshiri, Burn wound healing: present concepts, treatment strategies and future directions, J Wound Care 26 (2017) 5–19. https://doi.org/ 10.12968/jowc.2017.26.1.5.
[377] M.P. Rowan, L.C. Cancio, E.A. Elster, D.M. Burmeister, L.F. Rose, S. Natesan, R.K. Chan, R.J. Christy, K.K. Chung, Burn wound healing and treatment: review and advancements, Crit Care 19 (2015) 1–12. https://doi.org/ 10.1186/s13054-015-0961-2.
[378] J.A. Farina, M.J. Rosique, R.G. Rosique, Curbing inflammation in burn patients, Int J Inflam 2013 (2013) 715645. https://doi.org/ 10.1155/2013/715645.
[379] L.K. Branski, A. Al-Mousawi, H. Rivero, M.G. Jeschke, A.P. Sanford, D.N. Herndon, Emerging infections in burns, Surg Infect (Larchmt) 10 (2009) 389–397. https://doi.org/10.1089/SUR.2009.024.
[380] D.W. Edgar, J.S. Fish, M. Gomez, F.M. Wood, Local and systemic treatments for acute edema after burn injury: a systematic review of the literature, J Burn Care Res 32 (2011) 334–347. https://doi.org/ 10.1097/BCR.0b013e31820ab019.
[381] K. Sommer, A.L. Sander, M. Albig, R. Weber, D. Henrich, J. Frank, I. Marzi, H. Jakob, Delayed wound repair in sepsis is associated with reduced local pro-inflammatory cytokine expression, PLoS One 8 (2013) e73992. https://doi.org/10.1371/journal.pone.0073992.
[382] F. Ghieh, R. Jurjus, A. Ibrahim, A.G. Geagea, H. Daouk, B. El Baba, S. Chams, M. Matar, W. Zein, A. Jurjus, The use of stem cells in burn wound healing: a review, Biomed Res Int 2015 (2015) 684084. https://doi.org/ 10.1155/2015/684084.
[383] Y. Wang, J. Beekman, J. Hew, S. Jackson, A.C. Issler-Fisher, R. Parungao, S.S. Lajevardi, Z. Li, P.K.M. Maitz, Burn injury: challenges and advances in burn wound healing, infection, pain and scarring, Adv Drug Deliv Rev 123 (2018) 3–17. https://doi.org/ 10.1016/j.addr.2017.09.018.
[384] H. Cho, M.R. Blatchley, E.J. Duh, S. Gerecht, Acellular and cellular approaches to improve diabetic wound healing, Adv Drug Deliv Rev 146 (2019) 267–288. https://doi.org/10.1016/J.ADDR.2018.07.019.
[385] M. Abrigo, S.M.-M. bioscience, undefined 2014, Electrospun nanofibers as dressings for chronic wound care: advances, challenges, and future prospects, Macromol Biosci. 14 (2014) 772–792. https://doi.org/10.1002/mabi.201300561.
[386] S. Dhivya, V.V. Padma, E. Santhini, Wound dressings - A review, BioMedicine (Netherlands) 5 (2015) 24–28. https://doi.org/10.7603/S40681-015-0022-9.
[387] P. Cavanagh, B. Lipsky, A. Bradbury, G. Botek Treatment for diabetic foot ulcers, Lancet 366 (2005) 1725-1735. https://doi.org/ 10.1016/S0140-6736(05)67699-4.
[388] G. Akopian, S.P. Nunnery, J. Piangenti, P. Rankin, C. Rinoie, E. Lee, M. Alexander, Outcomes of conventional wound treatment in a comprehensive wound center, Am Surg 72 (2006) 314–317. https://doi.org/10.1177/000313480607200407.
[389] V. Falanga Wound healing and its impairment in the diabetic foot, 366 (2005) 1736 – 1743 https://doi.org/10.1016/S0140-6736(05)67700-8.
[390] S. Werner, T. Krieg, H. Smola, Keratinocyte–fibroblast interactions in wound healing, J Invest Dermatol 127 (2007) 998–1008. https://doi.org/ 10.1038/sj.jid.5700786.
[391] N.H. Mansoub, M. Gürdal, E. Karadadaş, H. Kabadayi, S. Vatansever, G. Ercan, The role of PRP and adipose tissue-derived keratinocytes on burn wound healing in diabetic rats, Bioimpacts 8

(2018) 5. https://doi.org/ 10.15171/bi.2018.02.
[392] P. Hiebert, S. Werner, Regulation of wound healing by the NRF2 transcription factor—More than cytoprotection, Int J Mol Sci 20 (2019) 3856. https://doi.org/ 10.3390/ijms20163856.
[393] P. Victor, D. Sarada, K.M. Ramkumar, Pharmacological activation of Nrf2 promotes wound healing, Eur J Pharmacol 886 (2020) 173395. https://doi.org/ 10.1016/j.ejphar.2020.173395.
[394] Q. Ma, Role of nrf2 in oxidative stress and toxicity, Annu Rev Pharmacol Toxicol 53 (2013) 401–426. https://doi.org/10.1146/annurev-pharmtox-011112-140320.
[395] T.A. Beyer, U. Auf dem Keller, S. Braun, M. Schäfer, S. Werner, Roles and mechanisms of action of the Nrf2 transcription factor in skin morphogenesis, wound repair and skin cancer, Cell Death Differ 14 (2007) 1250.https://doi.org/10.1038/sj.cdd.4402133.
[396] J. Kim, Y.-N. Cha, Y.-J. Surh, A protective role of nuclear factor-erythroid 2-related factor-2 (Nrf2) in inflammatory disorders, Mutat Res 690 (2010) 12–23. https://doi.org/ 10.1016/j.mrfmmm.2009.09.007.
[397] N. Ambrozova, J. Ulrichova, A. Galandakova, Models for the study of skin wound healing. The role of Nrf2 and NF-κB., Biomed Pap Med Fac Univ Palacky Olomouc Czech Repub 161 (2017) 1-13. https://doi.org/ 10.5507/bp.2016.063.
[398] Y. Liu, X. Yang, Y. Liu, T. Jiang, S. Ren, J. Chen, H. Xiong, M. Yuan, W. Li, H. Machens, NRF2 signalling pathway: new insights and progress in the field of wound healing, J Cell Mol Med 25 (2021) 5857–5868. https://doi.org/ 10.1111/jcmm.16597.
[399] P. Ramhormozi, J. Mohajer Ansari, S. Simorgh, M. Nobakht, Bone marrow-derived mesenchymal stem cells combined with simvastatin accelerates burn wound healing by activation of the Akt/mTOR pathway, J Burn Care Res 41 (2020) 1069–1078. https://doi.org/ 10.1093/jbcr/iraa005.
[400] S. Dağaşan, Insulin Structure, Function and Diabetes Models in Animals, Journal of Experimental and Basic Medical Sciences 1 (2021) 96–101. https://doi.org/10.5606/JEBMS.2020.75622.
[401] X. Li, Y. Liu, J. Zhang, R. You, J. Qu, M. Li, Functionalized silk fibroin dressing with topical bioactive insulin release for accelerated chronic wound healing.,Mater Sci Eng C Mater Biol Appl. 72 (2017) 394–404. https://doi.org/10.1016/J.MSEC.2016.11.085.
[402] D.H. Abdelkader, M.A. Osman, S.A. El-Gizawy, S.J. Hawthorne, A.M. Faheem, P.A. McCarron, Effect of poly(ethylene glycol) on insulin stability and cutaneous cell proliferation in vitro following cytoplasmic delivery of insulin-loaded nanoparticulate carriers – a potential topical wound management approach, Eur J Pharm Sci 114 (2018) 372–384. https://doi.org/10.1016/J.EJPS.2017.12.018.
[403] R. Khan, Functionalized nanomaterials targeting NLRP3 inflammasomes driven immunomodulation: Friend or Foe, Nanoscale 15 (2023) 15906-15928. https://doi.org/ 10.1039/d3nr03857b.
[404] V. Gowd, A. Ahmad, M. Tarique, M. Suhail, T.A. Zughaibi, S. Tabrez, R. Khan, Advancement of cancer immunotherapy using nanoparticles-based nanomedicine, in: Semin Cancer Biol, 86 (2022) 624–644. https://doi.org/ 10.1016/j.semcancer.2022.03.026.
[405] D.H. Abdelkader, M.M. Tambuwala, C.A. Mitchell, M.A. Osman, S.A. El-Gizawy, A.M. Faheem, M. El-Tanani, P.A. McCarron, Enhanced cutaneous wound healing in rats following topical delivery of insulin-loaded nanoparticles embedded in poly(vinyl alcohol)-borate hydrogels, Drug Deliv Transl Res 8 (2018) 1053–1065. https://doi.org/10.1007/S13346-018-0554-0/FIGURES/8.
[406] M. Quitério, S. Simões, A. Ascenso, M. Carvalheiro, A.P. Leandro, I. Correia, A.S. Viana, P. Faísca, L. Ascensão, J. Molpeceres, Development of a Topical Insulin Polymeric Nanoformulation for Skin Burn Regeneration: An Experimental Approach, Int J Mol Sci 22 (2021) 4087. https://doi.org/ 10.3390/ijms22084087.
[407] X. Sun, Y. Zhang, J. Cui, C. Zhang, C. Xing, H. Bian, J. Lv, D. Chen, L. Xiao, J. Su, Advanced multilayer composite dressing with co-delivery of gelsevirine and silk fibroin for burn wound healing, Compos B Eng 253 (2023) 110549. https://doi.org/0.1016/j.compositesb.2023.110549.
[408] R. Huang, J. Hu, W. Qian, L. Chen, D. Zhang, Recent advances in nanotherapeutics for the treatment of burn wounds, Burns Trauma 9 (2021) tkab026. https://doi.org/10.1093/burnst/tkab026.

[409] M. Repka, J. Reo, L. Felton, S. Howard, A. Chaudhury, S. Das, Recent Advancement of Chitosan-Based Nanoparticles for Oral Controlled Delivery of Insulin and Other Therapeutic Agents, AAPS PharmSciTech 12 (2010) 10–20. https://doi.org/10.1208/S12249-010-9561-2.
[410] S. Hajji, I. Younes, O. Ghorbel-Bellaaj, R. Hajji, M. Rinaudo, M. Nasri, K. Jellouli, Structural differences between chitin and chitosan extracted from three different marine sources, Int J Biol Macromol 65 (2014) 298–306. https://doi.org/10.1016/J.IJBIOMAC.2014.01.045.
[411] H. Liu, C. Wang, C. Li, Y. Qin, Z. Wang, F. Yang, Z. Li, J. Wang, A functional chitosan-based hydrogel as a wound dressing and drug delivery system in the treatment of wound healing, RSC Adv 8 (2018) 7533–7549. https://doi.org/10.1039/C7RA13510F.
[412] W. Gao, J.C.K. Lai, S.W. Leung, Functional enhancement of chitosan and nanoparticles in cell culture, tissue engineering, and pharmaceutical applications, Front Physiol 3 (2012) 321. https://doi.org/10.3389/fphys.2012.00321.
[413] T. Dai, M. Tanaka, Y.-Y. Huang, M.R. Hamblin, Chitosan preparations for wounds and burns: antimicrobial and wound-healing effects, Expert Rev Anti Infect Ther 9 (2011) 857–879. https://doi.org/10.1586/eri.11.59.
[414] B. Ter Horst, G. Chouhan, N.S. Moiemen, L.M. Grover, Advances in keratinocyte delivery in burn wound care, Adv Drug Deliv Rev 123 (2018) 18–32. https://doi.org/10.1016/j.addr.2017.06.012.
[415] M.M. Ansari, A. Ahmad, R.K. Mishra, S.S. Raza, R. Khan, Zinc gluconate-loaded chitosan nanoparticles reduce severity of collagen-induced arthritis in Wistar rats, ACS Biomater Sci Eng 5 (2019) 3380–3397. https://doi.org/10.1021/acsbiomaterials.9b00427.
[416] K.-T. Le, C.-T. Nguyen, T.-D. Lac, L.-G.T. Nguyen, T.L. Tran, H. Tran-Van, Facilely preparing carboxymethyl chitosan/hydroxyethyl cellulose hydrogel films for protective and sustained release of fibroblast growth factor 2 to accelerate dermal tissue repair, J Drug Deliv Sci Technol 82 (2023) 104318. https://doi.org/10.1016/j.ddst.2023.104318.
[417] Z. Zhu, F. He, H. Shao, J. Shao, Q. Li, X. Wang, H. Ren, C. You, Z. Zhang, C. Han, Chitosan/Alginate Nanoparticles with Sustained Release of Esculentoside A for Burn Wound Healing, ACS Appl Nano Mater 6 (2023) 573–587. https://doi.org/10.1021/acsanm.2c04714.
[418] K. Attri, B. Chudasama, R.L. Mahajan, D. Choudhury, Therapeutic potential of lactoferrin-coated iron oxide nanospheres for targeted hyperthermia in gastric cancer, Sci Rep 13 (2023) 17875. https://doi.org/10.1038/s41598-023-43725-3.
[419] A. Ahmad, M.M. Ansari, R.K. Mishra, A. Kumar, A. Vyawahare, R.K. Verma, S.S. Raza, R. Khan, Enteric-coated gelatin nanoparticles mediated oral delivery of 5-aminosalicylic acid alleviates severity of DSS-induced ulcerative colitis, Mater Sci Eng C 119 (2021) 111582. https://doi.org/10.1016/j.msec.2020.111582.
[420] M. Bin Ahmad, J.J. Lim, K. Shameli, N.A. Ibrahim, M.Y. Tay, Synthesis of silver nanoparticles in chitosan, gelatin and chitosan/gelatin bionanocomposites by a chemical reducing agent and their characterization, Molecules 16 (2011) 7237–7248. https://doi.org/10.3390/MOLECULES16097237.
[421] R. Punyamurthy, D. Sampathkumar, R.P.G. Ranganagowda, B. Bennehalli, C. V. Srinivasa, Mechanical properties of abaca fiber reinforced polypropylene composites: Effect of chemical treatment by benzenediazonium chloride, J King Saud Univ Eng Sci 29 (2017) 289–294. https://doi.org/10.1016/J.JKSUES.2015.10.004.
[422] R. Prakash, A. Vyawahare, R. Sakla, N. Kumari, A. Kumar, M.M. Ansari, Kanika, C. Jori, A. Waseem, A.J. Siddiqui, NLRP3 Inflammasome-Targeting Nanomicelles for Preventing Ischemia–Reperfusion-Induced Inflammatory Injury, ACS Nano 17 (2023) 8680–8693. https://doi.org/10.1021/acsnano.3c01760
[423] E.A. El-Hefian, M.M. Nasef, A.H. Yahaya, R.A. Khan, Preparation and characterization of chitosan/agar blends: Rheological and thermal studies. JChilean Chem Soc 55 (2010) 130–136. https://doi.org/10.4067/S0717-97072010000100031.
[424] S. Yasmeen, M. Kabiraz, B. Saha, Md. Qadir, Md. Gafur, S. Masum, Chromium (VI) Ions Removal from Tannery Effluent using Chitosan-Microcrystalline Cellulose Composite as Adsorbent, Int Res

J Pure Appl Chem 10 (2016) 1–14. https://doi.org/10.9734/IRJPAC/2016/23315.
[425] M. Szymanska-Chargot, A. Zdunek, Use of FT-IR Spectra and PCA to the Bulk Characterization of Cell Wall Residues of Fruits and Vegetables Along a Fraction Process, Food Biophys 8 (2013) 29–42. https://doi.org/10.1007/S11483-012-9279-7/TABLES/2.
[426] I. Kanungo, N.N. Fathima, R.R. Jonnalagadda, B.U. Nair, Go natural and smarter: fenugreek as a hydration designer of collagen based biomaterials, Phys Chem Chem Phys 17 (2015) 2778–2793. https://doi.org/10.1039/C4CP04363D.
[427] A.F. Martins, D.M. de Oliveira, A.G.B. Pereira, A.F. Rubira, E.C. Muniz, Chitosan/TPP microparticles obtained by microemulsion method applied in controlled release of heparin, Int J Biol Macromol 51 (2012) 1127–1133. https://doi.org/10.1016/J.IJBIOMAC.2012.08.032.
[428] Z. Chen, Y. Zhang, L. Ma, Y. Ni, H. Zhao, Nrf2 plays a pivotal role in protection against burn trauma-induced intestinal injury and death, Oncotarget 7 (2016) 19272. https://doi.org/10.18632/oncotarget.8189.
[429] J.J. Wen, K. Mobli, V.G. Rontoyanni, C.B. Cummins, G.L. Radhakrishnan, A. Murton, R.S. Radhakrishnan, Nuclear Factor Erythroid 2–Related Factor 2 Activation and Burn-Induced Cardiac Dysfunction, J Am Coll Surg 234 (2022) 660–671. https://doi.org/10.1097/XCS.0000000000000119.
[430] S.M. Moghimi, D. Peer, R. Langer, Reshaping the future of nanopharmaceuticals: ad iudicium, ACS Nano 5 (2011) 8454–8458. https://doi.org/10.1021/nn2038252.

Appendices

Appendix – I Challenges in the Synthesis and Applications of Protein-templated nano-formulations

The synthesis of protein-templated metal nano-formulations introduces unique challenges due to the specific interactions between proteins and metal ions or nanoparticles, which can affect their stability, bioavailability, and applications. Thus, addressing these issues is critical to have effective and efficient nano-formulations that can be used further in distinct biological applications.

1. **Synthesis of monometallic nanoformulations –** The synthesis of cobalt based nanoformulations was quite difficult. I have tried it with multiple concentrations and as I go on increasing the concentration of salt solution, the protein starts precipitating. Thereafter, I went on decreasing the salt concentration and used 3 distinct concentrations that is 50 µM, 60 µM and 70 µM and get the best results in particles synthesised using metal salt having concentration 60 µM.
2. **Synthesis of Bimetallic nanosubclusters –** For synthesising bimetallic nnaosublclusters, I have followed different methods. Firstly, I have added both the salt solutions that is silver nitrate and copper sulphate together in the insulin protein but no results were obtained. Thereafter, I have separately synthesised silver and copper nanoparticles using insulin protein and after 24 hours incubated them together for another 24 hours but no particles were obtained. Finally, I have separately synthesised silver nanoparticles using quercetin and simultaneously prepared insulin-copper quantum clusters using previously reported method and then incubated them together and hence obtained the desired bimetallic nano-subclusters.
3. **Protein stability and functionality** – Maintaining the stability and functionality of protein is essential as proteins are susceptible to denaturation by chemical and physical conditions provided during the synthesis of nanoparticles. Further, these conditions can affect or deactivate the functional groups or binding sites required for metal ions to bind. To avoid such issues, I used mild reaction conditions, which include near-neutral pH (~7.4) and a temperature of 37 ˚C to attain enhanced stability.
4. **Aggregation and size control issues** – High surface energy of nanoparticles leads to aggregation, and even protein-mediated aggregation can compromise the stability of synthesized nanoformulations. To prevent this aggregation, the formulations were stored in an inert atmosphere or at low temperatures (4 ˚C). Similarly, nucleation and growth can compete, causing polydispersity. Thus, to avoid that, I have followed a real-time monitoring technique (UV-Vis Spectroscopy) to track nanoparticle growth.
5. **Analytical and characterization challenges** – Generally, the difficulty is faced while analyzing the protein-nanoparticle interface at the molecular level. Also, tools are limited to examining the size, shape, and distribution of nanoparticles in the protein matrix. To overcome this issue, I have used high-resolution techniques like TEM (Transmission Electron Microscopy), STEM (Scanning Transmission Electron Microscopy), and FE-SEM (Field Emission Scanning Electron Microscopy). Further, to determine the protein's structural integrity, I used spectroscopy techniques like CD (Circular Dichroism) and FTIR (Fourier Transform Infrared Spectroscopy).
6. **Long-term stability** – Metal nanoparticles are prone to oxidation and reduction, and protein may also lose functionality over time, primarily based on storage conditions. To prevent that, I have freeze dried the samples and stored them at low temperature conditions to increase the shelf-life.
7. **Cell culture** – As I need to use cell culture for all the *in vitro* studies, thus maintaining the cell culture without any contamination is itself a task. To ensure a contamination-free environment, I have followed all the general guidelines to maintain aseptic conditions in the culture lab and get the tests done smoothly.

Despite facing multiple challenges in distinct stages of my research, I remained determined to get over them and achieve success. The entire journey was full of hardships, yet I was able to get through all the hurdles by remaining motivated and determined throughout. The guidance, mentorship, and expertise of my supervisor in this field were sufficient to get me through all difficulties and helped me ultimately positively complete my Ph.D. work. His contributions significantly uplifted my skills, boosted my confidence, and led to my professional and academic development.

LIST OF PUBLICATIONS

1. **Sharda. D,** and Choudhury. D. Insulin-cobalt core-shell nanoparticles for receptor-targeted bioimaging and diabetic wound healing, *RSC Advances*, 2023, 13, 20321-20335. **(IF: 3.9).**
2. **Sharda. D,** and Choudhury. D. Insulin-infused bimetallic nano-subclusters as a functional agent for ROS scavenging, antibacterial resilience, and accelerated *in vitro* cell migration, *Materials Advances*, 2024, Just accepted, Ahead of print **(IF: 5.0).**
3. **Sharda. D,** Attri. K, Kaur. P, and Choudhury. D. Protection of lead-induced cytotoxicity using paramagnetic nickel–insulin quantum clusters, *RSC Advances*, 2021, 11, 24656-24668. **(IF: 3.9).**
4. **Sharda. D,** Kaur. P, and Choudhury. D. Protein modified nanomaterials: Emerging trends in skin wound healing. *Discover Nano*, 2023. **(IF: 5.5).**
5. **Sharda. D,** Ghosh. S, Kaur. P, Basu. B, and Choudhury. D. Chitosan-insulin nano-formulations as critical modulators of inflammatory cytokines and Nrf-2 pathway to accelerate burn wound healing. *Discover Nano*, 2023. **(IF: 5.5).**
6. **Sharda. D,** Attri. K, and Choudhury. D. Greener healing: Sustainable Nanotechnology for Advanced Wound Care. *Discover Nano*, 2023. **(IF: 5.5).**

OTHER PUBLICATIONS

1. Aggarwal. M, **Sharda. D**, Srivastava. S, Kotnees. D.K., Choudhury. D and Das. P. Carbonized polymer dot-tannic acid nanoglue: Tissue reinforcement with concurrent fluorescent tracking, insulin delivery, and reactive oxygen species regulation for normal and diabetic wound healing, *Small*, 2024, 2405531. **(IF: 13.3).**
2. Attri. K, **Sharda. D**, Chudasama. B, Mahajan, R.L., and Choudhury. D. A Review on Terpenes for Treatment of Gastric Cancer: Current Status and Nanotechnology-enabled Future, *RSC Sustainability*, 2023, 1, 1109-1124.
3. Priya. R, Kaur. D, Attri. K, Kaur. S, **Sharda. D**, Choudhury. D, and Pandey. O.P. Structural, luminescent and in vitro studies of europium-doped soda lime phosphate glasses, *Luminescence*, 2023, 39. **(IF: 2.9).**
4. Datta. S, Chakroborty. N. K, **Sharda. D**, Attri. K, and Choudhury. D. COVID-19 Pandemic in India: Chronological comparison of the regional heterogeneity in the progression of the pandemic and gaps in mitigation strategies, *Journal of clinical trials*, 2021. **(IF: 2.76).**

BOOK CHAPTERS

1. **Sharda. D**, Attri. K, and Choudhury. D. Book Chapter "Regulation of cytokines in wound healing by silk fibroin," 2023. Book Title: *Silk fibroin: Advances in Applications and Research, by Nova Science Publishers, New York, USA*, Editor: Shivaji Pawar.

2. **Sharda. D**, Attri. K, and Choudhury. D. Book Chapter "Future research directions of antimicrobial wound dressings," 2023. Book Title: *Antimicrobial Dressings: The Wound Care Applications, by Elsevier,* Editor: Raju Khan and V. Sorna Gowri.

3. **Sharda. D**, Attri. K, and Choudhury. D. Book Chapter "Characterization techniques used for advanced materials describing physical, mechanical, thermal and biocompatibility properties" 2024. Book Title: *Advanced Materials: Production, Characterization and Multidisciplinary Applications. by Taylor & Francis,* Editor: Mahendra Gaikwad, Arpana Parihar, and Raju Khan.

CONFERENCES ATTENDED

1. International Conference on Emerging Trends in Science and Technology, Organised by Dept. of Applied Sciences, Punjab Engineering College, Chandigarh. (10-11 June, 2022). **(Poster Presentation)**
2. 14th Annual Meeting of the Korean Society of Medical Oncology and 2021 International Conference held in Seoul, Korea (2-3 September 2021). **(Online mode)**
3. 13th in series and 1st International Conference on Recent Advances in Chemistry- 2023, held at Dept. of Chemistry, Punjabi University, Patiala (**Poster Presentation**).
4. 16th Annual Meeting of the Korean Society of Medical Oncology & 2023 International Conference, 11th International FACO Conference, 7-8 September, 2023. **(Online mode)**
5. 3rd International Conference on Integrative Chemistry, Biology, and Translational Medicine, Jointly Organised by Pacific University Udaipur, Hansraj College (Delhi University), and Heterochem Innotech Private Limited at Udaipur, Rajasthan. (8-10 March, 2024). **(Oral presentation) (Certificate of Appreciation).**

RSC Advances

PAPER

Cite this: *RSC Adv.*, 2023, 13, 20321

Insulin–cobalt core–shell nanoparticles for receptor-targeted bioimaging and diabetic wound healing†

Deepinder Sharda[a] and Diptiman Choudhury *[ab]

Diabetic wounds represent a major issue in medical care and need advanced therapeutic and tissue imaging systems for better management. The utilization of nano-formulations involving proteins like insulin and metal ions plays significant roles in controlling wound outcomes by decreasing inflammation or reducing microbial load. This work reports the easy one-pot synthesis of extremely stable, biocompatible, and highly fluorescent insulin–cobalt core–shell nanoparticles (ICoNPs) with enhanced quantum yield for their highly specific receptor-targeted bioimaging and normal and diabetic wound healing *in vitro* (HEKa cell line). The particles were characterized using physicochemical properties, biocompatibility, and wound healing applications. FTIR bands at 670.35 cm^{-1}, 849.79, and 973.73 indicating the Co–O bending, CoO–OH bond, and Co–OH bending, respectively, confirm the protein–metal interactions, which is further supported by the Raman spectra. *In silico* studies indicate the presence of cobalt binding sites on the insulin chain B at 8 GLY, 9 SER, and 10 HIS positions. The particles exhibit a magnificent loading efficiency of 89.48 ± 0.049% and excellent release properties (86.54 ± 2.15% within 24 h). Further, based on fluorescent properties, the recovery process can be monitored under an appropriate setup, and the binding of ICoNPs to insulin receptors was confirmed by bioimaging. This work helps synthesize effective therapeutics with numerous wound-healing promoting and monitoring applications.

Received 5th March 2023
Accepted 28th June 2023

DOI: 10.1039/d3ra01473h

rsc.li/rsc-advances

1. Introduction

Wound healing is a complex process involving a sequential overlapping cascade of events that comes into action in response to some external chemical or physical stimuli and eventually causes healing by restoring lost tissue.[1] The healing process is categorized into four phases, hemostasis, inflammation, proliferation, and remodeling.[2] The hemostasis is initiated by clot formation due to platelets' activation, which prevents microbial infestation and promotes matrix organization. In proliferation, the accumulation of cells, connective tissue, growth factors, and angiogenesis factors across the wound occurs. The remodeling involves the resynthesis of the extracellular matrix to maintain the balance between the death of existing cells and the formation of new cells.[3,4] However, the progress monitoring of recovery of wounds always remains a significant challenge. In some instances, normal healing gets disrupted. It gets arrested in one of the phases due to the loss of balance in the physiological mechanism of healing due to infection, chronic irritation, trauma, the persistence of microbes or other foreign bodies, and ischemia, making the wound a chronic one[5–7] which can be prevented by keeping the wound moist, removing the dead tissues, covering the injury to avoid bacterial infection, and removing the excess tissue fluid.[8]

Apart from these issues, the major problem for delayed healing is diabetes mellitus or long-term hyperglycemia, which alters the secretion of cytokines, making wound healing cumbersome.[9] In diabetic conditions, there is the prolonged proinflammatory phase due to the persistent release of proteases, proinflammatory cytokines, and reactive oxygen species and the delayed anti-inflammatory phase because of the low secretion of anti-inflammatory cytokines.[10] Further, the transport of nutrients to the wound site is prevented by atherosclerosis caused by diabetes.[11] It also results in the dysfunction of endothelial cells due to vasodilation induced by pressure[12] and disrupts the processes essential for re-epithelialization; the proliferation of keratinocytes and fibroblasts, synthesis of proteins, and cell migration.[13–15] Further, it impairs the body's immune response, making the wounds prone to infection and leading to damaged structural components of the extracellular matrix.[7] It also causes free radical damage due to the reduced activity of certain antioxidant enzymes such as glutathione peroxidase and superoxide dismutase.[16] Various advanced

[a]*School of Chemistry and Biochemistry, Thapar Institute of Engineering and Technology, Patiala, 147004, Punjab, India. E-mail: diptiman@thapar.edu; Tel: +91-8196949843*

[b]*Thapar Institute of Engineering and Technology-Virginia Tech (USA) Center of Excellence in Emerging Materials, Thapar Institute of Engineering and Technology, Patiala, Punjab-147004, India*

† Electronic supplementary information (ESI) available. See DOI: https://doi.org/10.1039/d3ra01473h

Materials Advances

ROYAL SOCIETY OF CHEMISTRY

PAPER

View Article Online
View Journal

Cite this: DOI: 10.1039/d4ma00278d

Insulin-infused bimetallic nano-subclusters as a multifunctional agent for ROS scavenging, antibacterial resilience, and accelerated *in vitro* cell migration†

Deepinder Sharda[a] and Diptiman Choudhury *[ab]

This is the first report on the synthesis and wound healing application of green synthesized insulin-infused bimetallic (copper–silver) nano-subclusters (ICu–AgNSCs) with high stability, aqueous solubility, biocompatibility, and target specificity. HRTEM and SAED data confirm octahedral particles (with a diameter of 9.6 2.2 nm) composed of discrete copper clusters on the periphery and a silver core that are further infused with an insulin corona (0.5 0.2 nm), as confirmed by the characteristics of Cu–OH and Ag–O stretching bonds and alteration in insulin amide bonds. The ICu–AgNSCs had high insulin loading efficiency (93.90 1.05%) and a high drug release rate (92.69 0.90% within 40 h), making them ideal for sustained release applications. Wound healing in diabetic conditions gets delayed due to the pro - longed proinflammatory phase and microbial infestation, which may lead to clinical amputation. Therefore, advanced therapeutics that promote cell growth by reducing inflammation and microbial growth are required. ICu–AgNSCs may satisfy all these criteria. Insulin and quercetin have ROS scavenging and anti-inflammatory properties. Insulin and copper have cellular growth-promoting activity; additionally, silver has antimicrobial properties. ICu–AgNSCs have been shown to accelerate diabetic cell migration *in vitro*, making them an ideal choice for pre-clinical and clinical applications.

Received 16th March 2024,
Accepted 4th May 2024

DOI: 10.1039/d4ma00278d

rsc.li/materials-advances

1. Introduction

Wound healing is a significant challenge for the scientific community despite all the available treatments, and the global expenditure on healing wounds ranges from $28.1 to $96.8 billion.[1] Healing is a complex event involving overlapping phases, which work together against the damage and restore the lost tissue or organ.[2] Healing begins with hemostasis, which involves the activation of platelets, clot formation, and matrix organization. In proliferation, the accumulation of growth factors, connective tissues, and angiogenesis factors occurs at the wound site. In the inflammatory phase, the proinflammatory cytokines promote vasodilation and activate the different signaling pathways. The resynthesis of the extracellular matrix occurs in the remodeling phase to maintain the balance between dead and live cells.[3,4] However, certain factors disrupt the normal physiological mechanism of wound healing, including microbial infection, trauma, ischemia, and diabetes mellitus,[5,6] which can be avoided by preventing bacterial infestation, removing the dead tissue and debris, and keeping the wound moist.[7] In diabetes, there is persistent release of proteases, proinflammatory cytokines, reactive oxygen species, and low secretion of anti-inflammatory cytokines.[8] Diabetic wounds are more susceptible to infection due to the body's immune response impairment.[6] The activity of different antioxidant enzymes, including glutathione peroxidase and superoxide dismutase, is reduced, which leads to damage by free radical generation.[9] Diabetes also affects protein synthesis, re-epithelialization, cell migration, and proliferation of fibroblasts and keratinocytes by preventing the transport of nutrients to the wound site.[10,11] Reactive oxygen species (ROS) generation is also a major issue as their accumulation prevents the efficient functioning of macrophages and endogenous stem cells. Also, ROS causes endothelial dysfunction and restricts angiogenesis.[12] Additionally, ROS generation due to bacterial infection leads to chronic wound infection by damaging endothelial cells and blood vessels.[13,14]

To promote healing, tremendous research is going on to develop novel formulations that are biocompatible, efficient, environment-friendly, and cost-effective. Here, the role of nanoparticles comes into play as they possess massive potential in

[a] *Department of Chemistry and Biochemistry, Thapar Institute of Engineering and Technology (TIET), Patiala-147004, Punjab, India*
[b] *Center of Excellence in Emerging Materials (CEEMS), Thapar Institute of Engineering and Technology, Patiala, Punjab-147004, India. E-mail: diptiman@thapar.edu; Tel: +91-8196949843*

† Electronic supplementary information (ESI) available. See DOI: https://doi.org/10.1039/d4ma00278d

RSC Advances

PAPER

Cite this: *RSC Adv.*, 2021, 11, 24656

Protection of lead-induced cytotoxicity using paramagnetic nickel–insulin quantum clusters†

Deepinder Sharda,[a] Komal Attri,[ab] Pawandeep Kaur[a] and Diptiman Choudhury *[ab]

Received 8th May 2021
Accepted 29th June 2021

DOI: 10.1039/d1ra03597e

rsc.li/rsc-advances

Pb-toxicity is associated with inflammation which leads to delay in wound healing. Pb^{2+} utilizes calcium ion channels to enter the cell. Therefore, to achieve effective healing in a Pb-poisoned system, capturing Pb^{2+} from the circulatory system would be an effective approach without hampering the activity of the calcium ion channel. In this work insulin–nickel fluorescent quantum clusters (INiQCs) have been synthesized and used for the specific detection of Pb^{2+} ions *in vitro* and in cell-free systems. INiQCs (0.09 mM) can detect Pb^{2+} concentrations as low as 10 pM effectively in a cell-free system using the fluorescence turn-off method. *In vitro* INiQCs (0.45 mM) can detect Pb^{2+} concentrations as low as 1 mM. INiQCs also promote wound healing which can easily be monitored using the bright fluorescence of INiQCs. INiQCs also help to overcome the wound recovery inhibitory effect of Pb^{2+} *in vitro* using lead nitrate. This work helps to generate effective biocompatible therapeutics for wound recovery in Pb^{2+} poisoned individuals.

1. Introduction

Lead, a highly toxic, non-biodegradable element found ubiquitously in nature, causes environmental pollution, affects the human body to a large extent, and is among 275 most hazardous substances in the list of the Environmental Protection Agency (EPA), formulated by the Agency for Toxic Substances and Disease Registry (ATSDR).[1] Lead affects around 0.6% of the population globally[1] and causes acute and chronic toxicity even in minute quantities. Certain heavy metals, including Pb^{2+}, Cd^{2+}, and Hg^{2+}, can enter the body through food, water, smoking, industrial means, and even the skin surface, leading to heavy metal poisoning.[2,3] 600 ppm of lead is suggested as a "safe" level in the soil and would contribute under 5 mg dL^{-1} to total blood lead of children below 12 years.[4] There is no relaxation in the maximum permissible limit for lead in water which was set at 0.05 ppm and is the highest desirable amount in drinking water in India. According to WHO, 1993, 25 mg L^{-1} lead per kg body weight is the maximum tolerable amount weekly.[5] The daily exposure to Pb^{2+} causes its deposition in body parts including liver, kidneys, spleen, and brain, causing multiple tissue damage by inducing oxidative stress. Moreover, long-term exposure to lead causes inflammatory infiltration, alterations in tissues of testicles, reduction in spermatocytes, necrosis of hepatocytes, degeneration of renal tubules, hypertrophy in the renal epithelium and induces endoplasmic reticulum stress due to calcium imbalance in the liver and kidney.[6,7] Kidneys are prone to the oxidative reaction of lead as lead intoxication sometimes causes dysfunctioning of proximal tubule or irreversible nephropathy depending on exposure regimens, thus adversely affecting the health of kidney function along with cadmium and mercury[8–10] and can be excreted through urine and feces.[11] It affects central nervous system causing several neurological disturbances affects the blood–brain barrier and causes edema and loss of neurons. The astroglial activation in the brain leads to pathological processes causing the death of neuronal cells, which causes the release of cytokines and chemokines, causing the inflammatory effect.[12] Also, children exposed to environmental lead are at a higher risk of toxicity because of absorption of ingested lead from the gastrointestinal tract and nervous system becoming more susceptible to neurotoxins.[13] Pb^{2+} has a carcinogenic effect by damaging the DNA and disrupting its repair system by generating ROS (reactive oxygen species). It can even impair memory and learning in the brain by disrupting NMDAR (*N*-methyl-D-aspartate receptors).[14] Lead causes damage to epithelial tissues causes rashes and get accumulated over the epidermal surface.[15,16] Lead toxicity is dosage-dependent and include cellular traction forces, mechanical stiffness, focal adhesions, the shape of the cell, speed of migration, permeability, and wound healing efficacy in mammalian cells.[17–19]

At the molecular level, lead affects the humoral and cellular immune responses through various inflammatory biomarkers[20] including cytokines (IL-8, TNF, *etc.*), acute phase proteins including CRP, haptoglobin, and ceruloplasmin, enzymes involved in inflammation such as COX-2 and damages

[a]*School of Chemistry and Biochemistry, Thapar Institute of Engineering and Technology, Patiala, 147004, Punjab, India. E-mail: diptiman@thapar.edu; Tel: +91-8196949843*

[b]*Thapar Institute of Engineering and Technology-Virginia Tech (USA) Center of Excellence in Emerging Materials, Thapar Institute of Engineering and Technology, Patiala, Punjab-147004, India*

† Electronic supplementary information (ESI) available. See DOI: 10.1039/d1ra03597e

Discover Nano

Discover

Review

Protein-modified nanomaterials: emerging trends in skin wound healing

Deepinder Sharda[1] · Pawandeep Kaur[1] · Diptiman Choudhury[1,2]

Received: 13 May 2023 / Accepted: 23 September 2023
Published online: 16 October 2023

Abstract

Prolonged inflammation can impede wound healing, which is regulated by several proteins and cytokines, including IL -4, IL-10, IL-13, and TGF-β. Concentration-dependent effects of these molecules at the target site have been investigated by researchers to develop them as wound-healing agents by regulating signaling strength. Nanotechnology has provided a promising approach to achieve tissue-targeted delivery and increased effective concentration by developing protein-functionalized nanoparticles with growth factors (EGF, IGF, FGF, PDGF, TGF-β, TNF-α, and VEGF), antidiabetic wound-healing agents (insulin), and extracellular proteins (keratin, heparin, and silk fibroin). These molecules play critical roles in promoting cell proliferation, migration, ECM production, angiogenesis, and inflammation regulation. Therefore, protein-functionalized nanoparticles have emerged as a potential strategy for improving wound healing in delayed or impaired healing cases. This review summarizes the preparation and applications of these nanoparticles for normal or diabetic wound healing and highlights their potential to enhance wound healing.

Keywords Wound healing · Nanoformulations · Growth factors · Proteins · Antidiabetic agents

Introduction

Nanomaterials have high drug-loading efficacy, which can be attributed to a high surface area-to-volume ratio. They respond quickly to any minute alteration in the surrounding environment, like a magnetic field, pH, and temperature [1]. The bionanomaterials like peptides, biomolecules, enzymes, and protein-functionalized formulations have various biological applications ranging from bioimaging [2], catalysis [3], fluorescent biolabeling [4, 5] hyperthermia [6, 7] tissue engineering [8], gene and drug delivery [9, 10], and so on. Moreover, protein-functionalized and stabilized nanomaterials exhibit numerous features such as sensing, biocompatibility, plasmon-enhanced catalysis, targeted nanocarriers, and drug delivery [11, 12]. The constituting units of the proteins behave not only as reducing and chelating agents that help in developing nanoclusters but also allow crystalline [13, 14] and amorphous [15] growth of the nanostructures of different sizes and shapes [16]. The target-specific binding ability of proteins enhances their action efficiency and helps to cure the wound [15, 17]. However, the poor permeability through membranes, short half-life, and high enzymatic degradation risk pose a serious issue to the targeted delivery of potent therapeutic proteins to the site and thus require

Deepinder Sharda and Pawandeep Kaur have contributed equally to this work.

✉ Diptiman Choudhury, diptiman@thapar.edu | [1]School of Chemistry and Biochemistry, Thapar Institute of Engineering and Technology, Patiala, Punjab 147004, India. [2]Thapar Institute of Engineering and Technology-Virginia Tech Centre of Excellence for Emerging Materials, Thapar Institute of Engineering and Technology, Patiala, Punjab 147004, India.

Discover Nano

Research

Chitosan-insulin nano-formulations as critical modulators of inflammatory cytokines and Nrf-2 pathway to accelerate burn wound healing

Deepinder Sharda[1] · Sandip Ghosh[2] · Pawandeep Kaur[1] · Biswarup Basu[2] · Diptiman Choudhury[1,3]

Received: 20 September 2023 / Accepted: 8 December 2023
Published online: 12 December 2023

Abstract
Burn injuries are characterized by prolonged inflammatory phases, neurovascular damage, and hypermetabolism, eventually causing improper tissue regeneration. Insulin has gained considerable attention in normal and diabetic wound healing, yet its role in burn wounds remains poorly understood. In this study, insulin-chitosan nano-formulations (ICNP) were synthesized using a simple and robust mechanism and characterized to monitor specific interactions between insulin and chitosan, and the particles measuring approximately 30 nm in size exhibited mild alterations in the amide I, II, and III bonds of the insulin protein along with impressive insulin loading efficiency of 88.725 ± 0.295% under physiological conditions, and significantly improved burn wound healing in vitro (HEKa cells) and in vivo (murine third-degree burn model). The underlying mechanism behind superior wound closure and tissue remodeling was attributed to significant early phase reduction of pro-inflammatory cytokine IL-6 levels in ICNP-treated mice, while anti-inflammatory cytokine IL-10 levels became markedly elevated, resulting in enhanced re-epithelialization and collagen deposition. Furthermore, treatment of ICNP was associated with unregulated expression of Nrf-2, a key regulator of oxidative stress and inflammation, indicating their molecular crosstalk. These findings highlight the potential of ICNP as a promising therapeutic formulation for burn wound healing, promoting wound closure by modulating inflammatory phases, making it a valuable candidate for further clinical development in burn care.

Keywords Insulin · Chitosan · Burn wound healing · Inflammatory cytokines · Nrf-2 pathway

1 Introduction

Wound healing involves sequential phases, including inflammation, proliferation, and remodeling, to maintain tissue integrity [1, 2]. The cost of healing acute and chronic wounds ranges from $28.1 to $96.8 billion, with surgical wounds and diabetic ulcers incurring the highest expenses [3]. Burn injuries are particularly debilitating and painful, leading

Deepinder Sharda and Sandip Ghosh contributed equally.

Supplementary Information The online version contains supplementary material available at https://doi.org/10.1186/s11671-023-03941-2.

✉ Biswarup Basu, biswarup.basu@gmail.com; ✉ Diptiman Choudhury, diptiman@thapar.edu | [1]Department of Chemistry and Biochemistry, Thapar Institute of Engineering and Technology, Patiala, Punjab 147004, India. [2]Department of Neuroendocrinology and Experimental Hematology, Chittaranjan National Cancer Institute, Kolkata 700026, India. [3]Centre of Excellence for Emerging Materials, Thapar Institute of Engineering and Technology, Patiala, Punjab 147004, India.